

Superelastic Electron Scattering from Laser Excited States of Sodium

by

Robert Thomas Sang

B.Sc. (Hons.)

Griffith University

A thesis submitted in fulfilment of the
requirements for the degree of
Doctor of Philosophy

Faculty of Science and Technology

Griffith University

January, 1995

Abstract

This thesis presents the results of a series of experiments in which electrons are superelastically scattered from various laser excited states of sodium. The atoms, once in the optically prepared state, are forced to relax via the superelastic collision with an electron. The rate of detection of superelastically scattered electrons was measured as a function of the laser polarisation which enabled pseudo Stokes parameters to be determined. These pseudo Stokes parameters are functions of both optical pumping parameters and atomic collision parameters. The optical pumping parameters describe the laser-atom interaction and the atomic collision parameters describe the electron-atom collision process.

Three different laser excitation mechanisms were used to optically pump the atoms into various excited states. The first of these used a single laser tuned to the $3^2S_{1/2}(F'=2 \text{ hyperfine state}) \rightarrow 3^2P_{3/2}$ transition. The excited atoms underwent a superelastic collision with an electron leaving the atom in the ground state and pseudo Stokes parameters were measured as a function of both scattering angle and incident electron energy. The second superelastic experiment, utilised a folded step excitation mechanism which employed two lasers tuned from the two hyperfine states of the $3^2S_{1/2}$ ground state respectively to the $3^2P_{3/2}$ excited state. Power broadening effects in the single laser experiment cause the atoms to be optically pumped into the $F'=1$ hyperfine ground state. The laser powers used were not great enough to power broaden the hyperfine ground states and as such the $F'=1$ sublevel effectively acted as a sink. The folded step excitation method enabled the excited state population to be increased so that data at larger scattering angles could be obtained. Stokes parameters from both of these experiments which had an incident energy range of 10eV to 30eV and an angular range of 5° - 25° were compared to three current electron-atom scattering theories and previous experimental data. Overall, fair to good agreement was found between theory and

experiments for the individual Stokes parameters. Losses of coherence was observed at small scattering angles (5° - 20°) at 20eV and 25eV incident electron energies which were poorly modelled by the three different theories.

The third superelastic experiment involved the use of two lasers of specified polarisation to stepwise excite the atoms to the $3^2D_{5/2}$ excited state. Superelastic collisions with incident electron energies of 20eV from the $3^2D_{5/2} \rightarrow 3^2P_{3/2\&1/2}$ collision were studied at three different scattering angles and pseudo Stokes parameters for the case where the polarisations of the radiation from the lasers were parallel were measured.

The single step and folded step laser-atom interactions for π excitation were modelled using a full quantum electrodynamical treatment so that the optical pumping parameters from the single and folded step experiments could be investigated. Equations of motion were derived in the Heisenberg picture and it is shown that for the single laser case 59 equations of motion are required to fully model the interaction and for the folded step case 78 equations of motion are required. The results of calculations demonstrated that the optical pumping parameters were sensitive to laser intensity, laser detuning and the Doppler width of the atomic beam. The theoretical quantum electrodynamical calculation results were in good agreement with the experimental results.

Acknowledgments

I would like to thank all of the people who have assisted in one form or another with the work in this thesis.

Firstly I would like to thank my supervisors, Associate Professor Bill MacGillivray and Professor Max Standage, for their constant encouragement and many ideas that they conveyed to me throughout the course of the project. I would also like to thank them for the financial assistance that they have given me towards the end of my PhD.

I must also thank my fellow postgraduate students of the Laser Atomic Physics Laboratory. The friendship and comic relief from routine work were provided by Dr Gil Summy, Mr Brenton Hall, Mr Andrew Masters and Mr Ben Varcoe. Mr Peter Johnson (The Yowie) is also thanked for the assistance he provided in automating the experiment. Dr Ric Pascual, Dr Xian-Kun Meng and Dr Andrew Murray are also thanked for their assistance.

I must also thank the staff of the electronic and mechanical workshops of the Faculty of Science and Technology and for their assistance and construction of various apparatus.

My family has also played a large role in my studies. I would like to thank them for their support and encouragement.

My wife Patrice is also thanked for her support. There is much stress in completing a PhD and Patrice helped me to overcome this problem. This thesis is dedicated to her.

I would also like to acknowledge the Department of Employment, Education and Training for the scholarship that they have provided me with. The project was funded by an Australian Research Council Grant.

Table of Contents

Abstract	i
Acknowledgments	iii
Declaration	v
Chapter One: Introduction	1
1.1 Introduction	1
1.2 Electron-Atom Collision Experiments	2
1.3 Orientation and Alignment Experiments in Non-Spin Resolved Electron-Sodium Collision Experiments	10
1.4 Theoretical Modelling of the Laser-Atom Interaction in Superelastic Scattering Experiments in Sodium	13
1.5 Structure of This Thesis	14
Chapter Two: Electron-Atom Collision Theory	17
2.1 Introduction	17
2.2 Inelastic Electron-Atom Collision Theory	18
2.3 Inelastic S-P Collision	22
2.4 Single laser Superelastic Scattering	24
2.5 P-S Superelastic Collisions: Perpendicular Geometry	27
2.6 Superelastic Scattering in the Co-Planar Configuration	39
2.7 Folded Step Superelastic Scattering	42
2.8 The Superelastic P-S Collision In J Representation	45
2.9 Coherence in Electron-Atom Collisions	48
Chapter Three: Quantum Electrodynamic Theory	50
3.1 Introduction	50
3.2 The System Hamiltonian	51

3.3 The Derivation of the Equations of Motion for a Two Level Atom.....	58
3.4 Calculation of Rabi Frequencies and Branching Ratios.....	70
3.5 Solutions to the Equations of Motion	73
3.6 Folded Step Laser Excitation.....	77
3.7 Relation Between the Optical Pumping Parameters K , \bar{K} and the Line Polarisation	80
3.8 Single Step Calculation Results.....	86
3.9 Folded Step Results.....	89

Chapter Four: Superelastic Electron-Atom Collisions

Involving D States	92
4.1 Introduction	92
4.2 Parameterisation of the D State Collision Matrix	93
4.3 Stepwise Superelastic Scattering	97
4.4 Derivation of the Pseudo Stokes Parameters for Parallel Polarisation	99
4.5 Derivation of a pseudo Stokes Parameter with Non-Parallel Polarisations	107
4.6 Theoretical Treatment of the Stepwise Laser Excitation Process	113
4.7 Conclusion	118

Chapter 5: The Superelastic Scattering Experiment

5.1 Introduction.....	120
5.2 The Vacuum Chamber	121
5.3 The Sodium Oven	124
5.4 The Electron Gun.....	125
5.5 The Electron Analyser	127
5.6 The Laser Systems	129
5.7 The Photon Detection System.....	132
5.8 Detection Electronics.....	134

5.9 The Polarising Optics	134
5.10 Superelastic Scattering Experiment Protocol and Procedures.....	136
Chapter 6: Experimental Results and Discussion	141
6.1 Introduction	141
6.2 Electron-Atom Collision Theories.....	142
6.3 Determination of Errors for the Measured Pseudo Stokes Parameters and Coherence Parameters	147
6.4 Single Step and Folded Step Superelastic Scattering Experimental Results.....	152
6.5 The Finite Volume Effect.....	156
6.6 Single and Folded Step Experiment Discussion	160
6.7 Stepwise Superelastic Experimental Results	164
Chapter Seven: Conclusion.....	167
7.1 Summary	167
7.2 Extensions and Improvements.....	171
Appendix 1: Component Equations of Motion: Single Laser Case	173
Appendix 2: Component Equations of Motion: Folded Step Laser Excitation Case.....	185
References	201

List of Tables

Table 2.1: Density Matrix Elements in F Representation Reduced to L Representation.....	29
Table 3.1: Coefficients for Individual Rabi Frequencies in the $3^2S_{1/2} \rightarrow 3^2P_{3/2}$ Transition.....	72
Table 3.2: Branching Ratios for the $3^2P_{3/2} \rightarrow 3^2S_{1/2}$ Transition.....	73
Table 3.3: Emission Matrix Elements in F Representation in Terms of the Reduced Matrix Element.....	83
Table 4.1: Density Matrix Elements in J Representation Reduced to L Representation.....	100
Table 4.2: Relaxtion Rates of Excited Substates in J Representation.....	114
Table 4.3: Emission Matrix Elements in J Representation in Terms of the Reduced Matrix Element.....	116
Table 5.1: Typical Operating Voltages of the Electron Gun.....	126
Table 5.2: Typical Operating Voltages of the Lens Stack of the Analyser.....	127
Table 6.1: Comparison of the Optical Pumping Parameter K Determined Using the Various Methods.....	152

Table 6.2: Pseudo Stokes and Coherence Parameters Determined Using the Single and the Folded Step Experiments.....	152
---	-----

Table 6.3: Experimentally Determined Stepwise Stokes Parameters.....	165
---	-----

List of Figures

Figure 1.1: Comparison of the Coincidence and Superelastic Schemes.....	5
Figure 1.2: The Stepwise Coincidence Excitation Scheme.....	6
Figure 2.1: The Scattering Plane (Coincidence Experiment).....	18
Figure 2.2: The Scattering Plane (Superelastic Experiment).....	24
Figure 2.3: The Superelastic Scattering Scheme.....	25
Figure 2.4: Sodium D_2 Hyperfine Structure.....	27
Figure 2.5: Allowed Hyperfine Transitions Using π and σ Light.....	27
Figure 2.6: Rotation of the Laser Frame to the Collision Frame (Circularly Polarised Laser Case).....	36
Figure 2.7: The Coplanar Geometry.....	39
Figure 2.8: Folded Step Excitation form the Sodium D_2 Line.....	42
Figure 2.9: Laser Excitation of the Sodium D_2 Line in J Representation Using π Polarised Light.....	45
Figure 2.10: Laser Excitation of the Sodium D_2 Line in J Representation Using σ Polarised Light.....	46

Figure 2.11: The Singlet and Triplet Scattering Amplitudes in Complex Space.....	49
Figure 3.1: Feynman Diagrams Representing the Four Different Terms in the Electric-Dipole Interaction.....	56
Figure 3.2: The Doppler Effect.....	76
Figure 3.3: Overlap States in the Folded Step Excitation Scheme.....	79
Figure 3.4: Line Polarisation Geometry (Single Laser).....	81
Figure 3.5: Folded Step Line Polarisation Geometry.....	85
Figure 4.1: The Scattering Plane (Stepwise Superelastic Experiment).....	97
Figure 4.2: The Stepwise Superelastic Scattering Scheme.....	97
Figure 4.3: The Energy Levels of Sodium in J Representation.....	99
Figure 4.4: Stepwise Excited States in J Representation Using Circularly Polarised Light.....	104
Figure 4.5: Rotation of the Laser Frame to the Collision Frame (Circularly Polarised Laser Case) for Parallel Laser Polarisations.....	105
Figure 4.6: The Experimental Geometry for Stepwise Superelastic Experiments with Non-Parallel Laser Polarisations.....	108

Figure 4.7: The Direction of Polarisation Vectors for the Various Stepwise Superelastic Differential Cross Sections.....	108
Figure 4.8: Laser Excitation of the $J=3/2$ State Using π Laser Light.....	108
Figure 4.9: The Energy Levels of Sodium in J Representation Labelled According to the Rate Equations.....	113
Figure 4.10: The Stepwise Superelastic Line Polarisation Geometry.....	116
Figure 5.1: The Superelastic Scattering Experiment Apparatus.....	120
Figure 5.2: The Sodium Oven.....	124
Figure 5.3: The Electron Gun.....	125
Figure 5.4: The Filament Mount.....	126
Figure 5.5: The Electron Analyser.....	127
Figure 5.6: The Dye Laser System.....	129
Figure 5.7: The Titanium Sapphire Laser System.....	131
Figure 5.8: The Photon Detection System.....	132
Figure 5.9: The Detection Electronics.....	134

Figure 5.10: The Optics Configuration for the Superelastic Scattering	
Experiment.....	134
Figure 5.11: The Optics Configuration for the Folded Step Superelastic Scattering	
Experiment.....	135
Figure 5.12: The Optics Configuration for the Stepwise Superelastic Scattering	
Experiment.....	136
Figure 5.13: The Superelastic Energy Loss Spectrum (Single Laser).....	137
Figure 5.14: The Stepwise Superelastic Energy Loss Spectrum.....	139
Figure 6.1: The Volumetric Effect.....	157

List of Graphs

Graph 3.1: K Vs Rabi Frequency (Various Doppler Widths).....	86
Graph 3.2: K Vs Detuning (Various Laser Intensities).....	87
Graph 3.3: K Vs Detuning (Various Doppler Widths).....	88
Graph 3.4: Total Excited Populations Vs Time for Both Single Laser and Folded Step Laser Excitation Schemes.....	89
Graph 3.5: \bar{K} Vs Rabi Frequency of Laser 1 and Laser 2.....	89
Graph 3.6: \bar{K} Vs Detuning of Laser 1 and Laser 2.....	90
Graph 4.1: Populations Vs Energy Density (Stepwise Rate Equation Model).....	115
Graph 4.2: Total Sublevel Population Vs Energy Density (Stepwise Rate Equation Model).....	116
Graph 4.3: Stepwise Line Polarisation Vs Energy Density (Stepwise Rate Equation Model).....	117
Graph 4.4: K_D Vs Energy Density.....	117
Graph 6.1: Line Polarisation Vs Temperature.....	152
Graph 6.2: Stokes Parameters and Coherence Parameters Vs Scattering Angle for Incident Electron Energies: 10eV, 15eV, 20eV, 25eV, 30eV.....	153

Graph 6.3: P_{TOT} Vs Energy (Various Scattering Angles).....	156
Graph 6.4: Stokes Parameters for electron-Hydrogen Scattering.....	161
Graph 6.5: Spin Resolved Stokes Parameters and Coherence Parameters Calculated Using the DWBA2 Method Vs Scattering Angle.....	163
Graph 6.6: Stepwise Stokes Parameters Vs Scattering Angle 20eV Incident Electron Energy.....	165

Chapter One

Introduction

1.1 Introduction

Collision processes involving electrons and atoms have been of great interest since the evolution of quantum mechanics. One of the first experiments to investigate electron-atom collision processes was the Franck-Hertz experiment in 1914. In this particular experiment, electron-atom collisions were used to demonstrate the discrete energy levels or quantised nature of mercury atoms. Since that initial experiment, atomic collision physics has made many other important contributions to the growth of physics, both in the development of experimental apparatus and techniques and in the formulation of modern concepts and theories. Collision physics has also been used in many diverse applications such as to the study of planetary atmospheres and astrophysical phenomena where it has been revealed that atomic collision physics play much more of a role in nature than it was first previously thought. The development and understanding of many new devices have been dependent on the acquisition of new information about many kinds of atomic collisions. These devices include gas lasers, gas-filled radiation detectors to the common fluorescent lamp.

The observation of the effect of an incident particle after the collision with a particular target enables information on the structure of the target to be determined. In principle, two types of energetic processes may occur, elastic or inelastic collision processes. Elastic scattering is the most common form of scattering process, whereby the collision between a target and projectile interact in such a manner that there is no net transfer of energy during the collision. The second form of collision that may occur is the inelastic collision. In this collision process the particles under go a net transfer in energy. There are two forms of inelastic collision processes, the first of which the target particle gains

energy from a transfer of kinetic energy from the incident particle leaving the target particle in a higher energy internal state. The second inelastic process has been termed the "superelastic" collision process. In this process, energy from an excited internal state of the target particle is transferred to kinetic energy of the incident particle leaving the target particle in an internal state that is lower in energy.

The particular process studied here is the superelastic collision process. An electron beam with a well defined energy spread interacts with a collimated sodium beam which has been optically prepared using a laser or in some cases two lasers with a particular polarisation. A range of incident energies and excited states are studied and no spin analysis takes place so that averaging procedures must be used. Theoretical modelling of various laser-atom interactions is performed using a full quantum electrodynamical model which was developed by Farrell *et al.* 1988.

1.2 Electron-Atom Collision Experiments

Since the Franck-Hertz experiment more complex electron-atom collision experiments have been performed to measure total and differential cross sections (Heddle 1989, Zipf 1984, Trajmar and Cartwright 1984). In these types of experiments, a beam of atoms interact with a collimated beam of electrons of well defined energy. Inelastically or elastically scattered electrons are detected after the interaction with an atom which has one particular atomic bound state energy as a function of scattering angle, for the case of differential cross section measurements, or the sum of all the possible scattering angles to give the total relative cross section. This form of experiment does not give any information on the degenerate magnetic substate population since the experiment can not distinguish the individual excitation channels.

A further form of cross section measurement may be performed by the measurement of fluorescence emitted following an initial electron excitation of the target atom. An electron beam of variable, but well defined energy is passed through an atomic beam which excites the atoms to higher internal bound states. Measurement of the wavelength and the intensity of the optical radiation from the resulting spontaneous radiative transitions in de-excitation to lower levels, enables emission functions or emission cross sections to be determined as a function of the initial electron energy. This method has a low sensitivity because the only a small fraction of the photons produced are intercepted by the detector and not all of these photons arriving at the detector are registered (McDaniel 1989). A further disadvantage of this method is that because of their long excited lifetimes, metastable states can not be investigated using this method.

An advantage of the fluorescence method is that the polarisation of the emitted radiation may be monitored which enables information on the degenerate sublevel population to be available (Percival and Seaton 1958, Heddle 1983). The polarisation of the radiation is monitored at some angle, which is usually referenced to the incident electron beam. Since the scattered electron is not detected in this method, an averaging process over the scattering angles must be used.

In the two detection methods discussed above, either electron or photon detection alone limits the characterisation of the collision mechanism which is due to averaging procedures that are required to be used. The first method used to investigate collision processes in more detail were experiments that involved the detection of both the scattered electron plus the emitted photon. Complete information also requires that the polarisation of the emitted photon for each individual scattering process is known. This allows the alignment and the orientation of the atomic charge cloud to be determined for any given scattering angle of the incident particle. The alignment of the atomic charge cloud refers to the shape of the excited state charge cloud and its tilt with respect to the direction of the incident electron beam, and the orientation refers to the angular

momentum transferred to the atom during the collision interaction. Under certain conditions, these studies can also allow the complete determination of scattering amplitudes plus their relative phases and as such provides much more stringent tests of current scattering theories.

In this method, following the excitation of the atomic state, the scattered electron is detected in coincidence with the photon emitted from the subsequent decay from the excited atomic state. The theoretical framework of this method was discussed by Macek and Jaceks 1971 which was followed by a more general article by Fano and Macek 1973. The first coincidence experiment for electron impact excitation was reported by King *et al.* 1972 in which electron scattering from helium excitation at zero degree scattering angle was investigated. The first set of inelastic scattering amplitudes for the excitation of the 2^1P and 3^1P excited states of helium as a function of scattering angle were measured by Eminyan *et al.* 1973, 1974. In these experiments an electron-photon angular correlation technique was used in which the inelastically scattered electron was detected in delayed coincidence with the photon emitted coplanar to the scattering plane. The angular distribution of the emitted photon without polarisation analysis was measured as a function of the scattering angle. Using a least squares fit, the atomic collision parameters λ , the relative differential cross section, and $|\chi|$, the relative phase were obtained. The atomic collision parameters are functions of collision density matrix elements which describe the collision process. More detail on collision density matrix and atomic collision parameters are given in Chapter Two.

A natural extension of this analysis was to combine a polarisation analysis of the emitted photon with the coincidence technique. This first complete analysis involved the measurement of Stokes parameters which enabled the orientation parameter to be determined (Standage and Kleinpoppen 1976). This technique involved the detection of the scattered electron which excited the 3^1P state of He in delayed coincidence with

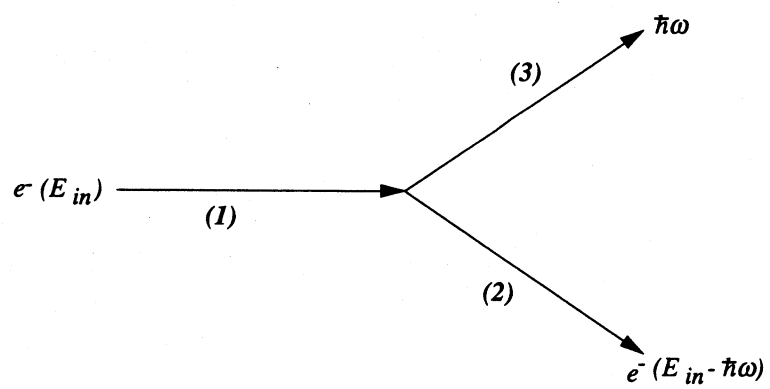


Figure 1.1a: The Coincidence Scheme

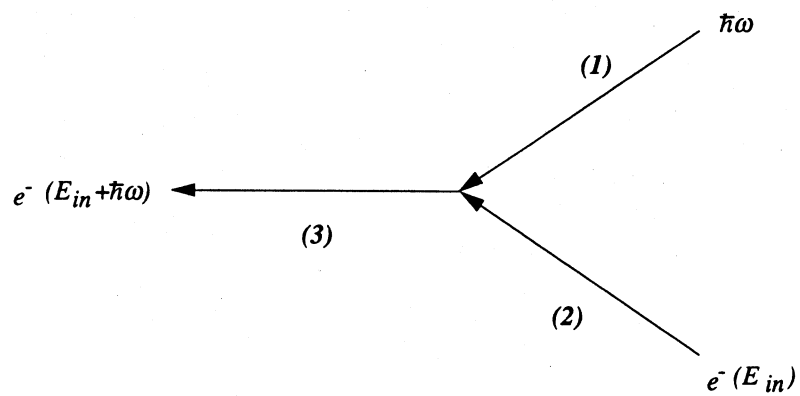


Figure 1.1b: The Superelastic Scheme

polarised fluorescence scattered perpendicular to the scattering plane. The Stokes parameters are defined as

$$P_1 = \frac{I(0) - I(90)}{I(0) + I(90)} \quad (1.1a)$$

$$P_2 = \frac{I(45) - I(135)}{I(45) + I(135)} \quad (1.1b)$$

$$P_3 = \frac{I(RHC) - I(LHC)}{I(RHC) + I(LHC)} \quad (1.1c)$$

where $I(\alpha)$ represents the coincidence signal with the polariser at angle α to the quantisation axis, which, for the coincidence experiment is chosen parallel to the incident electron beam. RHC and LHC represent the case when right and left hand circularly polarised light is detected. This analysis also enabled the total polarisation to be determined for the first time. The total polarisation is a measure of the coherence of the collision event. Standage and Kleinpoppen found that this particular collision process was fully coherent. It was during this time, with the advent of tunable dye lasers, that the study of laser assisted atomic collision processes such as the superelastic collision process became possible (Hertel and Stoll 1974a). This experimental technique required the atom to be initially prepared in the excited state using a polarised laser beam. The excited atom was then induced to relax via a superelastic collision with an electron. These experiments were carried out on the $3^2P_{3/2}$ state of sodium and Hertel and coworkers (Hertel and Stoll 1974 a&b) were able to show that the information obtained in these experiments was identical to that from the electron-photon coincidence experiment. A more rigorous theoretical treatment was provided by Macek and Hertel 1974 which was in terms of the of the Fano-Macek theory. A schematic of the two methods may be seen in figure 1.1. The numerals alongside the arrows indicate the time sequence.

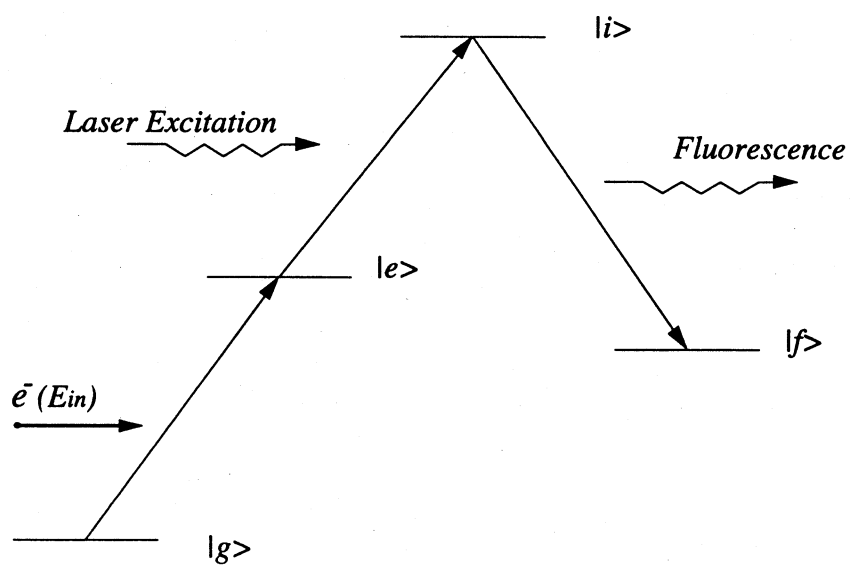


Figure 1.2: The Stepwise Coincidence Excitation Scheme

Since these pioneering experiments many atomic systems have been studied using these two techniques. In terms of electron-photon coincidence experiments, experiments have been performed on He, H, Hg, Na, Li, K, Ne, Ar, Kr, Xe and Ca. Anderson *et al.* 1988 provide a very useful review of these systems. The heavier atomic systems such as Hg, are interesting as they can give insight into the role of relativistic effects such as the spin-orbit interaction. Because of the high degree of experimental difficulty, only one electron-photon correlation experiment has been performed on molecules (McConkey *et al.* 1986).

Electron-photon coincidence experiments have a slow data collection time which can be attributed to a combination of both the finite solid angle and the efficiency of the photon detector at certain wavelengths. This method is also not suitable in the study of metastable states because of their long lifetimes. One method used to avoid the detection efficiency problems at certain wavelengths was to use a stepwise electron-photon coincidence experiment. This excitation technique is illustrated in figure 1.2. The atom is excited via an inelastic collision with an electron. The atom is then further excited to a higher atomic state via laser excitation. The scattered electron is then detected in delayed coincidence with the photon decay from the laser excited state into one particular cascade channel. The first experiment of this type was reported by Murray *et al.* 1989 in which a complete Stokes analysis of the 6^1P_1 state of mercury was performed. This technique also has the advantage that metastable states can be probed. A more recent technique to characterise metastable states was proposed by Summy *et al.* 1994 in which atoms, initially electronically excited to a metastable state, are deflected by an optical force using a laser beam of known polarisation. These deflected atoms are detected in coincidence with the scattered electron. The amount the atoms are deflected is proportional not only to the intensity, detuning of the light beam and the velocity distribution of the atomic beam but also to the initial state of the atom prior to the deflection. Summy *et al.* 1994 demonstrated for a model atom that it was possible to characterise the deflection in terms of pseudo Stokes parameters which in turn could be

related to the collision density matrix elements. To date no complete experiments have been performed using this method.

The experiment of Summy *et al.* 1994 is not the first type of deflection experiment that has been proposed. Bederson and coworkers (Bhasker *et al.* 1977, Jaduszliwer *et al.* 1984) have employed a method in which a deflection of an sodium atom, induced by the collision with an electron, is used to characterise collision processes. In this experiment only the deflected atom was detected and, as a result, limited the measurements to cross sectional information. Bederson's group have also measured absolute differential cross sections of laser excited atomic states of sodium by using double-recoil techniques (Zuo *et al.* 1990) in which atoms are deflected not only by the incident electron beam but also the exciting laser. It was found that the cross sections for the excited state atoms were four to ten times larger than that of ground state atoms.

A number of electron-atom superelastic collision studies have been performed on atomic species other than that of the original experiment performed on sodium. The number of these has been limited to transitions which are accessible by laser radiation and to date only experiments on Ba (Register *et al.* 1978) and more recently Ca (Law and Teubner 1993), Cr (McClelland *et al.* 1993) and Cs (Baum 1994). The results from the experiments on Ba reported a mysterious asymmetry with respect to the zero degree scattering angle. This was later found to be due to an experimental artefact now known as the finite volume effect (Zetner *et al.* 1989). No experimental results have been published for the Ca and Cs experiments. The major advantage of this method over the coincidence technique is that it only requires the detection of an electron which makes data collection much faster than that of any other method.

The experiments outlined so far have all involved non-spin resolved measurements which requires averaging over spin channels. The first spin resolved coincidence experiment was carried out by Kessler's group (Wolcke *et al.* 1984) at Münster in

which polarised electrons were incident on an atomic mercury beam exciting the atoms to the 6^3P_1 state. The scattered electrons were detected in delayed coincidence with the photon emitted perpendicular to the scattering plane from the 6^3P_1 to 6^1S_0 (254nm) decay channel. Linear polarisation analysis was carried out using a pile of plates analyser. The incident electrons were polarised such that the spin vector was oriented in the direction of the photon detector which preserved the reflection invariance in the scattering plane. Stokes parameters were measured over an energy range of 7 to 15eV at zero degree scattering angle. Bartschat and Blum 1982 showed that for this experiment, that if an unpolarised beam of electrons were used, the Stokes parameters P_2 and P_3 would be zero and hence this would provide a sensitive test of spin-dependent interactions. The experimental results indicated significant non-zero values for these parameters indicating that spin-dependent interactions played a large role in the excitation process studied.

Spin polarised superelastic experiments have also been performed. McClelland *et al.* 1985 used a polarised beam of electrons to superelastically scatter from laser prepared sodium atoms. The laser was linearly polarised and incident perpendicular to the scattering plane and was used to pump the atoms from the ground state to the $3^2P_{3/2}$ excited state. The electrons were spin polarised such that the spin vector was oriented either parallel (spin down) or anti-parallel (spin up) to the propagation vector of the laser beam. The spin asymmetry was determined via

$$A = P_e^{-1} \frac{N_{\downarrow} - N_{\uparrow}}{N_{\downarrow} + N_{\uparrow}} \quad (1.2)$$

where P_e is the magnitude of the incident electron spin polarisation and $N_{\downarrow, \uparrow}$ is the number of superelastically scattered electron with initial polarisation spin up (\uparrow) or down (\downarrow). McClelland *et al.* 1985 measured this parameter with an incident electron energy of 10eV as a function of scattering angle with the laser polarised at zero degrees to the incident electron momentum vector. Measurements at 30° scattering angle as a

function of the laser polarisation were also taken. Both of these analyses showed significant spin asymmetries. The author's attributed the spin asymmetry to exchange interactions, whereby the incident and atomic electron interchange during the collision interaction. The exchange interaction was induced by the "fine structure effect" (Hanne 1983). This effect is due to the simultaneous presence of two effects, the correlation between orbital angular momentum and spin in an L-S coupled atom, and the interaction of the orbital angular momenta of the scattered and target electrons (McClelland *et al.* 1985).

This group have also performed measurements in which both the incident electron beam and atom are spin polarised. Using the same excited state, the atoms were spin polarised by optical pumping using circularly polarised light. Two spin asymmetries, which were defined with respect to which orbital angular momentum state the atom was pumped into (either ± 1), were measured as a function of scattering angle and incident electron energies. Both of the types of measurements showed significant spin asymmetries, the most sensitive of which were for atoms which were prepared in the $m_L = -1$ excited state. The largest asymmetries were evident at lower energies and at larger scattering angles.

McClelland *et al.* 1989 have also performed orientation studies with both spin polarised atoms and electrons. In this particular experiment, the knowledge of both the incident particle and target particle's spins enable the singlet and triplet spin channels to be resolved. This resolution of the spin channels is of particular use as the individual spin channel contributions to the angular momentum transferred perpendicular to the scattering plane may be determined which can also give an indication of the role of exchange effects between the target electron and the incident electron. The ratio, r , of the (triplet/singlet) contributions were also measured. Good agreement with the Close Coupling calculation of (Moore and Norcross (1972) for the parameter r at all scattering angles was observed. This was not the case however for the comparison

between the individual singlet and triplet orientation parameters, where good agreement was observed at small scattering angles but not for larger scattering angles. Good agreement between experiment and the four state Close Coupling calculation of Mitroy *et al.* 1987 was also observed.

A comprehensive review of other spin resolved experiments and theory aspects is given by Hanne 1983. The book by Kessler 1976 also gives a comprehensive review of the theory.

1.3 Orientation and Alignment Experiments in Non-Spin Resolved Electron-Sodium Collision Experiments

A considerable amount of time and effort has been devoted to the investigation of orientation and alignment in electron-sodium collisions. The experiments can be separated into two categories: those experiments that involve spin dependent collisions and those experiments in which the spin variable is averaged over. Some of the spin resolved experiments were mentioned in the previous section. All of the non-spin resolved experiments have so far concentrated their studies on the 3^2P state and because of the accessibility of this state via laser excitation, only one coincidence experiment has been reported (Riley *et al.* 1985, Teubner *et al.* 1986). In this experiment, Teubner and coworkers utilised an electron-photon coincidence experiment, in which sodium atoms were excited to the 3^2P state of sodium with 22.1eV and 12.1eV electrons. The scattered electron was detected in coincidence with the decay photon from the 3^2P excited state emitted perpendicular to the scattering plane. The polarisation of the emitted photons is studied yielding Stokes parameters and subsequently atomic collision parameters. All three Stokes parameters were determined which enabled the coherence parameter, the total polarisation, P_{TOT} to be calculated. For a fully coherent

excitation process $P_{TOT}=1$ and with 22.1eV incident energy, for the angular range of 5° - 15° , to within experimental error full coherence was found for this experiment.

Superelastic electron-sodium collisions dominates the body of data that exists for orientation and alignment studies in sodium. As mentioned in the previous section Hertel's group was the first to perform this pioneering experiment (Hertel and Stoll 1974 a&b). Subsequent to this investigation Hertel and collaborators (Hertel and Stoll 1976,1977, Hermann *et al.* 1977) have performed several systematic studies of alignment parameters. In these experiments the laser was linearly polarised and incident coplanar to the scattering plane and the superelastic signal was taken as a function of the laser polarisation. This signal was fitted to the appropriate functions and collision parameters λ and $\cos\chi$ were determined as a function of energy and scattering angle. The full density matrix can not be characterised by these two parameters alone and hence information pertaining to the coherence of the collision process can not be obtained. The laser in the coplanar geometry does not allow the orientation parameter to be determined and as such a second geometry was required. The second geometry utilised the laser incident perpendicular to the collision plane which enabled the determination of the P_3 Stokes parameter and hence the orientation parameter (Hermann *et al.* 1980). Complete analysis of orientation and alignment parameters as a function of scattering angle were carried out on incident electron energies of 3eV, 10eV, 20eV with losses of coherence observed at 3eV and 20eV. The data at 20eV disagreed with the data of Riley *et al.* 1985 which did not display a loss of coherence.

The controversy surrounding the data of Hertel's group and Teubner's group instigated an investigation by Farrell *et al.* 1989 in which collision and coherence parameters were measured at this angle and energy. It was found, that like the data of Hermann *et al.* 1977 there was a loss of coherence in the collision process. Initially the Hermann *et al.* 1977 data produced a more significant loss than the data of Farrell *et al.* 1989 but an error in the analysis of Hermann *et al.* 1977 was found in which the value of λ was

significantly reduced. After correcting the data, the loss in coherence was in good agreement with the Farrell *et al.* 1989 data which was not in good accord with the coincidence experiment of Riley *et al.* 1986.

The experimental results induced speculation about the equivalence of the two techniques, however a recent investigation by MacGillivray and Standage 1991 confirmed the equivalence provided the principle of micro-reversibility holds for electron-atom collisions. This paper demonstrated that a comparison of the Stokes parameters for the two techniques were the same to within an overall coefficient. In the case of the coincidence experiment this was a factor representing the effect on the spectroscopic structure and in the case of the superelastic experiment the effect due to the laser induced optical pumping. In the case of the superelastic scattering experiment, these coefficients were labelled the optical pumping parameters.

Teubner and coworkers have also carried out a series of superelastic experiments (Scholten *et al.* 1988, 1993, Teubner *et al.* 1989, 1990) in which mainly two incident energies (10eV and 20eV) were investigated over a wide range of scattering angles. In this analysis, no loss of coherence at small scattering angles at either energy was observed. They did, however, find a significant loss of coherence at larger scattering angles. At 10eV, this occurred between 60° and 80° scattering angle and at 20eV this occurred in the range of 50° to 70° scattering angle.

Theoretical calculations in the intermediate energy regime using the Close Coupling methods of McCarthy and coworkers (Mitroy *et al.* 1987) have in the past tended to support the work of Teubner's group with no evidence of losses of coherence at small scattering angles but losses of coherence at larger scattering angles. Recent calculations of Madison *et al.* 1991, 1992 in which a Second Order Distorted Born calculation has been used to model the interaction have demonstrated a loss of coherence at both small and large scattering angles which has renewed interest in this area.

1.4 Theoretical Modelling of the Laser-Atom Interaction in Superelastic Scattering Experiments in Sodium

The first attempt at modelling the laser-atom interaction was performed by Hertel's group (Hertel and Stoll 1974 a&b, Macek and Hertel 1974 and Fischer and Hertel 1982) in which both the laser induced optical pumping and electron-atom collision processes were represented in terms of multipoles. The laser induced processes were modelled using a simplified representation of the $3^2P_{3/2}$ state. In the calculation it was assumed that the laser was tuned from the $F'=2$ hyperfine ground state to the $F=3$ hyperfine excite state. The combination of a highly collimated atomic beam with the dye laser, which had a natural line width of 1MHz, made resolution of the individual hyperfine states possible provided that the power of the laser was not sufficient to induce power broadening of the upper hyperfine state. A rate equation model was solved at steady state enabling the optical pumping parameters to be determined as a function of the laser intensity. It was also demonstrated that optical pumping parameters could be obtained in a separate line polarisation experiment of the laser induced fluorescence. The rate equation method is intrinsically a weak perturbation method and is therefore expected to fail at high laser intensities.

The rate equation method provides a simple and effective solution but Farrell 1992 pointed out a further potential problem which is associated with using steady state solutions. For the case of linearly polarised light, the total excited state probability reaches steady state very rapidly, but the individual substates do not reach steady state for 250 nanoseconds which is approximately 15 times the excited state life time. The situation is worse for circularly polarised light as it takes almost 1000 nanoseconds for the populations to reach steady state (Farrell 1992). The long times to reach steady state clearly point to some difficulty when using steady state results for experiments using crossed beam apparatus for which the transient time of the atom is in the order of one microsecond.

McClelland and Kelly recognised the potential problems associated with the approach of Hertel and coworkers, in particular the importance of the power broadening mechanisms and the resulting effect of the $F=1$ ground sub level acting as a sink. In their model, a semiclassical density matrix approach is used with only a selected number of density matrix elements solved for (McClelland and Kelly 1985). The atom was treated as a quantum entity and the light treated classically. The interaction between the light and the atom was treated quantum mechanically. Spontaneous emission is not intrinsically included in the model and has to be added in an *ad hoc* manner.

Farrell *et al.* 1988 introduced a full quantum electrodynamical treatment of the problem in which spontaneous emission appears naturally in the theory. No approximations were made except the usual rotating wave, harmonic and dipole approximations (these approximations are discussed in Chapter Three). A calculation using this method was made to theoretically model the optical pumping parameters (Farrell *et al.* 1991) which gave excellent agreement with fluorescence measurements. A detailed experimental investigation of the QED model was undertaken by Menget *et al.* 1992 in which line polarisation measurements under various conditions such as laser power and detuning were taken. These experimental results displayed excellent agreement with the theory.

1.5 Structure of This Thesis

This thesis consists of two sections; a theoretical section, which examine electron-atom collision processes as well a quantum electrodynamical model of the laser-atom interaction and an experimental section, which reports results of new electron-atom superelastic collision experiments.

Chapter Two is devoted to the development of the electron-atom collision density matrix. This derivation closely follows that of Blum (1981) and the density matrix

describing a S-P collision is derived. Following this, the general theory describing the superelastic P-S collision process is derived. This theory is applied to determine pseudo Stokes parameters for an electron-sodium superelastic collision experiment where it is shown that these parameters are not only functions of atomic collision parameters but also optical pumping parameters which are related to the populations and coherences formed by laser induced optical pumping processes. A superelastic experiment described as "folded step superelastic scattering" is introduced, in which two lasers are used to pump out of the two hyperfine ground states in sodium. Completing the chapter is a section on coherence in electron-atom collisions.

Chapter Three is devoted to the QED modelling of the laser-atom interaction. The chapter initially begins with the derivation of the system Hamiltonian which is followed by a derivation of the equation of motions for a single laser superelastic collision experiment. This work follows that of Farrell *et al.* 1988, 1991 and is extended later in the chapter to model the folded step laser excitation mechanism.

Chapter Four describes a new superelastic collision experiment in which collisionally induced excited state to excited state transitions are investigated. This is an initial investigation of a stepwise superelastic scattering experiment in which atoms are laser excited from the ground state to the $3^2P_{3/2}$ state and then further excited from the $3^2P_{3/2}$ state to the $3^2D_{5/2}$ state. The atoms are then induced to relax via a superelastic collision with an electron to the $3^2P_{1/2,3/2}$ state. Stepwise pseudo Stokes parameters are derived for the case when the lasers have parallel polarisations and also for one case with crossed polarisations. It is shown that the stepwise pseudo Stokes parameters are functions of both atomic collision parameters and optical pumping parameters and for parallel laser polarisation case it is shown that these optical parameters may be related to line polarisation measurements. The chapter is completed with a section modelling the stepwise laser interaction using rate equations.

Chapter Five presents the apparatus used in the experiments outlined in the previous chapters. Chapter Six presents the results of measurements taken from line polarisation measurements, single step superelastic data and folded step superelastic data. The data from superelastic collisions from the $3^2P_{3/2}$ to the ground state at five different energies as a function of scattering angle are compared to existing experimental data and three current electron-atom scattering theories. The effect of finite volume of the interaction region is also explored. The final section presents the data from the new stepwise superelastic scattering experiment discussed in Chapter Four.

Chapter Two

Electron-Atom Collision Theory

2.1 Introduction

This chapter provides the details for the general theory of the superelastic collision process. Owing to the fact that these experiments deal with ensembles of atoms which may or may not be described by a pure state requires the use of the density matrix formalism. The first section of the chapter deals with general inelastic electron excitation of a P state from an S state of an atom and introduces atomic collision parameters. A theory is then derived to determine the superelastic differential cross section for a P-S superelastic collision which is used to determine pseudo Stokes parameters. It will be also shown that these parameters are not only related to atomic collision parameters but also to optical pumping parameters. These optical pumping parameters are functions of the populations and coherences formed by the laser excitation. Following this section is one which deals with the theory of a folded step superelastic experiment. This experiment uses two lasers to pump out of the two hyperfine ground states in sodium giving a larger excited state population. The final section of the chapter deals with the question of coherence in electron-atom collisions.

Following this chapter is a chapter which deals with the laser excitation aspects of the single step and folded step superelastic scattering experiments. Also given in the next chapter is a method of determining the optical pumping parameters via fluorescence measurements.

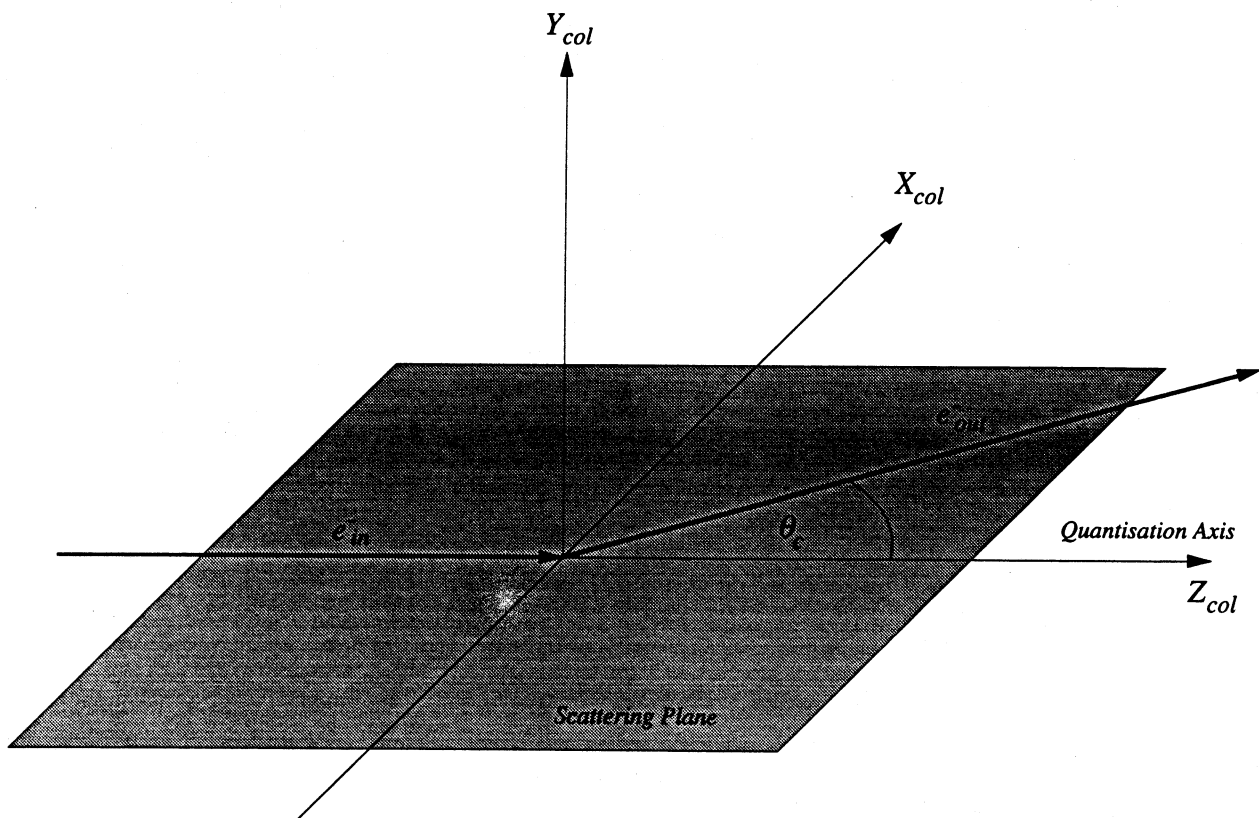


Figure 2.1: The scattering plane

2.2 Inelastic Electron-Atom Collision Theory

In this section the general theory for an electron-atom S-P collision is derived. Figure 2.1 depicts the scattering plane which is defined as the plane containing both the incident and scattered electron momentum vectors. By convention the quantisation axis (Z_{col}) is chosen parallel to the incident electron momentum vector. Consider now a beam of electrons of well defined momentum interacting with a ensemble of ground state atoms. The density operator representing the ground state atoms is given by

$$\rho^A = \left(\frac{1}{2J_g + 1} \right) \sum_{M_g} |\alpha_g J_g M_g\rangle \langle \alpha_g J_g M_g| \quad (2.1)$$

where J_g is the total angular momentum of the ground state, M_g is the projection quantum number of the angular momentum on the quantisation axis and α_g are all other quantum numbers required to specify the ground state. The density operator describing the initial electron beam is represented by

$$\rho^{el} = \frac{1}{2} \sum_{m_o} |P_o m_o\rangle \langle P_o m_o| \quad (2.2)$$

P_o is the momentum of the electrons and m_o is the spin. The incident electrons and ground state atoms have no correlations prior to the collision and as such the interaction density operator is formed by the direct product

$$\begin{aligned} \rho^{in} &= \rho^A \times \rho^{el} \\ &= \left(\frac{1}{2\{2J_g + 1\}} \right) \sum_{M_g m_o} |\alpha_g J_g M_g\rangle \langle \alpha_g J_g M_g| |P_o m_o\rangle \langle P_o m_o| \\ &= \left(\frac{1}{2\{2J_g + 1\}} \right) \sum_{M_g m_o} |\alpha_g J_g M_g P_o m_o\rangle \langle \alpha_g J_g M_g P_o m_o| \\ &= \left(\frac{1}{2\{2J_g + 1\}} \right) \sum_{M_g m_o} |M_g m_o\rangle \langle M_g m_o| \end{aligned} \quad (2.3)$$

where $|M_g m_o\rangle = |\alpha_g J_g M_g P_o m_o\rangle$. The transition between atomic states is denoted by

$$\Gamma_o = \gamma_o P_o M_o \longrightarrow \Gamma_f = \gamma_f P_f M_f \quad (2.4)$$

where γ_i represents all the necessary quantum numbers required to specify the atomic system. The transition may also be written in terms of a scattering amplitude as

$$f(\Gamma_f, \Gamma_o) = \langle \Gamma_f | T | \Gamma_o \rangle \quad (2.5)$$

where T is the transition operator. The scattering amplitude $f(\Gamma_f, \Gamma_o)$ is normalised according to the condition

$$|f(\Gamma_f, \Gamma_o)|^2 = \sigma(\Gamma_f, \Gamma_o) \quad (2.6)$$

$\sigma(\Gamma_f, \Gamma_o)$ represents the differential cross section for the transition. The density operator for the system after the collision is

$$\rho^e = T \rho^{in} T^\dagger \quad (2.7)$$

We now take the matrix elements between final states

$$\begin{aligned} \langle M' m_f | \rho^e | M m_f \rangle &= \left(\frac{1}{2 \{ 2J_g + 1 \}} \right) \\ &\sum_{M_g m_o} \langle M' m_f | T | M_g m_o \rangle \langle M_g m_o | T^\dagger | M m_f \rangle \end{aligned} \quad (2.8)$$

where $|M m_f\rangle = |\alpha_f J_f M_f P_f m_f\rangle$. From equation (2.5) this result can be re-expressed in terms of scattering amplitudes as

$$\langle M' m_f | \rho^e | M m_f \rangle = \left(\frac{1}{2 \{ 2J_g + 1 \}} \right) \sum_{M_g m_0} f(M' m_f M_g m_0) f^*(M m_f M_g m_0) \quad (2.9)$$

Sodium is a light atom and it is expected that spin orbit effects may be considered to be negligible during the collision and as such any change of the electron spin variable is due to the electron exchange process. Fine and hyperfine couplings may also be neglected during the collision because the orbital precession time of the atomic electron is much greater than the collision time. This is due to the spin vectors not precessing appreciably during the collision and L and S may be therefore be considered to be decoupled during the collision itself (Percival and Seaton 1957). When no electron spins have been observed, the density matrix is reduced to $\rho^e(L)$ which describes the orbital states of the atom only. We can reduce this matrix by applying (Blum 1981)

$$\langle \phi_j | \rho(\phi, t) | \phi_j \rangle = \sum_i \langle \Phi_i \phi_j | \rho(\phi, t) | \Phi_i \phi_j \rangle \quad (2.10)$$

The elements of ρ are diagonal in the unobserved variable m_f and therefore with the application of equation (2.10) we derive the result:

$$\begin{aligned} \rho_{M'M}^e &= \sum_{m_f} \langle M' m_f | \rho^e | M m_f \rangle \\ &= \left(\frac{1}{2 \{ 2J_g + 1 \}} \right) \sum_{m_f} \sum_{M_g m_0} f(M' m_f M_g m_0) f^*(M m_f M_g m_0) \\ &\equiv \langle f(M') f^*(M) \rangle \end{aligned} \quad (2.11)$$

where $\langle \dots \rangle$ indicates averages over the spins variables. The matrix is a $(2L+1)$ dimensional matrix which contains all the information on the orbital system of the excited atomic sub ensemble. The diagonal elements of the density matrix are normalised by

$$\rho_{MM}^e = \left(\frac{1}{2\{2J_g+1\}} \right) \sum_{m_f} \sum_{M_g m_0} |f(M m_f M_g m_0)|^2$$

$$= \sigma(M) \quad (2.12)$$

where $\sigma(M)$ is the differential cross section for excitation of the magnetic substate M averaged over all spins. The trace of $\rho^e(L)$ gives the total differential cross section σ

$$\rho^e(L) = \sum_M \sigma(M) = \sigma = 1 \quad (2.13)$$

The number of independent density matrix elements may be reduced by applying hermiticity such that

$$\langle M' | \rho^e(L) | M \rangle = \langle M | \rho^e(L) | M' \rangle^* \quad (2.14)$$

This number can be reduced further by invoking certain symmetry conditions. The scattering plane is defined by P_0 and P_f with no direction defined perpendicular to the scattering plane, that is, the excited system must be invariant under reflection in the scattering plane. As a consequence, the atomic ensemble can not distinguish between up and down with respect to this plane. This is expressed in the scattering amplitudes by (Blum 1981)

$$f(M m_f M_g m_0) = (-1)^{M+J_1-m_0} f(-M -m_f -M_g -m_0)$$

$$f(M' m_f M_g m_0) = (-1)^{M'+J_1-m_0} f(-M' -M_f -M_g -m_0) \quad (2.15)$$

where J_1 is the total angular momentum of the excited state. Equation (2.15) is now applied to equation (2.11) which yields the following

$$\begin{aligned}
\langle M' | \rho^e(L) | M \rangle &= \left(\frac{1}{2 \{ 2J_g + 1 \}} \right) \sum_{m_f} \sum_{M_g m_0} | f(M' m_f M_g m_0) f^*(M m_f M_g m_0) | \\
&= \left(\frac{1}{2 \{ 2J_g + 1 \}} \right) (-1)^{M+J_1-m_0} (-1)^{M'+J_1-m_0} \\
&\quad \sum_{m_f} \sum_{M_g m_0} f(-M' -m_f -M_g -m_0) f(-M -m_f -M_g -m_0) \\
&= (-1)^{M'+M} \langle -M' | \rho^e(L) | -M \rangle
\end{aligned} \tag{2.16}$$

Thus, for the partial differential cross sections,

$$\sigma(M) = \sigma(-M) \tag{2.17}$$

The number of independent elements of the density matrix may be reduced further if spin conservation is explicitly taken into account. In sodium this is a good approximation as the atom is light and it is expected that LS coupling will not break down, giving (Blum 1981)

$$\langle M' | \rho^e(L) | -M \rangle = (-1)^M \langle M' | \rho^e(L) | M \rangle \tag{2.18}$$

2.3 Inelastic S-P Collision

An explicit example of $\rho^e(L)$ will now be derived for the case when the atom is excited from an L=0 ground state to an L=1 excited state (i.e. an S-P collision). $\rho^e(L)$ is given by

$$\rho^e(1) = \begin{pmatrix} \sigma(1) & \langle f(1)f^*(0) \rangle & \langle f(1)f^*(-1) \rangle \\ \langle f(0)f^*(1) \rangle & \sigma(0) & \langle f(0)f^*(-1) \rangle \\ \langle f(-1)f^*(1) \rangle & \langle f(-1)f^*(0) \rangle & \sigma(-1) \end{pmatrix} \quad (2.19)$$

We now apply equation (2.14) which reduces the number independent elements giving the following

$$\rho^e(1) = \begin{pmatrix} \sigma(1) & \langle f(1)f^*(0) \rangle & \langle f(1)f^*(-1) \rangle \\ \langle f(1)f^*(0) \rangle^* & \sigma(0) & \langle f(0)f^*(-1) \rangle \\ \langle f(1)f^*(-1) \rangle^* & \langle f(0)f^*(-1) \rangle^* & \sigma(-1) \end{pmatrix} \quad (2.20)$$

Applying equation (2.16) - (2.18) yields the following relations

$$\langle f(0)f^*(-1) \rangle = -\langle f(0)f^*(1) \rangle = \langle f(1)f^*(0) \rangle^* \quad (2.21)$$

$$\langle f(1)f^*(-1) \rangle = \langle f(-1)f^*(1) \rangle \quad (2.22)$$

$$\langle f(1)f^*(-1) \rangle = -\langle f(1)f^*(1) \rangle = -\sigma(1) \quad (2.23)$$

Therefore the density matrix becomes

$$\rho^e(1) = \begin{pmatrix} \sigma(1) & \langle f(1)f^*(0) \rangle & -\sigma(1) \\ \langle f(1)f^*(0) \rangle^* & \sigma(0) & -\langle f(1)f^*(0) \rangle^* \\ -\sigma(1) & -\langle f(1)f^*(0) \rangle^* & \sigma(1) \end{pmatrix} \quad (2.24)$$

This density matrix is characterised by four parameters $\sigma(0)$, $\sigma(1)$ and the real and imaginary parts of $\langle f(1)f^*(0) \rangle$. It is useful to parameterize this matrix using four parameters labelled as the atomic collision parameters (Hertel and Stoll 1977).

$$\lambda = \frac{\rho_{00}^e}{2\rho_{11}^e + \rho_{00}^e} = \frac{\sigma(0)}{\sigma}$$

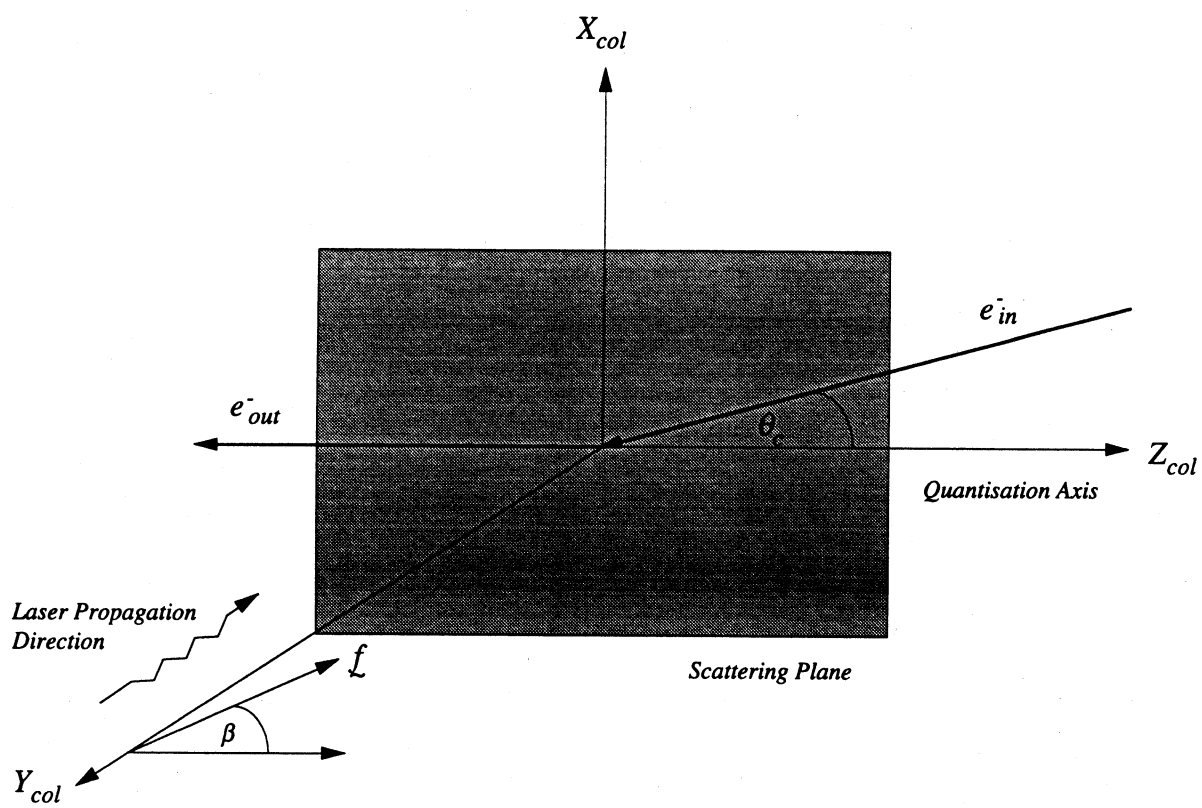


Figure 2.2: The Scattering Plane (Superelastic Experiment)

$$\begin{aligned}
\cos\chi &= \frac{\text{Re}\rho_{10}^e}{[\rho_{11}^e\rho_{00}^e]^{1/2}} = \frac{\text{Re}\langle f(1)f^*(0) \rangle}{[\sigma(1)\sigma(0)]^{1/2}} \\
\sin\phi &= \frac{\text{Im}\rho_{10}^e}{[\rho_{11}^e\rho_{00}^e]^{1/2}} = \frac{\text{Im}\langle f(1)f^*(0) \rangle}{[\sigma(1)\sigma(0)]^{1/2}} \\
\cos\delta &= \frac{\rho_{1-1}^e}{\rho_{11}^e} = \frac{\langle f(1)f^*(-1) \rangle}{\sigma(1)} = -1
\end{aligned} \tag{2.25}$$

$\sigma = \sigma(0) + 2\sigma(1)$ is the total differential cross section. Since $\cos\delta$ has a definite value for sodium (which implies a zero spin flip (Blum 1981)), only the three parameters λ, χ and ϕ are required to fully characterise the $L=1$ density matrix.

The atomic collision parameters defined by equations (2.25) are defined in the collision frame. Alternative frames have also been defined and one of the most used frames beside the collision frame was suggested by Hermann and Hertel 1982 which uses the symmetry of the problem. This alternative frame was denoted the "natural frame" and is characterised by $(X_{\text{nat}}, Y_{\text{nat}}, Z_{\text{nat}})$. The Z_{nat} axis takes the place of the Y collision axis and the X_{nat} axis takes the place of the Z collision axis. Parameterisation of the collision density matrix in this frame yielded the natural frame parameters. Typically, most theoretical calculations are in terms of parameters defined in the collision frame and for this reason all of the results presented in this thesis will be in terms of parameters defined in the collision frame. More detail on the natural frame and natural frame parameters may be found in the review given by Anderson *et al.* 1988.

2.4 Single laser Superelastic Scattering

In this section the general theory for a single laser step superelastic scattering experiment is derived. The scattering plane for the experiment is shown in figure 2.2. As with the case of inelastic scattering, the scattering plane is defined as the plane which contains both the incident and scattered electron momentum vectors. However the quantisation axis (Z_{col}) is chosen antiparallel to the scattered electron which is different to the inelastic

case where the quantisation axis is chosen parallel to the incident electron. The rationale behind this is that the superelastic scattering is the time reverse process of inelastic scattering.

A general superelastic scattering scheme may be seen in figure 2.3. The scheme involves the excitation of ground state atoms via resonant laser radiation of a known polarisation. These atoms are then induced to relax non-radiatively by a superelastic collision with an electron. Measurements of the superelastic differential cross section as a function of the laser polarisation may be used to obtain pseudo Stokes parameters which may be used in turn to deduce atomic collision parameters.

The density operator representing the optically excited atomic state is given by

$$\rho^o = \sum_{M'M} \rho_{M'M}^L |JM'\rangle \langle JM| \quad (2.26)$$

The matrix elements $\rho_{M'M}^L$ describe the ensemble distribution in the excited state. The electron de-excitation of the atom is represented by the de-excitation monitoring operator, L^D and is defined as

$$L^D = \sum_{J_g m_g} T_D |J_g m_g\rangle \langle J_g m_g| T_D^\dagger \quad (2.27)$$

The sum runs over the ground states. T_D is the de-excitation scattering operator. The superelastic differential cross section can be written as (MacGillivray and Standage 1991)

$$S = \text{Tr}(\rho^o L^D) \quad (2.28)$$

from (2.26) and (2.27) this expression becomes

$$S = \sum_{M'M} \rho_{M'M}^L L_{MM'}^D \quad (2.29)$$

The matrix elements of L^D are written as

$$L_{MM'}^D = \sum_{J_g m_g} \langle JM | T_D | J_g m_g \rangle \langle J_g m_g | T_D^\dagger | JM' \rangle \quad (2.30)$$

Applying the principle of micro-reversibility reveals that

$$\langle JM | T_D | J_g m_g \rangle = \langle J_g m_g | T^\dagger | JM \rangle \quad (2.31)$$

that is, the de-excitation process may be written in terms of the excitation process.

$$L_{MM'}^D = \sum_{J_g m_g} \langle JM' | T | J_g m_g \rangle \langle J_g m_g | T^\dagger | JM \rangle \quad (2.32)$$

Thus it follows from equation (2.8) that to within a normalisation constant

$$L_{MM'}^D = \rho_{M'M}^e \quad (2.33)$$

This allows the superelastic differential cross section to be written as

$$S = \sum_{M'M} \rho_{M'M}^L \rho_{M'M}^e \quad (2.34)$$

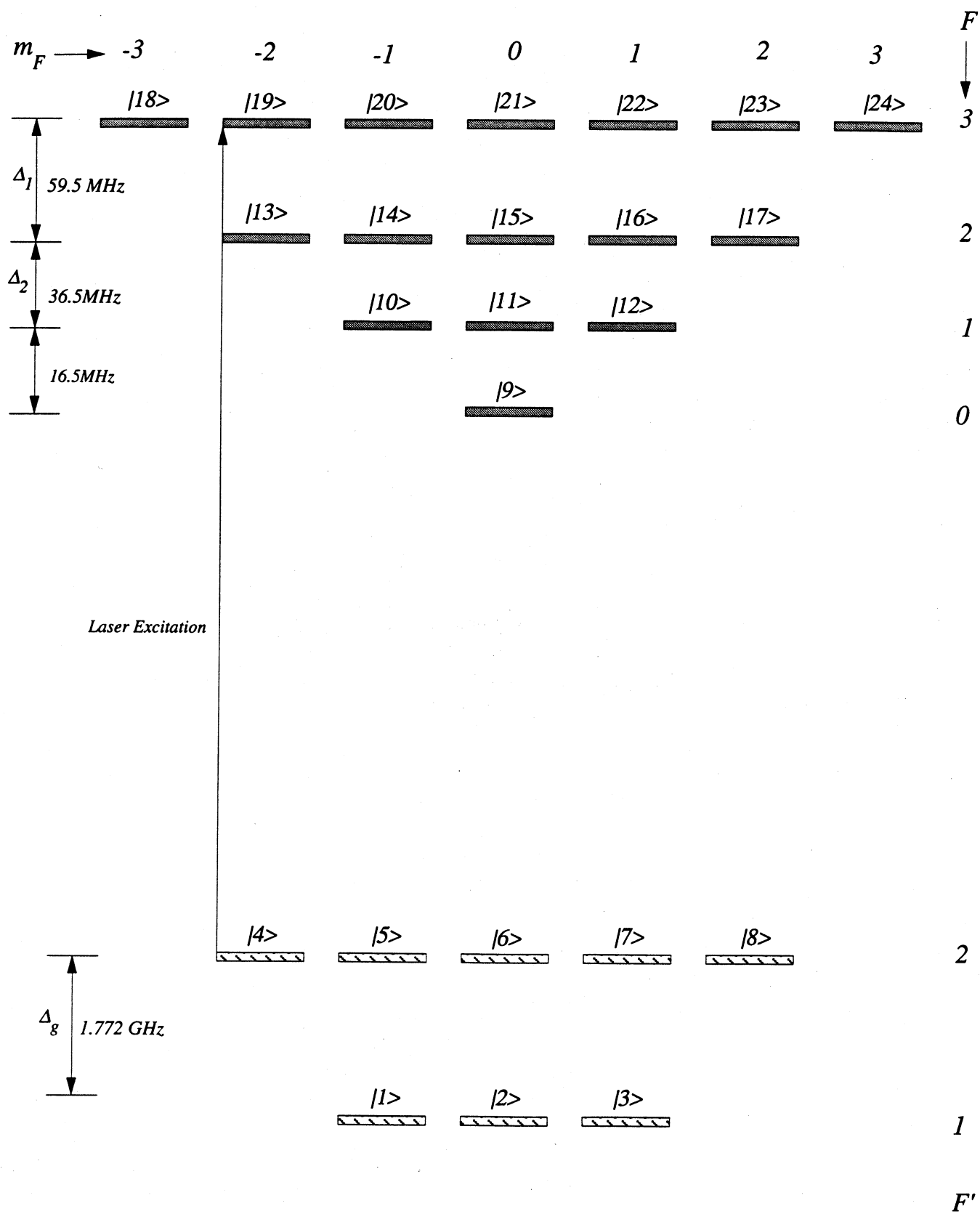


Figure 2.4: Sodium D_2 Line Hyperfine Structure

2.5 P-S Superelastic Collisions: Perpendicular Geometry

In this section the pseudo Stokes parameters will be derived for a superelastic scattering experiment in sodium and follows a description of Farrell *et al.* 1991 and MacGillivray and Standage 1991. The hyperfine structure of sodium is displayed in figure 2.4. In the case we consider here, the laser propagates in the negative Y_{col} direction (perpendicular to the scattering plane) and excites the $3^2S_{\frac{1}{2}}$ ($F'=2$) ground states to the $3^2P_{\frac{3}{2}}$ ($F=3,2,1$)

excited states. The laser is either linearly or circularly polarised and it is usual to rotate to a frame where the usual optical selection rules may be applied. Linearly polarised light induces electric dipole transitions of $\Delta m_F = 0$ (see figure 2.5a). Circularly polarised light induces transitions for the case of right hand circularly polarised light (σ^-) of $\Delta m_F = -1$ and $\Delta m_F = 1$ for left hand circularly polarised light (σ^+). These two situations are depicted in figures 2.5b and 2.5c.

Consider now the laser propagating with linearly polarised light with the electric field vector at an angle β to the quantisation axis (see figure 2.2). The superelastic differential cross section for the superelastically scattered electrons is given by equation (2.34). This sum may be simplified if the quantisation axis is rotated by the angle β to make the electric field vector and the quantisation axis parallel. The rotated collision frame is defined as the laser frame. The sum in equation (2.34) in the laser frame is considerably reduced due to optical selection rules and becomes block diagonal. The hyperfine structure of sodium plays an important role in the laser-induced optical pumping process and to take this into account the superelastic differential cross section must be defined in F representation viz:

$$S = \sum_{FF'm_F} \rho_{Fm_F F'm_F}^L \rho_{Fm_F F'm_F}^{e(L)} \quad (2.35)$$

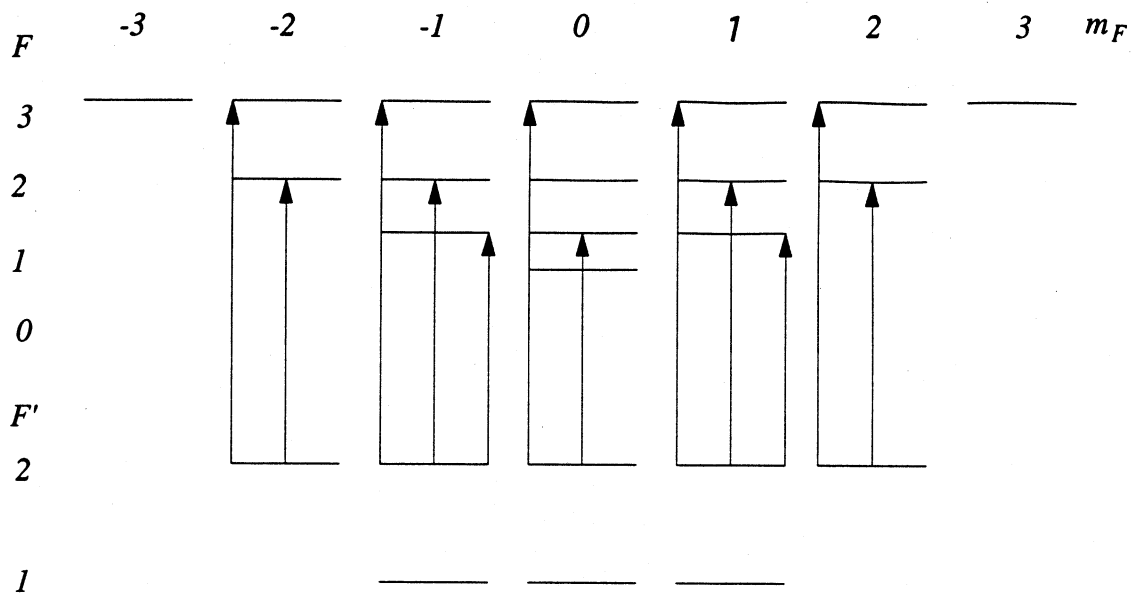


Figure 2.5(a): π allowed transitions

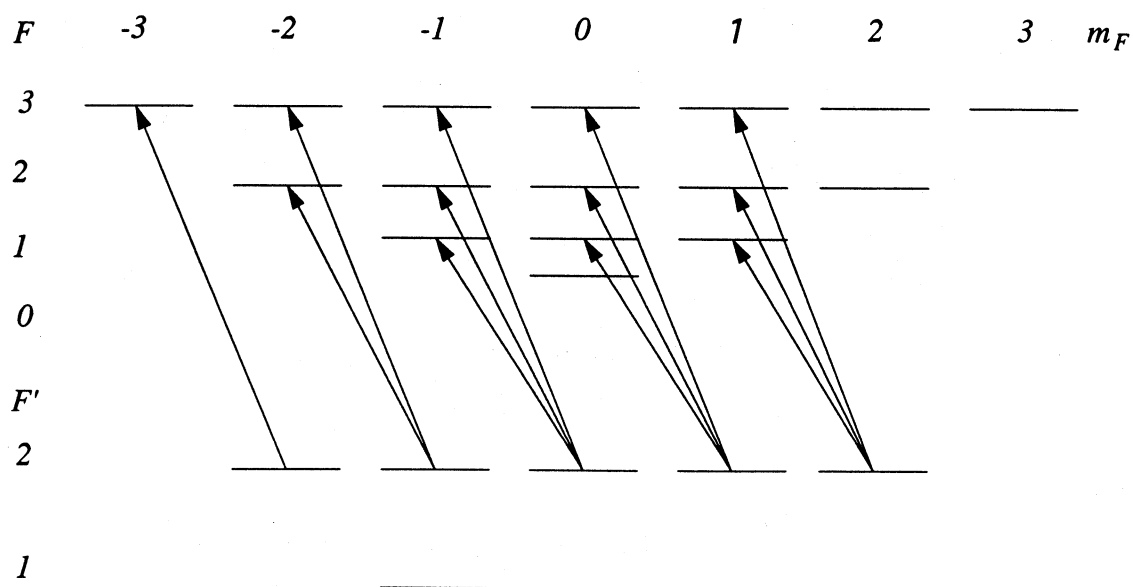


Figure 2.5(b): $\bar{\sigma}$ allowed transitions

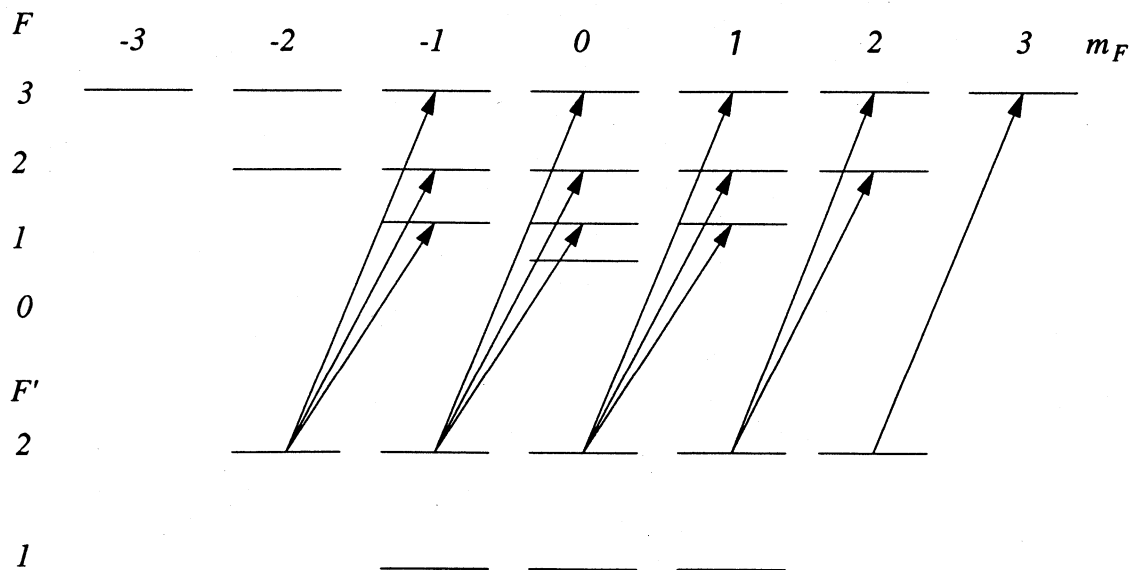


Figure 2.5(b): σ^+ allowed transitions

where $\rho_{Fm_F F'm_F}^{e(L)}$ represent the electron collision density matrix elements in the laser frame.

For the case of a linearly polarised laser S is given by

$$\begin{aligned}
 S = & \rho_{19\ 19}^L \rho_{19\ 19}^{e(L)} + \rho_{20\ 20}^L \rho_{20\ 20}^{e(L)} + \rho_{21\ 21}^L \rho_{21\ 21}^{e(L)} + \rho_{22\ 22}^L \rho_{22\ 22}^{e(L)} \\
 & + \rho_{23\ 23}^L \rho_{23\ 23}^{e(L)} + \rho_{13\ 13}^L \rho_{13\ 13}^{e(L)} + \rho_{14\ 14}^L \rho_{14\ 14}^{e(L)} + \rho_{16\ 16}^L \rho_{16\ 16}^{e(L)} \\
 & + \rho_{17\ 17}^L \rho_{17\ 17}^{e(L)} + \rho_{10\ 10}^L \rho_{10\ 10}^{e(L)} + \rho_{11\ 11}^L \rho_{11\ 11}^{e(L)} + \rho_{12\ 12}^L \rho_{12\ 12}^{e(L)} \\
 & + \rho_{19\ 13}^L \rho_{19\ 13}^{e(L)} + \rho_{13\ 19}^L \rho_{13\ 19}^{e(L)} + \rho_{20\ 14}^L \rho_{20\ 14}^{e(L)} + \rho_{14\ 20}^L \rho_{14\ 20}^{e(L)} \\
 & + \rho_{20\ 10}^L \rho_{20\ 10}^{e(L)} + \rho_{10\ 20}^L \rho_{10\ 20}^{e(L)} + \rho_{14\ 10}^L \rho_{14\ 10}^{e(L)} + \rho_{10\ 14}^L \rho_{10\ 14}^{e(L)} \\
 & + \rho_{21\ 11}^L \rho_{21\ 11}^{e(L)} + \rho_{11\ 21}^L \rho_{11\ 21}^{e(L)} + \rho_{22\ 16}^L \rho_{22\ 16}^{e(L)} + \rho_{16\ 22}^L \rho_{16\ 22}^{e(L)} \\
 & + \rho_{22\ 12}^L \rho_{22\ 12}^{e(L)} + \rho_{12\ 22}^L \rho_{12\ 22}^{e(L)} + \rho_{16\ 12}^L \rho_{16\ 12}^{e(L)} + \rho_{12\ 16}^L \rho_{12\ 16}^{e(L)} \\
 & + \rho_{23\ 17}^L \rho_{23\ 17}^{e(L)} + \rho_{17\ 23}^L \rho_{17\ 23}^{e(L)} \quad (2.36)
 \end{aligned}$$

The density matrix elements have been labelled according to the scheme displayed in figure 2.4. States $|9\rangle$, $|18\rangle$ and $|24\rangle$ are not excited due to selection rules. State $|15\rangle$ also has a zero contribution for reasons discussed later. The density matrix elements may now be reduced from F representation to J representation via (Sobelman 1979)

$$\begin{aligned}
 \rho_{Fm_F F'm_F}^e &= \langle nIJFm_F | \rho^e | nIJ'F'm_F \rangle \\
 &= \sum_{m_J m_{J'} m_{I'}} \sqrt{(2F+1)(2F'+1)} (-1)^{J-I-m_F+J'-I'-m_{F'}} \begin{pmatrix} I & J & F \\ m_F-m_J & m_J & -m_F \end{pmatrix} \\
 &\quad \begin{pmatrix} I' & J' & F' \\ m_F-m_{J'} & m_{J'} & -m_{F'} \end{pmatrix} \langle nJm_J | \rho^e | nJ'm_{J'} \rangle \langle Im_I | Im_{I'} \rangle \quad (2.37)
 \end{aligned}$$

where $(:::)$ represents a Wigner 3j symbol. The following assumptions may now applied to this case:

- (1) The projection of I , m_I is unaffected by the collision (Percival and Seaton 1957)
- (2) Elements with the same m_F are formed in the excitation process
- (3) Single J state that is: $J=J'$

Table 2.1

$\rho_{24}^e = \rho_{11}^e$	$\rho_{23}^e = \frac{1}{3} \{ 2\rho_{11}^e + \rho_{00}^e \}$
$\rho_{22}^e = \frac{1}{15} \{ 6\rho_{11}^e + 8\rho_{00}^e + \rho_{-1-1}^e \}$	$\rho_{21}^e = \frac{1}{5} \{ \rho_{11}^e + 3\rho_{00}^e + \rho_{-1-1}^e \}$
$\rho_{20}^e = \frac{1}{15} \{ \rho_{11}^e + 8\rho_{00}^e + 6\rho_{-1-1}^e \}$	$\rho_{19}^e = \frac{1}{3} \{ \rho_{00}^e + 2\rho_{-1-1}^e \}$
$\rho_{18}^e = \rho_{-1-1}^e$	$\rho_{17}^e = \frac{1}{3} \{ 2\rho_{11}^e + \rho_{00}^e \}$
$\rho_{16}^e = \frac{1}{6} \{ 3\rho_{11}^e + 2\rho_{00}^e + \rho_{-1-1}^e \}$	$\rho_{15}^e = \frac{1}{3} \{ \rho_{11}^e + \rho_{00}^e + \rho_{-1-1}^e \}$
$\rho_{14}^e = \frac{1}{6} \{ \rho_{11}^e + 2\rho_{00}^e + 3\rho_{-1-1}^e \}$	$\rho_{13}^e = \frac{1}{3} \{ \rho_{00}^e + 2\rho_{-1-1}^e \}$
$\rho_{12}^e = \frac{1}{30} \{ 13\rho_{11}^e + 14\rho_{00}^e + 3\rho_{-1-1}^e \}$	$\rho_{11}^e = \frac{1}{15} \{ 7\rho_{11}^e + \rho_{00}^e + 7\rho_{-1-1}^e \}$
$\rho_{10}^e = \frac{1}{30} \{ 3\rho_{11}^e + 14\rho_{00}^e + 13\rho_{-1-1}^e \}$	$\rho_{99}^e = \frac{1}{3} \{ \rho_{11}^e + \rho_{00}^e + \rho_{-1-1}^e \}$
$\rho_{23}^e = \rho_{17}^e = \frac{1}{3} \{ -\rho_{11}^e + \rho_{00}^e \}$	$\rho_{21}^e = \rho_{15}^e = \frac{1}{2\sqrt{5}} \{ \rho_{-1-1}^e - \rho_{11}^e \}$
$\rho_{22}^e = \rho_{16}^e = \frac{1}{3\sqrt{10}} \{ -3\rho_{11}^e + 2\rho_{00}^e + \rho_{-1-1}^e \}$	
$\rho_{21}^e = \rho_{15}^e = \frac{1}{2\sqrt{5}} \{ -\rho_{11}^e + \rho_{-1-1}^e \}$	$\rho_{15}^e = \rho_{11}^e = \frac{2}{3\sqrt{5}} \{ \rho_{-1-1}^e - \rho_{11}^e \}$
$\rho_{20}^e = \rho_{14}^e = \frac{1}{3\sqrt{10}} \{ -\rho_{11}^e - 2\rho_{00}^e + 3\rho_{-1-1}^e \}$	
$\rho_{19}^e = \rho_{13}^e = \frac{1}{3} \{ -\rho_{00}^e + \rho_{-1-1}^e \}$	
$\rho_{22}^e = \rho_{12}^e = \frac{1}{5\sqrt{6}} \{ \rho_{11}^e - 2\rho_{00}^e + \rho_{-1-1}^e \}$	
$\rho_{21}^e = \rho_{11}^e = \frac{1}{10} \{ \rho_{11}^e - 2\rho_{00}^e + \rho_{-1-1}^e \}$	
$\rho_{20}^e = \rho_{10}^e = \frac{1}{5\sqrt{6}} \{ \rho_{11}^e - 2\rho_{00}^e + \rho_{-1-1}^e \}$	
$\rho_{16}^e = \rho_{12}^e = \frac{1}{2\sqrt{15}} \{ -3\rho_{11}^e + 2\rho_{00}^e + \rho_{-1-1}^e \}$	
$\rho_{15}^e = \rho_{11}^e = \frac{2}{3\sqrt{5}} \{ -\rho_{11}^e + \rho_{-1-1}^e \}$	
$\rho_{14}^e = \rho_{10}^e = \frac{1}{2\sqrt{15}} \{ -\rho_{11}^e - 2\rho_{00}^e + 3\rho_{-1-1}^e \}$	
$\rho_{15}^e = \rho_{99}^e = \frac{1}{6} \{ \rho_{11}^e - 2\rho_{00}^e + \rho_{-1-1}^e \}$	

The F represented density matrix elements are labelled with the numbering system shown in figure 2.4 while the L represented matrix elements are labelled with the magnetic projection quantum number.

Applying these considerations to equation (2.37) yields

$$\begin{aligned}
 \rho_{Fm_F F'm_F}^e &= \langle nIJFm_F | \rho^e | nIJF'm_F \rangle \\
 &= \sum_{m_J} \sqrt{(2F+1)(2F'+1)} (-1)^{2J-2I-2m_F} \begin{pmatrix} I & J & F \\ m_F-m_J & m_J & -m_F \end{pmatrix} \\
 &\quad \begin{pmatrix} I & J & F' \\ m_F-m_J & m_J & -m_F \end{pmatrix} \rho_{Jm_J Jm_J}^e
 \end{aligned} \tag{2.38}$$

The density matrix elements may be reduced to L representation by (Sobelman 1985)

$$\rho_{Jm_J Jm_J}^e = \sum_{m_L} (2J+1) (-1)^{2L-2S-2m_J} \begin{pmatrix} S & L & J \\ m_J-m_L & m_L & -m_J \end{pmatrix}^2 \rho_{Lm_L Lm_L}^e \tag{2.39}$$

Applying equations (2.37) and (2.38) for the electron excited density matrix elements in equation (2.36) produce the reduced density matrix elements given in Table 2.1 (MacGillivray and Standage 1991). The number of terms involving $\rho_{Fm_F F'm_F}^L$ in equation (2.36) may be reduced by applying symmetry relations formed by the π excitation of the transition used. The relations are given by (Farrell *et al.* 1988)

$$\begin{aligned}
 \rho_{Fm_F Fm_F}^L &= \rho_{F-m_F F-m_F}^L \\
 \text{Re} \rho_{3m_F 2m_F}^L &= -\text{Re} \rho_{3-m_F 2-m_F}^L \\
 \text{Re} \rho_{3m_F 1m_F}^L &= \text{Re} \rho_{3-m_F 1-m_F}^L \\
 \text{Re} \rho_{2m_F 1m_F}^L &= -\text{Re} \rho_{2-m_F 1-m_F}^L
 \end{aligned} \tag{2.40}$$

Applying the above relations and using the results from Table 2.1 produce the following result for the superelastic differential cross section

$$S = \alpha \left\{ \rho_{11}^{e(L)} + \rho_{-1-1}^{e(L)} \right\} + \gamma \rho_{00}^{e(L)} \tag{2.41}$$

where

$$\begin{aligned} \alpha = & \frac{2}{3} \rho_{23}^L{}_{23} + \frac{7}{15} \rho_{22}^L{}_{22} + \frac{1}{5} \rho_{21}^L{}_{21} + \frac{2}{3} \rho_{17}^L{}_{17} + \frac{2}{3} \rho_{16}^L{}_{16} + \frac{8}{15} \rho_{12}^L{}_{12} \\ & + \frac{7}{15} \rho_{11}^L{}_{11} - \frac{2}{3} \text{Re} \rho_{23}^L{}_{17} - \frac{4}{3\sqrt{10}} \text{Re} \rho_{22}^L{}_{16} + \frac{4}{5\sqrt{6}} \text{Re} \rho_{22}^L{}_{12} \\ & - \frac{2}{\sqrt{15}} \text{Re} \rho_{16}^L{}_{12} + \frac{1}{5} \text{Re} \rho_{21}^L{}_{11} \end{aligned} \quad (2.41a)$$

$$\begin{aligned} \gamma = & \frac{2}{3} \rho_{23}^L{}_{23} + \frac{16}{15} \rho_{22}^L{}_{22} + \frac{3}{5} \rho_{21}^L{}_{21} + \frac{2}{3} \rho_{17}^L{}_{17} + \frac{2}{3} \rho_{16}^L{}_{16} + \frac{14}{15} \rho_{12}^L{}_{12} \\ & + \frac{1}{15} \rho_{11}^L{}_{11} + \frac{4}{3} \text{Re} \rho_{23}^L{}_{17} + \frac{8}{3\sqrt{10}} \text{Re} \rho_{22}^L{}_{16} - \frac{8}{5\sqrt{6}} \text{Re} \rho_{22}^L{}_{12} \\ & + \frac{4}{\sqrt{15}} \text{Re} \rho_{16}^L{}_{12} - \frac{2}{5} \text{Re} \rho_{21}^L{}_{11} \end{aligned} \quad (2.41b)$$

All measurements of differential cross sections are performed in the collision frame. The differential cross section given by equation (2.41) is defined with respect to the laser frame and as such the electron collision density matrix elements $\rho_{M_L M_L'}^{e(L)}$ must be rotated to the collision frame. The rotation of these density matrix elements may be accomplished by the use of rotation matrices via (Blum 1981):

$$\rho_{M_L M_L'}^{e(L)} = \sum_{i,j} D_{i M_L}^{J*}(\omega) D_{j M_L'}^J(\omega) \rho_{i j}^e \quad (2.42)$$

The sum extends over the range of the magnetic quantum numbers i.e. $-L, -L+1, \dots, 0, \dots, L-1, L$. $D_{i M_L}^{J*}(\omega)$ and $D_{j M_L'}^J(\omega)$ are rotation matrices. ω are the Euler angles defined as $\omega = (\alpha, \beta, \gamma)$ (Edmonds 1974) where

α = rotation about the Z axis of the initial frame

β = rotation about the new Y axis

γ = rotation about the new Z axis to produce the final frame

The rotation matrix is defined as (Edmonds 1977)

$$D_{m'm}^J(\omega) = e^{im'\gamma} d_{m'm}^J(\beta) e^{im\alpha} \quad (2.43)$$

$d_{m'm}^J$ is a sub matrix given by

$$d_{m'm}^J(\beta) = [(J+m')!(J-m')!(J+m)!(J-m)!]^{1/2} \sum_{\sigma} (-1)^{J-m'-\sigma} \frac{\cos(\frac{\beta}{2})^{2\sigma+m'+m} \sin(\frac{\beta}{2})^{2J-2\sigma-m'-m}}{\sigma!(J-m-\sigma)!(J-m'-\sigma)!(\sigma+m'+m)!} \quad (2.44)$$

The sum over σ continues until the factorials become undefined. The application of equation (2.44) to the $L=1$ case yields:

$$d_{m'm}^1(\beta) = \begin{pmatrix} \frac{1}{2} \{1+\cos\beta\} & \frac{1}{\sqrt{2}} \sin\beta & \frac{1}{2} \{1-\cos\beta\} \\ -\frac{1}{\sqrt{2}} \sin\beta & \cos\beta & \frac{1}{\sqrt{2}} \sin\beta \\ \frac{1}{2} \{1-\cos\beta\} & -\frac{1}{\sqrt{2}} \sin\beta & \frac{1}{2} \{1+\cos\beta\} \end{pmatrix} \quad (2.45)$$

The use of linearly polarised light necessitate only one non-zero Euler angle, $-\beta$ about the Y axis and as a consequence the following result is derived

$$D_{m'm}^J(\omega) = d_{m'm}^J(-\beta) = \begin{pmatrix} \frac{1}{2} \{1+\cos\beta\} & -\frac{1}{\sqrt{2}} \sin\beta & \frac{1}{2} \{1-\cos\beta\} \\ \frac{1}{\sqrt{2}} \sin\beta & \cos\beta & -\frac{1}{\sqrt{2}} \sin\beta \\ \frac{1}{2} \{1-\cos\beta\} & \frac{1}{\sqrt{2}} \sin\beta & \frac{1}{2} \{1+\cos\beta\} \end{pmatrix} \quad (2.46)$$

The applying equations (2.42), (2.46) and the relations (2.14)-(2.18) yield the following rotated density matrix elements

$$\rho_{11}^{e(L)} = \cos^2\beta \rho_{11}^e + \frac{1}{2} \sin^2\beta \rho_{00}^e + \sqrt{2} \sin\beta \cos\beta \text{Re} \rho_{10}^e$$

$$\begin{aligned}\rho_{00}^{e(L)} &= 2\sin^2\beta\rho_{11}^e + \cos^2\beta\rho_{00}^e - 2\sqrt{2}\sin\beta\cos\beta\text{Re}\rho_{10}^e \\ \rho_{-1-1}^{e(L)} &= \rho_{11}^{e(L)}\end{aligned}\quad (2.47)$$

Substitution of equation (2.47) into (2.41) yields for the superelastic differential cross section

$$\begin{aligned}S(\beta) &= \alpha\left\{2\cos^2\beta\rho_{11}^e + \sin^2\beta\rho_{00}^e + 2\sqrt{2}\sin\beta\cos\beta\text{Re}\rho_{10}^e\right\} \\ &\quad + \gamma\left\{2\sin^2\beta\rho_{11}^e + \cos^2\beta\rho_{00}^e - 2\sqrt{2}\sin\beta\cos\beta\text{Re}\rho_{10}^e\right\}\end{aligned}\quad (2.48)$$

Using linearly polarised laser light, two pseudo Stokes parameters are defined:

$$P_1^S = \frac{S(0) - S(90)}{S(0) + S(90)} \quad (2.49a)$$

$$P_2^S = \frac{S(45) - S(135)}{S(45) + S(135)} \quad (2.49b)$$

where $S(\beta)$ represents the superelastic differential cross section with the laser polarised at angle β with respect to the quantisation axis. Substitution of equation (2.48) into these expressions reveals the following result:

$$P_1^S = \frac{(\gamma - \alpha)(-2\rho_{11}^e + \rho_{00}^e)}{(\gamma + \alpha)(2\rho_{11}^e + \rho_{00}^e)} \quad (2.50a)$$

$$P_2^S = \frac{-2\sqrt{2}(\gamma - \alpha)\text{Re}\rho_{10}^e}{(\gamma + \alpha)(2\rho_{11}^e + \rho_{00}^e)} \quad (2.50b)$$

We now define a new parameter, K , as

$$K = \frac{\gamma - \alpha}{\gamma + \alpha} \quad (2.51)$$

K is denoted an "optical pumping parameter" and is a depolarising factor due to both optical pumping and the hyperfine structure of the sodium D_2 transition. Applying the relationships defined by equation (2.25) allow these pseudo Stokes parameters to be rewritten in terms of an optical pumping parameter and atomic collision parameters viz:

$$P_1^S = K \{2\lambda - 1\} \quad (2.52a)$$

$$P_2^S = -2K \{ \lambda[1 - \lambda] \}^{1/2} \cos\chi \quad (2.52b)$$

Expressing the pseudo Stokes parameters in this form, decouples the laser-atom and electron-atom interactions. This decoupling is due to K being only a function of the density matrix elements formed by the atom-laser interaction and the atomic collision parameters are related only to the electron collision density matrix. Once K is determined the individual atomic collision parameters may be obtained. The determination of K both theoretically and experimentally is discussed in the next chapter.

One further pseudo Stokes parameter is required to be able to fully characterise the P state charge cloud. Consider the case in which circularly polarised light is used to excite the ground state sodium atoms. This allows the P_3^S pseudo Stokes parameter to be defined viz:

$$P_3^S = \frac{S(\sigma^-) - S(\sigma^+)}{S(\sigma^+) + S(\sigma^-)} \quad (2.53)$$

Where $S(\sigma^+)$ represents the measured superelastic differential cross section using left hand circularly polarised light and $S(\sigma^-)$ is the superelastic differential cross section for the use of right hand circularly polarised light. The excited substates that are populated are shown, for the case of σ^- polarised light, in figure 2.5(b) and for the case when σ^+ polarised light is used, figure 2.5(c). The superelastic differential cross section for the two cases may be determined by employing equation (2.35) which yields:

$$\begin{aligned}
S(\sigma^+) = & \rho_{20\ 20}^L \rho_{20\ 20}^{e(L)} + \rho_{21\ 21}^L \rho_{21\ 21}^{e(L)} + \rho_{22\ 22}^L \rho_{22\ 22}^{e(L)} + \rho_{23\ 23}^L \rho_{23\ 23}^{e(L)} \\
& + \rho_{24\ 24}^L \rho_{24\ 24}^{e(L)} + \rho_{14\ 14}^L \rho_{14\ 14}^{e(L)} + \rho_{15\ 15}^L \rho_{15\ 15}^{e(L)} + \rho_{16\ 16}^L \rho_{16\ 16}^{e(L)} \\
& + \rho_{17\ 17}^L \rho_{17\ 17}^{e(L)} + \rho_{10\ 10}^L \rho_{10\ 10}^{e(L)} + \rho_{11\ 11}^L \rho_{11\ 11}^{e(L)} + \rho_{12\ 12}^L \rho_{12\ 12}^{e(L)} \\
& + \rho_{20\ 14}^L \rho_{20\ 14}^{e(L)} + \rho_{14\ 20}^L \rho_{14\ 20}^{e(L)} + \rho_{20\ 10}^L \rho_{20\ 10}^{e(L)} + \rho_{10\ 20}^L \rho_{10\ 20}^{e(L)} \\
& + \rho_{14\ 10}^L \rho_{14\ 10}^{e(L)} + \rho_{10\ 14}^L \rho_{10\ 14}^{e(L)} + \rho_{21\ 11}^L \rho_{21\ 11}^{e(L)} + \rho_{11\ 21}^L \rho_{11\ 21}^{e(L)} \\
& + \rho_{21\ 15}^L \rho_{21\ 15}^{e(L)} + \rho_{15\ 21}^L \rho_{15\ 21}^{e(L)} + \rho_{15\ 11}^L \rho_{15\ 11}^{e(L)} + \rho_{11\ 15}^L \rho_{11\ 15}^{e(L)} \\
& + \rho_{22\ 16}^L \rho_{22\ 16}^{e(L)} + \rho_{16\ 22}^L \rho_{16\ 22}^{e(L)} + \rho_{22\ 12}^L \rho_{22\ 12}^{e(L)} + \rho_{12\ 22}^L \rho_{12\ 22}^{e(L)} \\
& + \rho_{16\ 12}^L \rho_{16\ 12}^{e(L)} + \rho_{12\ 16}^L \rho_{12\ 16}^{e(L)} + \rho_{23\ 17}^L \rho_{23\ 17}^{e(L)} + \rho_{17\ 23}^L \rho_{17\ 23}^{e(L)}
\end{aligned} \tag{2.54a}$$

$$\begin{aligned}
S(\sigma^-) = & \rho_{18\ 18}^L \rho_{18\ 18}^{e(L)} + \rho_{19\ 19}^L \rho_{19\ 19}^{e(L)} + \rho_{20\ 20}^L \rho_{20\ 20}^{e(L)} + \rho_{21\ 21}^L \rho_{21\ 21}^{e(L)} \\
& + \rho_{22\ 22}^L \rho_{22\ 22}^{e(L)} + \rho_{13\ 13}^L \rho_{13\ 13}^{e(L)} + \rho_{14\ 14}^L \rho_{14\ 14}^{e(L)} + \rho_{15\ 15}^L \rho_{15\ 15}^{e(L)} \\
& + \rho_{16\ 16}^L \rho_{16\ 16}^{e(L)} + \rho_{10\ 10}^L \rho_{10\ 10}^{e(L)} + \rho_{11\ 11}^L \rho_{11\ 11}^{e(L)} + \rho_{12\ 12}^L \rho_{12\ 12}^{e(L)} \\
& + \rho_{19\ 13}^L \rho_{19\ 13}^{e(L)} + \rho_{13\ 19}^L \rho_{13\ 19}^{e(L)} + \rho_{20\ 14}^L \rho_{20\ 14}^{e(L)} + \rho_{14\ 20}^L \rho_{14\ 20}^{e(L)} \\
& + \rho_{20\ 10}^L \rho_{20\ 10}^{e(L)} + \rho_{10\ 20}^L \rho_{10\ 20}^{e(L)} + \rho_{14\ 10}^L \rho_{14\ 10}^{e(L)} + \rho_{10\ 14}^L \rho_{10\ 14}^{e(L)} \\
& + \rho_{21\ 11}^L \rho_{21\ 11}^{e(L)} + \rho_{11\ 21}^L \rho_{11\ 21}^{e(L)} + \rho_{21\ 15}^L \rho_{21\ 15}^{e(L)} + \rho_{15\ 21}^L \rho_{15\ 21}^{e(L)} \\
& + \rho_{15\ 11}^L \rho_{15\ 11}^{e(L)} + \rho_{11\ 15}^L \rho_{11\ 15}^{e(L)} + \rho_{22\ 16}^L \rho_{22\ 16}^{e(L)} + \rho_{16\ 22}^L \rho_{16\ 22}^{e(L)} \\
& + \rho_{22\ 12}^L \rho_{22\ 12}^{e(L)} + \rho_{12\ 22}^L \rho_{12\ 22}^{e(L)} + \rho_{16\ 12}^L \rho_{16\ 12}^{e(L)} + \rho_{12\ 16}^L \rho_{12\ 16}^{e(L)}
\end{aligned} \tag{2.54b}$$

The calculation proceeds in a similar manner to that of the linearly polarised excitation case by reducing the collision density matrix elements to L representation. Following the reduction of the matrix elements the expressions for the superelastic differential cross sections can be rewritten as:

$$S(\sigma^+) = a^+ \rho_{11}^{e(L)} + b^+ \rho_{00}^{e(L)} + c^+ \rho_{-1-1}^{e(L)} \tag{2.55a}$$

$$S(\sigma^-) = a^- \rho_{11}^{e(L)} + b^- \rho_{00}^{e(L)} + c^- \rho_{-1-1}^{e(L)} \tag{2.55b}$$

where

$$\begin{aligned}
 a^+ = & \frac{1}{15} \rho_{20\ 20}^L + \frac{1}{5} \rho_{21\ 21}^L + \frac{2}{5} \rho_{22\ 22}^L + \frac{2}{3} \rho_{23\ 23}^L + \rho_{24\ 24}^L + \frac{1}{6} \rho_{14\ 14}^L \\
 & + \frac{1}{3} \rho_{15\ 15}^L + \frac{1}{2} \rho_{16\ 16}^L + \frac{2}{3} \rho_{17\ 17}^L + \frac{1}{10} \rho_{10\ 10}^L + \frac{7}{15} \rho_{11\ 11}^L + \frac{13}{30} \rho_{12\ 12}^L \\
 & - \frac{2}{3\sqrt{10}} \text{Re} \rho_{20\ 14}^L + \frac{2}{5\sqrt{6}} \text{Re} \rho_{20\ 10}^L - \frac{1}{\sqrt{15}} \text{Re} \rho_{14\ 10}^L + \frac{1}{5} \text{Re} \rho_{21\ 11}^L \\
 & - \frac{1}{\sqrt{5}} \text{Re} \rho_{21\ 15}^L - \frac{4}{3\sqrt{5}} \text{Re} \rho_{15\ 11}^L - \frac{2}{\sqrt{10}} \text{Re} \rho_{22\ 16}^L + \frac{2}{5\sqrt{6}} \text{Re} \rho_{22\ 12}^L \\
 & - \frac{3}{\sqrt{15}} \text{Re} \rho_{16\ 12}^L - \frac{2}{3} \text{Re} \rho_{23\ 17}^L
 \end{aligned}$$

$$\begin{aligned}
 b^+ = & \frac{8}{15} \rho_{20\ 20}^L + \frac{3}{5} \rho_{21\ 21}^L + \frac{8}{15} \rho_{22\ 22}^L + \frac{1}{3} \rho_{23\ 23}^L + \frac{1}{3} \rho_{14\ 14}^L \\
 & + \frac{1}{3} \rho_{15\ 15}^L + \frac{1}{3} \rho_{16\ 16}^L + \frac{1}{3} \rho_{17\ 17}^L + \frac{7}{15} \rho_{10\ 10}^L + \frac{1}{15} \rho_{11\ 11}^L + \frac{7}{15} \rho_{12\ 12}^L \\
 & - \frac{4}{3\sqrt{10}} \text{Re} \rho_{20\ 14}^L - \frac{4}{5\sqrt{6}} \text{Re} \rho_{20\ 10}^L - \frac{2}{\sqrt{15}} \text{Re} \rho_{14\ 10}^L - \frac{2}{5} \text{Re} \rho_{21\ 11}^L \\
 & + \frac{4}{3\sqrt{10}} \text{Re} \rho_{22\ 16}^L - \frac{4}{5\sqrt{6}} \text{Re} \rho_{22\ 12}^L + \frac{2}{\sqrt{15}} \text{Re} \rho_{16\ 12}^L + \frac{2}{3} \text{Re} \rho_{23\ 17}^L
 \end{aligned}$$

$$\begin{aligned}
 c^+ = & \frac{2}{5} \rho_{20\ 20}^L + \frac{1}{5} \rho_{21\ 21}^L + \frac{1}{15} \rho_{22\ 22}^L + \frac{1}{2} \rho_{14\ 14}^L \\
 & + \frac{1}{3} \rho_{15\ 15}^L + \frac{1}{6} \rho_{16\ 16}^L + \frac{13}{30} \rho_{10\ 10}^L + \frac{7}{15} \rho_{11\ 11}^L + \frac{1}{10} \rho_{12\ 12}^L \\
 & + \frac{2}{\sqrt{10}} \text{Re} \rho_{20\ 14}^L + \frac{2}{5\sqrt{6}} \text{Re} \rho_{20\ 10}^L + \frac{3}{\sqrt{15}} \text{Re} \rho_{14\ 10}^L + \frac{1}{5} \text{Re} \rho_{21\ 11}^L \\
 & + \frac{1}{\sqrt{5}} \text{Re} \rho_{21\ 15}^L + \frac{4}{3\sqrt{5}} \text{Re} \rho_{15\ 11}^L + \frac{2}{3\sqrt{10}} \text{Re} \rho_{22\ 16}^L + \frac{2}{5\sqrt{6}} \text{Re} \rho_{22\ 12}^L \\
 & + \frac{1}{\sqrt{15}} \text{Re} \rho_{16\ 12}^L
 \end{aligned}$$

$$\begin{aligned}
 a^- = & \frac{1}{15} \rho_{20\ 20}^L + \frac{1}{5} \rho_{21\ 21}^L + \frac{2}{5} \rho_{22\ 22}^L + \frac{1}{6} \rho_{14\ 14}^L \\
 & + \frac{1}{3} \rho_{15\ 15}^L + \frac{1}{2} \rho_{16\ 16}^L + \frac{1}{10} \rho_{10\ 10}^L + \frac{7}{15} \rho_{11\ 11}^L + \frac{13}{30} \rho_{12\ 12}^L \\
 & - \frac{2}{3\sqrt{10}} \text{Re} \rho_{20\ 14}^L + \frac{2}{5\sqrt{6}} \text{Re} \rho_{20\ 10}^L - \frac{1}{\sqrt{15}} \text{Re} \rho_{14\ 10}^L + \frac{1}{5} \text{Re} \rho_{21\ 11}^L \\
 & - \frac{1}{\sqrt{5}} \text{Re} \rho_{21\ 15}^L - \frac{4}{3\sqrt{5}} \text{Re} \rho_{15\ 11}^L - \frac{2}{\sqrt{10}} \text{Re} \rho_{22\ 16}^L + \frac{2}{5\sqrt{6}} \text{Re} \rho_{22\ 12}^L \\
 & - \frac{3}{\sqrt{15}} \text{Re} \rho_{16\ 12}^L
 \end{aligned}$$

$$b^- = \frac{1}{3} \rho_{19\ 19}^L + \frac{8}{15} \rho_{20\ 20}^L + \frac{3}{5} \rho_{21\ 21}^L + \frac{8}{15} \rho_{22\ 22}^L + \frac{1}{3} \rho_{13\ 13}^L + \frac{1}{3} \rho_{14\ 14}^L$$

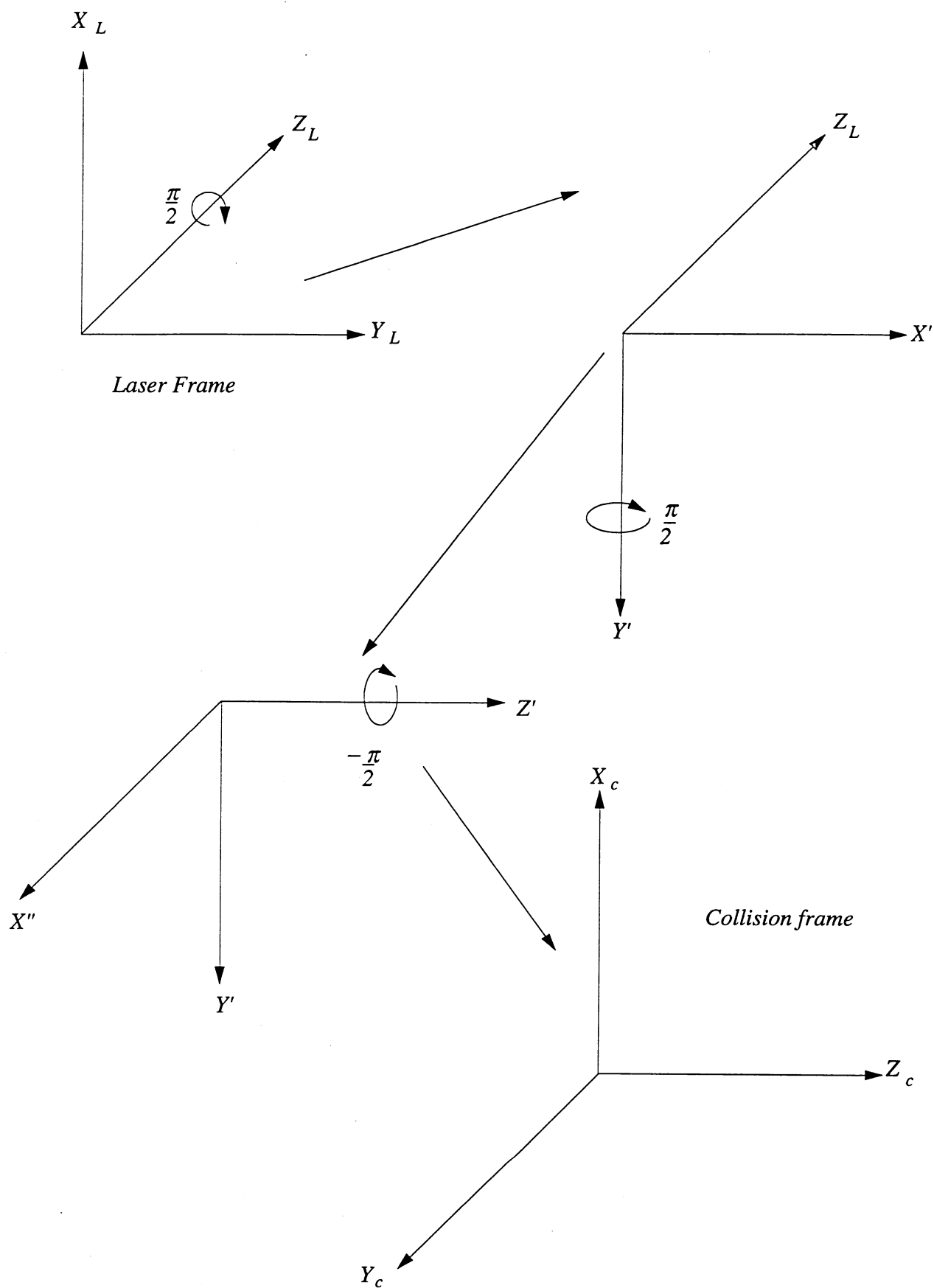


Figure 2.6: Rotation of the laser frame (circularly polarised laser case) to the collision frame

$$\begin{aligned}
& + \frac{1}{3} \rho_{15}^L{}_{15} + \frac{1}{3} \rho_{16}^L{}_{16} + \frac{7}{15} \rho_{10}^L{}_{10} + \frac{1}{15} \rho_{11}^L{}_{11} + \frac{7}{15} \rho_{12}^L{}_{12} \\
& - \frac{2}{3} \text{Re} \rho_{19}^L{}_{13} - \frac{4}{3\sqrt{10}} \text{Re} \rho_{20}^L{}_{14} - \frac{4}{5\sqrt{6}} \text{Re} \rho_{20}^L{}_{10} - \frac{2}{\sqrt{15}} \text{Re} \rho_{14}^L{}_{10} - \frac{2}{5} \text{Re} \rho_{21}^L{}_{11} \\
& + \frac{4}{3\sqrt{10}} \text{Re} \rho_{22}^L{}_{16} - \frac{4}{5\sqrt{6}} \text{Re} \rho_{22}^L{}_{12} + \frac{2}{\sqrt{15}} \text{Re} \rho_{16}^L{}_{12} \\
c = & \rho_{18}^L{}_{18} + \frac{2}{3} \rho_{19}^L{}_{19} + \frac{2}{5} \rho_{20}^L{}_{20} + \frac{1}{5} \rho_{21}^L{}_{21} + \frac{1}{15} \rho_{22}^L{}_{22} + \frac{2}{3} \rho_{13}^L{}_{13} + \frac{1}{2} \rho_{14}^L{}_{14} \\
& + \frac{1}{3} \rho_{15}^L{}_{15} + \frac{1}{6} \rho_{16}^L{}_{16} + \frac{13}{30} \rho_{10}^L{}_{10} + \frac{7}{15} \rho_{11}^L{}_{11} + \frac{1}{10} \rho_{12}^L{}_{12} + \frac{2}{3} \text{Re} \rho_{19}^L{}_{13} \\
& + \frac{2}{\sqrt{10}} \text{Re} \rho_{20}^L{}_{14} + \frac{2}{5\sqrt{6}} \text{Re} \rho_{20}^L{}_{10} + \frac{3}{\sqrt{15}} \text{Re} \rho_{14}^L{}_{10} + \frac{1}{5} \text{Re} \rho_{21}^L{}_{11} \\
& + \frac{1}{\sqrt{5}} \text{Re} \rho_{21}^L{}_{15} + \frac{4}{3\sqrt{5}} \text{Re} \rho_{15}^L{}_{11} + \frac{2}{3\sqrt{10}} \text{Re} \rho_{22}^L{}_{16} + \frac{2}{5\sqrt{6}} \text{Re} \rho_{22}^L{}_{12} \\
& + \frac{1}{\sqrt{15}} \text{Re} \rho_{16}^L{}_{12} \tag{2.56}
\end{aligned}$$

The cross sections given by equation (2.54) are now rotated to the collision frame using the same procedure as the linear case. The quantisation axis (Z_L) of the laser frame is given by the direction of laser propagation, in this case the negative Y_{col} direction. The X_L axis is a reference axis and as such is in the identical direction to the collision frame X_{col} axis. The Euler angles required to rotate the laser frame to the collision frame are given by $(\frac{\pi}{2}, \frac{\pi}{2}, -\frac{\pi}{2})$. These rotations are depicted in figure (2.6). Applying equations (2.43 - 2.45) yield the following rotation matrix:

$$D^J_{m'm}(\omega) = \begin{pmatrix} \frac{1}{2} & \frac{i}{\sqrt{2}} & \frac{1}{2} \\ \frac{i}{\sqrt{2}} & 0 & -\frac{i}{\sqrt{2}} \\ -\frac{1}{2} & \frac{i}{\sqrt{2}} & \frac{1}{2} \end{pmatrix} \tag{2.57a}$$

$$D^{I^*}_{m'm}(\omega) = \begin{pmatrix} \frac{1}{2} & \frac{i}{\sqrt{2}} & \frac{1}{2} \\ -\frac{i}{\sqrt{2}} & 0 & \frac{i}{\sqrt{2}} \\ -\frac{1}{2} & -\frac{i}{\sqrt{2}} & \frac{1}{2} \end{pmatrix} \quad (2.57b)$$

The application of this rotation matrix with equation (2.42) and the relations (2.14) - (2.18) give the following laser frame density matrix elements in terms of collision frame density matrix elements.

$$\begin{aligned} \rho_{11}^{e(L)} &= \rho_{11}^e + \frac{1}{2} \rho_{00}^e + \sqrt{2} \operatorname{Im} \rho_{10}^e \\ \rho_{00}^{e(L)} &= 0 \\ \rho_{-1-1}^{e(L)} &= \rho_{11}^e + \frac{1}{2} \rho_{00}^e - \sqrt{2} \operatorname{Im} \rho_{10}^e \end{aligned} \quad (2.58)$$

Upon substitution of equations (2.58) into equations (2.55) enable the superelastic cross sections to be written as:

$$S(\sigma^+) = a^+ \left\{ \rho_{11}^e + \frac{1}{2} \rho_{00}^e + \sqrt{2} \operatorname{Im} \rho_{10}^e \right\} + c^+ \left\{ \rho_{11}^e + \frac{1}{2} \rho_{00}^e - \sqrt{2} \operatorname{Im} \rho_{10}^e \right\} \quad (2.59a)$$

$$S(\sigma^-) = a^- \left\{ \rho_{11}^e + \frac{1}{2} \rho_{00}^e + \sqrt{2} \operatorname{Im} \rho_{10}^e \right\} + c^- \left\{ \rho_{11}^e + \frac{1}{2} \rho_{00}^e - \sqrt{2} \operatorname{Im} \rho_{10}^e \right\} \quad (2.59b)$$

The expressions for b^- and b^+ become redundant as a result of the rotation of the $\rho_{00}^{e(L)}$ to the collision frame. The number of terms in equations (2.55) may be reduced by applying symmetry relations of the σ excitation:

$$\begin{aligned} \rho_{Fm_F Fm_F}^L(\sigma^-) &= \rho_{F-m_F F-m_F}^L(\sigma^+) \\ \operatorname{Re} \rho_{3m_F 2m_F}^L(\sigma^-) &= -\operatorname{Re} \rho_{3-m_F 2-m_F}^L(\sigma^+) \end{aligned}$$

$$\begin{aligned}
\text{Re}\rho_{3m_F 1m_F}^L(\sigma^-) &= \text{Re}\rho_{3-m_F 1-m_F}^L(\sigma^+) \\
\text{Re}\rho_{2m_F 1m_F}^L(\sigma^-) &= -\text{Re}\rho_{2-m_F 1-m_F}^L(\sigma^+)
\end{aligned}
\tag{2.60}$$

Applying these relationships yield $a^+ = c^-$ and $a^- = c^+$ thus

$$S(\sigma^+) = a^+ \left\{ \rho_{11}^e + \frac{1}{2} \rho_{00}^e + \sqrt{2} \text{Im}\rho_{10}^e \right\} + c^+ \left\{ \rho_{11}^e + \frac{1}{2} \rho_{00}^e - \sqrt{2} \text{Im}\rho_{10}^e \right\}
\tag{2.61a}$$

$$S(\sigma^-) = c^+ \left\{ \rho_{11}^e + \frac{1}{2} \rho_{00}^e + \sqrt{2} \text{Im}\rho_{10}^e \right\} + a^+ \left\{ \rho_{11}^e + \frac{1}{2} \rho_{00}^e - \sqrt{2} \text{Im}\rho_{10}^e \right\}
\tag{2.61b}$$

Substituting equations (2.60) into equations (2.53) reveal for P_3^S :

$$P_3^S = \frac{\{c^+ - a^+\} 2\sqrt{2}\text{Im}\rho_{10}^e}{\{a^+ + c^+\} \{\rho_{00}^e + 2\rho_{11}^e\}}
\tag{2.62}$$

We now define a new optical pumping parameter K' as

$$K' = \frac{c^+ - a^+}{a^+ + c^+}
\tag{2.63}$$

Using this expression and employing equations (2.25) enable P_3^S to be written in a similar form as P_1^S and P_2^S that is, as a function of both an optical pumping parameter and atomic collision parameters such that:

$$P_3^S = 2K' \{ \lambda[1-\lambda] \}^{1/2} \sin\phi
\tag{2.64}$$

To correctly determine the atomic collision parameters the optical pumping parameters K and K' need to be found accurately. The three pseudo Stokes parameters defined by

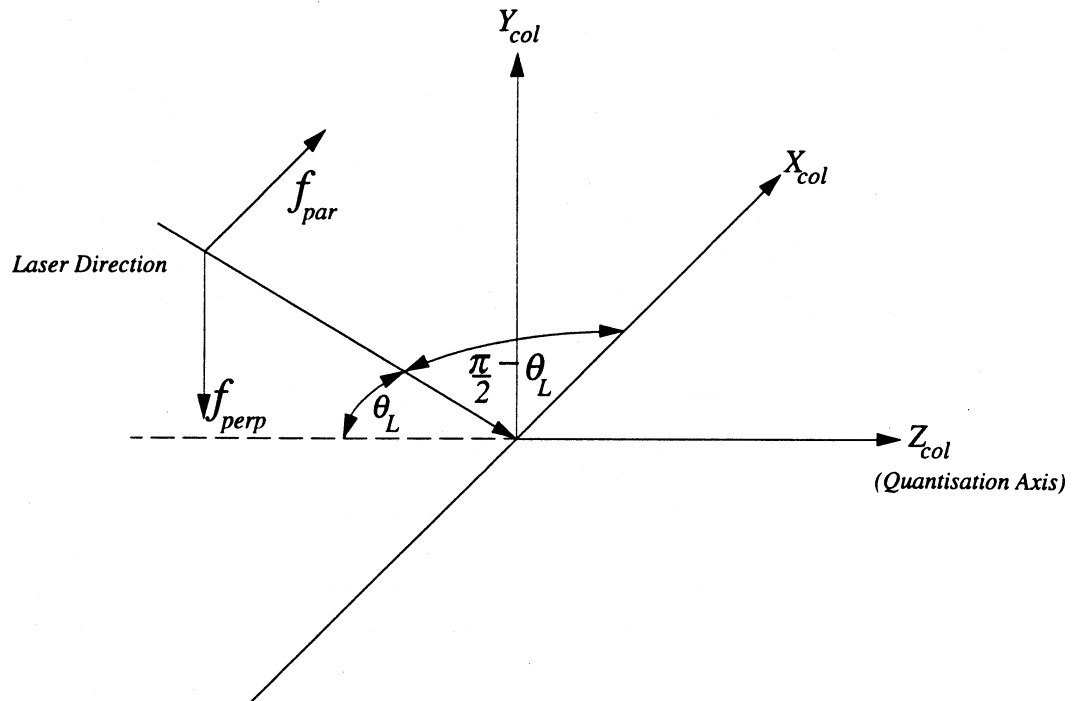


Figure (2.7a): The Co-Planar Geometry

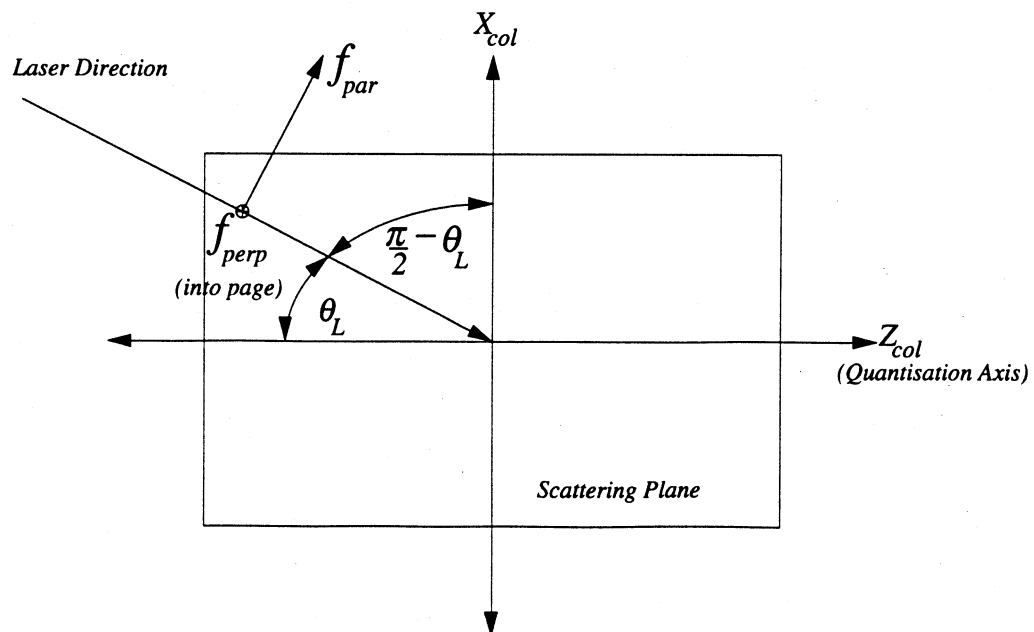


Figure (2.7b): The Scattering Plane. The laser is Parallel to the scattering plane and at angle θ_L the quantisation axis

equations (2.52) and (2.64) do not allow the determination of all of the atomic collision parameters and optical pumping parameters. It will, however, be shown in the following chapter that K may be determined by fluorescence measurements. K' is relatively insensitive to changes such as laser intensity, laser detuning and Doppler width of the atomic beam (Farrell *et al.* 1991), however it will be shown that K is much more sensitive to such changes. Once the optical pumping parameters are determined equations (2.52) and (2.64) enable the atomic collision parameters to be found. The next section will deal with the determination of K via the measurements of superelastic differential cross sections.

2.6 Superelastic Scattering in the Co-Planar Configuration

In this section one further single laser superelastic scattering experiment will be discussed. This experiment is identical to that of the previous experiment except that the laser is injected co-planar to the scattering plane and at an angle θ_L to the quantisation axis as shown in figure (2.7). For this geometry one further parameter, r may be defined as

$$r = \frac{S_{par}}{S_{perp}} \quad (2.65)$$

where S_{par} represents the superelastic differential cross section with the linearly polarised light polarised parallel to the scattering plane and S_{perp} is the superelastic differential cross section with linearly polarised light polarised perpendicular to the scattering plane. For the case of S_{par} the cross section in the laser frame is again given by

$$S_{par} = \alpha \left\{ \rho_{11}^{e(L)} + \rho_{-1-1}^{e(L)} \right\} + \gamma \rho_{00}^{e(L)} \quad (2.66)$$

The electron collision density matrix elements must now be rotated to the collision frame. The Euler angles for this rotation are $\omega = (0, \frac{\pi}{2} - \theta_L, 0)$. This is identical to the rotation with the perpendicular geometry linear case except that $-\beta = \frac{\pi}{2} - \theta_L$ which gives the following rotated density matrix elements

$$\begin{aligned}\rho_{11}^{e(L)} &= \sin^2 \theta_L \rho_{11}^e + \frac{1}{2} \cos^2 \theta_L \rho_{00}^e - \sqrt{2} \sin \theta_L \cos \theta_L \text{Re} \rho_{10}^e \\ \rho_{00}^{e(L)} &= 2 \cos^2 \theta_L \rho_{11}^e + \sin^2 \theta_L \rho_{00}^e + 2\sqrt{2} \sin \theta_L \cos \theta_L \text{Re} \rho_{10}^e \\ \rho_{-1-1}^{e(L)} &= \rho_{11}^{e(L)}\end{aligned}\tag{2.67}$$

Using equations (2.67) in equation (2.66) yields the expression for S_{par} in terms of collision frame elements

$$\begin{aligned}S_{par} &= 2\rho_{11}^e (\alpha \sin^2 \theta_L + \gamma \cos^2 \theta_L) + \rho_{00}^e (\alpha \cos^2 \theta_L + \gamma \sin^2 \theta_L) \\ &\quad + \sqrt{2} (\gamma - \alpha) \sin 2\theta_L \text{Re} \rho_{10}^e\end{aligned}\tag{2.68}$$

For the case when the laser polarisation is perpendicular to the scattering plane the expression for S_{perp} is again given by equation (2.66). The laser polarisation vector \underline{f} is anti-parallel to the Y_{col} axis and rotation of this vector to the quantisation axis is identical to the Euler angle rotation for the circularly polarised light case considered in the previous section i.e. $\omega = (\frac{\pi}{2}, \frac{\pi}{2}, \frac{\pi}{2})$. Applying the rotation to S_{perp} yields

$$S_{perp} = \alpha (2\rho_{11}^e + \rho_{00}^e)\tag{2.69}$$

Substituting equations (2.68) and (2.69) into equation (2.65) and applying the definitions of λ , χ and K gives (Farrell *et al.* 1991) (the expression in Farrell *et al.* 1991 has an error in the last term as it incorrectly subtracts this term rather than adding).

$$r = (1-\lambda) \left\{ \sin^2 \theta_L + \left[\frac{1+K}{1-K} \right] \cos^2 \theta_L \right\} + \lambda \left\{ \cos^2 \theta_L + \left[\frac{1+K}{1-K} \right] \sin^2 \theta_L \right\} + \left[\frac{2K}{1-K} \right] \sin 2\theta_L \cos \chi [\lambda(1-\lambda)]^{1/2} \quad (2.70)$$

If θ_L is set to 0° this expression is reduced significantly to

$$r = (1-\lambda) \left[\frac{1+K}{1-K} \right] + \lambda \quad (2.71)$$

Manipulating equations (2.52a) and (2.71) enables K and λ to be found as a function of co-planar parameter, r and the Stokes parameter P_I^S in the perpendicular geometry such that (Sang *et al.* 1991)

$$K = \frac{r-1}{(r+1) - \left(\frac{P_I^S(1+r) + (r-1)}{P_I^S + (r-1)} \right)} \quad (2.72)$$

$$\lambda = \left(\frac{P_I^S(1+r) + (r-1)}{P_I^S + (r-1)} \right) \quad (2.73)$$

Equation (2.72) allows an independent determination of the optical pumping parameter K . This can be a very accurate measure of K in the interaction region as this measurement is dependent on the superelastically scattered electrons and as such is not subject to radiation trapping outside the interaction region or the imaging of fluorescence from the interaction region as in the case when performing fluorescence measurements to determine the K parameter which is discussed in Chapter Three.

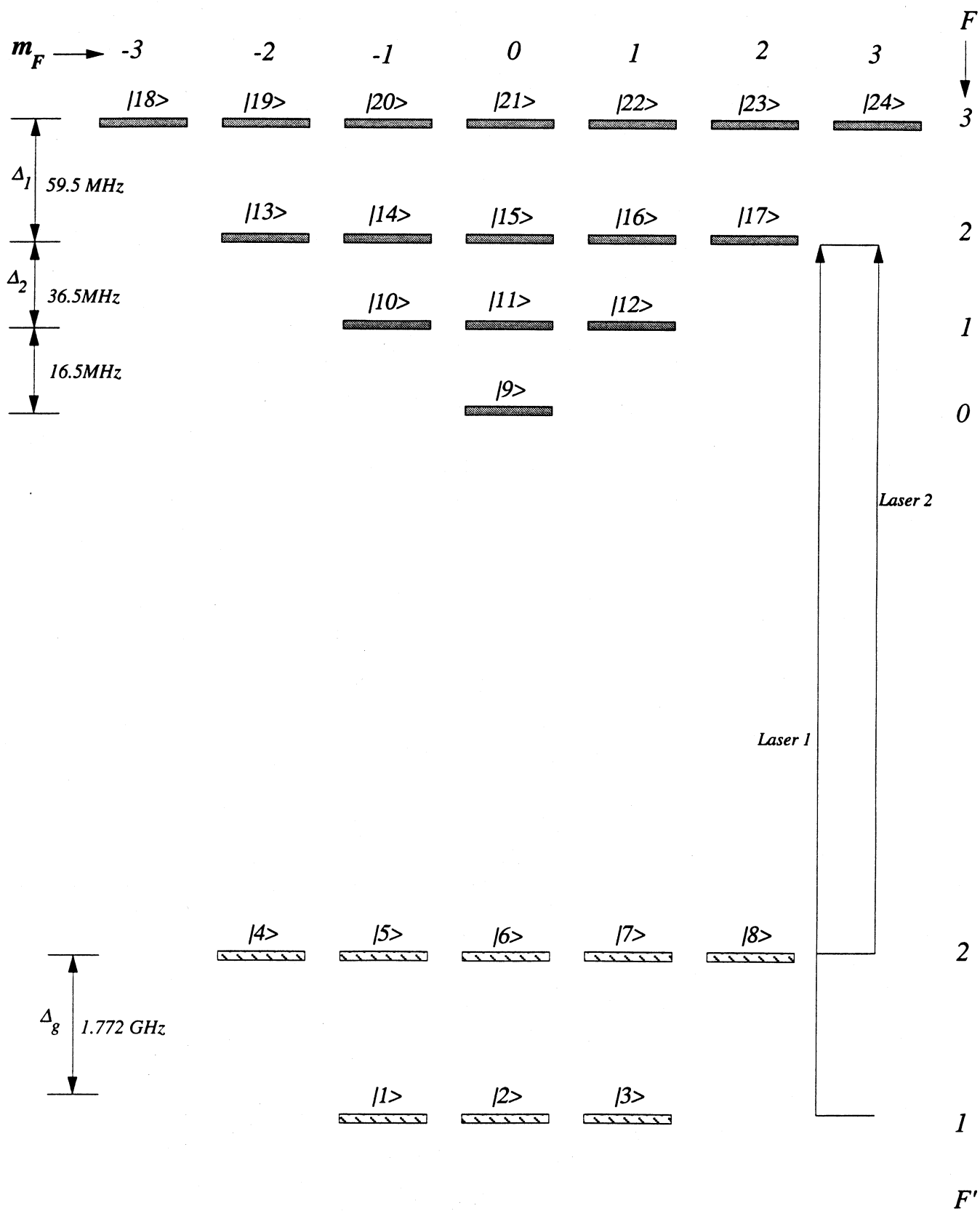


Figure 2.8: Folded step excitation of Sodium D_2 Line

2.7 Folded Step Superelastic Scattering

The design and construction of a superelastic scattering experiment is very dependent on the conditions required for stable operation. For the laser atom interaction it was found that one of the conditions was to have an atomic beam with a large Doppler spread in velocities (see the next chapter). The use of an atomic beam with a large Doppler widths also reduces the optical pumping efficiency and hence a reduced population in the excited state. For the single laser case in sodium exciting from the $F'=2$ ground state only $\frac{5}{8}$ of the population is able to be excited to the P state. The population in the excited state is further reduced due to power broadening effects in which the laser exciting from the $F'=2$ ground state to the $F=3$ excited states also excites the $F=2$ and $F=1$ sublevels. The $F=2$ and $F=1$ sub levels can relax to either the $F'=2$ ground state and be re-excited, or to the $F'=1$ ground state. The atoms in the $F'=1$ sub level can not be re-excited as the laser intensities used are not large enough to induce power broadening of the ground states and as such the $F'=1$ sub level acts as a sink to the population of the excited state. To enhance the population in the excited state, a second laser can be used to pump from the $F'=1$ sub level. This increase of population in the excited state can then be used so that atomic collision parameters at larger scattering angles may be deduced.

Consider now an experiment similar to that of the perpendicular geometry (figure 2.4) in which two lasers co-propagating in the $-Y_{\text{col}}$ with linearly polarised light at an angle β with respect to the quantisation axis. One laser is tuned from the $3^2S_{\frac{1}{2}}$ ($F'=1$) sublevel to the $3^2P_{\frac{3}{2}}$ ($F=2,1,0$) excited states and the second laser is tuned from the $3^2S_{\frac{1}{2}}$ ($F'=2$) sublevel to the $3^2P_{\frac{3}{2}}$ ($F=3,2,1$) excited states (see figure 2.8). Applying equation (2.35)

the superelastic signal is given by:

$$\begin{aligned}
 S_F = & \rho_{19}^L \rho_{19}^{e(L)} + \rho_{20}^L \rho_{20}^{e(L)} + \rho_{21}^L \rho_{21}^{e(L)} + \rho_{22}^L \rho_{22}^{e(L)} \\
 & + \rho_{23}^L \rho_{23}^{e(L)} + \rho_{13}^L \rho_{13}^{e(L)} + \rho_{14}^L \rho_{14}^{e(L)} + \rho_{16}^L \rho_{16}^{e(L)} \\
 & + \rho_{15}^L \rho_{15}^{e(L)} + \rho_{17}^L \rho_{17}^{e(L)} + \rho_9^L \rho_9^{e(L)} + \rho_{10}^L \rho_{10}^{e(L)}
 \end{aligned}$$

$$\begin{aligned}
& + \rho_{11\ 11}^L \rho_{11\ 11}^{e(L)} + \rho_{12\ 12}^L \rho_{12\ 12}^{e(L)} + \rho_{19\ 13}^L \rho_{19\ 13}^{e(L)} + \rho_{13\ 19}^L \rho_{13\ 19}^{e(L)} \\
& + \rho_{20\ 14}^L \rho_{20\ 14}^{e(L)} + \rho_{14\ 20}^L \rho_{14\ 20}^{e(L)} + \rho_{20\ 10}^L \rho_{20\ 10}^{e(L)} + \rho_{10\ 20}^L \rho_{10\ 20}^{e(L)} \\
& + \rho_{14\ 10}^L \rho_{14\ 10}^{e(L)} + \rho_{10\ 14}^L \rho_{10\ 14}^{e(L)} + \rho_{21\ 11}^L \rho_{21\ 11}^{e(L)} + \rho_{11\ 21}^L \rho_{11\ 21}^{e(L)} \\
& + \rho_{22\ 16}^L \rho_{22\ 16}^{e(L)} + \rho_{16\ 22}^L \rho_{16\ 22}^{e(L)} + \rho_{22\ 12}^L \rho_{22\ 12}^{e(L)} + \rho_{12\ 22}^L \rho_{12\ 22}^{e(L)} \\
& + \rho_{16\ 12}^L \rho_{16\ 12}^{e(L)} + \rho_{12\ 16}^L \rho_{12\ 16}^{e(L)} + \rho_{23\ 17}^L \rho_{23\ 17}^{e(L)} + \rho_{17\ 23}^L \rho_{17\ 23}^{e(L)} \\
& + \rho_{15\ 9}^L \rho_{15\ 9}^{e(L)} + \rho_{9\ 15}^L \rho_{9\ 15}^{e(L)}
\end{aligned} \tag{2.74}$$

This is identical to the expression for the single step superelastic differential cross section represented by equation (2.36) except for the addition of four more terms $\rho_{15\ 15}^L \rho_{15\ 15}^{e(L)}$, $\rho_{9\ 9}^L \rho_{9\ 9}^{e(L)}$, $\rho_{15\ 9}^L \rho_{15\ 9}^{e(L)}$ and $\rho_{9\ 15}^L \rho_{9\ 15}^{e(L)}$. The addition of the second laser creates some populations and coherences which are also formed by the first laser, in such cases their effect can be incorporated in the definition of the $\rho_{Fm_F F'm_F}^L$ terms which will be driven by two Rabi frequencies. Employing reduction methods previously used, this expression can be reduced to

$$S_F = \bar{\alpha} \left\{ \rho_{11}^{e(L)} + \rho_{-1\ -1}^{e(L)} \right\} + \bar{\gamma} \rho_{00}^{e(L)} \tag{2.75}$$

where

$$\begin{aligned}
\bar{\alpha} = & \frac{2}{3} \rho_{23\ 23}^L + \frac{7}{15} \rho_{22\ 22}^L + \frac{1}{5} \rho_{21\ 21}^L + \frac{2}{3} \rho_{17\ 17}^L + \frac{2}{3} \rho_{16\ 16}^L + \frac{8}{15} \rho_{12\ 12}^L \\
& + \frac{7}{15} \rho_{11\ 11}^L + \frac{1}{3} \rho_{15\ 15}^L + \frac{1}{3} \rho_{9\ 9}^L - \frac{2}{3} \text{Re} \rho_{23\ 17}^L - \frac{4}{3\sqrt{10}} \text{Re} \rho_{22\ 16}^L \\
& + \frac{4}{5\sqrt{6}} \text{Re} \rho_{22\ 12}^L - \frac{2}{\sqrt{15}} \text{Re} \rho_{16\ 12}^L + \frac{1}{5} \text{Re} \rho_{21\ 11}^L + \frac{1}{3} \text{Re} \rho_{15\ 9}^L
\end{aligned} \tag{2.76a}$$

$$\begin{aligned}
\bar{\gamma} = & \frac{2}{3} \rho_{23\ 23}^L + \frac{16}{15} \rho_{22\ 22}^L + \frac{3}{5} \rho_{21\ 21}^L + \frac{2}{3} \rho_{17\ 17}^L + \frac{2}{3} \rho_{16\ 16}^L + \frac{14}{15} \rho_{12\ 12}^L \\
& + \frac{1}{15} \rho_{11\ 11}^L + \frac{1}{3} \rho_{15\ 15}^L + \frac{1}{3} \rho_{9\ 9}^L + \frac{4}{3} \text{Re} \rho_{23\ 17}^L + \frac{8}{3\sqrt{10}} \text{Re} \rho_{22\ 16}^L \\
& - \frac{8}{5\sqrt{6}} \text{Re} \rho_{22\ 12}^L + \frac{4}{\sqrt{15}} \text{Re} \rho_{16\ 12}^L - \frac{2}{5} \text{Re} \rho_{21\ 11}^L - \frac{2}{3} \text{Re} \rho_{15\ 9}^L
\end{aligned} \tag{2.76b}$$

The electron collision density matrix elements are now rotated from the laser frame to the collision frame by the identical Euler angles as the single step linear case and are given by equation (2.47). Substitution of equations (2.47) enables the superelastic cross section to be written as

$$S(\beta) = \bar{\alpha} \left\{ 2\cos^2\beta \rho_{11}^e + \sin^2\beta \rho_{00}^e + 2\sqrt{2}\sin\beta\cos\beta \text{Re}\rho_{10}^e \right\} \\ + \bar{\gamma} \left\{ 2\sin^2\beta \rho_{11}^e + \cos^2\beta \rho_{00}^e - 2\sqrt{2}\sin\beta\cos\beta \text{Re}\rho_{10}^e \right\} \quad (2.77)$$

Using the definition for the pseudo Stokes parameters equations (2.49) yield

$$P_1^S = \bar{K} \{ 2\lambda - 1 \} \quad (2.78a)$$

$$P_2^S = -2\bar{K} \{ \lambda[1-\lambda] \}^{1/2} \cos\chi \quad (2.78b)$$

Where \bar{K} is an optical pumping parameter defined as

$$\bar{K} = \frac{\bar{\gamma} - \bar{\alpha}}{\bar{\gamma} + \bar{\alpha}} \quad (2.79)$$

This optical pumping parameter differs from the single step linear case by a few terms in $\bar{\gamma}$ and $\bar{\alpha}$. As with the single step case the proper determination of the optical pumping parameter is required so that accurate measurement of the atomic collision parameters can be performed. A full quantum electrodynamic calculation to determine \bar{K} will be given in detail in the following chapter.

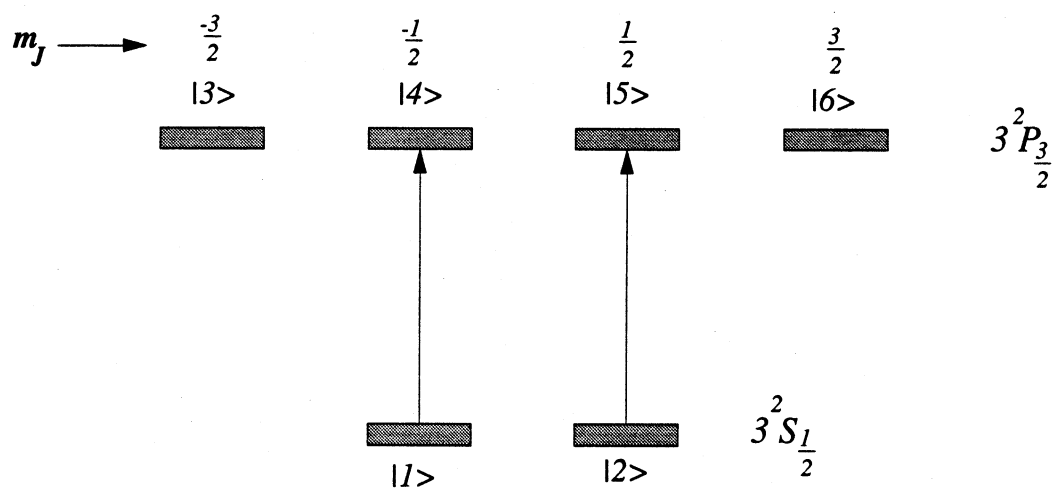


Figure 2.9: Laser excitation of the Sodium D_2 Line Using π Laser Light

2.8 The Superelastic P-S Collision In J Representation

At very high laser intensities the hyperfine energy levels of the sodium D_2 line may be power broadened sufficiently to be considered to be degenerate. In this case the hyperfine interaction is a smaller perturbation than the dipole interaction and as such J representation is more appropriate. The energy level structure of the sodium D_2 line in this representation is depicted in figure (2.9). The exciting radiation is linearly polarised and, in the laser frame, optical selection rules only allow $\Delta m_j = 0$ transitions. After applying equation (2.34), the following superelastic differential cross section is derived

$$S = \rho_{44}^L \rho_{44}^{e(L)} + \rho_{55}^L \rho_{55}^{e(L)} \quad (2.80)$$

where the labelling scheme of figure (2.9) is applied to the density matrix elements. Using equation (2.39) this expression may be reduced to L representation giving the superelastic differential cross section as

$$S = \rho_{44}^L \left(\frac{2}{3} \rho_{00}^{e(L)} + \frac{1}{3} \rho_{-1-1}^{e(L)} \right) + \rho_{55}^L \left(\frac{2}{3} \rho_{00}^{e(L)} + \frac{1}{3} \rho_{11}^{e(L)} \right) \quad (2.81)$$

The symmetry of the fine structure energy levels and the use of π radiation invokes the following relationship for the laser excited density matrix elements:

$$\rho_{Jm_J Jm_J}^L = \rho_{J-m_J J-m_J}^L \quad (2.82)$$

Thus equation (2.81) becomes

$$S = \rho_{55}^L \left(\frac{4}{3} \rho_{00}^{e(L)} + \frac{1}{3} \rho_{11}^{e(L)} + \frac{1}{3} \rho_{-1-1}^{e(L)} \right) \quad (2.83)$$

As with the other cases examined in this chapter the electron collision density matrix elements must be rotated from the laser frame to the collision frame. This is identical to

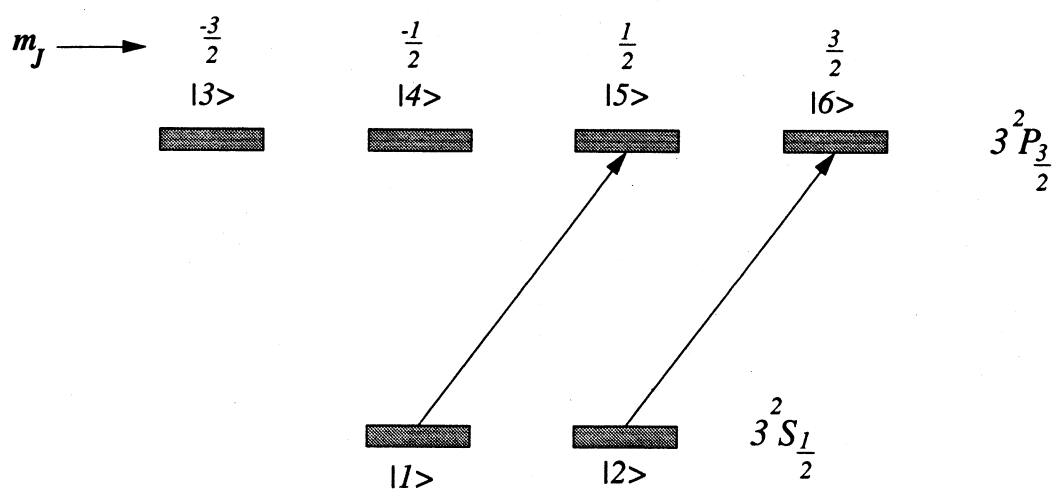


Figure 2.10a: Laser excitation of the Sodium D_2 Line Using σ^+ Laser Light

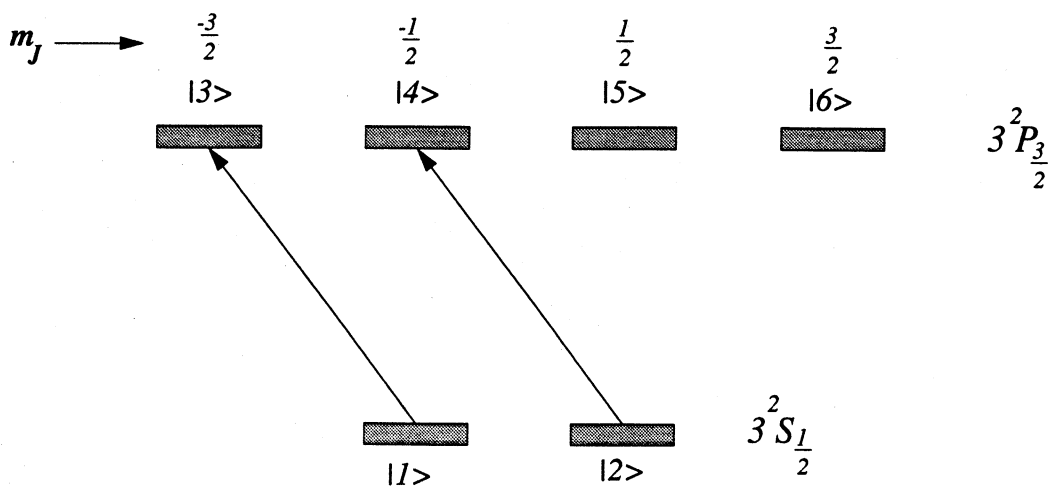


Figure 2.10b: Laser excitation of the Sodium D_2 Line Using σ Laser Light

the rotation given in section (2.5) and as such the rotated electron collision density matrix elements are given by equations (2.47). Transforming to the collision frame gives

$$S(\beta) = \frac{4}{3} \rho_{55}^L \left\{ 2\sin^2\beta \rho_{11}^e + \cos^2\beta \rho_{00}^e - 2\sqrt{2}\sin\beta\cos\beta \text{Re}\rho_{10}^e \right\} + \frac{2}{3} \rho_{55}^L \left\{ \cos^2\beta \rho_{11}^e + \frac{1}{2}\sin^2\beta \rho_{00}^e + \sqrt{2}\sin\beta\cos\beta \text{Re}\rho_{10}^e \right\} \quad (2.84)$$

Upon substitution of this expression into the definitions of the pseudo Stokes parameters P_1^S and P_2^S reveals

$$P_1^S = \left(\frac{3}{5}\right) \{2\lambda - 1\} \quad (2.85a)$$

$$P_2^S = -2 \left(\frac{3}{5}\right) \{ \lambda[1-\lambda] \}^{1/2} \cos\chi \quad (2.85b)$$

Thus this J representation result for the pseudo Stokes parameters P_1^S and P_2^S yields a high laser intensity value for K which is $\left(\frac{3}{5}\right)$.

Consider this same energy level scheme except that circularly polarised laser light is used as shown in figure (2.10a and 2.10b). Optical selection rules allow $\Delta m_j = \pm 1$ transitions to occur. Employing equation (2.34) yields the following superelastic differential cross sections

$$S(\sigma^+) = \rho_{55}^L \rho_{55}^{e(L)} + \rho_{66}^L \rho_{66}^{e(L)} \quad (2.86a)$$

$$S(\sigma^-) = \rho_{44}^L \rho_{44}^{e(L)} + \rho_{33}^L \rho_{33}^{e(L)} \quad (2.86a)$$

where $S(\sigma^+)$ and $S(\sigma^-)$ are the superelastic differential cross sections using left hand and right hand circularly polarised light respectively. Using equation (2.39) the electron collision density matrix elements may be reduced to L representation yielding

$$S(\sigma^+) = \rho_{55}^L \left(\frac{2}{3} \rho_{00}^{e(L)} + \frac{1}{3} \rho_{11}^{e(L)} \right) + \rho_{66}^L \rho_{11}^{e(L)} \quad (2.87a)$$

$$S(\sigma^-) = \rho_{44}^L \left(\frac{2}{3} \rho_{00}^{e(L)} + \frac{1}{3} \rho_{-1-1}^{e(L)} \right) + \rho_{33}^L \rho_{-1-1}^{e(L)} \quad (2.87b)$$

Applying the transformations given by equations (2.58) which rotate the electron collision density matrix elements from the laser frame to the collision frame yield

$$S(\sigma^+) = \left\{ \frac{1}{3} \rho_{55}^L + \rho_{66}^L \right\} \left(\rho_{11}^e + \frac{1}{2} \rho_{00}^e + \sqrt{2} \operatorname{Im} \rho_{10}^e \right) \quad (2.88a)$$

$$S(\sigma^-) = \left\{ \frac{1}{3} \rho_{44}^L + \rho_{33}^L \right\} \left(\rho_{11}^e + \frac{1}{2} \rho_{00}^e - \sqrt{2} \operatorname{Im} \rho_{10}^e \right) \quad (2.88b)$$

The symmetry of the fine structure energy levels and the use of σ light gives the following symmetry rule

$$\rho_{Jm_J Jm_J}^L(\sigma^-) = \rho_{J-m_J J-m_J}^L(\sigma^+) \quad (2.89)$$

Therefore equations (2.88) become

$$S(\sigma^+) = \alpha \left(\rho_{11}^e + \frac{1}{2} \rho_{00}^e + \sqrt{2} \operatorname{Im} \rho_{10}^e \right) \quad (2.90a)$$

$$S(\sigma^-) = \alpha \left(\rho_{11}^e + \frac{1}{2} \rho_{00}^e - \sqrt{2} \operatorname{Im} \rho_{10}^e \right) \quad (2.90b)$$

where

$$\alpha = \left\{ \frac{1}{3} \rho_{55}^L + \rho_{66}^L \right\} \quad (2.91)$$

Substitution of equations (2.90) into the definition of the pseudo Stokes parameter P_3^S equation (2.53) yields

$$P_3^S = -2 \{ \lambda[1-\lambda] \}^{1/2} \sin\phi \quad (2.92)$$

This result yields a high laser intensity value for the optical pumping parameter K' which is found to be equal to -1.

2.9 Coherence in Electron-Atom Collisions

The purpose of a superelastic scattering experiment is to determine atomic collision parameters which are related to various elements of the electron-atom scattering density matrix which in turn, are functions of scattering amplitudes. The total wave function of a fully coherent electron-atom collision process may be described by a pure state, where a pure state is defined as a fully coherent superposition of basis states (Anderson *et al.* 1988). The coherence of an electron atom collision may be measured experimentally by two parameters P_{TOT} and $|\mu|$ which may be defined in terms of pseudo Stokes parameters and optical pumping parameters as

$$P_{TOT} = \sqrt{\left(\frac{P_1^S}{K}\right)^2 + \left(\frac{P_2^S}{K}\right)^2 + \left(\frac{P_3^S}{K'}\right)^2} \quad (2.93)$$

$$|\mu| = \left(\frac{\left(\frac{P_2^S}{K}\right)^2 + \left(\frac{P_3^S}{K'}\right)^2}{1 - \left(\frac{P_1^S}{K}\right)^2} \right)^{1/2} \quad (2.94)$$

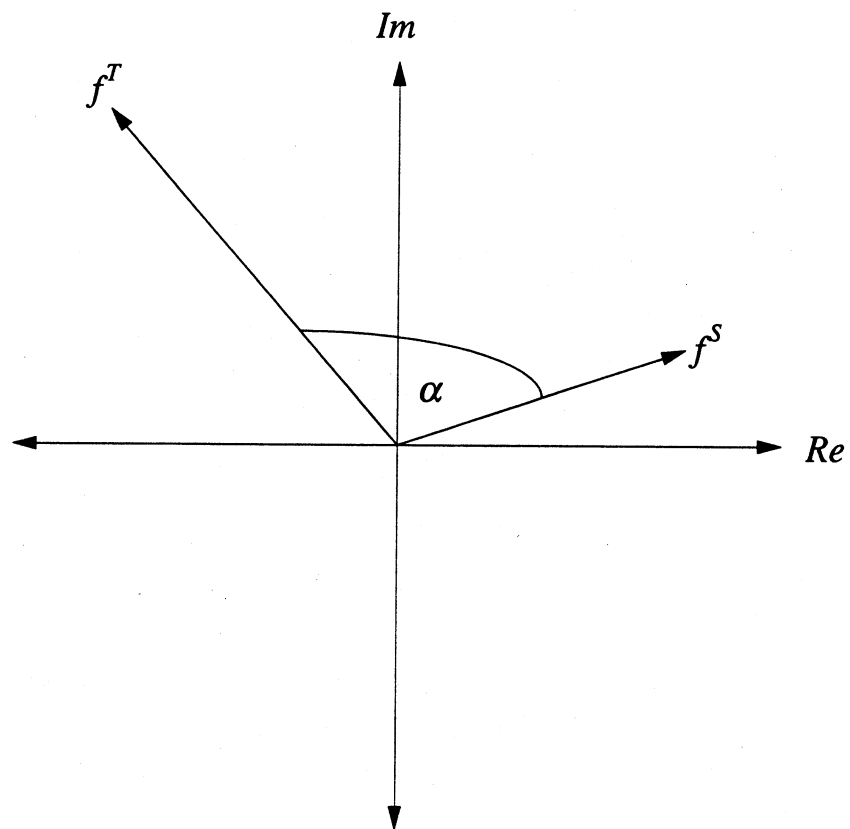


Figure 2.11: Singlet and Triplet Scattering Amplitudes in Complex Space

For a fully coherent collision process P_{TOT} and $|\mu|$ are equal to unity and for the totally incoherent collision process both parameters are equal to zero. In general the following inequality holds:

$$1 \geq P_{TOT} \geq |\mu| \quad (2.95)$$

One further way to examine coherence is by examining the complex phase relationship of the spin scattering amplitudes of the collision process. In the case of sodium, two spin scattering amplitudes are required. Sodium has a single outer shell electron and at the time of impact between the incident electron and the atom, singlet or triplet spin states form from the atomic electron and the incoming electron and as such, two spin channels are open. The two spin scattering amplitudes are denoted f^S for the singlet amplitude and f^T for the triplet scattering amplitude. In general the scattering amplitudes are complex and at angle α to each other in complex space as in figure 2.11. When the electron-atom collision process is fully coherent $\alpha = 0^\circ$ and the two vectors are parallel, for the totally incoherent case $\alpha = 90^\circ$ (Mitroy *et al.* 1987).

Chapter Three

Quantum Electrodynamic Theory

3.1 Introduction

To fully determine the atomic collision parameters in a superelastic scattering experiment it is necessary to obtain the optical pumping parameters with a high degree of accuracy. To complement experimental determination of these optical pumping parameters, it is advantageous to have a theoretical perspective on the laser-atom interaction. This chapter provides the theoretical details of the laser-atom interaction using linearly polarised laser light which was used in the superelastic experiments discussed in the previous chapter. The case of circularly polarised light will not be modelled as it has been shown previously (Farrell *et al.* 1991) that this parameter is relatively insensitive to changes such as laser power, detuning and the velocity spread of the atomic beam which is not the case for linearly polarised light. The derivation follows that of Ackerhalt *et al.* (1973), Ackerhalt and Eberly (1974), Allen and Eberly (1975) and recently extended by Farrell *et al.* (1988) and MacGillivray (1993).

The derivation is performed in the Heisenberg picture because it is possible to find an equation of motion for each field mode operator unlike the Schrödinger or interaction pictures and as such gives a more tractable solution. The first section of the chapter deals with the construction of a system Hamiltonian which is followed by the derivation of the equations of motion describing a general two level atom. A section on the determination of Rabi frequencies and branching ratios is then given which is followed by a section which investigates the folded step excitation scheme discussed in section 2.7. Following this is a section which relates the line polarisation to the optical pumping parameters from both the single and the folded step laser excitation schemes. Concluding the chapter are computational results from the single and folded step excitation schemes.

3.2 The System Hamiltonian

In this section a Hamiltonian describing the laser excitation of an atom is derived. This derivation employs the Coulomb gauge and as a consequence the vector potential is purely transverse (Knight 1992). The Hamiltonian of the system may be determined via the quantisation of the Hamiltonian of a classical field interacting with a classical atom. The quantised Hamiltonian is characterised by (Loudon 1983)

$$\hat{H} = \frac{1}{2m} \sum_j \left(\hat{p}_j + e \hat{A}(\underline{r}_j) \right)^2 + \frac{1}{2} \int \sigma(r) \phi(r) dr + \frac{1}{2} \int \left(\epsilon_o \hat{E}_T^2 + \mu_o^{-1} \hat{B}^2 \right) dr \quad (3.1)$$

where \hat{p}_j is the momentum operator, $\hat{A}(\underline{r}_j)$ is the vector potential operator, $\sigma(r)$ is the charge density, $\phi(r)$ is the scalar potential, \hat{B} is the magnetic field operator and \hat{E}_T is the transverse electric field operator. In the dipole approximation, which specifies that the electromagnetic fields do not vary spatially over the atomic dimensions, the system Hamiltonian may be partitioned into three Hamiltonians such that:

$$\hat{H} = \hat{H}_A + \hat{H}_F + \hat{H}_I \quad (3.2)$$

where \hat{H}_A is the freely evolving atom term, \hat{H}_F is a field term and \hat{H}_I is an atom-field interaction term. The freely evolving atom term is given by

$$\hat{H}_A = \frac{1}{2m} \sum_j \hat{p}_j^2 + \frac{1}{2} e \sum_j \phi(\underline{r}_j) + \frac{1}{2} e Z \phi(0) \quad (3.3)$$

where Z is the atomic number. It may be shown (Loudon 1983) that if $|m\rangle$ is an energy eigenstate with eigenvalue $\hbar \omega_m$ then

$$\hat{H}_A |m\rangle = \hbar \omega_m |m\rangle \quad (3.4)$$

Applying the closure theorem twice yields

$$\hat{H}_A = \sum_m |m\rangle \langle m| \hat{H}_A \sum_n |n\rangle \langle n| \quad (3.5)$$

where the sums run over all the eigenstates of \hat{H}_A . Then from equation (3.4) we obtain

$$\langle m| \hat{H}_A |n\rangle = \hbar \omega_m \delta_{mn} \quad (3.6)$$

Thus the atomic Hamiltonian may be rewritten as

$$\hat{H}_A = \hbar \sum_m \omega_m \hat{\sigma}_{mm} \quad (3.7)$$

$\hat{\sigma}_{mm}$ where is an atomic operator defined as

$$\hat{\sigma}_{mm} = |m\rangle \langle m| \quad (3.8)$$

The field Hamiltonian term is given by

$$\hat{H}_F = \frac{1}{2} \int (\epsilon_o \hat{\tilde{E}}_T^2 + \mu_o^{-1} \hat{\tilde{B}}^2) dr \quad (3.9)$$

$\hat{\tilde{E}}_T$ and $\hat{\tilde{B}}$ may be rewritten in terms of field modes as (Loudon 1983)

$$\hat{\tilde{E}}_T = \sum_k \hat{\tilde{E}}_k = -\frac{\partial \hat{A}}{\partial t} \quad (3.10a)$$

$$\hat{\tilde{B}} = \sum_k \hat{\tilde{B}}_k = \nabla \times \hat{A} \quad (3.10b)$$

where k is a particular mode which specifies both the wavevector and polarisation mode. $\hat{\underline{A}}$ is the vector potential defined as (Loudon 1983)

$$\hat{\underline{A}} = \sum_k \left(\frac{\hbar}{2\epsilon_o V \omega_k} \right)^{1/2} \underline{\epsilon}_k \left\{ \hat{a}_k e^{(-i\omega_k t + i\mathbf{k} \cdot \underline{r})} + \hat{a}_k^\dagger e^{(i\omega_k t - i\mathbf{k} \cdot \underline{r})} \right\} \quad (3.11)$$

$\underline{\epsilon}_k$ is the transverse polarisation vector, V is the mode volume and \hat{a}_k and \hat{a}_k^\dagger are the annihilation and creation operators respectively which obey the following commutation relation for bosons (Allen and Eberly 1975)

$$[\hat{a}_k(t), \hat{a}_{k'}^\dagger(t)] = \delta_{kk'} \quad (3.12)$$

Applying equations (3.9) - (3.12) yields the field Hamiltonian in terms of creation and annihilation operators as

$$\hat{H}_F = \sum_k \hbar \omega_k \left\{ \hat{a}_k^\dagger \hat{a}_k + \frac{I}{2} \right\} \quad (3.13)$$

Finally the interaction Hamiltonian term is

$$\hat{H}_I = \frac{e}{m} \sum_j \hat{\underline{A}}(\underline{r}_j) \cdot \hat{\underline{p}}_j + \frac{e^2}{2m} \sum_j \hat{\underline{A}}(\underline{r}_j)^2 \quad (3.14)$$

This term contains four contributions (Loudon 1983)

$$\hat{H}_I = \hat{H}_{ED} + \hat{H}_{EQ} + \hat{H}_{MD} + \hat{H}_{NL} \quad (3.15)$$

\hat{H}_{ED} is the electric dipole interaction

$$\hat{H}_{ED} = e \sum_j \underline{r}_j \cdot \hat{\underline{E}}_T(0) = \underline{D} \cdot \hat{\underline{E}}_T(0) \quad (3.16)$$

where $\hat{\underline{E}}_T(0)$ refers to the transverse electric field evaluated at the origin of the atom and

$$\underline{D} = \sum_j e \underline{r}_j \quad (3.17)$$

is the atomic dipole moment. The electric-quadrupole interaction term is represented by

$$\hat{H}_{EQ} = \frac{1}{2} e \sum_j (\underline{r}_j \cdot \nabla) (\underline{r}_j \cdot \hat{\underline{E}}_T(0)) = -\nabla \cdot \underline{Q} \cdot \hat{\underline{E}}_T(0) \quad (3.18)$$

where

$$\underline{Q} = \frac{1}{2} \sum_j \underline{r}_j \underline{r}_j \quad (3.19)$$

is the electric quadrupole interaction. The third term in equation (3.15) is the magnetic dipole interaction given by

$$\begin{aligned} \hat{H}_{MD} &= -\left(\frac{e}{4m}\right) \sum_j \left\{ \hat{\underline{p}}_j \cdot \underline{r}_j \times \hat{\underline{B}}(0) + \underline{r}_j \times \hat{\underline{B}}(0) \cdot \hat{\underline{p}}_j \right\} \\ &= -\left(\frac{e}{2m}\right) \hat{\underline{M}} \cdot \hat{\underline{B}}(0) \end{aligned} \quad (3.20)$$

where $\hat{\underline{B}}(0)$ is the magnetic field at origin of the atom and

$$\hat{\underline{M}} = \sum_j \underline{r}_j \times \hat{\underline{p}}_j = \sum_j \hat{\underline{l}}_j \quad (3.21)$$

where $\hat{\underline{L}}_j$ is the angular momentum of the j th electron. The final term of equation (3.15) is a non linear term involving the square of the magnetic field such that:

$$\hat{H}_{NL} = \left(\frac{e^2}{8m} \right) \sum_j \left\{ \underline{r}_j \cdot \hat{\underline{B}}(0) \right\}^2 \quad (3.22)$$

The relative sizes of the electric-quadrupole, magnetic-dipole and the non linear terms are small compared to the electric-dipole term (in the order of the fine structure constant (Loudon 1983)) and as such will be ignored for the present calculation. The interaction Hamiltonian is then given by

$$\hat{H}_I = \underline{D} \cdot \hat{\underline{E}}_T(0) \quad (3.23)$$

The interaction Hamiltonian may be written in terms of annihilation and creation operators by substituting equations (3.10 and 3.11) into equation (3.16) and for greater generality we take the position of the nucleus to be at position \underline{r}' rather than the origin of the coordinates, thus yielding (MacGillivray 1993)

$$\hat{H}_I = i \sum_k \left(\frac{\hbar \omega_k}{2 \epsilon_0 V} \right)^{1/2} \underline{\epsilon}_k \cdot \underline{D} \left\{ \hat{\underline{a}}_k e^{(-i\omega_k t + i\mathbf{k} \cdot \underline{r}')} - \hat{\underline{a}}_k^\dagger e^{(i\omega_k t - i\mathbf{k} \cdot \underline{r}')} \right\} \quad (3.24)$$

Applying closure twice to the vector \underline{D} yields the dipole operator

$$\begin{aligned} \hat{\underline{D}} &= \sum_i |i\rangle \langle i| \underline{D} \sum_j |j\rangle \langle j| = \sum_{i,j} \langle i| \underline{D} |j\rangle |i\rangle \langle j| \\ &= \sum_{i,j} \underline{D}_{ij} \hat{\sigma}_{ij} \end{aligned} \quad (3.25)$$

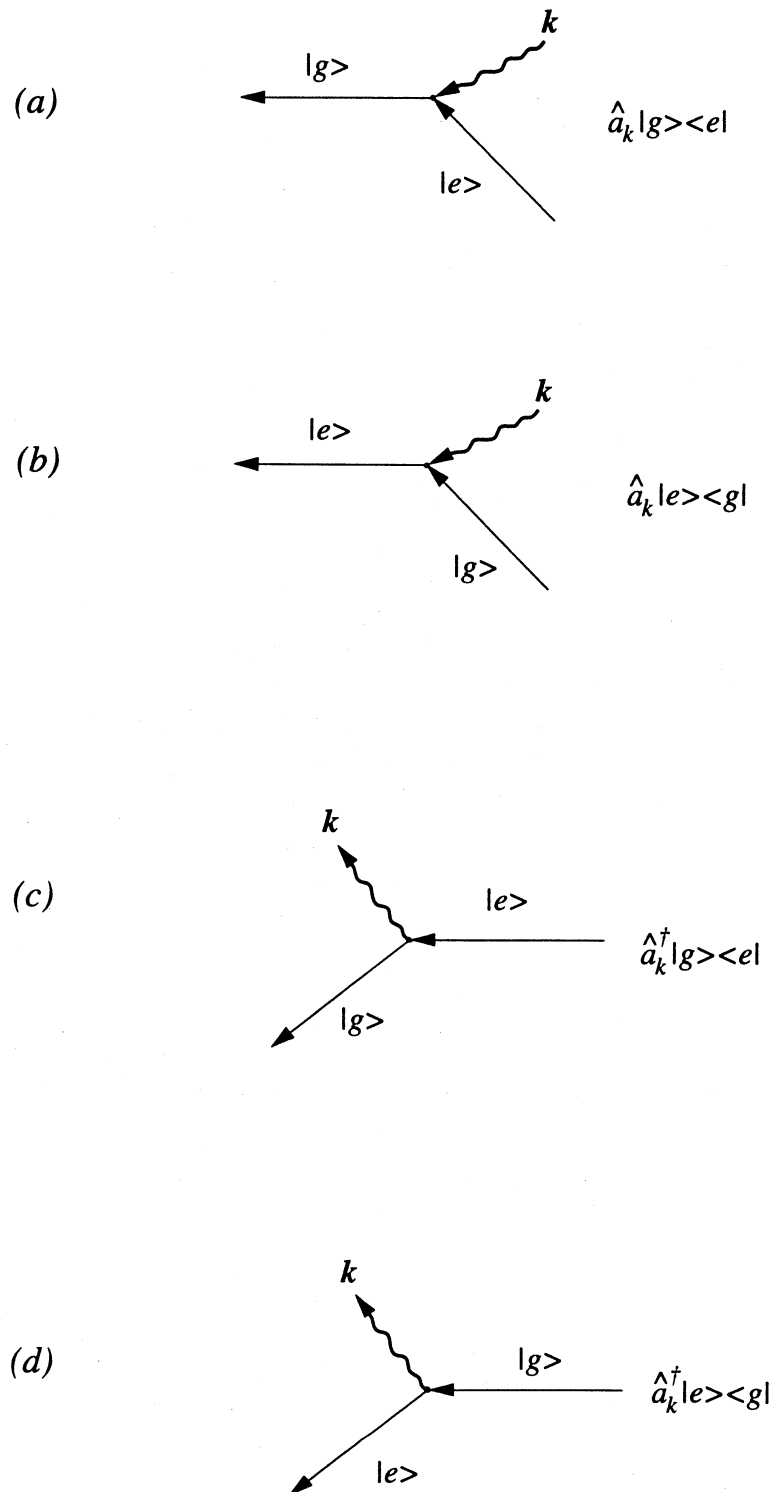


Figure 3.1: Feynman Diagrams representing the four different terms in the electric-dipole interaction

Substitution of equation (3.25) into equation (3.24) reveals

$$\hat{H}_I = i \sum_k \sum_{ij} \left(\frac{\hbar \omega_k}{2\epsilon_0 V} \right)^{1/2} \underline{\epsilon}_k \cdot \underline{D}_{ij} \left\{ \hat{a}_k e^{(-i\omega_k t + i\mathbf{k} \cdot \mathbf{r}')} - \hat{a}_k^\dagger e^{(i\omega_k t - i\mathbf{k} \cdot \mathbf{r}')} \right\} \hat{\sigma}_{ij} \quad (3.26)$$

The dipole operator is only non zero for transitions between ground and excited states which enables the dipole operator to be written as

$$\underline{\hat{D}} = \sum_{eg} \left(\underline{D}_{eg} \hat{\sigma}_{eg} + \underline{D}_{ge} \hat{\sigma}_{ge} \right) \quad (3.27)$$

Using (3.27) the interaction Hamiltonian becomes

$$\hat{H}_I = i \sum_k \sum_{eg} \left(\frac{\hbar \omega_k}{2\epsilon_0 V} \right)^{1/2} \left\{ \hat{a}_k e^{(-i\omega_k t + i\mathbf{k} \cdot \mathbf{r}')} - \hat{a}_k^\dagger e^{(i\omega_k t - i\mathbf{k} \cdot \mathbf{r}')} \right\} \left(\underline{\epsilon}_k \cdot \underline{D}_{eg} \hat{\sigma}_{eg} + \underline{\epsilon}_k \cdot \underline{D}_{ge} \hat{\sigma}_{ge} \right) \quad (3.28)$$

The expansion of equation (3.28) give rise to four electric-dipole interaction terms which are represented in figure (3.1) using Feynman diagrams. The wavy lines characterise photons and the straight lines atomic states. The initial state is represented by the term on the right and the final state by the term on the left. $|e\rangle$ represents an excited state which is higher in energy than the ground state denoted $|g\rangle$. Figure (3.1a) depicts a non-energy conserving process whereby a photon with mode k is absorbed and an electron in state $|e\rangle$ is destroyed to produce the ground state $|g\rangle$. A similar non-energy conserving process is depicted in figure (3.1d). In this case a photon of mode k is created as an electron in state $|g\rangle$ is annihilated to create an electron in state $|e\rangle$. These two non-energy conserving processes contribute to higher order energy processes. Figure (3.1b) shows the energy conserving process in which a photon of mode k is destroyed and an electron in ground state $|g\rangle$ is destroyed to produce

an electron in the excited state $|e\rangle$. Figure (3.1c) is the inverse of this process. Applying the rotating wave approximation, which allows the neglect of the non-energy conserving processes and using normal ordering (i.e. the field creation operators are written to the left of atomic operators and the field annihilation operators are written to the right of the atomic operators (Allen and Eberly 1975)). Using only energy conserving processes enables the interaction Hamiltonian, equation (3.28) to be rewritten as

$$\hat{H}_I = \hbar \sum_k \sum_e \sum_g \left\{ g_{eg}^k \hat{\sigma}_{eg} \hat{a}_k(t) e^{i\mathbf{k} \cdot \mathbf{r}'} + g_{eg}^{k*} \hat{a}_k^\dagger(t) e^{-i\mathbf{k} \cdot \mathbf{r}'} \hat{\sigma}_{ge} \right\} \quad (3.29)$$

where

$$g_{eg}^k = i \left(\frac{\omega_k}{2\epsilon_0 \hbar V} \right)^{1/2} \boldsymbol{\varepsilon}_k \cdot \mathbf{D}_{eg} \quad (3.30)$$

and

$$\hat{a}_k(t) = \hat{a}_k e^{-i\omega_k t} \text{ and } \hat{a}_k^\dagger(t) = \hat{a}_k^\dagger e^{i\omega_k t} \quad (3.31)$$

The use of normal ordering is equivalent to the use of any other ordering since field operators and atomic operators act on different spaces and as such commute. During the course of this derivation, approximations are used which destroy the commutation and normal ordering avoids this problem. In the following section this Hamiltonian will be applied to obtain the time evolution of operators using the Heisenberg equation of motion.

3.3 The Derivation of the Equations of Motion for a Two Level Atom

In the Heisenberg representation, operators are time dependent and the wavefunctions are time independent. The time evolution of a general operator \hat{O} is governed by the Heisenberg equation of motion:

$$\dot{\hat{O}} = -\frac{i}{\hbar} [\hat{O}, \hat{H}] \quad (3.32)$$

Consider a two level atom consisting of a ground state $|g\rangle$ and an excited state $|e\rangle$ each of which consists of a set of degenerate and near degenerate substates interacting with a laser mode frequency ω_L propagating in the Z direction. The Heisenberg equation of motion for the field operator $\hat{a}_k(t)$ is given by

$$\dot{\hat{a}}_k(t) = -\frac{i}{\hbar} [\hat{a}_k(t), \hat{H}] \quad (3.33)$$

where \hat{H} is given by equation (3.2). Since field operators and atomic operators commute, this may be written as

$$\dot{\hat{a}}_k(t) = -\frac{i}{\hbar} [\hat{a}_k(t), \hat{H}_F + \hat{H}_I] \quad (3.34)$$

Applying the expressions for \hat{H}_F and \hat{H}_I given by equations (3.13 and 3.29) yield

$$\begin{aligned} \dot{\hat{a}}_k(t) = & -i \hat{a}_k(t) \sum_{k'} \omega_{k'} \hat{a}_{k'}^\dagger(t) \hat{a}_{k'}(t) + i \sum_{k'} \omega_{k'} \hat{a}_{k'}^\dagger(t) \hat{a}_{k'}(t) \hat{a}_k(t) \\ & -i \hat{a}_k(t) \sum_{k'} \sum_e \left\{ g_{eg}^{k'} \hat{\sigma}_{eg} \hat{a}_{k'}(t) e^{ikz} + g_{eg}^{k'*} \hat{a}_{k'}^\dagger(t) e^{-ikz} \hat{\sigma}_{ge} \right\} \end{aligned}$$

$$+i \sum_{k'} \sum_e \sum_g \left\{ g_{eg}^{k'} \hat{\sigma}_{eg} \hat{a}_k(t) e^{ikz} + g_{eg}^{k'*} \hat{a}_k^\dagger(t) e^{-ikz} \hat{\sigma}_{ge} \right\} \hat{a}_k(t) \quad (3.35)$$

Using the commutation relation (3.12) this expression may be reduced to

$$\dot{\hat{a}}_k(t) = -i \omega_k \hat{a}_k(t) - i \sum_e \sum_g g_{eg}^{k*} \hat{\sigma}_{ge} e^{-ikz} \quad (3.36)$$

This may be integrated formally (Allen and Eberly 1975) to give

$$\hat{a}_k(t) = \hat{a}_k(0) e^{-i\omega_k t} - i \sum_e \sum_g g_{eg}^{k*} e^{-ikz} \int_0^t \hat{\sigma}_{ge}(t') G_k(t, t') dt' \quad (3.37)$$

where $G_k(t, t')$ is the retarded Green's function defined as

$$G_k(t, t') = \lim_{\epsilon \rightarrow 0} \begin{cases} 0 & \text{if } t < t' \\ e^{-i(\omega_k - i\epsilon)(t-t')} & \text{if } t > t' \end{cases} \quad (3.38)$$

Taking the limit of equation (3.38) and substituting into equation (3.37) reveals

$$\hat{a}_k(t) = \hat{a}_k(0) e^{-i\omega_k t} - i \sum_e \sum_g g_{eg}^{k*} e^{-ikz} \int_0^t \hat{\sigma}_{ge}(t') e^{-i\omega_k(t-t')} dt' \quad (3.39)$$

The right hand side of equation (3.39) contains two terms. The term on the left is the freely evolving field term or sometimes called the vacuum term which depends on the initial field operator and the term on the right which only depends on atomic operators and describes spontaneous decay. Removal of the atomic operator under the integral may be accomplished by the following argument: the sum over the frequency modes causes destructive interference

of the phase terms within the integral except for values of $t \approx t'$. The characteristic time scales associated with spontaneous emission are long compared to the free evolution time, which is in the order of the field mode frequency. As a consequence, the harmonic approximation can be made which assumes that the operator element under the integral evolves freely. Then from equation (3.32)

$$\dot{\hat{\sigma}}_{ge} = -\frac{i}{\hbar} [\hat{\sigma}_{ge}, \hat{H}_A] \quad (3.39)$$

Products of atomic operators give the following rule

$$\hat{\sigma}_{ab} \hat{\sigma}_{cd} = \hat{\sigma}_{ad} \delta_{bc} \quad (3.40)$$

The time evolution of the operator is

$$\dot{\hat{\sigma}}_{ge} = -i(\omega_e - \omega_g) \hat{\sigma}_{ge} \quad (3.41)$$

Integrating gives

$$\int_{t'}^t \frac{d\hat{\sigma}_{ge}}{\hat{\sigma}_{ge}} = -i(\omega_e - \omega_g)(t - t') \quad (3.42)$$

where ω_e and ω_g are the frequencies of states $|e\rangle$ and $|g\rangle$ respectively. Manipulation after the integration of equation (3.42) enables the atomic operator $\hat{\sigma}_{ge}$ at t' to be determined

$$\hat{\sigma}_{ge}(t') = \hat{\sigma}_{ge}(t) e^{i(\omega_e - \omega_g)(t - t')} \quad (3.43)$$

Substituting equation (3.43) into the expression for the field operator yields

$$\hat{a}_k(t) = \hat{a}_k(0) e^{-i\omega_k t} - i \sum_e \sum_g g_{eg}^{k*} e^{-ikz} \hat{\sigma}_{ge} \int_0^t e^{-i(\omega_k - \omega_e + \omega_g)(t-t')} dt' \quad (3.44)$$

Following a similar derivation the creation operator is given by

$$\hat{a}_k^\dagger(t) = \hat{a}_k^\dagger(0) e^{i\omega_k t} + i \sum_e \sum_g g_{eg}^k e^{ikz} \hat{\sigma}_{eg} \int_0^t e^{i(\omega_k - \omega_e + \omega_g)(t-t')} dt' \quad (3.45)$$

The Heisenberg equation of motion may now be applied to derive an expression for the atomic operator

$$\dot{\hat{\sigma}}_{eg} = -\frac{i}{\hbar} [\hat{\sigma}_{eg}, \hat{H}] \quad (3.46)$$

Substitution of equations (3.7, 3.13 and 3.29) reveals

$$\dot{\hat{\sigma}}_{eg} = -i(\omega_g - \omega_e) \hat{\sigma}_{eg} - i \sum_k \sum_{e'} g_{e'g}^{k*} \hat{a}_k^\dagger(t) e^{-ikz} \hat{\sigma}_{ee'} + i \sum_k \sum_{g'} g_{eg}^{k*} \hat{a}_k^\dagger(t) e^{-ikz} \hat{\sigma}_{g'g} \quad (3.47)$$

Substitution of the field operator expression equation (3.45) yields

$$\begin{aligned} \dot{\hat{\sigma}}_{eg} = & -i(\omega_g - \omega_e) \hat{\sigma}_{eg} - i \sum_k \sum_{e'} g_{e'g}^{k*} \hat{a}_k^\dagger(0) e^{i(\omega_k t - kz)} \hat{\sigma}_{ee'} + i \sum_k \sum_{g'} g_{eg}^{k*} \hat{a}_k^\dagger(0) e^{i(\omega_k t - kz)} \hat{\sigma}_{g'g} \\ & - \sum_k \sum_{g'} \sum_{e'} g_{eg}^{k*} g_{e'g}^k \hat{\sigma}_{e'g} \int_0^t e^{i(\omega_k - \omega_{e'} + \omega_g)(t-t')} dt' \end{aligned} \quad (3.48)$$

Equation (3.48) contains four terms. The first term in the equation describes the freely evolving atomic operator term. The second and third terms correspond to an interaction of the atom with the field which are commonly referred to as driving terms. The final term corresponds to spontaneous emission of the atom. The integral in this term has been the subject of many investigations (Allen and Eberly 1975, Ackerhalt *et al.* 1973, 1974, Milonni 1976, (Knight 1980, Cardimona *et al.* 1982, 1983)) and gives rise to damping terms for the real parts and frequency shifts for the imaginary parts. The damping terms are proportional to the Einstein A coefficients and the imaginary terms correspond to Lamb shifts which are non-zero only when the non-degenerate excited states have different principal quantum numbers. In the case examined here, excitation of the sodium D lines, all states involved share the same principal quantum number and as such the generalised shift terms are set to zero. Performing the integration reveals, for the real part (Allen and Eberly 1975)

$$\int_0^t e^{i(\omega_k - \omega_e + \omega_g)(t-t')} dt' \approx \pi \delta(\omega_k - \omega_e + \omega_g) \quad (3.49)$$

Thus the time evolution of the atomic operator $\hat{\sigma}_{eg}$ becomes

$$\begin{aligned} \dot{\hat{\sigma}}_{eg} = & -i(\omega_g - \omega_e) \hat{\sigma}_{eg} - i \sum_k \sum_{e'} g_{e'g}^{k*} \hat{a}_k^\dagger(0) e^{i(\omega_k t - kz)} \hat{\sigma}_{ee'} + i \sum_k \sum_{g'} g_{eg}^{k*} \hat{a}_k^\dagger(0) e^{i(\omega_k t - kz)} \hat{\sigma}_{g'g} \\ & - \sum_k \sum_{g'} \sum_{e'} g_{eg}^{k*} g_{e'g}^k \hat{\sigma}_{e'g} \pi \delta(\omega_k - \omega_e + \omega_g) \end{aligned} \quad (3.50)$$

The derivation of the time evolution of the atomic operator $\hat{\sigma}_{gg'}$ and $\hat{\sigma}_{ee'}$ follows that of $\hat{\sigma}_{eg}$ and are given by

$$\begin{aligned}
\dot{\hat{\sigma}}_{g'g} = & -i(\omega_g - \omega_{g'})\hat{\sigma}_{g'g} - i \sum_k \sum_{e''} g_{e''g}^{k*} \hat{a}_k^\dagger(0) e^{i(\omega_k t - kz)} \hat{\sigma}_{g'e''} \\
& + i \sum_k \sum_{e''} g_{e''g'}^k \hat{\sigma}_{e''g} \hat{a}_k(0) e^{-i(\omega_k t - kz)} \\
& + \sum_k \sum_{e''} \sum_{e'''} g_{e''g}^{k*} g_{e''g'}^k \hat{\sigma}_{e''e'''} \pi \delta(\omega_k - \omega_{e'''} + \omega_{g'}) \\
& + \sum_k \sum_{e''} \sum_{e'''} g_{e''g}^k g_{e''g'}^{k*} \hat{\sigma}_{e''e'''} \pi \delta(\omega_k - \omega_{e'''} + \omega_g)
\end{aligned} \tag{3.51}$$

$$\begin{aligned}
\dot{\hat{\sigma}}_{ee'} = & -i(\omega_{e'} - \omega_e)\hat{\sigma}_{ee'} - i \sum_k \sum_{g''} g_{e'g''}^k \hat{\sigma}_{eg''} \hat{a}_k(0) e^{-i(\omega_k t - kz)} \\
& + i \sum_k \sum_{g''} g_{eg''}^{k*} \hat{a}_k^\dagger(0) e^{i(\omega_k t - kz)} \hat{\sigma}_{g''e'} \\
& - \sum_k \sum_{g''} \sum_{e'''} g_{e'g''}^k g_{e''g}^{k*} \hat{\sigma}_{ee'''} \pi \delta(\omega_k - \omega_{e'''} + \omega_{g''}) \\
& - \sum_k \sum_{g''} \sum_{e'''} g_{eg''}^{k*} g_{e''g}^k \hat{\sigma}_{e''e'''} \pi \delta(\omega_k - \omega_{e'''} + \omega_{g''})
\end{aligned} \tag{3.52}$$

These equations are of a similar form to equation (3.50) and contain freely evolving atom terms, driving terms and damping terms. The rapidly oscillating terms in equations (3.50), (3.51) and (3.52) may be removed by transforming the operators to slowly varying operators which rotate at the mode frequency (Whitley and Stroud 1976)

$$\hat{\sigma}_{ee'} = \hat{\chi}_{ee'} \tag{3.53a}$$

$$\hat{\sigma}_{g'g} = \hat{\chi}_{g'g} \tag{3.53b}$$

$$\hat{\sigma}_{eg} = \hat{\chi}_{eg} e^{i(\omega_k t - kz)} \tag{3.53c}$$

$$\dot{\hat{\sigma}}_{eg} = \dot{\hat{\chi}}_{eg} e^{i(\omega_k t - kz)} + i(\omega_k - kv_z) \hat{\chi}_{eg} e^{i(\omega_k t - kz)} \tag{3.53d}$$

where the z coordinate of the atom has been written as $z = z_0 + v_z t$ which describes the motion of the atom through the laser beam in the direction of the mode propagation. Applying equations (3.53) to equation (3.50) and restricting the problem to a single laser mode enables equation (3.50) to be rewritten as

$$\begin{aligned} \dot{\hat{\chi}}_{eg} = & -i \Delta_{eg} \hat{\chi}_{eg} - i \sum_{e'} g_{e'g}^{k_L*} \hat{a}_{k_L}^\dagger(0) \hat{\chi}_{ee'} + i \sum_{g'} g_{eg}^{k_L*} \hat{a}_{k_L}^\dagger(0) \hat{\chi}_{g'g} \\ & - \sum_k \sum_{g'} \sum_{e'} g_{eg}^{k*} g_{e'g}^k \hat{\chi}_{e'g} \pi \delta(\omega_k - \omega_{e'} + \omega_g) \end{aligned} \quad (3.54)$$

where Δ_{eg} is the detuning given by

$$\Delta_{eg} = \omega_{k_L} - k_L v_z - \omega_{eg} \quad \text{and} \quad \omega_{eg} = \omega_e - \omega_g \quad (3.55)$$

Similarly applying (3.53) to equations (3.51) and (3.52) and restricting to a single laser mode, gives

$$\begin{aligned} \dot{\hat{\chi}}_{g'g} = & -i(\omega_g - \omega_{g'}) \hat{\chi}_{g'g} - i \sum_{e''} g_{e''g}^{k_L*} \hat{a}_{k_L}^\dagger(0) \hat{\chi}_{g'e''} + i \sum_{e''} g_{e''g}^{k_L} \hat{\chi}_{e''g} \hat{a}_{k_L}(0) \\ & + \sum_k \sum_{e''} \sum_{e'''} g_{e''g}^{k*} g_{e'''g}^k \hat{\chi}_{e'''e''} \pi \delta(\omega_k - \omega_{e'''} + \omega_g) \\ & + \sum_k \sum_{e''} \sum_{e'''} g_{e''g}^k g_{e'''g}^{k*} \hat{\chi}_{e''e'''} \pi \delta(\omega_k - \omega_{e'''} + \omega_g) \end{aligned} \quad (3.56)$$

$$\begin{aligned} \dot{\hat{\chi}}_{ee'} = & -i(\omega_e - \omega_{e'}) \hat{\chi}_{ee'} - i \sum_{g''} g_{e'g''}^{k_L} \hat{\chi}_{eg''} \hat{a}_{k_L}(0) + i \sum_{g''} g_{eg''}^{k_L*} \hat{a}_{k_L}^\dagger(0) \hat{\chi}_{g''e'} \\ & - \sum_k \sum_{g''} \sum_{e'''} g_{e'g''}^k g_{e'''g''}^{k*} \hat{\chi}_{ee'''} \pi \delta(\omega_k - \omega_{e'''} + \omega_{g''}) \end{aligned}$$

$$- \sum_k \sum_{g''} \sum_{e'''} g_{eg''}^{k*} g_{e''g'''}^k \hat{\chi}_{e''e'''} \pi \delta(\omega_k - \omega_{e'''} + \omega_{g''}) \quad (3.57)$$

The expectation value of equations (3.54), (3.56) and (3.57) yield

$$\begin{aligned} \langle \dot{\chi}_{eg} \rangle &= -i \Delta_{eg} \langle \hat{\chi}_{eg} \rangle - i \sum_{e'} \Omega_{e'g} \langle \hat{\chi}_{ee'} \rangle + i \sum_{g'} \Omega_{eg'} \langle \hat{\chi}_{g'g} \rangle \\ &\quad - \sum_k \sum_{g'} \sum_{e'} g_{eg''}^{k*} g_{e'g''}^k \pi \delta(\omega_k - \omega_{e'} + \omega_{g'}) \langle \hat{\chi}_{e'g} \rangle \end{aligned} \quad (3.58)$$

$$\begin{aligned} \langle \dot{\chi}_{g'g} \rangle &= -i(\omega_g - \omega_{g'}) \langle \hat{\chi}_{g'g} \rangle - i \sum_{e''} \Omega_{e''g} \langle \hat{\chi}_{g'e''} \rangle + i \sum_{e''} \Omega_{e''g'} \langle \hat{\chi}_{e''g} \rangle \\ &\quad + \sum_k \sum_{e''} \sum_{e'''} g_{e''g}^{k*} g_{e''e'''}^k \pi \delta(\omega_k - \omega_{e'''} + \omega_{g'}) \langle \hat{\chi}_{e''e'''} \rangle \\ &\quad + \sum_k \sum_{e''} \sum_{e'''} g_{e''g}^k g_{e''e'''}^{k*} \pi \delta(\omega_k - \omega_{e'''} + \omega_g) \langle \hat{\chi}_{e''e'''} \rangle \end{aligned} \quad (3.59)$$

$$\begin{aligned} \langle \dot{\chi}_{ee'} \rangle &= -i(\omega_e - \omega_{e'}) \langle \hat{\chi}_{ee'} \rangle - i \sum_{g''} \Omega_{e'g''} \langle \hat{\chi}_{eg''} \rangle + i \sum_{g''} \Omega_{eg''} \langle \hat{\chi}_{g''e'} \rangle \\ &\quad - \sum_k \sum_{g''} \sum_{e'''} g_{e'g''}^k g_{e''g'''}^{k*} \pi \delta(\omega_k - \omega_{e'''} + \omega_{g''}) \langle \hat{\chi}_{ee'''} \rangle \\ &\quad - \sum_k \sum_{g''} \sum_{e'''} g_{eg''}^{k*} g_{e''g'''}^k \pi \delta(\omega_k - \omega_{e'''} + \omega_{g''}) \langle \hat{\chi}_{e''e'} \rangle \end{aligned} \quad (3.60)$$

where

$$\Omega_{eg} = g_{eg}^{k_L} \langle \hat{a}_{k_L} \rangle (0) = g_{eg}^{k_L*} \langle \hat{a}_{k_L}^\dagger \rangle (0) \quad (3.61)$$

is defined as the half Rabi frequency (MacGillivray 1993). The Rabi frequency may be evaluated from the definition (Corney 1977)

$$\Omega = \frac{-\langle \hat{E} \cdot \hat{D} \rangle}{\hbar} \quad (3.62)$$

Ω is called the Rabi frequency and has units of radians per second. The half Rabi frequencies have been chosen to be real as we are free to choose the phase of the field and the phases of the states connecting the induced dipole (Ducloy 1973).

The sum over the excited states in the damping terms of equations (3.58-3.60) leads to generalised damping terms. For a single mode excitation the generalised damping terms are non-zero when two or more degenerate or near-degenerate excited states are excited from a common ground state. The general definition of a decay term is given by

$$\Gamma_{ee'g'} = \sum_k g_{e'g}^k g_{eg}^{k*} \pi \delta(\omega_k - \omega_{e'} + \omega_g) + g_{eg}^{k*} g_{e'g}^k \pi \delta(\omega_k - \omega_e + \omega_g) \quad (3.63)$$

The hyperfine ground state of sodium consists of two nearly degenerate sublevels which are separated by 1.77 GHz. The laser powers used in the experiment are such that power broadening of these levels does not occur and excitation out of only one ground sublevel can occur. Excitation from a single ground state yields the following generalised relaxation term

$$\Gamma_{ee'g} = \sum_k g_{e'g}^k g_{eg}^{k*} \pi \delta(\omega_k - \omega_{e'} + \omega_g) + g_{eg}^{k*} g_{e'g}^k \pi \delta(\omega_k - \omega_e + \omega_g) \quad (3.64)$$

The decay rate from a state $|e\rangle$ to $|g\rangle$ follows as

$$\Gamma_{eg} = 2 \sum_k |g_{eg}^k|^2 \pi \delta(\omega_k - \omega_e + \omega_g) \quad (3.65)$$

and the total decay rate from state $|e\rangle = (1/\text{lifetime})$ is

$$\Gamma_e = 2 \sum_k \sum_g |g_{eg}^k|^2 \pi \delta(\omega_k - \omega_e + \omega_g) \quad (3.66)$$

The generalised decay rates may be written in terms of the channel decay rates as

$$\Gamma_{ee'g} = |\Gamma_{eg} \Gamma_{e'g}|^{1/2} \quad (3.67)$$

As a consequence of choosing the Rabi frequencies to be real, the generalised decay rates in equations (3.58-3.60) are also real by the following argument: We are dealing with coherent states of light, which is defined as (Knight 1992)

$$|\alpha_k\rangle = \exp(-1/2 |\alpha_k|^2) \sum_n \frac{\alpha_k^n}{(n!)^{1/2}} |n\rangle \quad (3.68)$$

These states are normalised because $\langle \alpha_k | \alpha_k \rangle = 1$, but they are not necessarily orthogonal since

$$\begin{aligned} \langle \alpha_k | \beta_k \rangle &= \exp(-1/2 |\alpha_k|^2 - 1/2 |\beta_k|^2) \sum_n \frac{\alpha_k^{*n} \beta_k^n}{n!} \\ &= \exp(-1/2 |\alpha_k|^2 - 1/2 |\beta_k|^2 + \alpha_k^* \beta_k) \end{aligned} \quad (3.69)$$

Coherent states are also eigenstates of the destruction and creation operators since

$$\begin{aligned}
\hat{a}_k |\alpha_k\rangle &= \exp(-1/2 |\alpha_k|^2) \sum_n \frac{\alpha_k^n}{(n!)^{1/2}} n^{1/2} |n\rangle \\
&= \alpha_k |\alpha_k\rangle
\end{aligned} \tag{3.70}$$

α_k labels the coherent state and is an eigenvalue of the destruction operator. α_k can also be written as

$$\alpha_k = |\alpha_k| e^{i\theta} \tag{3.71}$$

where θ is the phase of the field. The expectation values of the destruction and creation operators are thus given by

$$\begin{aligned}
\langle \alpha_k | \hat{a}_k | \alpha_k \rangle &= \alpha_k \\
\langle \alpha_k | \hat{a}_k^\dagger | \alpha_k \rangle &= \alpha_k^*
\end{aligned} \tag{3.72}$$

The half Rabi frequency term defined by equation (3.61) may be rewritten as (Farrell *et al.* 1988)

$$\Omega_{eg} = |g_{eg}^{k_L}| e^{i\alpha} \langle \hat{a}_{k_L}(0) \rangle e^{i\beta} \tag{3.73}$$

The Rabi frequency has been chosen to be real which implies,

$$\alpha + \beta = n\pi \tag{3.74}$$

where n is an integer. Similarly we can write

$$\Omega_{e'g} = |g_{e'g}^{k_L}| e^{i\gamma} \langle \hat{a}_{k_L}(0) \rangle e^{i\beta} \tag{3.75}$$

where

$$\gamma + \beta = m\pi \quad (3.76)$$

The generalised decay terms involve products of the form

$$g_{eg}^k g_{e'g}^{k*} = |g_{eg}^k| |g_{e'g}^{k*}| e^{i(\alpha-\gamma)} \quad (3.77)$$

Then from equations (3.73) and (3.75)

$$\alpha - \gamma = (n - m)\pi \quad (3.78)$$

Therefore if both n and m are either both even or both odd, the product will be real and positive. If one of n and m is even and the other odd, the product will be real and negative.

Figure 2.5a depicts the energy level scheme for the sodium D_2 line with the allowed transitions for π radiation. The laser radiation is tuned from the $F'=2$ ground state to the $F=3$ excited state and has a bandwidth of approximately 1MHz. Because the natural linewidth of sodium is 10MHz, in principle all of the hyperfine structure should be resolvable at low laser powers. However at higher laser powers, power broadening dominates and as a result any of the upper hyperfine sub states may be excited with the exception of states $|9\rangle$ and $|15\rangle$. State $|9\rangle$ can not be populated due to selection rules and $|15\rangle$ does not get excited because the Clebsch-Gordan coefficient for this mode of excitation is equal to zero. In a typical superelastic scattering experiment such as the one considered here, the laser powers are high enough so that power broadening must be taken into account. Using the knowledge of which states are populated the equations (3.58-3.60) may be applied to obtain the equations of motion for the system given in Appendix 1.

3.4 Calculation of Rabi Frequencies and Branching Ratios

The equations of motion derived in the previous chapter are dependent on terms which are proportional to Rabi frequencies of hyperfine transitions. The Rabi frequency is a direct measure of the strength of interaction between the transition induced dipole and the light field. Consider the electric field operator \hat{E}_{\sim} which may be written in terms of spherical unit vectors $e_{\sim q}$ as (Corney 1977)

$$\hat{E}_{\sim} = \sum_{q=-1}^1 (-1)^q \hat{E}_q e_{\sim -q} \quad (3.79)$$

where the spherical unit vectors may be written in terms of Cartesian unit vectors as

$$e_{\sim \pm 1} = \mp \frac{1}{\sqrt{2}} (i \pm j) \quad (3.80a)$$

$$e_{\sim 0} = k \quad (3.80b)$$

The dipole operator may be written in the same basis as

$$\hat{D}_{\sim} = \sum_{q=-1}^1 (-1)^q \hat{D}_q e_{\sim -q} \quad (3.81)$$

Substitution of equations (3.79-3.81) into the definition of the Rabi frequency equation (3.62) yields

$$\Omega_q = \frac{-\langle \hat{E}_q \hat{D}_q \rangle}{\hbar} \quad (3.82)$$

where q refers to the field mode and \hat{D}_q is the element of the atomic induced dipole operator which is an irreducible tensor of rank one. Using the definitions for σ^{\pm} and π transitions, the Rabi frequencies for each field mode may be written as (MacGillivray and Standage 1991)

$$\Omega_{\pi} = \frac{-E_0}{\hbar} \langle Fm_F | D_0 | F'm_F \rangle \quad (3.83a)$$

$$\Omega_{\sigma^+} = \frac{E_c}{\hbar} \langle Fm_F + 1 | D_1 | F'm_F \rangle \quad (3.83b)$$

$$\Omega_{\sigma^-} = \frac{-E_c}{\hbar} \langle Fm_F - 1 | D_{-1} | F'm_F \rangle \quad (3.83c)$$

where E_0 is the electric field amplitude of linearly polarised radiation and E_c is the electric field amplitude for circularly polarised light. The primed state refers to the lower state. The Rabi frequencies for each transition may be calculated explicitly by firstly reducing the matrix element from hyperfine representation to fine structure representation by applying (MacGillivray and Standage 1991)

$$\begin{aligned} \langle Fm_F | D_q | F'm_F \rangle &= \sum_{m_J} \sum_{m_{J'}} \sum_{m_I} \sum_{m_{I'}} \langle IJm_I m_J | Fm_F \rangle \langle IJ'm_I m_{J'} | F'm_F \rangle \\ &\quad \langle Jm_J | D_q | J'm_{J'} \rangle \langle m_I | I | m_{I'} \rangle \end{aligned} \quad (3.84)$$

where $\langle \dots | \dots \rangle$ are Clebsch-Gordan coefficients. Since D does not operate on the nuclear spin the projection of I , m_I remains unchanged during the interaction and as such the sum over yields a Kronecker delta $\delta_{m_I m_{I'}}$. In a similar reduction the fine structure representation may be reduced to L representation via (MacGillivray and Standage 1991)

$$\begin{aligned} \langle Jm_J | D_q | J'm_{J'} \rangle &= \sum_{m_L} \sum_{m_{L'}} \sum_{m_S} \langle SLm_S m_L | Jm_J \rangle \langle SL'm_S m_{L'} | J'm_{J'} \rangle \\ &\quad \langle Lm_L | D_q | L'm_{L'} \rangle \end{aligned} \quad (3.85)$$

Equations (3.84) and (3.85) are not the only method used to reduce from F representation to L representation and other methods can be found in Farrell and MacGillivray 1994. The

Table 3.1
 $C(F, m_F, F', m_{F'}, q)$ Coefficients

$$3^2S_{1/2}(F'=1) \rightarrow 3^2P_{3/2}(F)$$

Δm_F	F	$m_{F'}$		
		-1	0	1
1	0	$\frac{1}{\sqrt{3}}$		
1	1	$\frac{5}{\sqrt{60}}$	$\frac{5}{\sqrt{60}}$	
1	2	$\frac{1}{\sqrt{12}}$	$\frac{1}{2}$	$\frac{1}{\sqrt{2}}$
0	0		$\frac{1}{\sqrt{3}}$	
0	1	$\frac{5}{\sqrt{60}}$		$\frac{5}{\sqrt{60}}$
0	2	$\frac{1}{2}$	$\frac{1}{\sqrt{3}}$	$\frac{1}{2}$
-1	0			$\frac{1}{\sqrt{3}}$
-1	1		$\frac{5}{\sqrt{60}}$	$\frac{5}{\sqrt{60}}$
-1	2	$\frac{1}{\sqrt{2}}$	$\frac{1}{2}$	$\frac{1}{\sqrt{12}}$

$$3^2S_{1/2}(F'=2) \rightarrow 3^2P_{3/2}(F)$$

Δm_F	F'	$m_{F'}$				
		-2	-1	0	1	2
1	1	$\frac{1}{\sqrt{10}}$	$\frac{1}{\sqrt{20}}$	$\frac{1}{\sqrt{60}}$		
1	2	$\frac{1}{\sqrt{6}}$	$\frac{1}{2}$	$\frac{1}{2}$	$\frac{1}{\sqrt{6}}$	
1	3	$\frac{1}{\sqrt{15}}$	$\frac{1}{\sqrt{5}}$	$\frac{2}{\sqrt{10}}$	$\frac{2}{\sqrt{6}}$	-1
0	1		$\frac{1}{\sqrt{20}}$	$\frac{1}{\sqrt{15}}$	$\frac{1}{\sqrt{20}}$	
0	2	$\frac{1}{\sqrt{3}}$	$\frac{1}{\sqrt{12}}$		$\frac{1}{\sqrt{12}}$	$\frac{1}{\sqrt{3}}$
0	3	$\frac{1}{\sqrt{3}}$	$\frac{4}{\sqrt{30}}$	$\frac{3}{\sqrt{15}}$	$\frac{4}{\sqrt{30}}$	$\frac{1}{\sqrt{3}}$
-1	1			$\frac{1}{\sqrt{60}}$	$\frac{1}{\sqrt{20}}$	$\frac{1}{\sqrt{10}}$
-1	2		$\frac{1}{\sqrt{6}}$	$\frac{1}{2}$	$\frac{1}{2}$	$\frac{1}{\sqrt{6}}$
-1	3	-1	$\frac{2}{\sqrt{6}}$	$\frac{2}{\sqrt{10}}$	$\frac{1}{\sqrt{5}}$	$\frac{1}{\sqrt{15}}$

Wigner-Eckart theorem allows the geometrical or the m dependence to be removed (Blum 1981) such that

$$\langle L m_L | T_{kq} | L' m_{L'} \rangle = (-1)^{L-m_L} \begin{pmatrix} L & k & L' \\ m_L & q & m_{L'} \end{pmatrix} \langle L || T_{kq} || L' \rangle \quad (3.86)$$

where k is the rank of the tensor. The reduced matrix element may be evaluated numerically as (Sobelman 1979)

$$\langle L || T_{kq} || L' \rangle = \sqrt{2L+1} \left(\frac{3\epsilon_o \hbar \lambda^3 \Gamma_{LL'}}{8\pi^2} \right)^{1/2} \quad (3.87)$$

where λ is the wavelength of the transition and $\Gamma_{LL'}$ is the relaxation rate which is equal to the inverse of the lifetime of the excited state. The electric field amplitudes in equations (3.83) may be expressed in terms of the radiation intensity, I ,

$$E = \sqrt{\frac{2}{\epsilon_o c}} \sqrt{I} \quad (3.88)$$

Applying equations (3.84-3.88) allow the Rabi frequencies for the individual hyperfine transitions as

$$\Omega(F, m_F, F', m_{F'}, q) = C(F, m_F, F', m_{F'}, q) \sqrt{I} \text{ MHz}/(mW/mm^2)^{1/2} \quad (3.89)$$

Table 3.1 gives the various values for the $C(F, m_F, F', m_{F'}, q)$ coefficients for each hyperfine transition of the sodium D_2 line.

The relaxation rate from an excited state to a ground state is proportional to the square of the dipole matrix element. The Rabi frequencies as shown by equation (3.86) are proportional to the dipole matrix element and thus the relaxation rate from an excited state $|e\rangle$ to a ground state $|g\rangle$ is proportional to the square of the Rabi frequency. Therefore it may be shown that

Table 3.2
 $B(F, m_F, F', m_{F'}, q)$ Coefficients

$$3^2S_{1/2}(F'=1) \rightarrow 3^2P_{3/2}(F)$$

Δm_F	$m_{F'}$			
	F	-1	0	1
1	0	$\frac{1}{3}$		
1	1	$\frac{5}{12}$	$\frac{5}{12}$	
1	2	$\frac{1}{12}$	$\frac{1}{4}$	$\frac{1}{2}$
0	0		$\frac{1}{3}$	
0	1	$\frac{5}{12}$		$\frac{5}{12}$
0	2	$\frac{1}{4}$	$\frac{1}{3}$	$\frac{1}{4}$
-1	0			$\frac{1}{3}$
-1	1		$\frac{5}{12}$	$\frac{5}{12}$
-1	2	$\frac{1}{2}$	$\frac{1}{4}$	$\frac{1}{12}$

$$3^2S_{1/2}(F'=2) \rightarrow 3^2P_{3/2}(F)$$

Δm_F	$m_{F'}$					
	F'	-2	-1	0	1	2
1	1	$\frac{1}{10}$	$\frac{1}{20}$	$\frac{1}{60}$		
1	2	$\frac{1}{6}$	$\frac{1}{4}$	$\frac{1}{4}$	$\frac{1}{6}$	
1	3	$\frac{1}{15}$	$\frac{1}{5}$	$\frac{2}{5}$	$\frac{2}{3}$	1
0	1		$\frac{1}{20}$	$\frac{1}{15}$	$\frac{1}{20}$	
0	2	$\frac{1}{3}$	$\frac{1}{12}$		$\frac{1}{12}$	$\frac{1}{3}$
0	3	$\frac{1}{3}$	$\frac{8}{15}$	$\frac{3}{5}$	$\frac{8}{15}$	$\frac{1}{3}$
-1	1			$\frac{1}{60}$	$\frac{1}{20}$	$\frac{1}{10}$
-1	2		$\frac{1}{6}$	$\frac{1}{4}$	$\frac{1}{4}$	$\frac{1}{6}$
-1	3	1	$\frac{2}{3}$	$\frac{2}{5}$	$\frac{1}{5}$	$\frac{1}{15}$

$$\Gamma_{eg} = \frac{\Omega_{eg}^2}{\sum_{g'} \Omega_{eg'}^2} \Gamma_e \quad (3.90a)$$

$$= B(F, m_F, F', m_{F'}, q) \Gamma_e \quad (3.90b)$$

where Γ_e is the total relaxation rate from the excited state $|e\rangle$ and is the inverse of the lifetime of the state. The coefficients $B(F, m_F, F', m_{F'}, q)$ are known as branching ratios and are given by

$$B(F, m_F, F', m_{F'}, q) = (C(F, m_F, F', m_{F'}, q))^2 \quad (3.91)$$

The branching ratios for the sodium D_2 line may be seen in Table 3.2 expressed as fractions of the total relaxation rate.

3.5 Solutions to the Equations of Motion

The system of equations described in section 3.3 form a set of linear first order differential equations which may be written in the form

$$\dot{y} = \underline{A} y \quad (3.92)$$

where \underline{A} is a matrix consisting of real and imaginary numbers which represent Rabi frequencies, relaxation rates, detunings and energy level splittings. y is a vector whose elements represent the various populations and coherences. A solution to equation (3.92) may

be found by first diagonalizing \underline{A} to produce eigenvalues λ_m with an associated matrix of eigenvectors \underline{X} which are related to \underline{A} by

$$\underline{A} = \underline{X} \underline{\lambda} \underline{X}^{-1} \quad (3.93)$$

where $\underline{\lambda}$ is a diagonal matrix of eigenvalues. Substituting (3.93) into (3.92) yields

$$\dot{y} = \underline{X} \underline{\lambda} \underline{X}^{-1} y \quad (3.94)$$

Multiplying the equation by \underline{X}^{-1} yields

$$\underline{X}^{-1} \dot{y} = \underline{\lambda} \underline{X}^{-1} y \quad (3.95)$$

We now define $Z = \underline{X}^{-1} y$ and note that \underline{X} is time independent since \underline{A} is a matrix of constants then

$$\dot{Z} = \underline{\lambda} Z \quad (3.96)$$

This has the simple solution

$$Z = Z(0) e^{\underline{\lambda} t} \quad (3.97)$$

Re-expressing Z in terms of y and multiplying by \underline{X} gives

$$y = \underline{X} e^{\underline{\lambda} t} \underline{X}^{-1} y(0) \quad (3.98)$$

The individual matrix elements are then given by

$$y_j = \sum_i Z_i X_{ij} e^{\lambda_i t} \quad (3.99)$$

where Z relates to the initial conditions by

$$\underline{X} Z(0) = y(0) \quad (3.100)$$

Using the two equations (3.99) and (3.100) the system of equations may be solved.

To correctly model the atom-laser interaction the effect of the atomic evolution of the atom traversing the laser beam must also be taken into consideration in the calculation. This may be accomplished by time averaging the probabilities such that

$$\langle \bar{\chi}_{ee} \rangle = \frac{1}{T} \int_0^T \langle \chi_{ee} \rangle(t) dt \quad (3.101)$$

where $\langle \bar{\chi}_{ee} \rangle$ is the time averaged probability. Applying this result to equation (3.99) yields

$$y_j = \sum_i Z_i X_{ij} \left(\frac{e^{\lambda_i T}}{\lambda_i T} - I \right) \quad (3.102)$$

One effect that should also be taken into account is the detuning from resonance of the atomic transition compared to the laser frequency. One such detuning is caused by the Doppler profile of the atomic beam. In this experiment, atoms are produced at the interaction region via an oven which also collimates the effused atom beam. The atoms leave the oven with a principle velocity component perpendicular to the laser beam direction as well as a velocity component parallel or anti-parallel to the direction of the laser propagation. Those atoms with the velocity component travelling antiparallel to the laser propagation direction will be blue

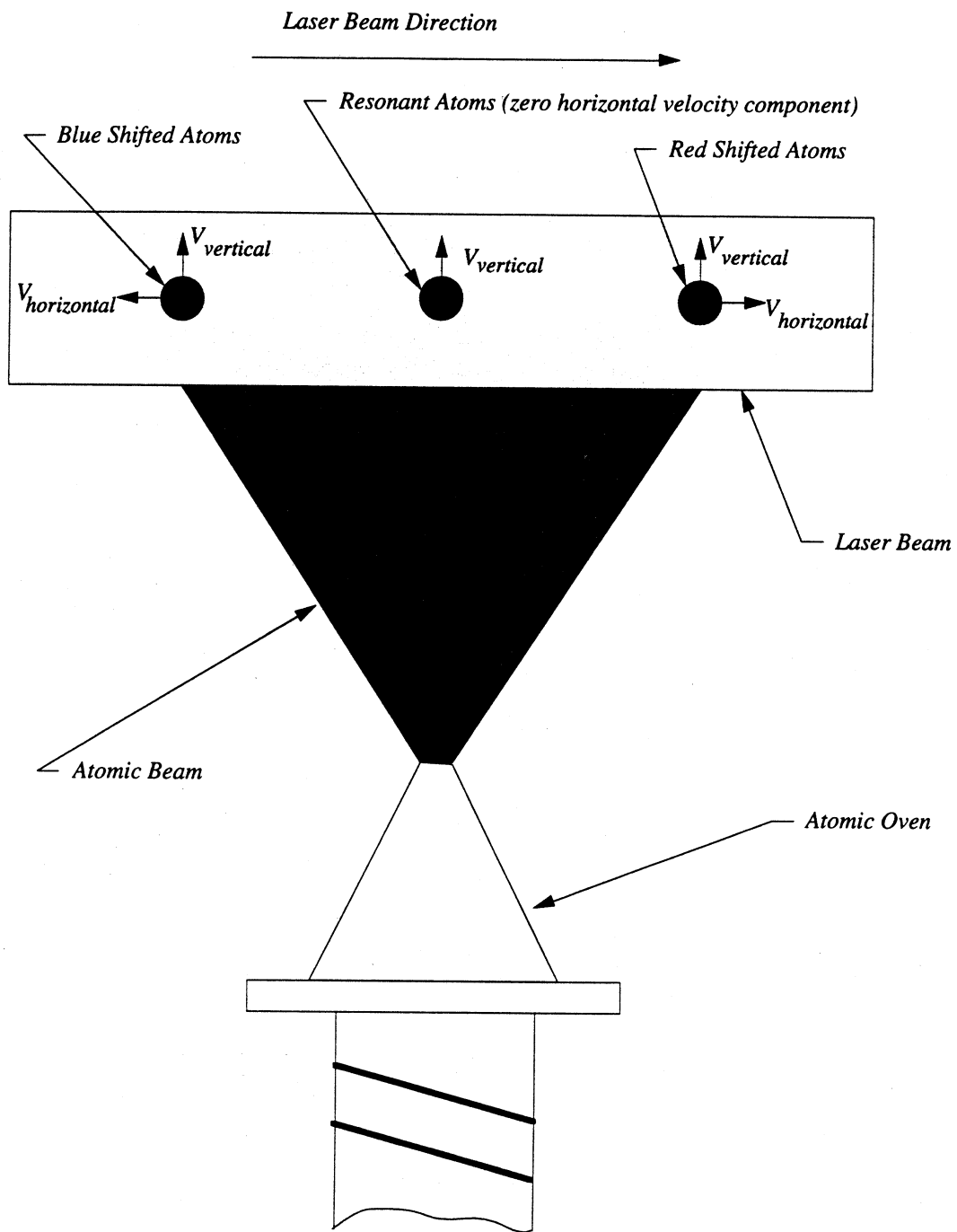


Figure 3.2: The Doppler Effect

shifted from the resonant frequency and those atoms with the opposite velocity component will be red shifted from the resonant frequency as shown in figure 3.2. In this experiment the atoms are assumed to be tuned to the class of atoms with a zero velocity component along the beam axis and so the Doppler profile is centred on this class of atoms. The number of atoms in a particular detuning class follows a Gaussian distribution which is centred on the zero velocity group. To include the Doppler shift effect the solution to the equations of motion must be thus weighted by (Farrell *et al.* 1988)

$$y_j = \frac{I}{\Delta_0 \sqrt{\pi}} \int_{-\infty}^{\infty} y_j(t, \Delta) \exp\left(-\left(\frac{\Delta}{\Delta_0}\right)^2\right) d\Delta \quad (3.103)$$

where Δ is the detuning of the laser from the $F'=2$ hyperfine ground substate to the $F=3$ hyperfine excited state due to atomic velocity. Δ_0 is related to the full width half maximum frequency in the Doppler profile by

$$\Delta_0 = \pi \frac{f_{FWHM}}{\sqrt{\ln(2)}} \quad (3.104)$$

The integration of the equation (3.103) was performed numerically by using a Simpsons numerical integration technique (see for example Burden and Fairs 1989). Both the interval and the stepsize was set by the user.

An alternative solution to the above method may be accomplished by directly solving equation (3.92) that is

$$y = y(0) e^{\underline{A}t} \quad (3.105)$$

The exponential factor is complicated as it contains the matrix \underline{A} . This exponential factor may be evaluated numerically by Taylor expanding about the origin giving

$$\begin{aligned}
e^{At} &= I + At + \frac{A^2 t^2}{2!} + \frac{A^3 t^3}{3!} + \dots + \frac{A^m t^m}{m!} + \dots \\
&= \sum_{n=0}^{\infty} \frac{A^n t^n}{n!}
\end{aligned} \tag{3.106}$$

Substitution of equation (3.106) into equation (3.105) reveals

$$y = y(0) \left(\sum_{n=0}^{\infty} \frac{A^n t^n}{n!} \right) \tag{3.113}$$

The sum is performed to a specified numerical convergence. In the calculations used in this thesis, numerical convergence occurred when the infinity norm of two sequential terms was less than 10^{-12} . The infinity norm is defined as the absolute value of largest row sum (Burden and Fairs 1989). This method is one third faster than the eigenvalue method but has the disadvantage that no eigenvalue check can be made. The calculations reported here have used the Taylor's expansion method which was chosen for the speed of the method and were checked using the results of the eigenvalue method.

3.6 Folded Step Laser Excitation

In this section the QED model is applied to the folded step excitation scheme discussed in section 2.7 in which two lasers are used to pump from the two near degenerate $3^2S_{1/2}$ ($F'=2,1$) ground states to the $3^2P_{3/2}$ ($F=3,2,1,0$) excited state manifold. The laser exciting from the $F'=1$ ground state will be denoted laser 1 and the laser exciting from the $F'=2$ ground state will be denoted laser 2. The lasers are copropagating and are resonantly tuned so that they excite from the two hyperfine ground states to the $F=2$ excited state sublevel. The lasers are not phased locked and because the time scales at which observables are measured

are much greater than the coherence time of the lasers, no two photon coherences created by the two lasers will exist. The general equations of motion derived for the single laser case (equations (3.58-3.60)) may be modified for two lasers. This modification can be made at the point where the sum over the modes k is restricted to one term as done in equations (3.54), (3.56) and (3.57). Allowing the sum to include the second laser yields the following general equations of motion

$$\begin{aligned}
\dot{\langle \hat{\chi}_{eg} \rangle} = & -i \Delta_{eg} \langle \hat{\chi}_{eg} \rangle - i \sum_{e'} \Omega_{e'g}^{L_1} \langle \hat{\chi}_{ee'} \rangle - i \sum_{e'} \Omega_{e'g}^{L_2} \langle \hat{\chi}_{ee'} \rangle \\
& + i \sum_{g'} \Omega_{eg'}^{L_1} \langle \hat{\chi}_{g'g} \rangle + i \sum_{g'} \Omega_{eg'}^{L_2} \langle \hat{\chi}_{g'g} \rangle \\
& - \sum_k \sum_{g'} \sum_{e'} g_{eg}^{k*} g_{e'g'}^k \pi \delta(\omega_k - \omega_{e'} + \omega_{g'}) \langle \hat{\chi}_{e'g'} \rangle
\end{aligned} \tag{3.114}$$

$$\begin{aligned}
\dot{\langle \hat{\chi}_{g'g} \rangle} = & -i(\omega_g - \omega_{g'}) \langle \hat{\chi}_{g'g} \rangle - i \sum_{e''} \Omega_{e''g}^{L_1} \langle \hat{\chi}_{g'e''} \rangle - i \sum_{e''} \Omega_{e''g}^{L_2} \langle \hat{\chi}_{g'e''} \rangle \\
& + i \sum_{e''} \Omega_{e''g'}^{L_1} \langle \hat{\chi}_{e''g} \rangle + i \sum_{e''} \Omega_{e''g'}^{L_2} \langle \hat{\chi}_{e''g} \rangle \\
& + \sum_k \sum_{e''} \sum_{e'''} g_{e''g}^{k*} g_{e''g'}^k \pi \delta(\omega_k - \omega_{e''} + \omega_{g'}) \langle \hat{\chi}_{e''e'''} \rangle \\
& + \sum_k \sum_{e''} \sum_{e'''} g_{e''g}^k g_{e''g'}^{k*} \pi \delta(\omega_k - \omega_{e''} + \omega_{g'}) \langle \hat{\chi}_{e''e'''} \rangle
\end{aligned} \tag{3.115}$$

$$\begin{aligned}
\dot{\langle \hat{\chi}_{ee'} \rangle} = & -i(\omega_{e'} - \omega_e) \langle \hat{\chi}_{ee'} \rangle - i \sum_{g''} \Omega_{e'g''}^{L_1} \langle \hat{\chi}_{eg''} \rangle - i \sum_{g''} \Omega_{e'g''}^{L_2} \langle \hat{\chi}_{eg''} \rangle \\
& + i \sum_{g''} \Omega_{eg''}^{L_1} \langle \hat{\chi}_{g''e'} \rangle + i \sum_{g''} \Omega_{eg''}^{L_2} \langle \hat{\chi}_{g''e'} \rangle \\
& - \sum_k \sum_{g''} \sum_{e'''} g_{e'g''}^k g_{e''g'''}^{k*} \pi \delta(\omega_k - \omega_{e''} + \omega_{g''}) \langle \hat{\chi}_{ee''} \rangle
\end{aligned}$$

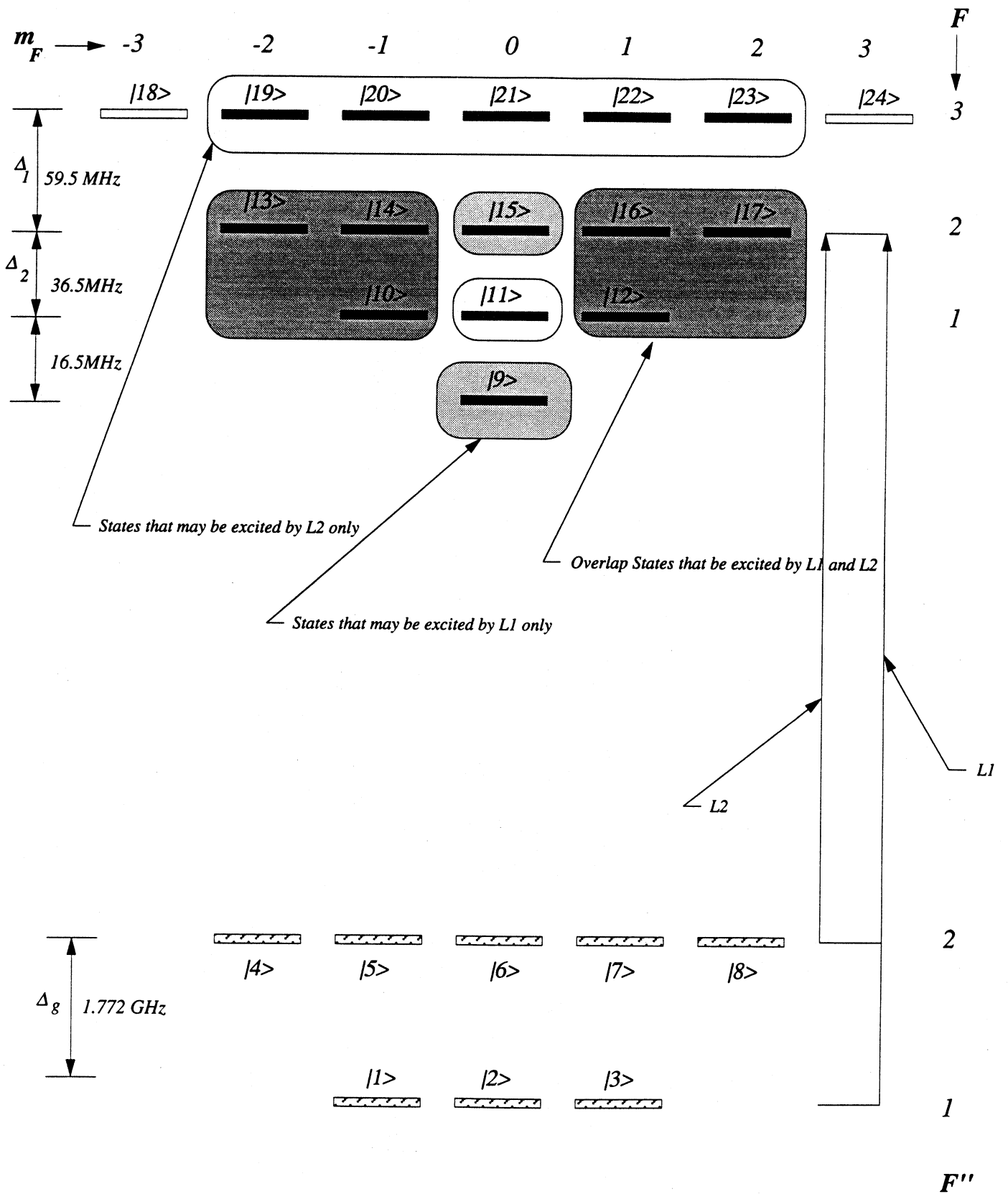


Figure 3.3: Folded Step Excitation of the sodium D2 line. Both lasers are tuned to the $F=2$ excited substate. Highlighted are the states that may be formed by either laser 1 or laser 2 and overlap states which can be excited by either laser.

$$- \sum_k \sum_{g''} \sum_{e'''} g_{eg}^{k*} g_{e''g''}^k \pi \delta(\omega_k - \omega_{e'''} + \omega_{g''}) \langle \hat{\chi}_{e''e'} \rangle \quad (3.116)$$

where

$$\Omega_{eg}^{L_1} = g_{eg}^{L_1} \langle \hat{a}_{L_1}(0) \rangle = g_{eg}^{L_1*} \langle \hat{a}_{L_1}^\dagger(0) \rangle \quad (3.117a)$$

$$\Omega_{eg}^{L_2} = g_{eg}^{L_2} \langle \hat{a}_{L_2}(0) \rangle = g_{eg}^{L_2*} \langle \hat{a}_{L_2}^\dagger(0) \rangle \quad (3.117b)$$

are defined as the half Rabi frequencies for each laser. The Rabi frequency may be evaluated from the definition given by equation (3.62). Equation (3.114) contains six terms. The first term is a freely evolving term. The second, third, fourth and fifth terms are atom-field interaction terms and the sixth term is related to relaxation. Equations (3.115) and (3.116) contain one extra relaxation term.

Applying these general equations of motion to this folded step system yields 78 coupled differential equations which are given in Appendix 2. The major difference between these equations and the single laser equations is that there are equations which are driven by a single laser and equations which are driven by the two different lasers which is a result of overlap states in the excited state manifold which may be excited by both lasers. Figure 3.3 depicts the states which may be excited by laser 1 or laser 2 as well as the overlap states which are accessible by both lasers.

The 78 coupled differential equations were solved by directly integrating and using the Taylor's expansion method discussed in section 3.5. The computation time was significantly larger than that of the single laser model due to the increase in the number of coupled differential equations. The usual cpu time for one solution was in the order of four minutes.

3.7 Relation Between the Optical Pumping Parameters K, \bar{K} and the Line Polarisation

In this section it is demonstrated that the optical pumping parameter K , for a P-S transition, is identical to the line polarisation of fluorescence scattered perpendicular to the plane formed by the polarisation of the laser and the propagation direction of the laser. Similarly it is shown that the optical pumping parameter \bar{K} is identical to the line polarisation of fluorescence scattered perpendicular to the plane formed by the polarisation vectors of the two exciting lasers and the propagation direction of the lasers. Consider now the single laser case. The fluorescence intensity for an ensemble of excited atoms is given by (Fano 1957)

$$I = C \sum_e \sum_{e'} \rho_{ee'}^L F_{e'e} \quad (3.118)$$

where C is a constant which depends on the solid angle of the photon detector, the efficiency of the detector and the number of atoms. $\rho_{ee'}^L$ are the populations and coherences of the excited state created by the laser excitation process. $F_{e'e}$ is the emission matrix which represents the spontaneous emission process for an excited state $|e\rangle$ to a ground state $|g\rangle$ and is given by

$$F_{e'e} = \sum_g \langle e | f_{\underline{a}} \cdot \underline{D} | g \rangle \langle g | f_{\underline{a}} \cdot \underline{D}^* | e \rangle \quad (3.119)$$

where the sum runs over the ground hyperfine substates. $f_{\underline{a}}$ is a unit vector denoting the polarisation of the polarisation analyser and \underline{D} is the electric dipole operator. Applying equation (3.118) to the excitation scheme depicted in figure (2.5a) yields

$$I = C \left\{ \rho_{10\ 10}^L F_{10\ 10} + \rho_{11\ 11}^L F_{11\ 11} + \rho_{12\ 12}^L F_{12\ 12} + \rho_{13\ 13}^L F_{13\ 13} \right. \\ \left. + \rho_{14\ 14}^L F_{14\ 14} + \rho_{16\ 16}^L F_{16\ 16} + \rho_{17\ 17}^L F_{17\ 17} + \rho_{19\ 19}^L F_{19\ 19} \right.$$

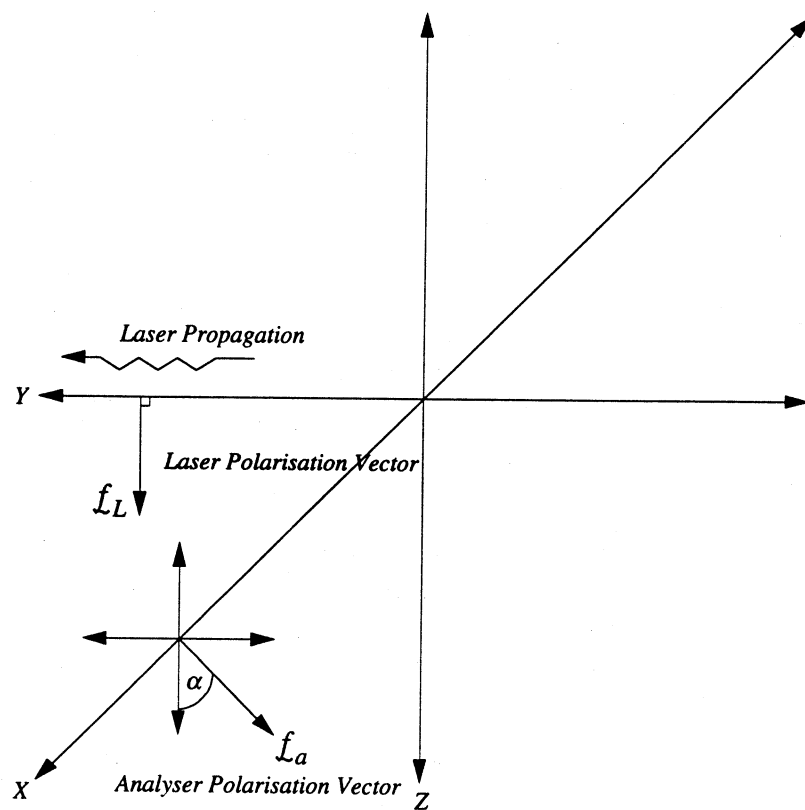


Figure 3.4: Line Polarisation Geometry

$$\begin{aligned}
& + \rho_{20}^L F_{20\ 20} + \rho_{21}^L F_{21\ 21} + \rho_{22}^L F_{22\ 22} + \rho_{23}^L F_{23\ 23} \\
& + \rho_{19}^L F_{13\ 19} + \rho_{13}^L F_{19\ 13} + \rho_{20}^L F_{14\ 20} + \rho_{14}^L F_{20\ 14} \\
& + \rho_{20}^L F_{10\ 20} + \rho_{10}^L F_{20\ 10} + \rho_{14}^L F_{10\ 14} + \rho_{10}^L F_{14\ 10} \\
& + \rho_{21}^L F_{11\ 21} + \rho_{11}^L F_{21\ 11} + \rho_{22}^L F_{16\ 22} + \rho_{16}^L F_{22\ 16} \\
& + \rho_{22}^L F_{12\ 22} + \rho_{12}^L F_{22\ 12} + \rho_{16}^L F_{12\ 16} + \rho_{12}^L F_{16\ 12} \\
& + \rho_{23}^L F_{17\ 23} + \rho_{17}^L F_{23\ 17} \} \quad (3.120)
\end{aligned}$$

The line polarisation is defined as

$$P_L = \frac{I(0) - I(90)}{I(0) + I(90)} \quad (3.121)$$

where $I(\alpha)$ represents the intensity of the fluorescence scattered perpendicular to the plane formed by the polarisation of the laser and the propagation direction of the laser measured at angle α to the quantisation axis. In this experiment, the quantisation axis is chosen parallel to the laser polarisation vector \underline{f}_L , and in this case the Z axis. The experimental configuration is shown in figure 3.4. The laser propagates in the Y direction with linearly polarised light and photons scattered in the X direction are passed through a linear polariser at angle α to the quantisation axis. The polarisation vector of the analyser may be expressed in terms of Cartesian unit vectors as

$$\underline{f}_a = \sin\alpha \underline{j} + \cos\alpha \underline{k} \quad (3.122)$$

The expression for the fluorescence intensity equation (3.120) contain terms like $\langle Fm_F | \underline{f}_a \cdot \underline{D} | F'm_F \rangle$ which are in F representation. These terms may be reduced to L representation by firstly removing the m dependence then reducing to fine structure representation. Terms which are in fine structure representation are then reduced to a common reduced matrix element in L representation. The m dependence may be removed by applying the following relations (Condon and Shortley 1967)

$$\langle Fm_F | f_{\sim a} \cdot D | F+1m_{F\pm 1} \rangle = \pm \langle F || D || F+1 \rangle \frac{i}{2} \sqrt{(F+m_F+1)(F+m_F+2)} \sin \alpha \quad (3.123a)$$

$$\langle Fm_F | f_{\sim a} \cdot D | F+1m_F \rangle = \langle F || D || F+1 \rangle \sqrt{(F+1)^2 - m_F^2} \cos \alpha \quad (3.123b)$$

$$\langle Fm_F | f_{\sim a} \cdot D | Fm_{F\pm 1} \rangle = \pm \langle F || D || F \rangle \frac{i}{2} \sqrt{(F+m_F)(F+m_F+1)} \sin \alpha \quad (3.123c)$$

$$\langle Fm_F | f_{\sim a} \cdot D | Fm_F \rangle = \langle F || D || F \rangle m_F \cos \alpha \quad (3.123d)$$

$$\langle Fm_F | f_{\sim a} \cdot D | F-1m_{F\pm 1} \rangle = \pm \langle F || D || F-1 \rangle \frac{i}{2} \sqrt{(F+m_F)(F+m_F-1)} \sin \alpha \quad (3.123e)$$

$$\langle Fm_F | f_{\sim a} \cdot D | F-1m_F \rangle = \langle F || D || F-1 \rangle \sqrt{F^2 - m_F^2} \cos \alpha \quad (3.123f)$$

Substitution of these elements into the expression for I , will give terms like $\langle F || D || F' \rangle$ which may also be expressed as $\langle JIF || D || J'I'F' \rangle$. Since the electric dipole operator does not act on the nuclear spin then

$$\langle JIF || D || J'I'F' \rangle = \langle JIF || D || J'I'F' \rangle \delta_{II'} \quad (3.124)$$

The terms of this form may be reduced to J representation by applying (Condon and Shortley 1967)

$$\langle J'I'F || D || J-II'F+1 \rangle = -\langle J || D || J-I \rangle \frac{\sqrt{(I'+J-F)(F+I'-J+1)(I'-J-F+1)(F+I'-J+2)}}{2(F+1)\sqrt{(2F+1)(2F+3)}} \quad (3.125a)$$

$$\langle J'I'F || D || J-II'F \rangle = -\langle J || D || J-I \rangle \frac{\sqrt{(F-I'+J)(F+I'+J+1)(I'+J-F)(F+I'-J+1)}}{2F(F+1)} \quad (3.125b)$$

Table 3.3

F_{ee}	Reduced Matrix Element
F_{99}	$\frac{1}{3} \langle I \ D \ 0 \rangle ^2$
F_{1010}	$\frac{1}{3} \left(\frac{7}{5} - \frac{3}{5} \sin^2 \alpha \right) \langle I \ D \ 0 \rangle ^2$
F_{1111}	$\frac{1}{3} \left(\frac{1}{5} + \frac{6}{5} \sin^2 \alpha \right) \langle I \ D \ 0 \rangle ^2$
F_{1212}	$\frac{1}{3} \left(\frac{7}{5} - \frac{3}{5} \sin^2 \alpha \right) \langle I \ D \ 0 \rangle ^2$
F_{1313}	$\frac{1}{3} \langle I \ D \ 0 \rangle ^2$
F_{1414}	$\frac{1}{3} \langle I \ D \ 0 \rangle ^2$
F_{1515}	$\frac{1}{3} \langle I \ D \ 0 \rangle ^2$
F_{1616}	$\frac{1}{3} \langle I \ D \ 0 \rangle ^2$
F_{1717}	$\frac{1}{3} \langle I \ D \ 0 \rangle ^2$
F_{1919}	$\frac{1}{3} \langle I \ D \ 0 \rangle ^2$
F_{2020}	$\frac{1}{3} \left(\frac{8}{5} - \frac{9}{10} \sin^2 \alpha \right) \langle I \ D \ 0 \rangle ^2$
F_{2121}	$\frac{1}{3} \left(\frac{9}{5} - \frac{6}{5} \sin^2 \alpha \right) \langle I \ D \ 0 \rangle ^2$
F_{2222}	$\frac{1}{3} \left(\frac{8}{5} - \frac{9}{10} \sin^2 \alpha \right) \langle I \ D \ 0 \rangle ^2$
F_{2323}	$\frac{1}{3} \langle I \ D \ 0 \rangle ^2$
$F_{915} F_{159}$	$-\frac{1}{3} \left(1 - \frac{3}{2} \sin^2 \alpha \right) \langle I \ D \ 0 \rangle ^2$
$F_{1913} F_{1319}$	$-\frac{1}{3} \left(1 - \frac{3}{2} \sin^2 \alpha \right) \langle I \ D \ 0 \rangle ^2$
$F_{1410} F_{1014}$	$-\frac{1}{3} \left(\frac{\sqrt{15}}{5} - \frac{3\sqrt{15}}{10} \sin^2 \alpha \right) \langle I \ D \ 0 \rangle ^2$
$F_{2014} F_{1420}$	$-\frac{1}{3} \left(\frac{\sqrt{10}}{5} - \frac{3\sqrt{10}}{10} \sin^2 \alpha \right) \langle I \ D \ 0 \rangle ^2$
$F_{2010} F_{1020}$	$-\frac{1}{3} \left(\frac{\sqrt{6}}{5} - \frac{3\sqrt{6}}{10} \sin^2 \alpha \right) \langle I \ D \ 0 \rangle ^2$
$F_{2111} F_{1121}$	$-\frac{1}{3} \left(\frac{3}{5} - \frac{9}{10} \sin^2 \alpha \right) \langle I \ D \ 0 \rangle ^2$
$F_{1612} F_{1216}$	$\frac{1}{3} \left(\frac{\sqrt{15}}{5} - \frac{3\sqrt{15}}{10} \sin^2 \alpha \right) \langle I \ D \ 0 \rangle ^2$
$F_{2216} F_{1622}$	$\frac{1}{3} \left(\frac{\sqrt{10}}{5} - \frac{3\sqrt{10}}{10} \sin^2 \alpha \right) \langle I \ D \ 0 \rangle ^2$
$F_{2212} F_{1222}$	$-\frac{1}{3} \left(\frac{\sqrt{6}}{5} - \frac{3\sqrt{6}}{10} \sin^2 \alpha \right) \langle I \ D \ 0 \rangle ^2$
$F_{2317} F_{1723}$	$\frac{1}{3} \left(1 - \frac{3}{2} \sin^2 \alpha \right) \langle I \ D \ 0 \rangle ^2$

The emission matrix elements in terms of the reduced matrix element $\langle I \| D \| 0 \rangle$

$$\langle J'I'F||D||J-II'F-I\rangle = \langle J||D||J-I\rangle \frac{\sqrt{(F-I'+J)(F+I'+J+I)(F-I-I'+J)(F+I'+J)}}{2F\sqrt{(2F-I)(2F+I)}} \quad (3.125c)$$

Finally the $\langle J||D||J'\rangle$ elements may be reduced to a common reduced matrix element in L representation by applying (Condon and Shortley)

$$\langle SLJ||D||SL-IJ-I\rangle = \langle L||D||L-I\rangle \frac{\sqrt{(J-S+L)(J+S+L+I)(J-S+L-I)(J+S+L)}}{2J\sqrt{(2J-I)(2J+I)}} \quad (3.126)$$

The application of the reduction formulas (equations (3.123-3.126)) to the elements $F_{e'e}$ give the reduced elements in Table 3.3. Substitution of these reduced elements into equation (3.120) and applying the symmetry relations (2.40) defined in Chapter Two for π excitation yield an expression for I as a function of the analyser polarisation angle α such that

$$\begin{aligned} I(\alpha) = C \frac{|\langle J||D||0\rangle|^2}{3} \Big\{ & 2\left(\frac{7}{5} - \frac{3}{5} \sin^2 \alpha\right) \rho_{12\ 12}^L + \left(\frac{1}{5} + \frac{6}{5} \sin^2 \alpha\right) \rho_{11\ 11}^L + 2\rho_{16\ 16}^L \\ & + 2\rho_{17\ 17}^L + 2\rho_{23\ 23}^L + 2\left(\frac{8}{5} - \frac{9}{10} \sin^2 \alpha\right) \rho_{22\ 22}^L + \left(\frac{9}{5} - \frac{6}{5} \sin^2 \alpha\right) \rho_{21\ 21}^L \\ & + 4\left(1 - \frac{3}{2} \sin^2 \alpha\right) \text{Re} \rho_{23\ 17}^L + 4\left(\frac{\sqrt{10}}{5} - \frac{3\sqrt{10}}{10} \sin^2 \alpha\right) \text{Re} \rho_{22\ 16}^L \\ & - 4\left(\frac{\sqrt{6}}{5} - \frac{3\sqrt{6}}{10} \sin^2 \alpha\right) \text{Re} \rho_{22\ 12}^L + 4\left(\frac{\sqrt{15}}{5} - \frac{3\sqrt{15}}{10} \sin^2 \alpha\right) \text{Re} \rho_{16\ 12}^L \\ & - 2\left(\frac{3}{5} - \frac{9}{10} \sin^2 \alpha\right) \text{Re} \rho_{21\ 11}^L \Big\} \quad (3.127) \end{aligned}$$

Substitution of $\alpha = 0$ into this expression gives

$$\begin{aligned} I(0) = C |\langle J||D||0\rangle|^2 \Big\{ & \frac{2}{3} \rho_{23\ 23}^L + \frac{16}{15} \rho_{22\ 22}^L + \frac{3}{5} \rho_{21\ 21}^L + \frac{2}{3} \rho_{17\ 17}^L \\ & + \frac{2}{3} \rho_{16\ 16}^L + \frac{14}{15} \rho_{12\ 12}^L + \frac{1}{15} \rho_{11\ 11}^L + \frac{4}{3} \text{Re} \rho_{23\ 17}^L \\ & + \frac{8}{3\sqrt{10}} \text{Re} \rho_{22\ 16}^L - \frac{8}{5\sqrt{6}} \text{Re} \rho_{22\ 12}^L + \frac{4}{\sqrt{15}} \rho_{16\ 12}^L \\ & - \frac{2}{5} \text{Re} \rho_{21\ 11}^L \Big\} \quad (3.128) \end{aligned}$$

Similarly substitution of $\alpha = 90$ into (3.127) reveals

$$\begin{aligned}
 I(90) = C | \langle I || D || 0 \rangle |^2 \left\{ \frac{2}{3} \rho_{23}^L{}_{23} + \frac{7}{15} \rho_{22}^L{}_{22} + \frac{1}{5} \rho_{21}^L{}_{21} + \frac{2}{3} \rho_{17}^L{}_{17} \right. \\
 + \frac{2}{3} \rho_{16}^L{}_{16} + \frac{8}{15} \rho_{12}^L{}_{12} + \frac{7}{15} \rho_{11}^L{}_{11} - \frac{2}{3} \text{Re} \rho_{23}^L{}_{17} \\
 - \frac{4}{3\sqrt{10}} \text{Re} \rho_{22}^L{}_{16} + \frac{4}{5\sqrt{6}} \text{Re} \rho_{22}^L{}_{12} - \frac{2}{\sqrt{15}} \rho_{16}^L{}_{12} \\
 \left. + \frac{1}{5} \text{Re} \rho_{21}^L{}_{11} \right\} \quad (3.129)
 \end{aligned}$$

By inspection of equations (2.41a) and (2.41b) equations (3.128) and (3.129) may be re-expressed as

$$I(0) = C | \langle I || D || 0 \rangle |^2 \gamma \quad (3.130a)$$

$$I(90) = C | \langle I || D || 0 \rangle |^2 \alpha \quad (3.130a)$$

where α and γ were given by equations (2.41). Substitution of these two expressions into the definition of the line polarisation (equation (3.121)) yields

$$P_L = \frac{\gamma - \alpha}{\gamma + \alpha} \quad (3.131)$$

Comparing this to equation (2.51), the definition of the optical pumping parameter K , reveals

$$P_L = K \quad (3.132)$$

This implies that the line polarisation is an independent method that may be used to obtain K . The combination of co-planar superelastic measurements, fluorescence measurements and QED theory developed earlier in the chapter, enable K to be determined accurately.

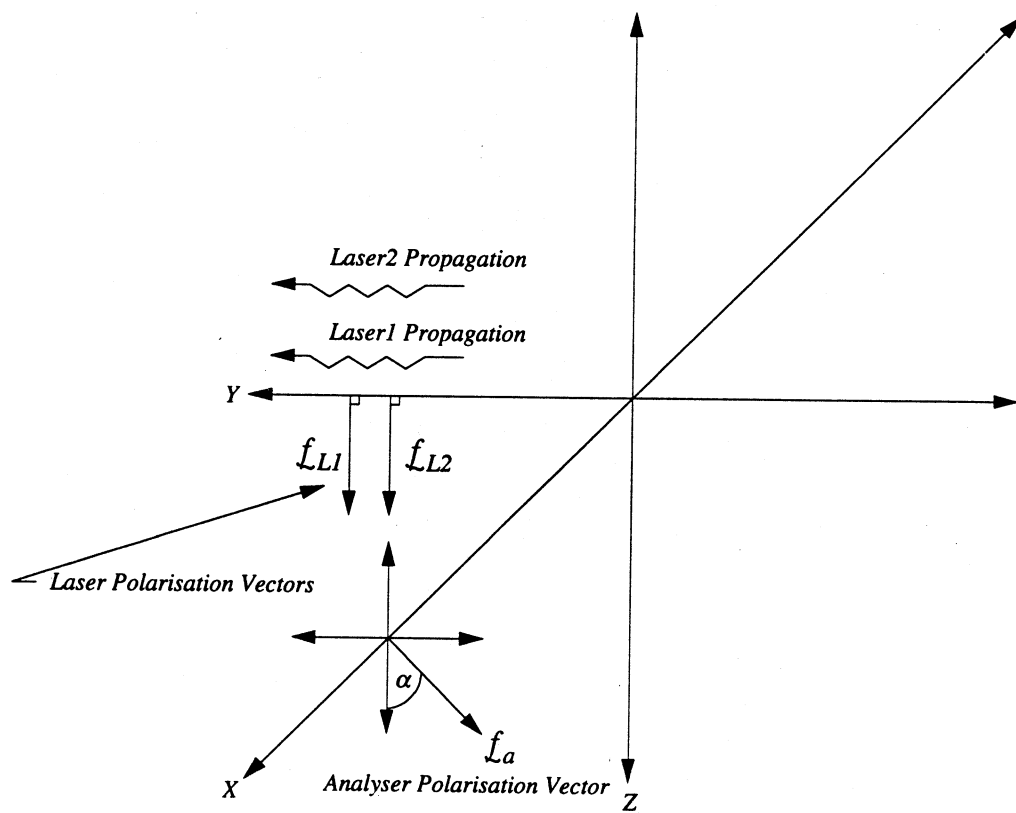


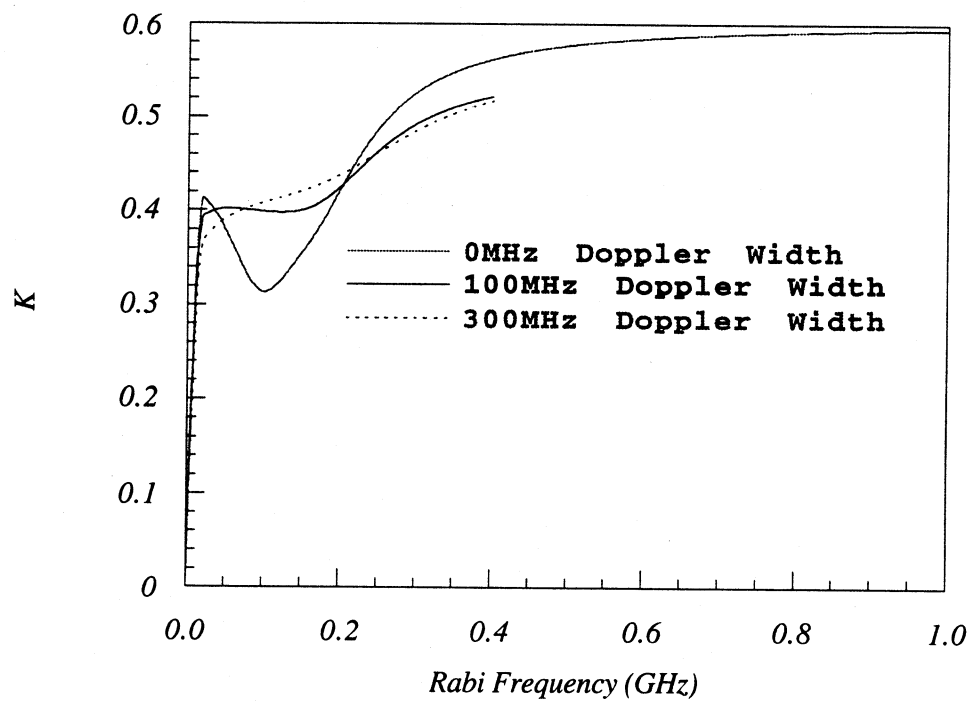
Figure 3.5: The Folded Step Line Polarisation Geometry

As with the single laser excitation case, the optical pumping parameter \bar{K} is also related to the line polarisation of the fluorescence scattered at right angles to the plane formed by the lasers propagation and the polarisation vectors of the lasers. Figure 3.5 displays the geometrical arrangement. The two lasers propagate in the Y direction with linearly polarised light and photons scattered in the X direction are passed through a linear polariser at angle α to the quantisation axis. The quantisation axis is chosen parallel to the polarisation vectors of the two lasers, \underline{f}_{L_1} and \underline{f}_{L_2} which is also the Z axis. Applying equation (3.118), the expression for the fluorescence intensity to the folded step excitation scheme yields

$$\begin{aligned}
 I = C \Big\{ & \rho_{99}^L F_{99} + \rho_{1010}^L F_{1010} + \rho_{1111}^L F_{1111} + \rho_{1212}^L F_{1212} \\
 & + \rho_{1313}^L F_{1313} + \rho_{1414}^L F_{1414} + \rho_{1515}^L F_{1515} + \rho_{1616}^L F_{1616} \\
 & + \rho_{1717}^L F_{1717} + \rho_{1919}^L F_{1919} + \rho_{2020}^L F_{2020} + \rho_{2121}^L F_{2121} \\
 & + \rho_{2222}^L F_{2222} + \rho_{2323}^L F_{2323} + \rho_{1913}^L F_{1319} + \rho_{1319}^L F_{1913} \\
 & + \rho_{2014}^L F_{1420} + \rho_{1420}^L F_{2014} + \rho_{2010}^L F_{1020} + \rho_{1020}^L F_{2010} \\
 & + \rho_{1410}^L F_{1014} + \rho_{1014}^L F_{1410} + \rho_{915}^L F_{159} + \rho_{159}^L F_{915} \\
 & + \rho_{2111}^L F_{1121} + \rho_{1121}^L F_{2111} + \rho_{2216}^L F_{1622} + \rho_{1622}^L F_{2216} \\
 & + \rho_{2212}^L F_{1222} + \rho_{1222}^L F_{2212} + \rho_{1612}^L F_{1216} + \rho_{1216}^L F_{1612} \\
 & + \rho_{2317}^L F_{1723} + \rho_{1723}^L F_{2317} \Big\} \quad (3.133)
 \end{aligned}$$

where the emission matrix elements $F_{e'e}$, were defined previously by equation (3.119). The $F_{e'e}$ terms in equation (3.133) are in F representation and may be reduced to L representation by applying the results in Table 3.3. Substitution of these elements into equation (3.133) and applying symmetry relations for π excitation defined by equations (2.40) gives the result

$$\begin{aligned}
 I(\alpha) = C \frac{|\langle 1||D||0 \rangle|^2}{3} \Big\{ & \rho_{99}^L + 2\left(\frac{7}{5} - \frac{3}{5} \sin^2 \alpha\right) \rho_{1212}^L + \left(\frac{1}{5} + \frac{6}{5} \sin^2 \alpha\right) \rho_{1111}^L \\
 & + 2\rho_{1616}^L + 2\rho_{1717}^L + 2\rho_{2323}^L + 2\left(\frac{8}{5} - \frac{9}{10} \sin^2 \alpha\right) \rho_{2222}^L \\
 & + \left(\frac{9}{5} - \frac{6}{5} \sin^2 \alpha\right) \rho_{2121}^L + 4\left(1 - \frac{3}{2} \sin^2 \alpha\right) \text{Re} \rho_{2317}^L \\
 & + 4\left(\frac{\sqrt{10}}{5} - \frac{3\sqrt{10}}{10} \sin^2 \alpha\right) \text{Re} \rho_{2216}^L - 4\left(\frac{\sqrt{6}}{5} - \frac{3\sqrt{6}}{10} \sin^2 \alpha\right) \text{Re} \rho_{2212}^L
 \end{aligned}$$



Graph 3.1: K Vs Rabi Frequency Various Doppler Widths

$$\begin{aligned}
& + 4\left(\frac{\sqrt{15}}{5} - \frac{3\sqrt{15}}{10} \sin^2 \alpha\right) \text{Re} \rho_{16\ 12}^L - 2\left(\frac{3}{5} - \frac{9}{10} \sin^2 \alpha\right) \text{Re} \rho_{21\ 11}^L \\
& - 2\left(1 - \frac{3}{2} \sin^2 \alpha\right) \rho_{15\ 9}^L \} \quad (3.134)
\end{aligned}$$

Using the definition of the line polarisation (equation (3.121)) and putting $\alpha = 0$ and $\alpha = 90$ yields the following

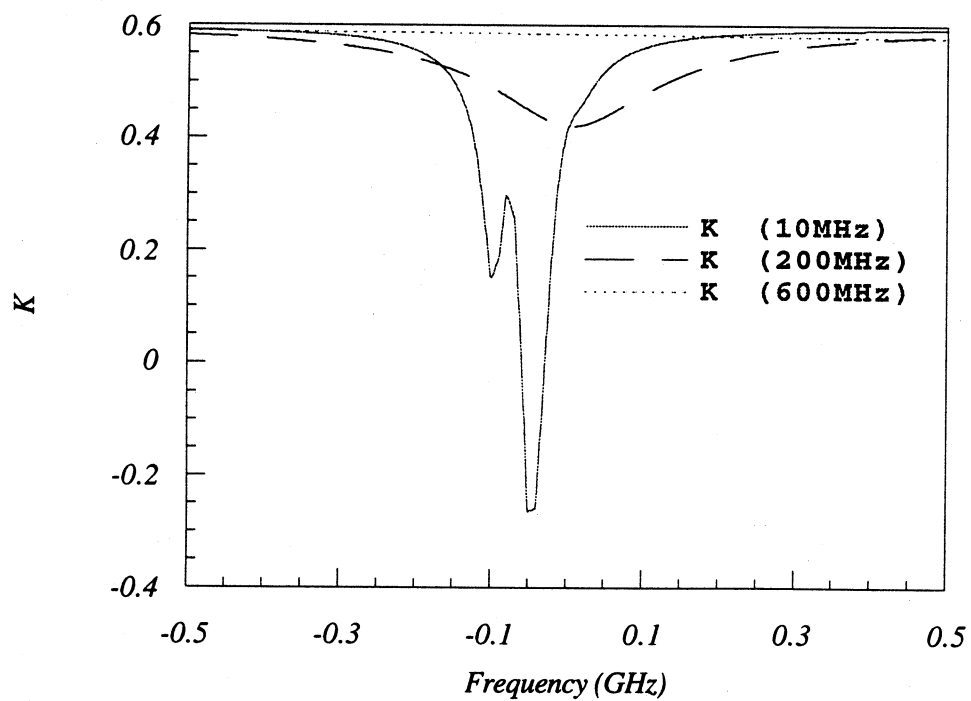
$$P_L = \frac{\bar{\gamma} - \bar{\alpha}}{\bar{\gamma} + \bar{\alpha}} \quad (3.135)$$

where $\bar{\alpha}$ and $\bar{\gamma}$ are given by equation (2.76). Comparing this to the expression for \bar{K} shows that the two expressions are identical and as such line polarisation measurements gives a useful independent method of measuring \bar{K} .

3.8 Single Step Calculation Results

The results of the QED calculation for the single laser excitation of the sodium D_2 line are presented in this section. As mentioned in section 3.5 all results have been calculated using the Taylor's expansion method. The program was encoded using Fortran 2.01 which was compiled and executed on a Sun Sparc Server 100. Typical run times varied as this computing facility was shared with many other users but the actual cpu time for the solution of one set of conditions was in the order of 30 seconds. The initial conditions for all of the calculations were set such that the ground states were all equally populated at 0.125 and the laser tuned from the $3^2S_{1/2}$ ($F=2$) ground sublevel to the $3^2P_{3/2}$ ($F=3$) excited sublevel.

Graph 3.1 depicts the optical pumping parameter K as a function of the laser intensity for three different Doppler width atomic beams. The laser intensities have been expressed as Rabi



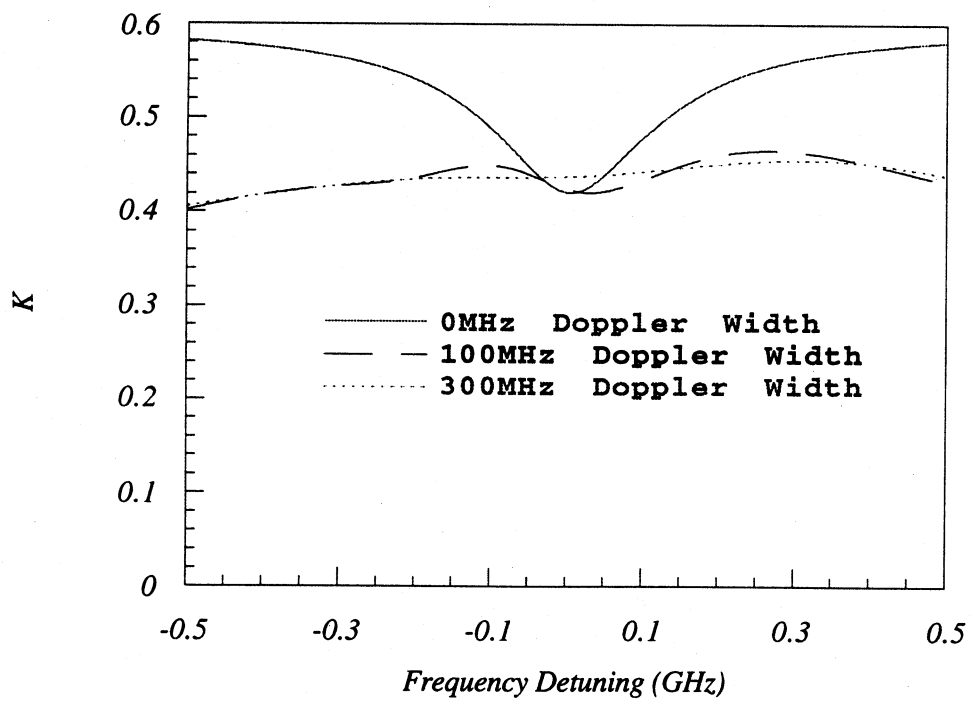
Graph 3.2: K Vs Laser Detuning Various Laser Intensities

frequency of the $3^2S_{1/2} (F'=2 M_F=0) \rightarrow 3^2P_{3/2} (F'=3 M_F=0)$ transition. The light is assumed to have a constant intensity and the populations and coherences used to determine the K parameter were time averaged over transit time of the atoms through the laser beam of 2mm in diameter which was estimated to be one microsecond. The case of a zero Doppler width atomic beam shows that K varies rapidly as the intensity of the laser is changed. The greatest variation occurs between 0MHz to 300MHz. These variations are due to the onset of power broadening effects. At low laser intensities laser will only populate the $F=3$ excited state sublevel. Raising the laser power to more moderate powers induces power broadening effects and as such other excited state hyperfine states become populated and hence the variation in K . At higher intensities, the value of K tends to 0.6 which is consistent with the J representation calculation in Chapter Two.

The effect of high laser intensities exciting the D_2 transition in sodium has been investigated previously by Pegg and MacGillivray 1986. At laser intensities such that the power broadening of individual hyperfine transitions occurs, Pegg and MacGillivray 1986 demonstrated that the atom-field interaction may be simplified by transforming the excited states to a new set of basis states. In this new basis, it can be shown, that the line polarisation yields a constant value of 0.6 (Farrell *et al.* 1991) which is identical to the J representation calculation and is in good agreement with the single step calculation results at high intensity.

Also depicted in graph 3.1 are the results of calculations with two other Doppler widths. The 100MHz Doppler width atomic beam displays some variation at low laser intensities but is much less varied than the zero Doppler width case. A Doppler width of 300MHz shows less features and is much less varied than the other two Doppler width calculations. Once again, the larger Doppler width calculations are tending towards the 0.6 high intensity limit.

Graph 3.2 depicts K as a function of the laser detuning for three different laser powers for a zero Doppler width atomic beam. At the low laser power of 10MHz most of the structure of the excited state hyperfine manifold is clearly resolved and as such K is very sensitive to

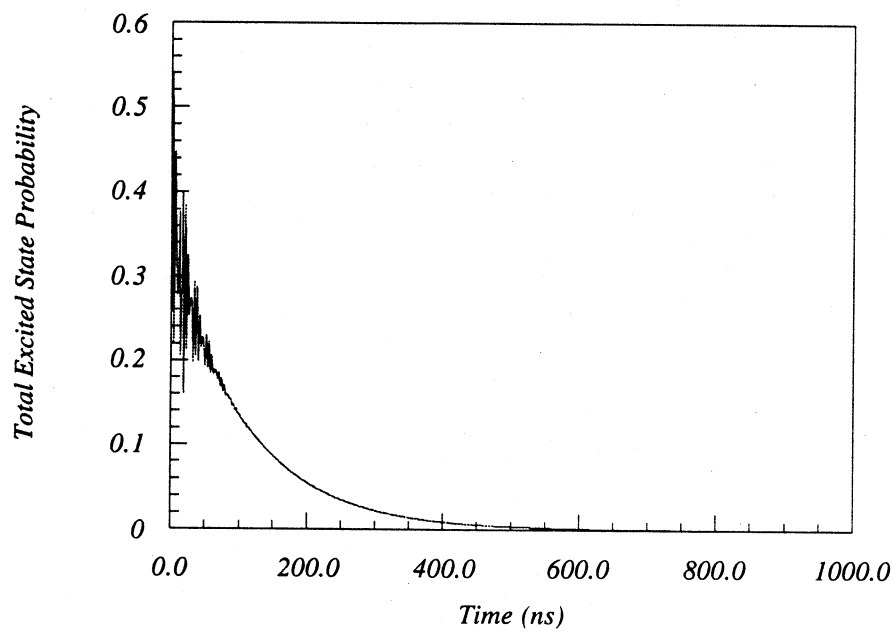


Graph 3.3: K Vs Laser Detuning Various Doppler Widths

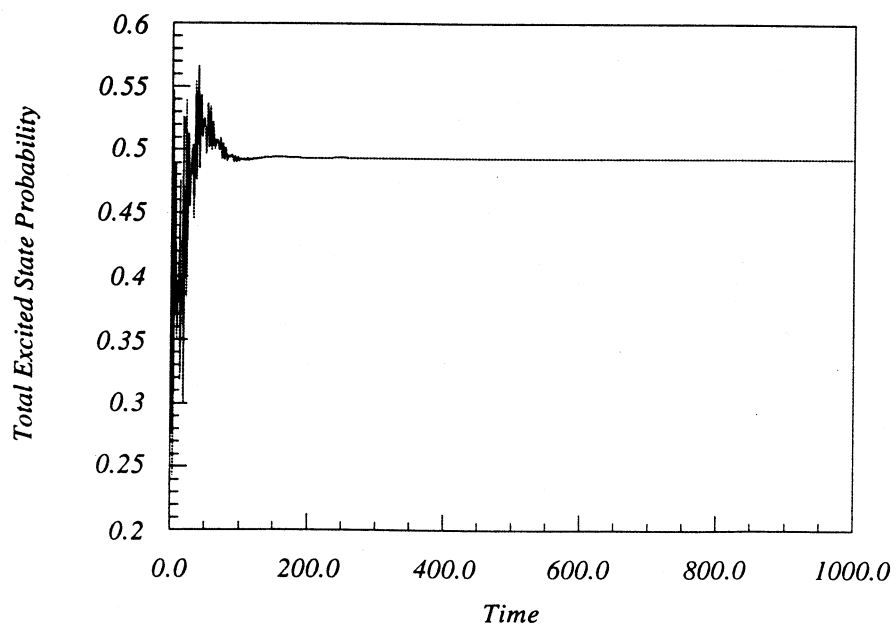
various detunings. With an increase of the laser power to 200MHz the hyperfine structure is no longer resolvable due to power broadening effects and no structure due to the excited hyperfine sublevels is seen. At the high intensity of 600MHz, K takes the constant value of 0.6.

Graph 3.3 shows K as a function of the of the laser detuning for three different Doppler widths at a laser intensity of 200MHz which corresponded to the approximate intensity used in the superelastic and line polarisation experiments. The zero Doppler width case shows that there is a significant variation in the value of K . As the Doppler width is increased to 100MHz the variations become much smaller and at 300MHz which is almost identical to the experimental conditions used in the superelastic experiments. At zero detuning, K takes almost a constant value of 0.42.

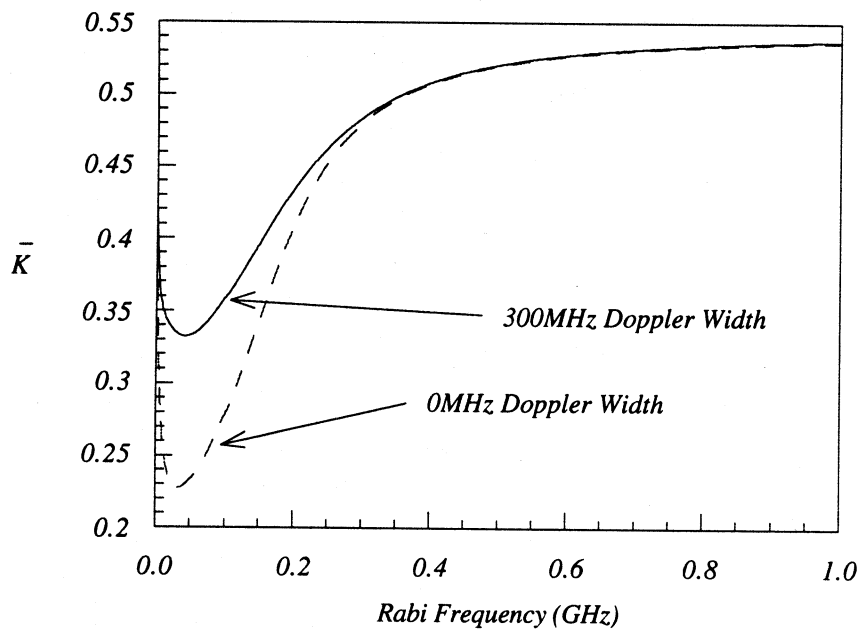
It is clear from these calculations that K is very sensitive to experimental conditions such as the laser intensity, laser detuning and the Doppler width of the atomic beam. In the determination of the atomic collision parameters using the pseudo Stokes parameters it is therefore vital to keep the experimental conditions of the laser-atom interaction as constant as possible. The theoretical calculations displayed here, show that larger Doppler width atomic beams and high laser intensities provide very stable operating conditions so that the optical pumping parameter K has a low sensitivity to various experimental conditions. Having a large Doppler width atomic beam has the disadvantage that smaller populations in the excited state are produced. This limitation can be significant in terms of the superelastic signals at large scattering angle where the differential cross section is small.



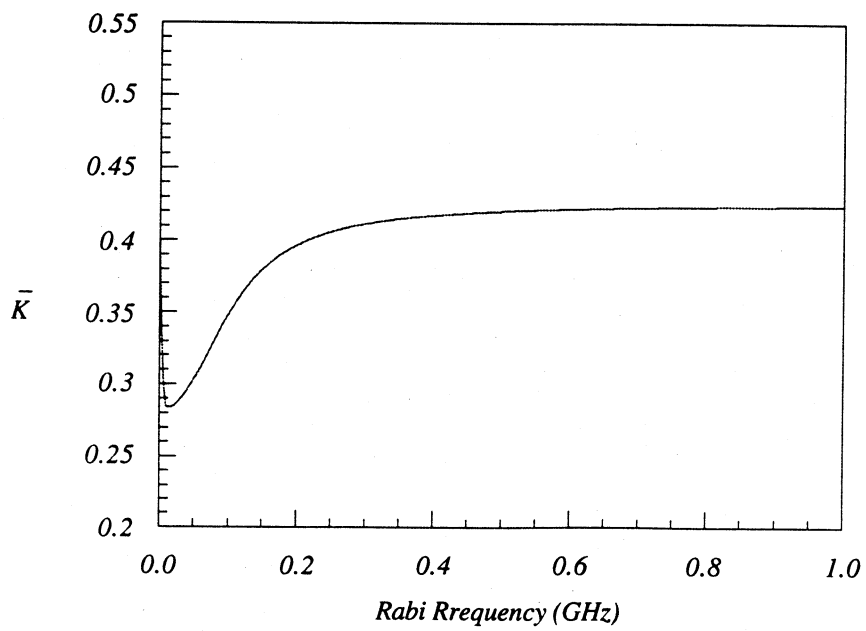
Graph 3.4a: Total Excited Population Vs Time (Single Laser)



Graph 3.4b: Total Excited Population Vs Time (Two Lasers)



Graph 3.5a: \bar{K} Vs Rabi Frequency of Laser 2

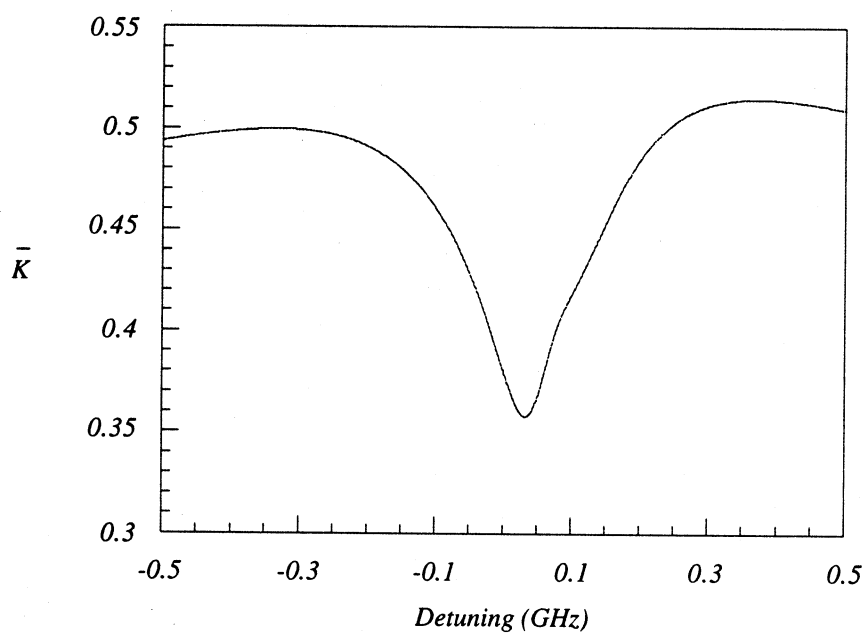


Graph 3.5b: \bar{K} Vs Rabi Frequency of Laser 1

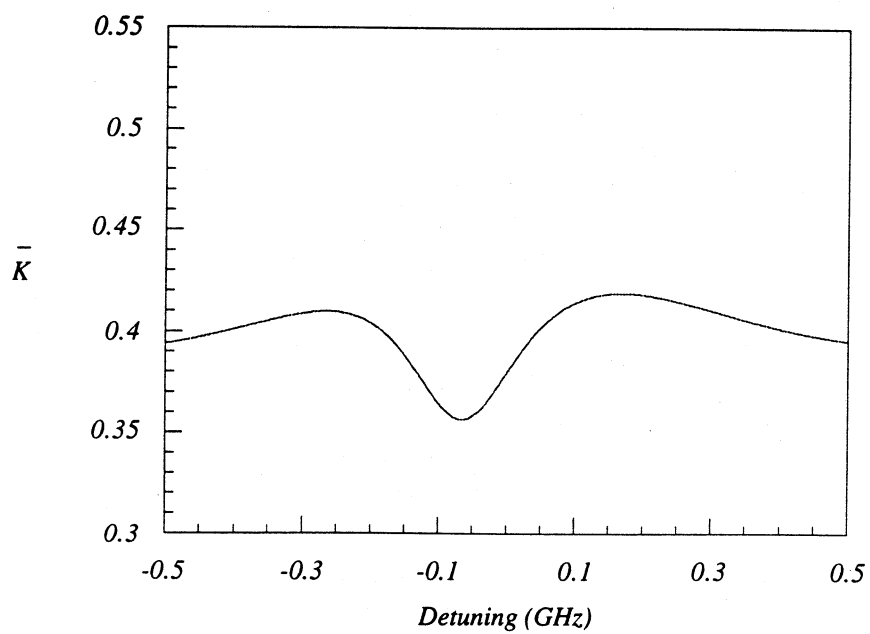
3.9 Folded Step Results

Graph 3.4 shows the total excited state probability as a function of time for the single laser excitation case and the folded step laser excitation case. In both examples the lasers are tuned, in the case of the single laser from the $F'=2$ hyperfine ground state and for the folded step case from the two hyperfine ground states to the $F=2$ state in the excited $3^2P_{3/2}$ manifold. In the single laser case the laser has an intensity of 80mw/mm^2 and for the folded step case the laser 2 has an intensity of 80mW/mm^2 and laser 1 a power of 10mW/mm^2 . The results of the single laser calculation shows that the total excited population very quickly tends to zero probability. The laser is tuned the $F=2$ hyperfine states which can relax to both hyperfine ground states which shows that the atoms are quickly pumped into the $F'=1$ hyperfine ground state. The oscillations are due to Rabi frequencies of the individual hyperfine states. Graph 3.4b shows the results of a folded step calculation. The conditions are identical to the single step calculation except that a second laser pumping with low power from the $F'=1$ ground state has been added. Oscillations are seen once again and the effect of the second laser is immediately obvious with the system acting in a similar way to a two state system with the total excited state probability of close to fifty percent is achieved. This result also shows that it is not necessary to have a high laser power exciting this transition to produce a significant increase in the excited state population.

Graph 3.5a shows the optical pumping parameter \bar{K} as a function of the intensity of laser 2 for two different Doppler widths with zero detuning for both lasers. The intensity has been expressed in Rabi frequency of the $3^2S_{1/2}(F'=2, m_{F'}=0) \rightarrow 3^2P_{3/2}(F=3, m_F=0)$ transition which is the strongest transition in the manifold for π excitation. Laser 1 has an intensity of 150MHz which is approximately the intensity used in experiments. The results show that this parameter, as in the single step experiments, is sensitive to both the Doppler width of the atomic beam and the intensity of the laser light. Both Doppler width cases have a similar appearance with the zero Doppler width case showing the greatest variation. The greatest



Graph 3.6a: \bar{K} Vs Frequency Detuning of Laser 2



Graph 3.6b: \bar{K} Vs Frequency Detuning of Laser 1

amount of variation occurs at lower powers and at higher powers the parameter is limiting, as expected, towards the J representation calculation of 0.6.

Graph 3.5b depicts a similar picture to graph 3.5a except in this case the laser 2 is maintained at a constant intensity of 170MHz and laser 1 is scanned. The atomic beam has a 0MHz Doppler Width. The intensity is once again expressed in terms of Rabi frequency of the identical transition that was used in graph 3.5a. Again, the greatest variation is seen at low laser intensity and is not as varied as the case when the power of the laser 2 is changed for the same Doppler width. It is expected at higher laser intensities that this parameter will limit to 0.6.

Graphs 3.6a and 3.6b show \bar{K} as a function of the laser detuning for laser 2 and laser 1 respectively and illustrate the importance of the laser tuning in the experiment. Both calculations assume a zero Doppler width atomic beam. In both cases the laser which is not scanned is tuned to the $F=2$ excited state. Laser 2 has an intensity of 170MHz and laser 2 an intensity of 150MHz. The greatest variation occurs for the detuning of laser 2 and displays similar behaviour to the single laser detuning case. The minimum value of \bar{K} occurs when the second laser is positively detuned so that it is in resonance with the $F=3$ excited state hyperfine sub level. The nature of the optical pumping using π light, pumps the atoms to the smaller m_F substates (Hertel and Stoll 1974a) which are angular momentum states that provide more spherical charge clouds. It was shown in the previous section that \bar{K} was directly related to the line polarisation of the fluorescence scattered perpendicular to the plane formed by the propagation direction of the lasers and the polarisation vector of the lasers. The line polarisation of a perfectly spherical charge cloud such as an S state produces a line polarisation of zero so the more spherical the charge cloud the smaller the value of \bar{K} . The detuning of laser 1 is interesting as a negative detuning shows the minimum value of \bar{K} .

Using the results from graphs 3.5 it is possible to predict a value for \bar{K} for the conditions used in the folded step experiments. The atomic beam had a Doppler width of 300MHz and

laser 1 an intensity of 150MHz. Laser 2 had an intensity of 170MHz. These conditions yield a value of approximately 0.4 which is in excellent agreement with experimentally determined value given in Chapter six.

Chapter Four

Superelastic Electron-Atom Collisions Involving D States

4.1 Introduction

Much of the work to date on electron-atom correlation experiments has involved the study of the collision processes in which atoms are excited from ground S states to excited P states. Collision processes which involve higher angular momentum states are interesting because larger angular momentum transfers are involved in the excitation/de-excitation process and as such would more than likely require a stronger interaction between the target atom and the incident electron. Continuum effects also play a larger role as atoms are excited closer to their ionisation threshold. Nienhuis (1980) began the first studies in which states with higher angular momentum were excited, in particular the S-D collision process and the first experiments were carried out by the same group employing the electron-photon angular correlation technique (van Linden van den Heuvell *et al.* 1981) using helium as the target atom. In this experiment the scattered electrons resulting from the 3^1D excitation were measured in coincidence with the photons from the $2^1P \rightarrow 1^1S$ cascade. Three parameters, which were functions of the excitation amplitudes and their relative phases, were determined by using a theoretical fit to the measured data.

This chapter involves new preliminary work on the theory for electron-atom stepwise superelastic collisions involving excited D states of sodium. Atoms are stepwise excited to the D state using two lasers which have specific polarisations. The excited atoms are induced to relax via a superelastic collision with an electron. Superelastic differential cross sections are obtained which are functions of both the laser polarisations to determine pseudo Stokes parameters.

Density matrix formalism will be used as in Chapter Two to describe the collision system. The first section deals with the parametrisation of a D state collision matrix. Following this section is a derivation for a stepwise superelastic signal and the derivation of stepwise pseudo Stokes parameters for laser polarisations which are parallel. This is followed by a derivation of a more complicated stepwise pseudo Stokes parameter that involves two lasers with crossed polarisations and completing the chapter is a section devoted to the modelling of the laser excitation process using rate equations.

4.2 Parameterisation of the D State Collision Matrix

Chapter Two discussed the collision density matrix and the elements of the density matrix were given by equation (2.11). The collisions involving the D state which is an L=2 angular momentum state which requires a 5x5 matrix or 25 density matrix elements to specify the system. The matrix is given by

$$\rho^e(2) = \begin{pmatrix} \rho_{22}^e & \rho_{21}^e & \rho_{20}^e & \rho_{2-1}^e & \rho_{2-2}^e \\ \rho_{12}^e & \rho_{11}^e & \rho_{10}^e & \rho_{1-1}^e & \rho_{1-2}^e \\ \rho_{02}^e & \rho_{01}^e & \rho_{00}^e & \rho_{0-1}^e & \rho_{0-2}^e \\ \rho_{-12}^e & \rho_{-11}^e & \rho_{-10}^e & \rho_{-1-1}^e & \rho_{-1-2}^e \\ \rho_{-22}^e & \rho_{-21}^e & \rho_{-20}^e & \rho_{-2-1}^e & \rho_{-2-2}^e \end{pmatrix} \quad (4.1)$$

where

$$\rho_{M'M}^e = \left(\frac{1}{2\{2J_g+1\}} \right) \sum_{M_g m_0} f(M' m_f M_g m_0) f^*(M m_f M_g m_0) \quad (4.2)$$

The sum runs over the initial states that the atoms are excited from. For example a D-S collision, the S state is the initial state and there will only be one term in the sum. For a D-P

collision process, the P state is the initial state and therefore there are three such terms. The L=2 system is much more complicated than the P state described in Chapter Two which only required a 3x3 matrix to describe the collision. The number of density matrix elements can, however be reduced by applying symmetry conditions. In Chapter Two it was shown that the P-S collision system could be reduced from a maximum of nine independent parameters to three independent parameters for the case when no spin flips occur. Under the identical conditions, applying equations (2.16)-(2.18) to the L=2 density matrix elements yield the following relationships.

$$\begin{aligned}
 \rho_{-2-2}^e &= \rho_{22}^e \\
 \rho_{-1-1}^e &= \rho_{11}^e \\
 \rho_{-20}^e &= \rho_{20}^e \\
 \rho_{-10}^e &= -\rho_{10}^e \\
 \rho_{0-2}^e &= \rho_{02}^e \\
 \rho_{0-1}^e &= -\rho_{0-1}^e \\
 \rho_{-1-2}^e &= -\rho_{12}^e \\
 \rho_{2-1}^e &= -\rho_{21}^e \\
 \rho_{2-2}^e &= \rho_{22}^e \\
 \rho_{1-2}^e &= -\rho_{12}^e \\
 \rho_{-11}^e &= -\rho_{11}^e \\
 \rho_{1-2}^e &= \rho_{12}^e \\
 \rho_{-22}^e &= \rho_{22}^e \\
 \rho_{-21}^e &= \rho_{21}^e \\
 \rho_{-2-1}^e &= -\rho_{21}^e \\
 \rho_{-12}^e &= -\rho_{12}^e
 \end{aligned} \tag{4.3}$$

Applying the above relations and the hermiticity condition given by (2.14) reduces the matrix to

$$\rho^e(2) = \begin{pmatrix} \rho_{22}^e & \rho_{21}^e & \rho_{20}^e & -\rho_{21}^e & \rho_{22}^e \\ \rho_{21}^{e*} & \rho_{11}^e & \rho_{10}^e & -\rho_{11}^e & \rho_{21}^{e*} \\ \rho_{20}^{e*} & \rho_{10}^{e*} & \rho_{00}^e & -\rho_{10}^{e*} & \rho_{20}^{e*} \\ -\rho_{21}^{e*} & -\rho_{11}^e & -\rho_{10}^e & \rho_{11}^e & -\rho_{21}^{e*} \\ \rho_{22}^e & \rho_{21}^e & \rho_{20}^e & -\rho_{21}^e & \rho_{22}^e \end{pmatrix} \quad (4.4)$$

The matrix given by equation (4.4) shows that for a D-S collision there are six independent elements ρ_{22}^e , ρ_{21}^e , ρ_{20}^e , ρ_{11}^e , ρ_{10}^e , ρ_{00}^e . In terms of cross sections and scattering amplitudes these elements are given by $\sigma(2)$, $\sigma(1)$, $\sigma(0)$, $\langle f(1)f^*(0) \rangle$, $\langle f(2)f^*(0) \rangle$, $\langle f(2)f^*(1) \rangle$. Following the notation of Blum 1981 and Nienhuis 1980 the density matrix may be parameterised as

$$\sigma = |\alpha(0)| + 2|\alpha(1)| + 2|\alpha(2)| \quad (4.5a)$$

$$\lambda = \frac{\sigma(0)}{\sigma} = \frac{\rho_{00}^e}{\sigma} \quad (4.5b)$$

$$\mu = \frac{2\sigma(1)}{\sigma} = \frac{2\rho_{11}^e}{\sigma} \quad (4.5c)$$

$$\cos\chi = \frac{\text{Re}\langle f(1)f^*(0) \rangle}{[\sigma(1)\sigma(0)]^{1/2}} = \frac{\text{Re}\rho_{10}^e}{[\rho_{11}^e\rho_{00}^e]^{1/2}} \quad (4.5d)$$

$$\sin\phi = \frac{\text{Im}\langle f(1)f^*(0) \rangle}{[\sigma(1)\sigma(0)]^{1/2}} = \frac{\text{Im}\rho_{10}^e}{[\rho_{11}^e\rho_{00}^e]^{1/2}} \quad (4.5e)$$

$$\cos\psi = \frac{\text{Re}\langle f(2)f^*(1) \rangle}{[\sigma(2)\sigma(1)]^{1/2}} = \frac{\text{Re}\rho_{21}^e}{[\rho_{22}^e\rho_{11}^e]^{1/2}} \quad (4.5f)$$

$$\sin\xi = \frac{\text{Im}\langle f(2)f^*(1) \rangle}{[\sigma(2)\sigma(1)]^{1/2}} = \frac{\text{Im}\rho_{21}^e}{[\rho_{22}^e\rho_{11}^e]^{1/2}} \quad (4.5g)$$

$$\cos(\chi+\psi) = \frac{\text{Re}\langle f(2)f^*(0) \rangle}{[\sigma(2)\sigma(0)]^{1/2}} = \frac{\text{Re}\rho_{20}^e}{[\rho_{22}^e\rho_{00}^e]^{1/2}} \quad (4.5h)$$

$$\sin(\phi+\xi) = \frac{\text{Im}\langle f(2)f^*(0) \rangle}{[\sigma(2)\sigma(0)]^{1/2}} = \frac{\text{Im}\rho_{20}^e}{[\rho_{22}^e\rho_{00}^e]^{1/2}} \quad (4.5i)$$

$$\cos\delta = \frac{\langle f(1)f^*(-1) \rangle}{\sigma(1)} = \frac{\rho_{1-1}^e}{\rho_{11}^e} = -1 \quad (4.5j)$$

$$\cos\eta = \frac{\langle f(2)f^*(-2) \rangle}{\sigma(2)} = \frac{\rho_{2-2}^e}{\rho_{22}^e} = 1 \quad (4.5k)$$

σ is the total differential cross section and is normalised to unity. $\cos\delta$ and $\cos\eta$ are denoted spin flip parameters and in sodium have definite values of -1 and 1 respectively and therefore only six parameters, λ , μ , χ , ϕ , ψ and ξ are required to characterise the L=2 density matrix. λ and μ are ratios of partial differential cross sections and χ , ϕ , ψ and ξ are the real and imaginary parts of relative phases. The experiment that will be studied in this chapter is the superelastic D-P collision process. The D-P collision process may use the same parameterisation except that the underlying sum over the P states must be considered. This sum greatly complicates the problem in that more excitation amplitudes and relative phases are involved in the collision process and hence more parameters are required to fully specify the system. In this preliminary analysis only the parameters defined above will be considered and hence only the sums of combined excitation amplitudes and their relative phases will be determined. Therefore this analysis of the superelastic D-P collision experiment can not be described as a fully "complete" experiment (Bederson 1969).

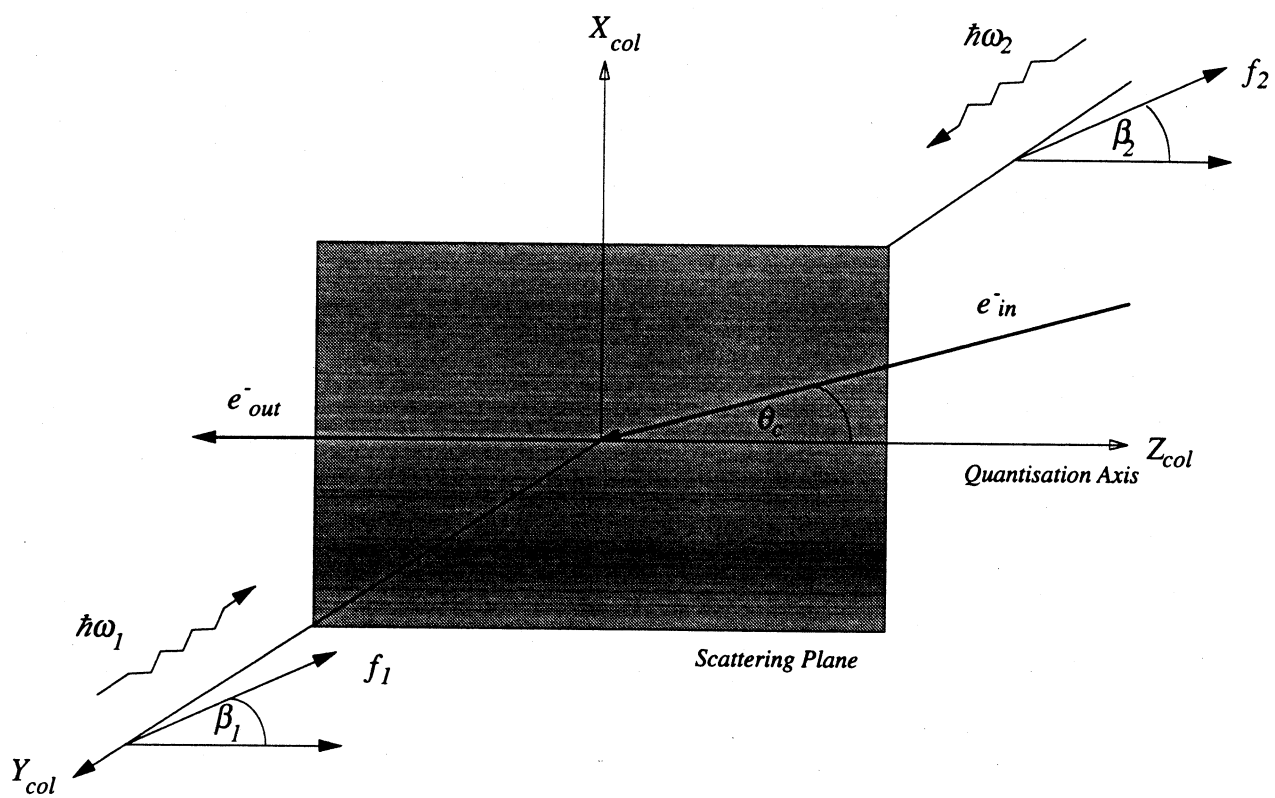


Figure 4.1: The Scattering Plane (Stepwise Superelastic Experiment)

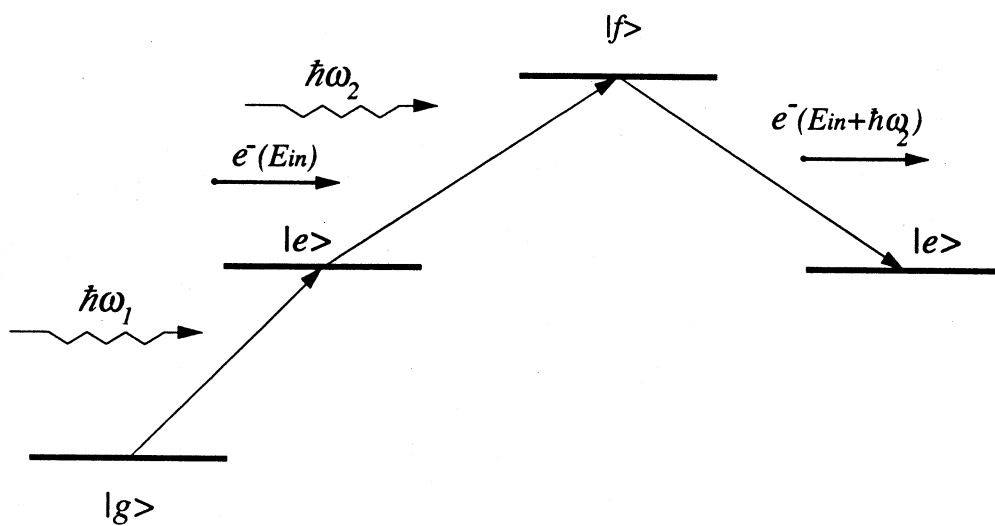


Figure 4.2: The Stepwise Superelastic Scattering Scheme

4.3 Stepwise Superelastic Scattering

In this section the general theory for the derivation of the stepwise superelastic differential cross section is given. The scattering plane for the experiment may be seen in figure 4.1. This is identical to the single step superelastic scattering experiment except that a second laser, tuned to the appropriate P to D transition, is incident on the interaction region in a counter-propagating direction to the first laser.

A general stepwise superelastic scattering scheme may be seen in figure 4.2. Resonant laser radiation of a known polarisation excites a ground state atom $|g\rangle$ to an excited state $|e\rangle$, a second laser also of a known polarisation then excites the atom from the excited state $|e\rangle$ to a state higher in energy $|f\rangle$. The atom is then induced to relax via a superelastic collision with an electron back to the excited state $|e\rangle$. In this case the ground state $|g\rangle$ is an S state ($L=0$), $|e\rangle$ is a P ($L=1$) state and $|f\rangle$ is a D ($L=2$) state.

Drawing the analogy with an optically prepared P state (equation (2.26)) the optically prepared D state is represented by

$$\rho^{oD} = \sum_{m_D n_D} \rho_{m_D n_D}^{L_D} |Jm_D\rangle \langle Jn_D| \quad (4.6)$$

where $\rho_{m_D n_D}^{L_D}$ describe the ensemble distribution in the excited D state. The electron de-excitation of the atom to the P state is represented by L^D , the de-excitation monitoring operator which is given by

$$L^D = \sum_{J_P m_P} T_D |J_P m_P\rangle \langle J_P m_P| T_D^\dagger \quad (4.7)$$

T_D where is a scattering operator. The superelastic differential cross section is given by the usual expression (MacGillivray and Standage 1988)

$$S = Tr(\rho^o D L^D) \quad (4.8)$$

Substituting the expression from (4.6) and (4.7) yields

$$S = \sum_{m_D n_D} \rho_{m_D n_D}^{L_D} L_{n_D m_D}^D \quad (4.9)$$

Where $L_{n_D m_D}^D$ is given by

$$L_{n_D m_D}^D = \sum_{J_P m_P} \langle J_D n_D | T_D | J_P m_P \rangle \langle J_P m_P | T_D^\dagger | J_D m_D \rangle \quad (4.10)$$

The density matrix elements of the D state formed by a collision with an electron of the P state using equation (2.8) this is represented by

$$\rho_{m_D n_D}^f = \left(\frac{1}{2(2J_P + 1)} \right) \sum_{J_P m_P} \langle J_D m_D | T | J_P m_P \rangle \langle J_P m_P | T^\dagger | J_D n_D \rangle \quad (4.11)$$

Applying the principle of micro-reversibility reveals that

$$\langle J_D n_D | T_D | J_P m_P \rangle = \langle J_P m_P | T_D^\dagger | J_D n_D \rangle \quad (4.12a)$$

$$\langle J_P m_P | T_D^\dagger | J_D m_D \rangle = \langle J_D m_D | T_D | J_P m_P \rangle \quad (4.12b)$$

Then to within a normalisation constant

$$L_{n_D m_D}^D = \rho_{m_D n_D}^f \quad (4.13)$$

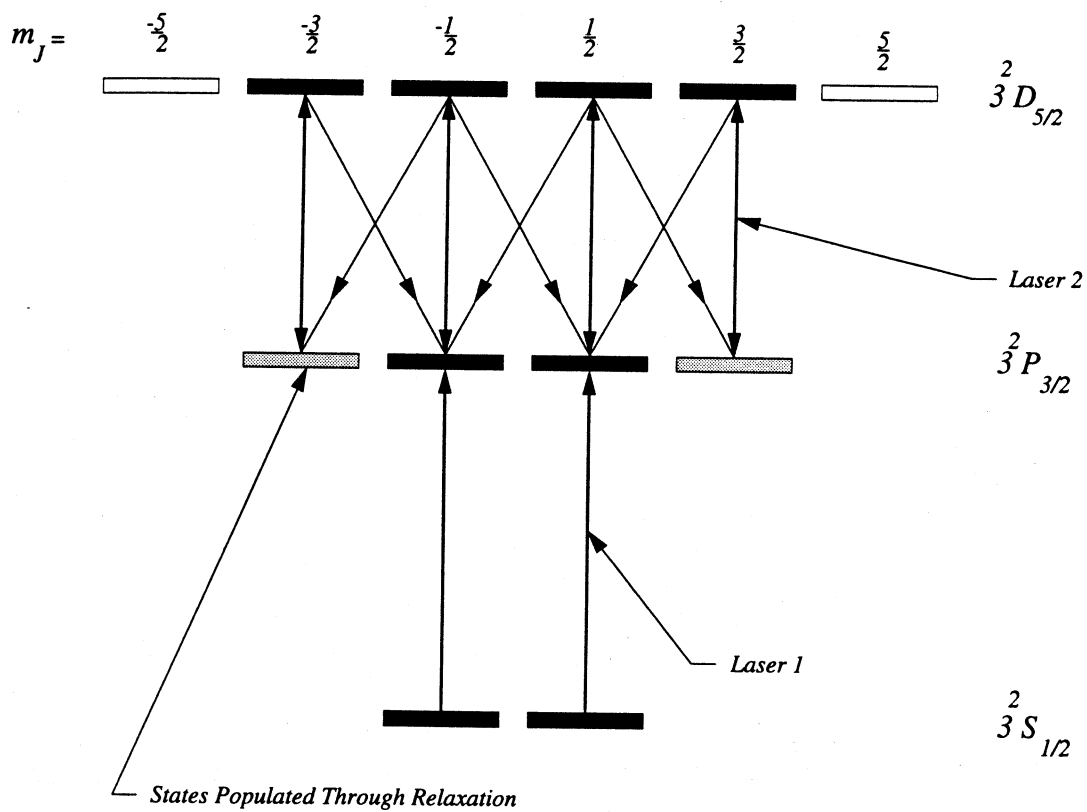


Figure 4.3: Energy levels of Sodium in J representation

Thus the superelastic signal is given by

$$S = \sum_{m_D n_D} \rho_{m_D n_D}^{L_D} \rho_{m_D n_D}^f \quad (4.14)$$

4.4 Derivation of the Pseudo Stokes Parameters for Parallel Polarisation

In this section the pseudo Stokes parameters for the case when both polarisations of the lasers are kept parallel are considered. This is the most simple case because if the two exciting lasers have two different polarisations, then two different excitation frames are required to describe the two laser excitation steps. This has the implication that instead of the calculation only needing one rotation as in the single step laser excitation case and the case presented here, a second rotation would be required. This type of calculation will be demonstrated later in the chapter.

The calculation is applied to the sodium atom and the superelastic differential cross section will be kept in J representation. The sodium atoms are initially excited from the $3^2S_{1/2}$ ground state to the $3^2P_{3/2}$ excited state. The atoms are then further excited from this state to the $3^2D_{5/2}$ state. The energy level structure in fine structure representation may be seen in figure 4.3. Applying linearly polarised light by both lasers excites the shaded states. The $J=\frac{5}{2}, M_J=\pm\frac{3}{2}$ states are excited due to relaxation of the $M_J=\pm\frac{1}{2}$ states. These relaxation channels are also depicted in figure 4.3. In the frame defined by the electric field vectors of the lasers, the expression for the superelastic differential cross section (equation (4.14)) is diagonal in the m_J quantum number yielding

$$S = \rho_{-3/2-3/2}^{L_2} \rho_{-3/2-3/2}^{f_L} + \rho_{-1/2-1/2}^{L_2} \rho_{-1/2-1/2}^{f_L} + \rho_{1/21/2}^{L_2} \rho_{1/21/2}^{f_L} + \rho_{3/23/2}^{L_2} \rho_{3/23/2}^{f_L} \quad (4.15)$$

Table 4.1

The J Representation Density Matrix Elements Reduced to L Representation

J Representation	L Representation
$\rho_{5/2-5/2}^f$	ρ_{-2-2}^f
$\rho_{3/2-3/2}^f$	$\frac{4}{5}\rho_{-1-1}^f + \frac{1}{5}\rho_{-2-2}^f$
$\rho_{1/2-1/2}^f$	$\frac{3}{5}\rho_{00}^f + \frac{2}{5}\rho_{-1-1}^f$
$\rho_{1/21/2}^f$	$\frac{3}{5}\rho_{00}^f + \frac{2}{5}\rho_{11}^f$
$\rho_{3/23/2}^f$	$\frac{4}{5}\rho_{11}^f + \frac{1}{5}\rho_{22}^f$
$\rho_{5/25/2}^f$	ρ_{22}^f

were $\rho_{mm}^{L_2}$ are the populations formed by laser 2 and $\rho_{mm}^{f_L}$ are the collision density matrix elements in the laser frame. The $\rho_{mm}^{f_L}$ elements are in J representation and may be reduced to L representation by employing the state reduction methods given in Chapter Two by equation (2.39). Applying this reduction formula to the collision matrix elements give the results expressed in Table 4.1. Substitution of the results from Table 4.1 into equation (4.15) reveals

$$S = \rho_{-3/2-3/2}^{L_2} \left(\frac{4}{5}\rho_{-1-1}^{f_L} + \frac{1}{5}\rho_{-2-2}^{f_L} \right) + \rho_{-1/2-1/2}^{L_2} \left(\frac{3}{5}\rho_{00}^{f_L} + \frac{2}{5}\rho_{-1-1}^{f_L} \right) \\ + \rho_{1/21/2}^{L_2} \left(\frac{3}{5}\rho_{00}^{f_L} + \frac{2}{5}\rho_{11}^{f_L} \right) + \rho_{3/23/2}^{L_2} \left(\frac{4}{5}\rho_{11}^{f_L} + \frac{1}{5}\rho_{22}^{f_L} \right) \quad (4.16)$$

This expression may be reduced by using symmetry relations formed by π excitation such that

$$\rho_{-m-m}^{L_2} = \rho_{mm}^{L_2} \quad (4.17)$$

Applying equation (4.17) to the expression for the superelastic differential cross section yields

$$S = \rho_{3/23/2}^{L_2} \left(\frac{1}{5}\rho_{-2-2}^{f_L} + \frac{4}{5}\rho_{-1-1}^{f_L} + \frac{4}{5}\rho_{11}^{f_L} + \frac{1}{5}\rho_{22}^{f_L} \right) + \rho_{1/21/2}^{L_2} \left(\frac{2}{5}\rho_{-1-1}^{f_L} + \frac{3}{5}\rho_{00}^{f_L} + \frac{2}{5}\rho_{11}^{f_L} \right) \quad (4.18)$$

The $\rho_{mm}^{f_L}$ elements have been expressed in the laser frame and because measurements are made in the collision frame these collision density matrix elements must be transformed to this frame. This transformation has been performed previously for the L=1 density matrix in Chapter Two by applying equation (2.42). By inspection of figure 4.1 the Euler angles required to rotate from the laser frame to the collision frame are $(0, -\beta, 0)$ which are the identical Euler angles used for the linearly excited single step superelastic scattering experiment. The rotation matrix $D_{M_L M_L}^J(\omega)$ may be generated by applying equation (2.43).

For a rotation of β about the Y_{col} axis using equation (2.44) allows the sub matrix for the $L=2$ case to be determined as

$$d^2_{m'm}(\beta) = \frac{1}{2} \begin{pmatrix} \frac{1}{2}(1+\cos\beta)^2 & \sin\beta(1+\cos\beta) & \sqrt{\frac{3}{2}}\sin^2\beta & \sin\beta(1-\cos\beta) & \frac{1}{2}(1-\cos\beta)^2 \\ -\sin\beta(1+\cos\beta) & (1+\cos\beta)(2\cos\beta-1) & \sqrt{6}\sin\beta\cos\beta & (1-\cos\beta)(2\cos\beta+1) & \sin\beta(1-\cos\beta) \\ \sqrt{\frac{3}{2}}\sin^2\beta & -\sqrt{6}\sin\beta\cos\beta & 3\cos^2\beta-1 & \sqrt{6}\sin\beta\cos\beta & \sqrt{\frac{3}{2}}\sin^2\beta \\ -\sin\beta(1-\cos\beta) & (1-\cos\beta)(2\cos\beta+1) & -\sqrt{6}\sin\beta\cos\beta & (1+\cos\beta)(2\cos\beta-1) & \sin\beta(1+\cos\beta) \\ \frac{1}{2}(1-\cos\beta)^2 & -\sin\beta(1-\cos\beta) & \sqrt{\frac{3}{2}}\sin^2\beta & -\sin\beta(1+\cos\beta) & \frac{1}{2}(1+\cos\beta)^2 \end{pmatrix} \quad (4.19)$$

Hence for the case of $-\beta$ the rotation matrix is given by

$$D^2_{m'm}(-\beta) = \frac{1}{2} \begin{pmatrix} \frac{1}{2}(1+\cos\beta)^2 & -\sin\beta(1+\cos\beta) & \sqrt{\frac{3}{2}}\sin^2\beta & -\sin\beta(1-\cos\beta) & \frac{1}{2}(1-\cos\beta)^2 \\ \sin\beta(1+\cos\beta) & (1+\cos\beta)(2\cos\beta-1) & -\sqrt{6}\sin\beta\cos\beta & (1-\cos\beta)(2\cos\beta+1) & -\sin\beta(1-\cos\beta) \\ \sqrt{\frac{3}{2}}\sin^2\beta & \sqrt{6}\sin\beta\cos\beta & 3\cos^2\beta-1 & -\sqrt{6}\sin\beta\cos\beta & \sqrt{\frac{3}{2}}\sin^2\beta \\ \sin\beta(1-\cos\beta) & (1-\cos\beta)(2\cos\beta+1) & \sqrt{6}\sin\beta\cos\beta & (1+\cos\beta)(2\cos\beta-1) & -\sin\beta(1+\cos\beta) \\ \frac{1}{2}(1-\cos\beta)^2 & \sin\beta(1-\cos\beta) & \sqrt{\frac{3}{2}}\sin^2\beta & \sin\beta(1+\cos\beta) & \frac{1}{2}(1+\cos\beta)^2 \end{pmatrix} \quad (4.20)$$

Applying equation (2.42) and the rotation matrix defined above yield the following rotated density matrix elements

$$\begin{aligned} \rho_{22}^{fL} &= \frac{1}{4}(1+\cos^2\beta)^2 \rho_{22}^f + \sin^2\beta \cos^2\beta \rho_{11}^f + \frac{3}{8}\sin^4\beta \rho_{00}^f + \sin\beta \cos\beta (1+\cos^2\beta) \text{Re}\rho_{21}^f \\ &\quad + \frac{1}{2}\sqrt{\frac{3}{2}}\sin^2\beta (1+\cos^2\beta) \text{Re}\rho_{20}^f + \sqrt{\frac{3}{2}}\sin^3\beta \cos\beta \text{Re}\rho_{10}^f \end{aligned} \quad (4.21a)$$

$$= \rho_{-2-2}^{fL} \quad (4.21b)$$

$$\begin{aligned} \rho_{11}^{fL} &= \sin^2\beta \cos^2\beta \rho_{22}^f + (1-2\cos^2\beta)^2 \rho_{11}^f + \frac{3}{2}\sin^2\beta \cos^2\beta \rho_{00}^f - \sqrt{6}\sin^2\beta \cos^2\beta \text{Re}\rho_{20}^f \\ &\quad - 2\sin\beta \cos\beta (2\cos^2\beta-1) \text{Re}\rho_{21}^f - \sqrt{6}\sin\beta \cos\beta (1-2\cos^2\beta) \text{Re}\rho_{10}^f \end{aligned} \quad (4.21c)$$

$$= \rho_{-1-1}^{fL} \quad (4.21d)$$

$$\begin{aligned} \rho_{00}^{fL} = & \frac{3}{2} \sin^4 \beta \rho_{22}^f + 6 \sin^2 \beta \cos^2 \beta \rho_{11}^f + \frac{1}{4} (3 \cos^2 \beta - 1)^2 \rho_{00}^f - 6 \sin^3 \beta \cos \beta \operatorname{Re} \rho_{21}^f \\ & + \sqrt{\frac{3}{2}} \sin^2 \beta (3 \cos^2 \beta - 1) \operatorname{Re} \rho_{20}^f - \sqrt{6} \sin \beta \cos \beta (3 \cos^2 \beta - 1) \operatorname{Re} \rho_{10}^f \end{aligned} \quad (4.21e)$$

Substituting the rotated elements into equation (4.18) enables the superelastic differential cross section to be written as

$$\begin{aligned} S(\beta) = & \rho_{3/23/2}^{L_2} \left\{ \frac{2}{5} \left(\frac{1}{4} (1 + \cos^2 \beta)^2 \rho_{22}^f + \sin^2 \beta \cos^2 \beta \rho_{11}^f + \frac{3}{8} \sin^4 \beta \rho_{00}^f \right. \right. \\ & + \sin \beta \cos \beta (1 + \cos^2 \beta) \operatorname{Re} \rho_{21}^f + \frac{1}{2} \sqrt{\frac{3}{2}} \sin^2 \beta (1 + \cos^2 \beta) \operatorname{Re} \rho_{20}^f + \sqrt{\frac{3}{2}} \sin^3 \beta \cos \beta \operatorname{Re} \rho_{10}^f \left. \right) \\ & + \frac{8}{5} \left(\sin^2 \beta \cos^2 \beta \rho_{22}^f + (1 - 2 \cos^2 \beta)^2 \rho_{11}^f + \frac{3}{2} \sin^2 \beta \cos^2 \beta \rho_{00}^f - \sqrt{6} \sin^2 \beta \cos^2 \beta \operatorname{Re} \rho_{20}^f \right. \\ & - 2 \sin \beta \cos \beta (2 \cos^2 \beta - 1) \operatorname{Re} \rho_{21}^f - \sqrt{6} \sin \beta \cos \beta (1 - 2 \cos^2 \beta) \operatorname{Re} \rho_{10}^f \left. \right) \left. \right\} \\ & + \rho_{1/21/2}^{L_2} \left\{ \frac{6}{5} \left(\frac{3}{2} \sin^4 \beta \rho_{22}^f + 6 \sin^2 \beta \cos^2 \beta \rho_{11}^f + \frac{1}{4} (3 \cos^2 \beta - 1)^2 \rho_{00}^f - 6 \sin^3 \beta \cos \beta \operatorname{Re} \rho_{21}^f \right. \right. \\ & + \sqrt{\frac{3}{2}} \sin^2 \beta (3 \cos^2 \beta - 1) \operatorname{Re} \rho_{20}^f - \sqrt{6} \sin \beta \cos \beta (3 \cos^2 \beta - 1) \operatorname{Re} \rho_{10}^f \left. \right) + \frac{4}{5} \left(\sin^2 \beta \cos^2 \beta \rho_{22}^f \right. \\ & + (1 - 2 \cos^2 \beta)^2 \rho_{11}^f + \frac{3}{2} \sin^2 \beta \cos^2 \beta \rho_{00}^f - \sqrt{6} \sin^2 \beta \cos^2 \beta \operatorname{Re} \rho_{20}^f \\ & - 2 \sin \beta \cos \beta (2 \cos^2 \beta - 1) \operatorname{Re} \rho_{21}^f - \sqrt{6} \sin \beta \cos \beta (1 - 2 \cos^2 \beta) \operatorname{Re} \rho_{10}^f \left. \right) \left. \right\} \end{aligned} \quad (4.22)$$

This expression for the superelastic differential cross section enables the determination of the pseudo Stokes parameter P_j^S given by equation (2.49a). The terms $S(0)$ and $S(90)$ are given by

$$S(0) = \rho_{3/23/2}^{L_2} \left(\frac{2}{5} \rho_{22}^f + \frac{8}{5} \rho_{11}^f \right) + \rho_{1/21/2}^{L_2} \left(\frac{6}{5} \rho_{00}^f + \frac{4}{5} \rho_{11}^f \right) \quad (4.23a)$$

$$\begin{aligned} S(90) = & \rho_{3/23/2}^{L_2} \left(\frac{2}{5} \left\{ \frac{1}{4} \rho_{22}^f + \frac{3}{8} \rho_{00}^f + \frac{1}{2} \sqrt{\frac{3}{2}} \operatorname{Re} \rho_{20}^f \right\} + \frac{8}{5} \rho_{11}^f \right) \\ & + \rho_{1/21/2}^{L_2} \left(\frac{6}{5} \left\{ \frac{3}{2} \rho_{22}^f + \frac{1}{4} \rho_{00}^f - \sqrt{\frac{3}{2}} \operatorname{Re} \rho_{20}^f \right\} + \frac{4}{5} \rho_{11}^f \right) \end{aligned} \quad (4.23b)$$

Substitution of these differential cross sections into the definition of the pseudo Stokes parameter P_j^S equation (2.49a) and using equation (4.5a) reveals

$$P_I^S = \frac{\left\{ \rho_{3/2/32}^L - 6\rho_{1/2/12}^L \right\} \left[\frac{3}{2} \sigma - 3\rho_{00}^f - 3\rho_{11}^f - \sqrt{6} \operatorname{Re} \rho_{20}^f \right]}{\left\{ 5\rho_{3/2/32}^L + 18\rho_{1/2/12}^L \right\} \frac{\sigma}{2} - \left\{ \frac{7}{2} \rho_{3/2/32}^L + 3\rho_{1/2/12}^L \right\} \rho_{00}^f + \left\{ 54\rho_{3/2/32}^L - 4\rho_{1/2/12}^L \right\} \frac{\rho_{11}^f}{2} + \left\{ \rho_{3/2/32}^L - 6\rho_{1/2/12}^L \right\} \sqrt{6} \operatorname{Re} \rho_{20}^f}$$
(4.24)

Manipulation of equations (4.5) give the following relationships

$$\operatorname{Re} \rho_{20}^f = \frac{1}{\sqrt{2}} \cos(\chi + \psi) \frac{\rho_{00}^f}{\sqrt{\lambda}} (1 - \mu - \lambda)^{1/2} \quad (4.25a)$$

$$\operatorname{Re} \rho_{10}^f = \frac{1}{\sqrt{2}} \cos(\chi) \frac{\rho_{00}^f}{\sqrt{\lambda}} (1 - \lambda)^{1/2} \quad (4.25b)$$

$$\operatorname{Re} \rho_{21}^f = \cos(\psi) \frac{\rho_{11}^f}{\sqrt{\mu}} (\mu - \lambda - 1)^{1/2} \quad (4.25c)$$

$$\operatorname{Im} \rho_{20}^f = \frac{1}{\sqrt{2}} \sin(\chi + \psi) \frac{\rho_{00}^f}{\sqrt{\lambda}} (1 - \mu - \lambda)^{1/2} \quad (4.25d)$$

$$\operatorname{Im} \rho_{10}^f = \frac{1}{\sqrt{2}} \sin(\phi) \frac{\rho_{00}^f}{\sqrt{\lambda}} (1 - \lambda)^{1/2} \quad (4.25e)$$

$$\operatorname{Im} \rho_{21}^f = \cos(\xi) \frac{\rho_{11}^f}{\sqrt{\mu}} (\mu - \lambda - 1)^{1/2} \quad (4.25f)$$

Applying these relationships and the relationships given by equations (4.5) enable P_I^S to be written terms of atomic collision parameters as

$$P_I^S = \frac{\left\{ K_D - 6 \right\} [3 - 3\mu - 6\lambda - 2\Lambda]}{\left\{ 5K_D + 18 \right\} + \left\{ 54K_D - 1 \right\} \frac{\mu}{2} - \left\{ 7K_D + 6 \right\} \lambda + \left\{ K_D - 6 \right\} 2\Lambda} \quad (4.26)$$

where Λ is given by

$$\Lambda = \sqrt{3} \cos(\chi + \psi) [\lambda(1 - \mu - \lambda)]^{1/2} \quad (4.27a)$$

and K_D is an optical parameter given by

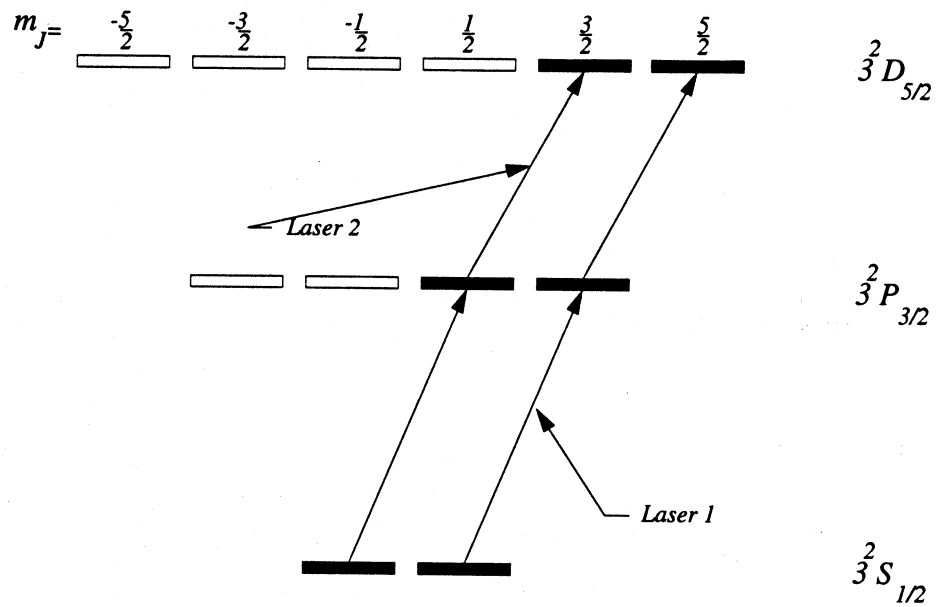


Figure 4.4a: States which have been excited using LHC polarised light

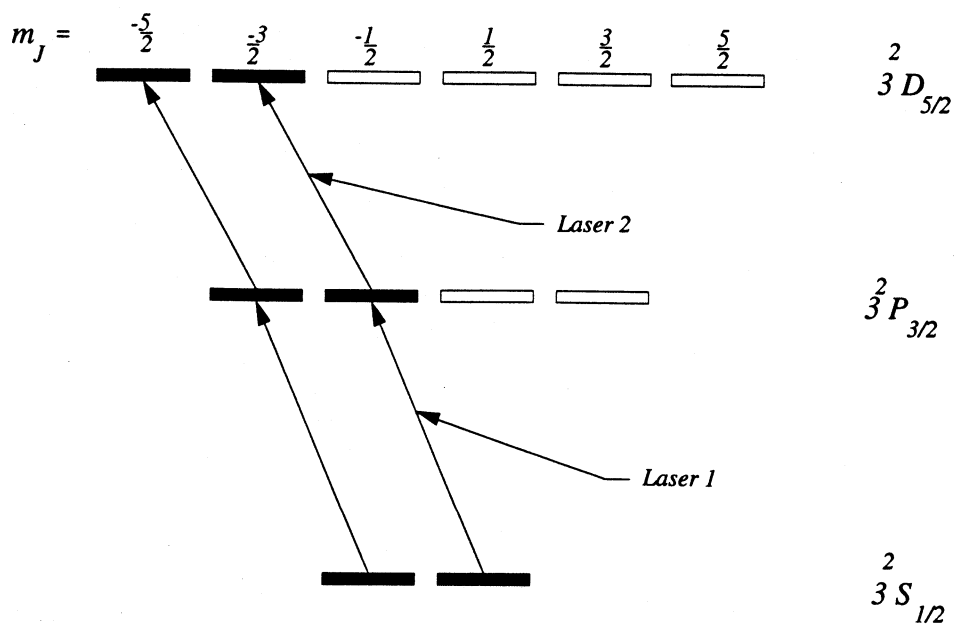


Figure 4.4b States which have been excited using RHC polarised light

$$K_D = \frac{\rho_{3/23/2}^{L_2}}{\rho_{1/21/2}^{L_2}} \quad (4.27b)$$

In a similar derivation P_2^S is given as

$$P_2^S = \frac{\left\{ K_D - 6 \right\} \left[6 \cos \psi [\mu(\mu - \lambda - 1)]^{1/2} + 2\sqrt{3} \cos \chi [\lambda(1 - \lambda)]^{1/2} \right]}{\left\{ \frac{25}{2} K_D + 13 \right\} + \left\{ \frac{101}{2} K_D + 41 \right\} \lambda - \left\{ \frac{29}{2} K_D - 49 \right\} \mu - \left\{ 13 K_D + 2 \right\} \Lambda} \quad (4.28)$$

To obtain the third pseudo Stokes parameter P_3^S , circularly polarised light must be used. The states excited using either left or right hand circularly polarised light is depicted in figure 4.4. The superelastic differential cross section may be found by applying equation (4.14) viz:

$$S(\sigma^+) = \rho_{3/23/2}^{L_2} \rho_{3/23/2}^{f_L} + \rho_{5/25/2}^{L_2} \rho_{5/25/2}^{f_L} \quad (4.29a)$$

$$S(\sigma^-) = \rho_{-3/2-3/2}^{L_2} \rho_{-3/2-3/2}^{f_L} + \rho_{-5/2-5/2}^{L_2} \rho_{-5/2-5/2}^{f_L} \quad (4.29b)$$

The electron collision density matrix elements are in J representation and may be reduced to L representation by applying the results in Table 4.1. Substitution of these results yields

$$S(\sigma^+) = \rho_{3/23/2}^{L_2} \left(\frac{4}{5} \rho_{11}^{f_L} + \frac{1}{5} \rho_{22}^{f_L} \right) + \rho_{5/25/2}^{L_2} \rho_{22}^{f_L} \quad (4.30a)$$

$$S(\sigma^-) = \rho_{-3/2-3/2}^{L_2} \left(\frac{4}{5} \rho_{-1-1}^{f_L} + \frac{1}{5} \rho_{-2-2}^{f_L} \right) + \rho_{-5/2-5/2}^{L_2} \rho_{-2-2}^{f_L} \quad (4.30b)$$

The symmetry of σ excitation gives the following relationships

$$\rho_{-3/2-3/2}^{L_2}(\sigma^-) = \rho_{3/23/2}^{L_2}(\sigma^+) \quad (4.31a)$$

$$\rho_{-5/2-5/2}^{L_2}(\sigma^-) = \rho_{5/25/2}^{L_2}(\sigma^+) \quad (4.31b)$$

Therefore the differential cross sections may be re-expressed as

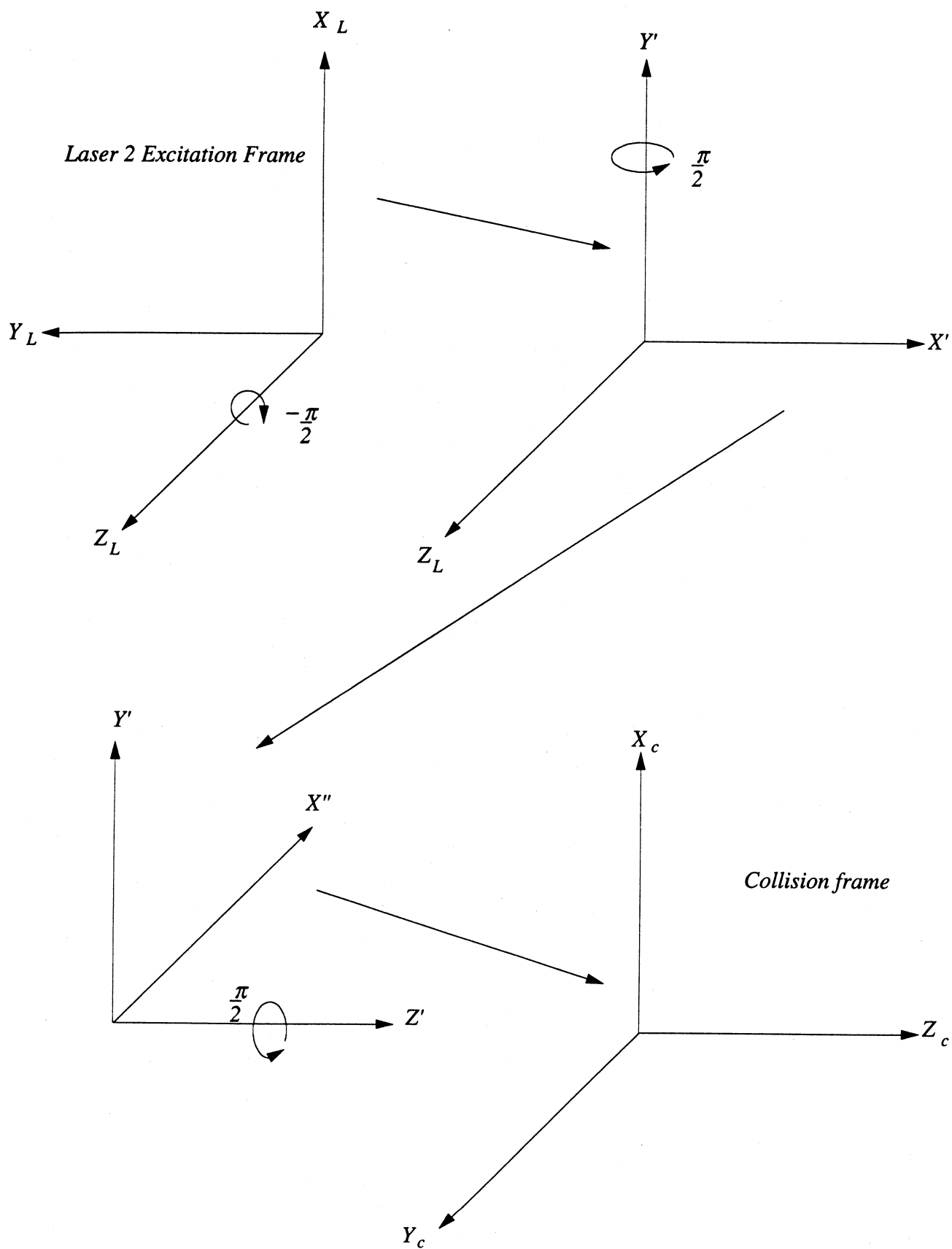


Figure4.5: Rotation of the laser frame defined by laser 2 (circularly polarised laser case) to the collision frame

$$S(\sigma^+) = \rho_{3/23/2}^{L_2} \left(\frac{4}{5} \rho_{11}^{f_L} + \frac{1}{5} \rho_{22}^{f_L} \right) + \rho_{5/25/2}^{L_2} \rho_{22}^{f_L} \quad (4.32a)$$

$$S(\sigma^-) = \rho_{3/23/2}^{L_2} \left(\frac{4}{5} \rho_{-1-1}^{f_L} + \frac{1}{5} \rho_{-2-2}^{f_L} \right) + \rho_{5/25/2}^{L_2} \rho_{-2-2}^{f_L} \quad (4.32b)$$

The electron collision density matrix elements must now be rotated to the collision frame. This is accomplished by employing equation (2.42). The second laser beam propagation direction defines the quantisation axis for the excitation frame and in this case is in the Y_{col} direction. The Euler angles for a rotation of this excitation frame to the collision frame are given by $\omega = (\frac{\pi}{2}, \frac{\pi}{2}, \frac{\pi}{2})$. This rotation is shown in figure 4.5. Applying these Euler angles to the rotation matrix generator given by equation (2.43) and using the submatrix defined by equation (4.19) yields the following rotation matrices

$$D_{m'm}^{2^2}(\omega) = \frac{1}{2} \begin{pmatrix} \frac{1}{2} & -i & -\sqrt{\frac{3}{2}} & i & \frac{1}{2} \\ -i & -1 & 0 & -1 & i \\ -\sqrt{\frac{3}{2}} & 0 & -1 & 0 & -\sqrt{\frac{3}{2}} \\ i & -1 & 0 & -1 & -i \\ \frac{1}{2} & i & -\sqrt{\frac{3}{2}} & -i & \frac{1}{2} \end{pmatrix} \quad (4.33a)$$

$$D_{m'm}^{2^*}(\omega) = \frac{1}{2} \begin{pmatrix} \frac{1}{2} & i & -\sqrt{\frac{3}{2}} & -i & \frac{1}{2} \\ i & -1 & 0 & -1 & -i \\ -\sqrt{\frac{3}{2}} & 0 & -1 & 0 & -\sqrt{\frac{3}{2}} \\ -i & -1 & 0 & -1 & i \\ \frac{1}{2} & -i & -\sqrt{\frac{3}{2}} & i & \frac{1}{2} \end{pmatrix} \quad (4.33b)$$

Using equation (2.42) and the above rotation matrices yields the following transformed density matrix elements

$$\rho_{22}^{f_L} = \frac{1}{4} \rho_{22}^f + \rho_{11}^f + \frac{3}{8} \rho_{00}^f - \text{Im} \rho_{21}^f - \frac{1}{2} \sqrt{\frac{3}{2}} \text{Re} \rho_{20}^f - \sqrt{\frac{3}{2}} \text{Im} \rho_{10}^f \quad (4.34a)$$

$$\rho_{-2-2}^{f_L} = \frac{1}{4} \rho_{22}^f + \rho_{11}^f + \frac{3}{8} \rho_{00}^f + \text{Im} \rho_{21}^f - \frac{1}{2} \sqrt{\frac{3}{2}} \text{Re} \rho_{20}^f + \sqrt{\frac{3}{2}} \text{Im} \rho_{10}^f \quad (4.34b)$$

$$\rho_{11}^{f_L} = \rho_{-1-1}^{f_L} = 0 \quad (4.34c)$$

$$\rho_{00}^{f_L} = \frac{3}{2} \rho_{22}^f + \frac{1}{4} \rho_{00}^f + \sqrt{\frac{3}{2}} \text{Re} \rho_{20}^f \quad (4.35e)$$

The expressions for the rotated elements may now be substituted into equations (4.32) revealing

$$\begin{aligned} S(\sigma^+) = & \rho_{3/23/2}^{L_2} \frac{1}{5} \left(\frac{1}{4} \rho_{22}^f + \rho_{11}^f + \frac{3}{8} \rho_{00}^f - \text{Im} \rho_{21}^f - \frac{1}{2} \sqrt{\frac{3}{2}} \text{Re} \rho_{20}^f - \sqrt{\frac{3}{2}} \text{Im} \rho_{10}^f \right) \\ & + \rho_{5/25/2}^{L_2} \left(\frac{1}{4} \rho_{22}^f + \rho_{11}^f + \frac{3}{8} \rho_{00}^f - \text{Im} \rho_{21}^f - \frac{1}{2} \sqrt{\frac{3}{2}} \text{Re} \rho_{20}^f - \sqrt{\frac{3}{2}} \text{Im} \rho_{10}^f \right) \end{aligned} \quad (4.36a)$$

$$\begin{aligned} S(\sigma^-) = & \rho_{3/23/2}^{L_2} \frac{1}{5} \left(\frac{1}{4} \rho_{22}^f + \rho_{11}^f + \frac{3}{8} \rho_{00}^f + \text{Im} \rho_{21}^f - \frac{1}{2} \sqrt{\frac{3}{2}} \text{Re} \rho_{20}^f + \sqrt{\frac{3}{2}} \text{Im} \rho_{10}^f \right) \\ & + \rho_{5/25/2}^{L_2} \left(\frac{1}{4} \rho_{22}^f + \rho_{11}^f + \frac{3}{8} \rho_{00}^f + \text{Im} \rho_{21}^f - \frac{1}{2} \sqrt{\frac{3}{2}} \text{Re} \rho_{20}^f + \sqrt{\frac{3}{2}} \text{Im} \rho_{10}^f \right) \end{aligned} \quad (4.36b)$$

Applying these superelastic differential cross sections to the definition of P_3^S in combination with equation (4.5a) yields

$$P_3^S = \frac{\left\{ \frac{2}{5} \rho_{3/23/2}^L + 2 \rho_{5/25/2}^L \right\} \left[\text{Im} \rho_{21}^f + \sqrt{\frac{3}{2}} \text{Im} \rho_{10}^f \right]}{\frac{1}{8} \left\{ \frac{2}{5} \rho_{3/23/2}^L + 2 \rho_{5/25/2}^L \right\} \left[\sigma + 2 \rho_{00}^f + 6 \rho_{11}^f - 4 \sqrt{\frac{3}{2}} \text{Im} \rho_{20}^f \right]} \quad (4.37)$$

Applying the relationships given by both equations (4.5) and equations (4.25) to this expression yield

$$P_3^S = \frac{4 \left\{ \cos \xi [\mu(\mu - \lambda - 1)]^{1/2} + \sqrt{3} \sin \phi [\lambda(1 - \lambda)]^{1/2} \right\}}{1 + 2\lambda + 3\mu - 2\Lambda} \quad (4.38)$$

Equations (4.26), (4.28) and (4.38) involve six parameters which are complicated functions of the scattering amplitudes and their relative phases. Because only three pseudo Stokes parameters are measured, not all of the information on the collision system can be obtained, however these measured parameters still provide a new test on current electron-sodium scattering theories. Equations (4.26) and (4.28) also contain an optical term K_D which is related to the laser excitation process. It will be shown in the final section of this chapter that this parameter may be related to the line polarisation of the fluorescence from the D-P transition.

4.5 Derivation of a pseudo Stokes Parameter with Non-Parallel Polarisations

In this section an example derivation of stepwise pseudo Stokes parameter is performed for the case when the two exciting lasers do not have parallel polarisations. Having non-parallel polarisations makes the calculation much more complicated, in that it is not possible to rotate to an excitation frame where the superelastic signal given by equation (4.14) is diagonal. So that normal optical selection rules can be applied, two laser frames are used for each of the lasers polarisation. The use of two laser frames requires two rotations to be performed instead of the usual one rotation such as the proceeding superelastic scattering experiments considered so far. The laser designated laser 1, excites the first transition will be the reference laser for laser frame 1. Similarly laser 2, which is the laser stepwise exciting from the first excited state to the second excited state, is the reference laser for laser frame 2.

The calculation begins initially in laser frame 1 so that optical selection rules allow the populations to be determined in the intermediate state. These populations are then rotated to laser frame 2. This rotation may form horizontal coherences in this frame which will in turn create horizontal coherences in the second excited state. Knowing the populations and coherences formed in the intermediate state in laser frame 2, allows the populations and coherences created by the second laser to be determined by again applying optical selection

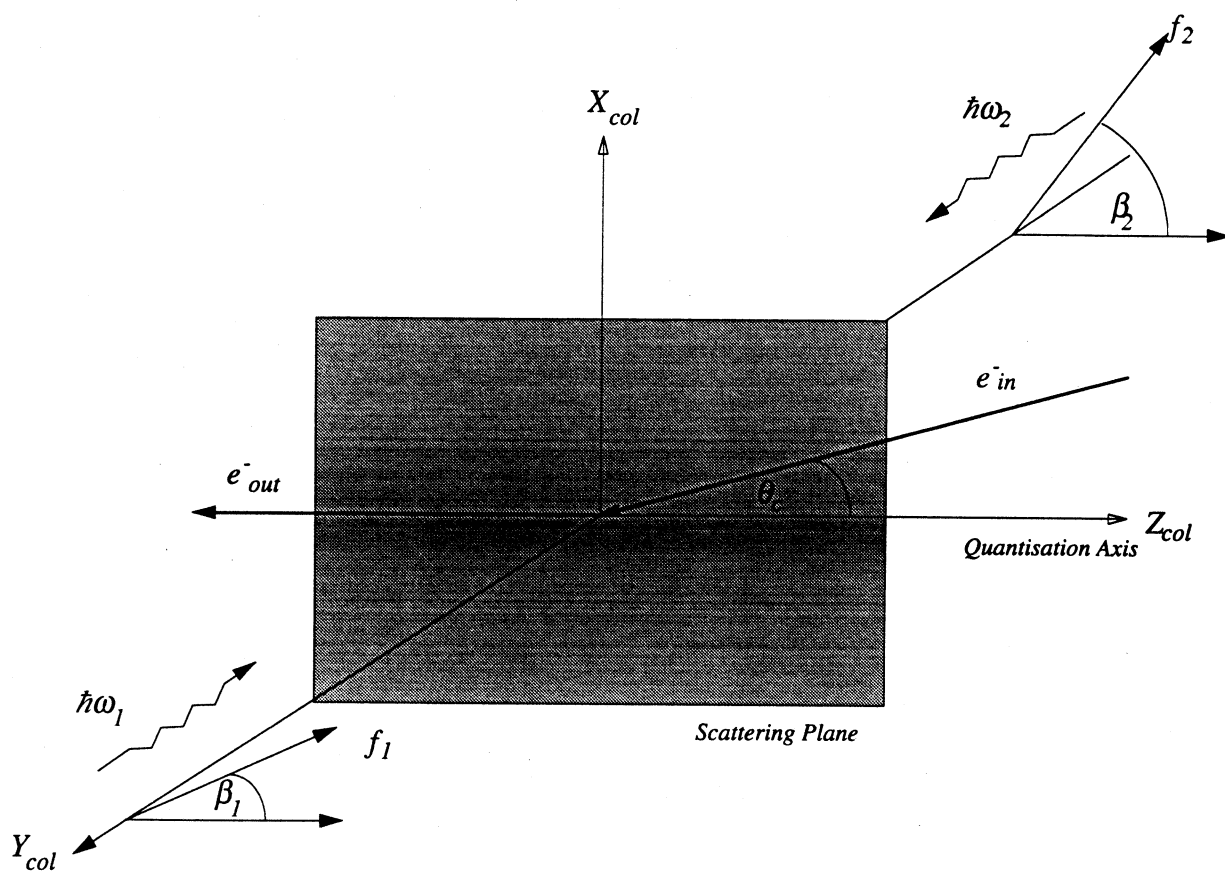


Figure 4.6: The Experimental geometry for Stepwise Experiments with Non-Parallel Laser Polarisations

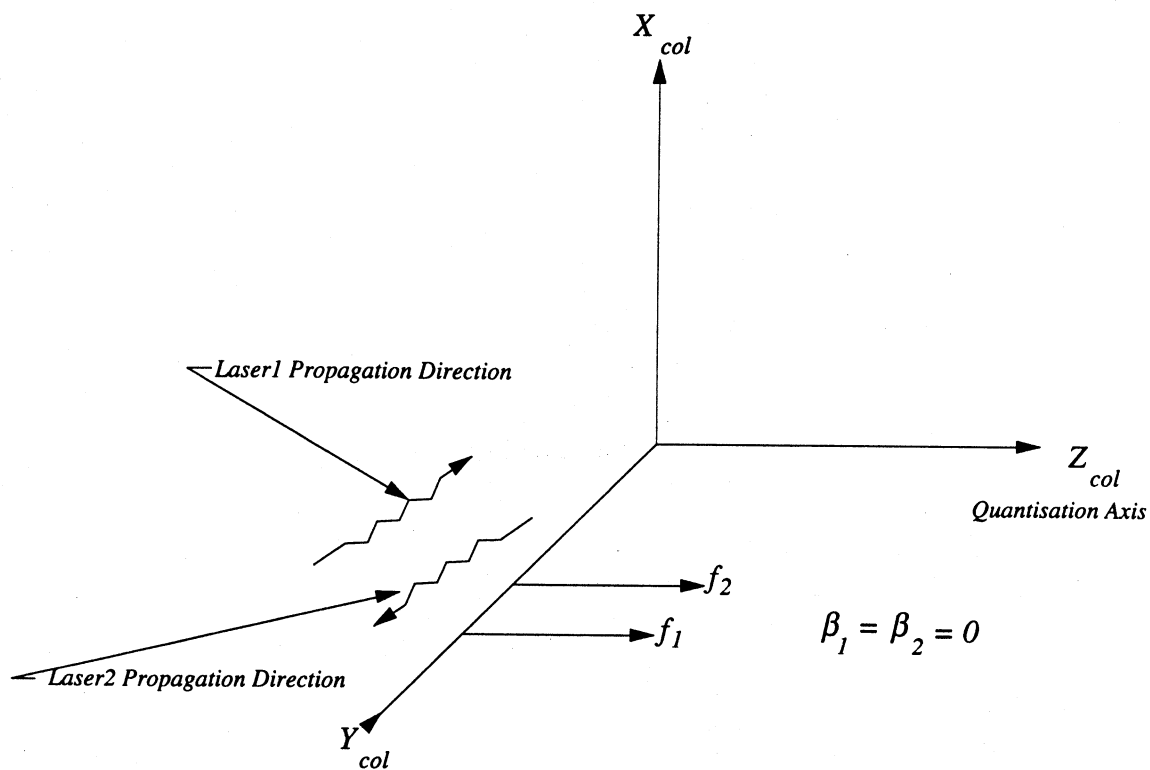


Figure 4.7a: The Geometry for $S_0(0)$

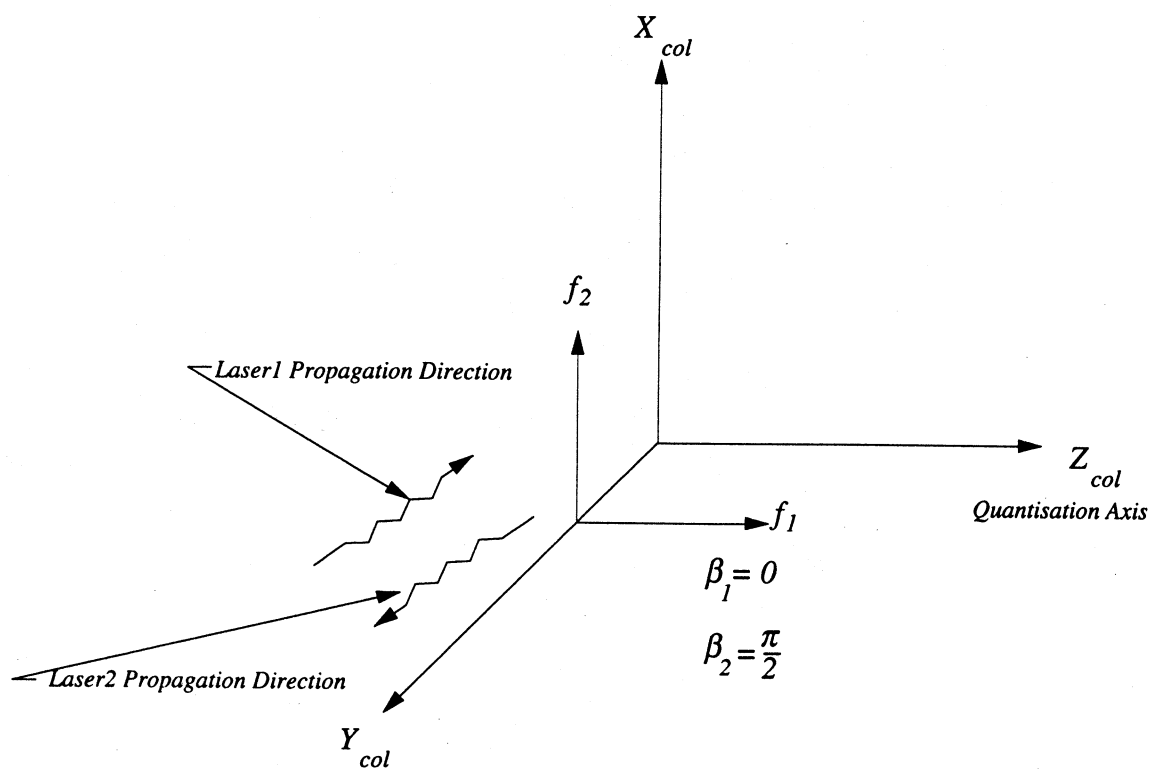


Figure 4.7a: The Geometry for $S_0(90)$

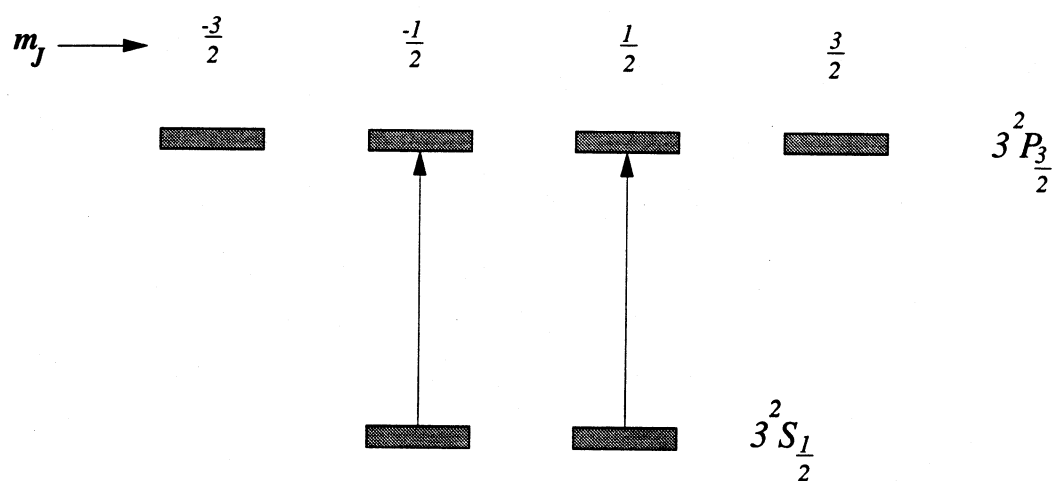


Figure 4.8: Laser excitation of the $J = 3/2$ State Using π Laser Light

rules for π excitation and as such, the superelastic differential cross section may be determined.

In this calculation, both laser 1 and laser 2 will be linearly polarised at angles β_1 and β_2 with respect to the quantisation axis as shown in figure 4.6. Some nomenclature is required in defining the stepwise pseudo Stokes parameters such that $P_{\sigma\beta_1}$ represents a stepwise pseudo Stokes parameter where σ is the type of Stokes parameter ($\sigma=1, 2, 3$) and β_1 defines the polarisation angle of laser 1 with respect to the quantisation axis. In this example calculation P_{10} is derived for the same transitions used in the previous section. P_{10} is defined as

$$P_{10} = \frac{S_0(0) - S_0(90)}{S_0(0) + S_0(90)} \quad (4.39)$$

where $S_{\beta_1}(\beta_2)$ represent the superelastic differential cross section with laser 1 polarised at angle β_1 and laser 2 at angle β_2 . For the case of $S_0(0)$ the geometry depicted in figure 4.7a applies. In this case both laser polarisations are parallel and thus the excitation frames of the two lasers are parallel and the states depicted in figure 4.3 in the previous section are populated. Applying equation (4.14) yields an expression for the differential cross section which is identical to the $S(0)$ case for the linearly polarised case derived in the previous section such that

$$S_0(0) = \rho_{-3/2-3/2}^{L_2(0)}(0)\rho_{-3/2-3/2}^{f_L} + \rho_{-1/2-1/2}^{L_2(0)}(0)\rho_{-1/2-1/2}^{f_L} + \rho_{1/21/2}^{L_2(0)}(0)\rho_{1/21/2}^{f_L} + \rho_{3/23/2}^{L_2(0)}(0)\rho_{3/23/2}^{f_L} \quad (4.40)$$

where $\rho_{mm}^{L_2(\beta_2)}(\beta_1)$ are populations formed with the lasers polarised at the angles indicated by β_1 and β_2 . For the case of $S_0(90)$ the geometry shown in figure 4.7b applies. In the frame defined by laser 1, the states depicted in figure 4.8 are populated. To determine the population in the D state, the states populated by laser 1 are rotated to laser 2's excitation frame. This rotation is carried out in the usual manner by applying the rotation operators defined by equation (2.42) and the Euler angles for the rotation are given by $(0, \frac{\pi}{2}, 0)$ where β

$= \beta_2 - \beta_1$. The rotation matrices may be generated by applying equations (2.43) and (2.44).

Thus for $J=\frac{3}{2}$ the rotation matrix $D_{m'm}^J(\omega)$ is given by

$$D_{m'm}^{3/2}(\omega) = \begin{pmatrix} \cos^3 \frac{\beta}{2} & \sqrt{3} \cos^2 \frac{\beta}{2} \sin \frac{\beta}{2} & \sqrt{3} \cos \frac{\beta}{2} \sin^2 \frac{\beta}{2} & \sin^3 \frac{\beta}{2} \\ -\sqrt{3} \cos^2 \frac{\beta}{2} \sin \frac{\beta}{2} & \cos^3 \frac{\beta}{2} - 2 \cos \frac{\beta}{2} \sin^2 \frac{\beta}{2} & 2 \cos^2 \frac{\beta}{2} \sin \frac{\beta}{2} - \sin^3 \frac{\beta}{2} & \sqrt{3} \cos \frac{\beta}{2} \sin^2 \frac{\beta}{2} \\ \sqrt{3} \cos \frac{\beta}{2} \sin^2 \frac{\beta}{2} & \sin^3 \frac{\beta}{2} - 2 \cos^2 \frac{\beta}{2} \sin \frac{\beta}{2} & \cos^3 \frac{\beta}{2} - 2 \cos \frac{\beta}{2} \sin^2 \frac{\beta}{2} & \sqrt{3} \cos^2 \frac{\beta}{2} \sin \frac{\beta}{2} \\ -\sin^3 \frac{\beta}{2} & \sqrt{3} \cos^2 \frac{\beta}{2} \sin \frac{\beta}{2} & -\sqrt{3} \cos \frac{\beta}{2} \sin^2 \frac{\beta}{2} & \cos^3 \frac{\beta}{2} \end{pmatrix} \quad (4.41)$$

The rotation populates the $m_J = \pm \frac{3}{2}$ and $\pm \frac{1}{2}$ substates and creates the following horizontal coherences $\rho_{-3/2, 1/2}^{f_L}$, $\rho_{3/2, -1/2}^{f_L}$, $\rho_{-1/2, 3/2}^{f_L}$ and $\rho_{1/2, -3/2}^{f_L}$. Using π excitation, populations and coherences with identical m_J quantum numbers are formed in the D state. This has the implication that the expression for the superelastic differential cross section $S_0(0)$, is no longer diagonal in the m_J quantum number and after applying equation (4.14) is given by

$$S_0(90) = \rho_{-3/2, -3/2}^{L_2(90)}(0) \rho_{-3/2, -3/2}^{f_L} + \rho_{-1/2, -1/2}^{L_2(90)}(0) \rho_{-1/2, -1/2}^{f_L} + \rho_{1/2, 1/2}^{L_2(90)}(0) \rho_{1/2, 1/2}^{f_L} + \rho_{3/2, 3/2}^{L_2(90)}(0) \rho_{3/2, 3/2}^{f_L} \\ + \rho_{-3/2, 1/2}^{L_2(90)}(0) \rho_{-3/2, 1/2}^{f_L} + \rho_{3/2, -1/2}^{L_2(90)}(0) \rho_{3/2, -1/2}^{f_L} + \rho_{1/2, -3/2}^{L_2(90)}(0) \rho_{1/2, -3/2}^{f_L} + \rho_{-1/2, 3/2}^{L_2(90)}(0) \rho_{-1/2, 3/2}^{f_L} \quad (4.42)$$

The electron collision density matrix elements in equations (4.40) and (4.42) are in J representation and may be reduced to L representation by applying, for the case of $S_0(0)$ the results of Table 4.1. For the case of $S_0(90)$ the following reduction formula must be applied (Sobelman 1979)

$$\rho_{m_J m_{J'}}^J = \sum_{m_L m_{L'}} (2J+1) (-1)^{2L-2S-m_J-m_{J'}} \begin{pmatrix} S & L & J \\ m_J - m_L & m_L & -m_J \end{pmatrix} \begin{pmatrix} S & L & J \\ m_{J'} - m_{L'} & m_{L'} & -m_{J'} \end{pmatrix} \rho_{L m_L L m_{L'}}^e \quad (4.43)$$

The sum in equation (4.43) involved the calculation of many Wigner 3j symbols which is a laborious task and was accomplished using the symbolic maths program Maple. The Maple

code initially calculated the Wigner 3j symbols by calculating Clesbch-Gordan coefficients which are easily computed. The Wigner 3j symbols were converted to Clebsch-Gordan coefficients using following relationship (Varshalovich *et al.* 1988)

$$\begin{pmatrix} j_1 & j_2 & j_3 \\ m_1 & m_2 & m_3 \end{pmatrix} = (-1)^{j_3+m_3+2j_1} \frac{1}{\sqrt{2j_3+1}} C_{j_1-m_1 j_2-m_2}^{j_3 m_3} \quad (4.45)$$

The Clebsch-Gordan coefficients were determined using Wigner's formula given by (Varshalovich *et al.* 1988)

$$C_{\alpha\beta}^{c\gamma} = \delta_{\gamma, \alpha+\beta} \Delta(a, b, c) \left(\frac{(c+\gamma)!(c-\gamma)!(2c+1)}{(a+\alpha)!(a-\alpha)!(b+\beta)!(b-\beta)!} \right)^{1/2} \sum_z \left(\frac{(-1)^{b+\beta+z}(c+b+\alpha-z)!(a-\alpha+z)!}{z!(c-a+b-z)!(c+\gamma z)!(a-b-\gamma+z)!} \right) \quad (4.46)$$

where δ is the Kronecker delta and

$$\Delta(a, b, c) = \left(\frac{(a+b-c)!(a-b+c)!(-a+b+c)!}{(a+b+c+1)!} \right)^{1/2} \quad (4.47)$$

Substituting the results from Table 4.1 and the results derived by applying equation (4.43) into the expressions for the superelastic differential cross sections and rotating the electron collision density matrix elements to the collision frame yield

$$S_0(0) = \rho_{-3/2-3/2}^{L_2(0)}(0) \left(\frac{4}{5}\rho_{11}^f + \frac{1}{5}\rho_{22}^f \right) + \rho_{-1/2-1/2}^{L_2(0)}(0) \left(\frac{3}{5}\rho_{00}^f + \frac{2}{5}\rho_{11}^f \right) \\ + \rho_{1/2 1/2}^{L_2(0)}(0) \left(\frac{3}{5}\rho_{00}^f + \frac{2}{5}\rho_{11}^f \right) + \rho_{3/2 3/2}^{L_2(0)}(0) \left(\frac{4}{5}\rho_{11}^f + \frac{1}{5}\rho_{22}^f \right) \quad (4.48a)$$

$$S_0(90) =$$

$$\rho_{-3/2-3/2}^{L_2(90)}(0) \left(\frac{1}{20}\rho_{22}^f + \frac{4}{5}\rho_{11}^f + \frac{3}{40}\rho_{00}^f + \frac{\sqrt{6}}{40}\rho_{20}^f + \frac{\sqrt{6}}{40}\rho_{02}^f + \frac{1}{5}\rho_{21}^f + \frac{1}{5}\rho_{12}^f + \frac{\sqrt{6}}{10}\rho_{10}^f + \frac{\sqrt{6}}{10}\rho_{01}^f \right)$$

$$\begin{aligned}
& + \rho_{-1/2-1/2}^{L_2(90)}(0) \left(\frac{9}{10} \rho_{22}^f + \frac{2}{5} \rho_{11}^f + \frac{3}{20} \rho_{00}^f - \frac{3\sqrt{6}}{20} \rho_{02}^f - \frac{3\sqrt{6}}{20} \rho_{20}^f + \frac{\sqrt{6}}{5} \left(-\frac{1}{2} \rho_{01}^f + \frac{1}{2} \rho_{21}^f \right) + \frac{\sqrt{6}}{5} \left(-\frac{1}{2} \rho_{10}^f + \frac{1}{2} \rho_{12}^f \right) \right) \\
& + \rho_{1/21/2}^{L_2(90)}(0) \left(\frac{9}{10} \rho_{22}^f + \frac{2}{5} \rho_{11}^f + \frac{3}{20} \rho_{00}^f - \frac{3\sqrt{6}}{20} \rho_{02}^f - \frac{3\sqrt{6}}{20} \rho_{20}^f + \frac{\sqrt{6}}{5} \left(\frac{1}{2} \rho_{01}^f - \frac{1}{2} \rho_{21}^f \right) + \frac{\sqrt{6}}{5} \left(\frac{1}{2} \rho_{10}^f - \frac{1}{2} \rho_{12}^f \right) \right) \\
& + \rho_{3/23/2}^{L_2(90)}(0) \left(\frac{1}{20} \rho_{22}^f + \frac{4}{5} \rho_{11}^f + \frac{3}{40} \rho_{00}^f + \frac{\sqrt{6}}{40} \rho_{20}^f + \frac{\sqrt{6}}{40} \rho_{02}^f - \frac{1}{5} \rho_{21}^f - \frac{1}{5} \rho_{12}^f - \frac{\sqrt{6}}{10} \rho_{10}^f - \frac{\sqrt{6}}{10} \rho_{10}^f \right) \\
& + \rho_{-3/21/2}^{L_2(90)}(0) \\
& \left(-\frac{2\sqrt{18}}{15} \rho_{11}^f + \frac{\sqrt{12}}{5} \left(-\frac{1}{2} \rho_{10}^f + \frac{\sqrt{6}}{2} \rho_{12}^f \right) + \frac{\sqrt{18}}{15} \left(-\frac{1}{2} \rho_{21}^f - \frac{\sqrt{6}}{4} \rho_{01}^f \right) + \frac{\sqrt{12}}{10} \left(\frac{\sqrt{6}}{4} \rho_{22}^f + \frac{3}{4} \rho_{02}^f - \frac{1}{4} \rho_{20}^f - \frac{\sqrt{6}}{8} \rho_{00}^f \right) \right) \\
& + \rho_{3/2-1/2}^{L_2(90)}(0) \\
& \left(-\frac{2\sqrt{18}}{15} \rho_{11}^f + \frac{\sqrt{12}}{5} \left(-\frac{1}{2} \rho_{10}^f + \frac{\sqrt{6}}{2} \rho_{12}^f \right) + \frac{\sqrt{18}}{15} \left(-\frac{1}{2} \rho_{21}^f - \frac{\sqrt{6}}{4} \rho_{01}^f \right) + \frac{\sqrt{12}}{10} \left(\frac{\sqrt{6}}{4} \rho_{22}^f + \frac{3}{4} \rho_{02}^f - \frac{1}{4} \rho_{20}^f - \frac{\sqrt{6}}{8} \rho_{00}^f \right) \right) \\
& + \rho_{1/2-3/2}^{L_2(90)}(0) \\
& \left(-\frac{2\sqrt{18}}{15} \rho_{11}^f + \frac{\sqrt{12}}{5} \left(-\frac{1}{2} \rho_{01}^f + \frac{\sqrt{6}}{2} \rho_{21}^f \right) + \frac{\sqrt{18}}{15} \left(-\frac{1}{2} \rho_{12}^f - \frac{\sqrt{6}}{4} \rho_{10}^f \right) + \frac{\sqrt{12}}{10} \left(\frac{\sqrt{6}}{4} \rho_{22}^f + \frac{3}{4} \rho_{02}^f - \frac{1}{4} \rho_{20}^f - \frac{\sqrt{6}}{8} \rho_{00}^f \right) \right) \\
& + \rho_{-1/23/2}^{L_2(90)}(0) \\
& \left(-\frac{2\sqrt{18}}{15} \rho_{11}^f + \frac{\sqrt{12}}{5} \left(\frac{1}{2} \rho_{01}^f - \frac{\sqrt{6}}{2} \rho_{21}^f \right) + \frac{\sqrt{18}}{15} \left(\frac{1}{2} \rho_{12}^f + \frac{\sqrt{6}}{4} \rho_{10}^f \right) + \frac{\sqrt{12}}{10} \left(\frac{\sqrt{6}}{4} \rho_{22}^f + \frac{3}{4} \rho_{02}^f - \frac{1}{4} \rho_{20}^f - \frac{\sqrt{6}}{8} \rho_{00}^f \right) \right)
\end{aligned} \tag{4.48b}$$

These expressions may be reduced by applying the symmetry relationship given by equation (4.17) and manipulation which yields

$$S_0(0) = \rho_{3/23/2}^{L_2(0)}(0) \left(\frac{2}{5} \rho_{22}^f + \frac{8}{5} \rho_{11}^f \right) + \rho_{1/21/2}^{L_2(0)}(0) \left(\frac{6}{5} \rho_{00}^f + \frac{4}{5} \rho_{11}^f \right) \tag{4.49a}$$

$$\begin{aligned}
S_0(90) = & \rho_{3/23/2}^{L_2(90)}(0) \left(\frac{2}{20} \rho_{22}^f + \frac{8}{5} \rho_{11}^f + \frac{6}{40} \rho_{00}^f + \frac{\sqrt{6}}{10} \text{Re} \rho_{20}^f \right) + \rho_{1/21/2}^{L_2(90)}(0) \left(\frac{18}{10} \rho_{22}^f + \frac{4}{5} \rho_{11}^f + \frac{6}{20} \rho_{00}^f - \frac{3\sqrt{6}}{5} \text{Re} \rho_{20}^f \right) \\
& - \text{Re} \rho_{3/2-1/2}^{L_2(90)}(0) \left(\frac{8\sqrt{18}}{15} \rho_{11}^f + \frac{\sqrt{18}}{5} \left(\rho_{22}^f - \frac{1}{2} \rho_{00}^f \right) + \frac{4\sqrt{3}}{10} \text{Re} \rho_{20}^f \right) - \frac{8\sqrt{3}}{20} \text{Im} \rho_{3/2-1/2}^{L_2(90)}(0) \text{Im} \rho_{20}^f
\end{aligned} \tag{4.49b}$$

Substitution of these superelastic differential cross sections into the definitions of the stepwise pseudo Stokes parameter P_{10} and applying the relationships for the electron collision density matrix elements used in the previous section reveals

$$\begin{aligned}
P_{10} = & \frac{1}{2} \left\{ \frac{2}{5} \beta_0(0) - \frac{1}{10} \beta_0(90) - \frac{9}{5} \alpha_0(90) - \frac{\sqrt{18}}{5} \text{Re } \gamma_0(90) \right\} + \left\{ \frac{6}{5} \beta_0(0) + \frac{4}{5} \alpha_0(0) - \frac{3}{2} \beta_0(90) + \alpha_0(90) + \frac{11\sqrt{18}}{10} \text{Re } \gamma_0(90) \right\} \frac{\mu}{2} \\
& + \left\{ -\frac{1}{5} \beta_0(0) + \frac{6}{5} \alpha_0(0) - \frac{1}{10} \beta_0(90) + \frac{3}{5} \alpha_0(90) + \frac{\sqrt{18}}{5} \text{Re } \gamma_0(90) \right\} \lambda + \left\{ -\frac{1}{10} \beta_0(90) + \frac{3}{5} \alpha_0(90) - \frac{\sqrt{2}}{5} \text{Re } \gamma_0(90) \right\} \Lambda \\
& - \frac{4}{5} \sqrt{\frac{3}{2}} \text{Im } \gamma_0(90) \Theta \\
& \frac{1}{2} \left\{ \frac{2}{5} \beta_0(0) + \frac{1}{10} \beta_0(90) + \frac{9}{5} \alpha_0(90) + \frac{\sqrt{18}}{5} \text{Re } \gamma_0(90) \right\} + \left\{ \frac{6}{5} \beta_0(0) + \frac{4}{5} \alpha_0(0) + \frac{3}{2} \beta_0(90) - \alpha_0(90) - \frac{11\sqrt{18}}{10} \text{Re } \gamma_0(90) \right\} \frac{\mu}{2} \\
& + \left\{ -\frac{1}{5} \beta_0(0) + \frac{6}{5} \alpha_0(0) + \frac{1}{10} \beta_0(90) - \frac{3}{5} \alpha_0(90) - \frac{\sqrt{18}}{5} \text{Re } \gamma_0(90) \right\} \lambda + \left\{ \frac{1}{10} \beta_0(90) - \frac{3}{5} \alpha_0(90) + \frac{\sqrt{2}}{5} \text{Re } \gamma_0(90) \right\} \Lambda \\
& + \frac{4}{5} \sqrt{\frac{3}{2}} \text{Im } \gamma_0(90) \Theta
\end{aligned} \tag{4.50}$$

where

$$\beta_0(0) = \rho_{3/23/2}^{L_2(0)}(0) \tag{4.51a}$$

$$\alpha_0(0) = \rho_{1/21/2}^{L_2(0)}(0) \tag{4.51b}$$

$$\beta_0(90) = \rho_{3/23/2}^{L_2(90)}(0) \tag{4.51c}$$

$$\alpha_0(90) = \rho_{1/21/2}^{L_2(90)}(0) \tag{4.51d}$$

$$\gamma_0(90) = \rho_{3/2-1/2}^{L_2(90)}(0) \tag{4.51e}$$

and

$$\Theta = \frac{1}{\sqrt{2}} \sin(\chi + \psi) \frac{\rho_{00}^f}{\sqrt{\lambda}} (1 - \mu - \lambda)^{1/2} \tag{4.52}$$

Equation (4.50) yields a further measurable quantity and it is possible to obtain more of these stepwise pseudo Stokes parameters by applying other combinations of polarisations. Since this is a preliminary investigation only the stepwise pseudo Stokes parameters for the parallel polarisation case were measured. Equation (4.50) contain terms that are related to the laser excitation process and a method of determining them experimentally will have to be developed.

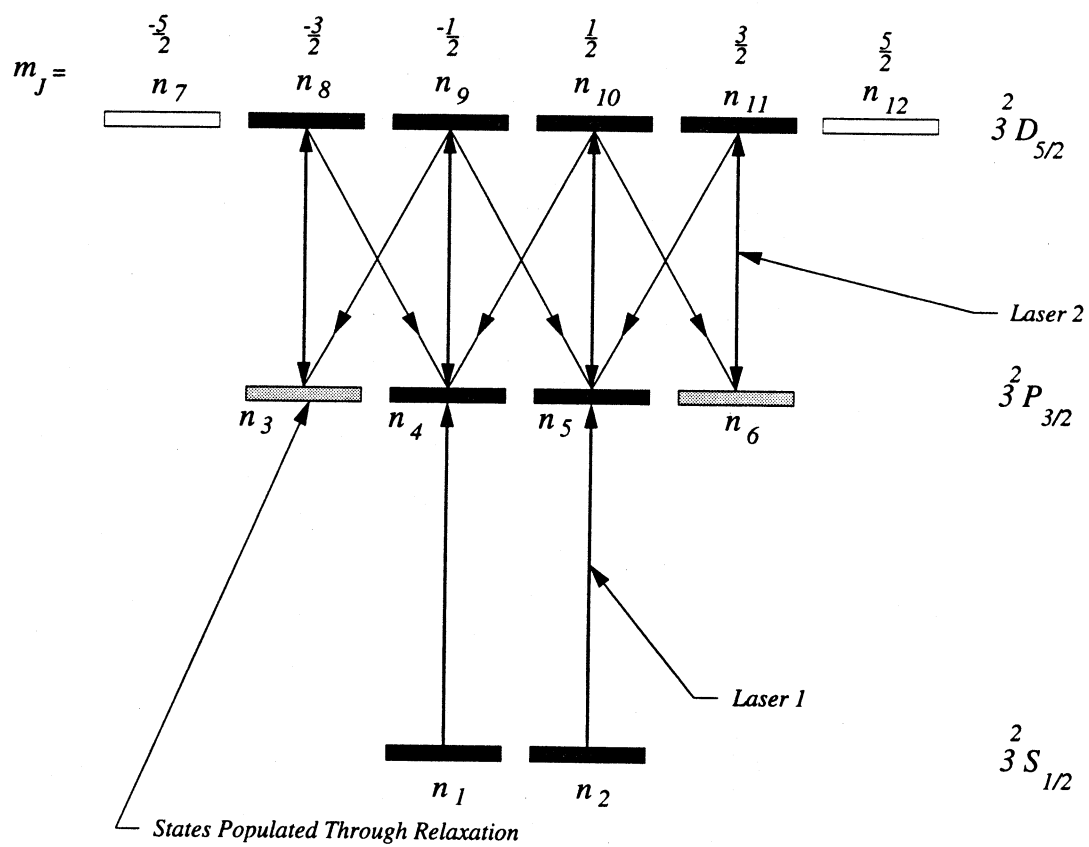


Figure 4.9: The Energy levels of Sodium in J representation

4.6 Theoretical Treatment of the Stepwise Laser Excitation Process

In this section the laser excitation process is treated using rate equations. It is expected that this approach be reasonably accurate as no coherences are formed in the D state for the parallel polarisation case treated in J representation. Only the linear case is treated as the pseudo Stokes parameter P_3^S is independent of the laser excited populations. The rate equation model is tested by comparison with a line polarisation measurement of the fluorescence from the D-P transition scattered perpendicular to the plane formed by the second laser's propagation direction and the polarisation vector. The excitation scheme is depicted in figure 4.9 for linearly polarised excitation and the rate equations for this system is given by

$$\dot{n}_1 = -B_{14}W_1(n_1 - n_4) + \Gamma_{31}n_3 + \Gamma_{41}n_4 + \Gamma_{51}n_5 \quad (4.53)$$

$$\dot{n}_2 = -B_{25}W_1(n_2 - n_5) + \Gamma_{42}n_4 + \Gamma_{52}n_5 + \Gamma_{62}n_6 \quad (4.54)$$

$$\dot{n}_3 = -B_{38}W_2(n_3 - n_8) + \Gamma_{83}n_8 + \Gamma_{93}n_9 - \Gamma_{31}n_3 \quad (4.55)$$

$$\begin{aligned} \dot{n}_4 = & -B_{49}W_2(n_4 - n_9) + B_{14}W_1(n_1 - n_4) + \Gamma_{84}n_8 + \Gamma_{94}n_9 + \Gamma_{104}n_{10} \\ & - (\Gamma_{41} + \Gamma_{41})n_4 \end{aligned} \quad (4.56)$$

$$\begin{aligned} \dot{n}_5 = & -B_{510}W_2(n_5 - n_{10}) + B_{25}W_1(n_2 - n_5) + \Gamma_{95}n_9 + \Gamma_{105}n_{10} + \Gamma_{115}n_{11} \\ & - (\Gamma_{51} + \Gamma_{52})n_5 \end{aligned} \quad (4.57)$$

$$\dot{n}_6 = -B_{611}W_2(n_6 - n_{11}) + \Gamma_{116}n_{11} + \Gamma_{106}n_{10} - \Gamma_{62}n_6 \quad (4.58)$$

$$\dot{n}_8 = B_{83}W_2(n_3 - n_8) - (\Gamma_{83} + \Gamma_{84})n_8 \quad (4.59)$$

$$\dot{n}_9 = B_{94}W_2(n_4 - n_9) - (\Gamma_{93} + \Gamma_{94} + \Gamma_{95})n_9 \quad (4.60)$$

$$\dot{n}_{10} = B_{105}W_2(n_5 - n_{10}) - (\Gamma_{104} + \Gamma_{105} + \Gamma_{106})n_{10} \quad (4.61)$$

$$\dot{n}_{11} = B_{116}W_2(n_6 - n_{11}) - (\Gamma_{115} + \Gamma_{116})n_{11} \quad (4.62)$$

where the labelling scheme of figure 4.9 has been used and n_i is the population of the i th substate, which is labelled according to figure 4.9. W_i is the energy density of the i th laser which has the units of energy per unit volume per unit frequency interval. Γ_{ij} is the spontaneous relaxation rate from substate i to substate j and is identical to the Einstein A coefficient. The individual relaxation rates for each transition has been calculated using the

Table 4.2: Relaxation Rates of the Excited Substates

(Expressed as a fraction of the various Total Relaxation Rates)

$3^2P_{3/2} \rightarrow 3^2S_{1/2}$	
$\tau = 16ns$	
Γ_{31}	$\frac{1}{3}$
Γ_{41}	$\frac{2}{3}$
Γ_{51}	$\frac{1}{3}$
Γ_{42}	$\frac{1}{3}$
Γ_{52}	$\frac{2}{3}$
Γ_{62}	$\frac{1}{3}$
$3^2D_{5/2} \rightarrow 3^2P_{3/2}$	
$\tau = 19ns$	
Γ_{83}	$\frac{2}{5}$
Γ_{84}	$\frac{3}{5}$
Γ_{93}	$\frac{1}{10}$
Γ_{94}	$\frac{3}{5}$
Γ_{95}	$\frac{3}{10}$
Γ_{104}	$\frac{3}{10}$
Γ_{105}	$\frac{3}{5}$
Γ_{106}	$\frac{1}{10}$
Γ_{115}	$\frac{3}{5}$
Γ_{116}	$\frac{2}{5}$

methods given in section 3.4 and are expressed as functions of the total relaxation rates in Table 4.2. $B_{ij} = B_{ji}$ is the Einstein B coefficient for the transitions between substates i and j and may be related to the Einstein A coefficient by (Hermann *et al.* 1977)

$$B_{ij} = \frac{3\lambda_{ij}^3}{8\pi h} A_{ij} \quad (4.63)$$

The populations are also normalised according to the condition

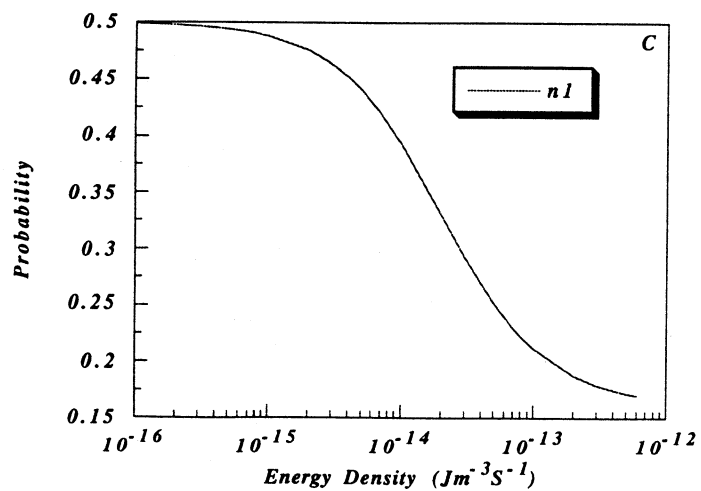
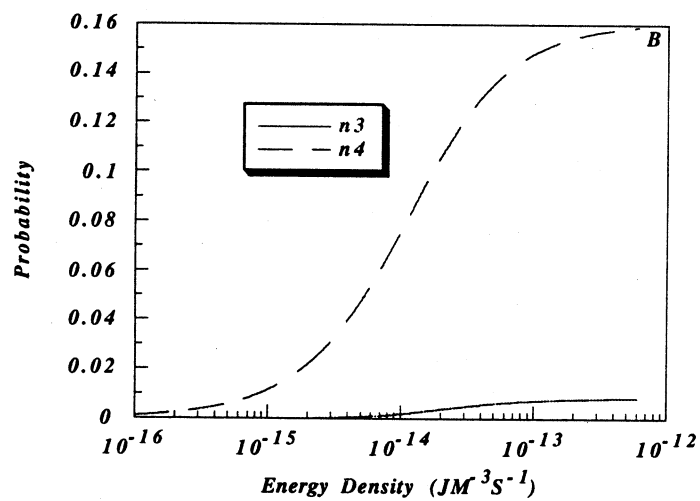
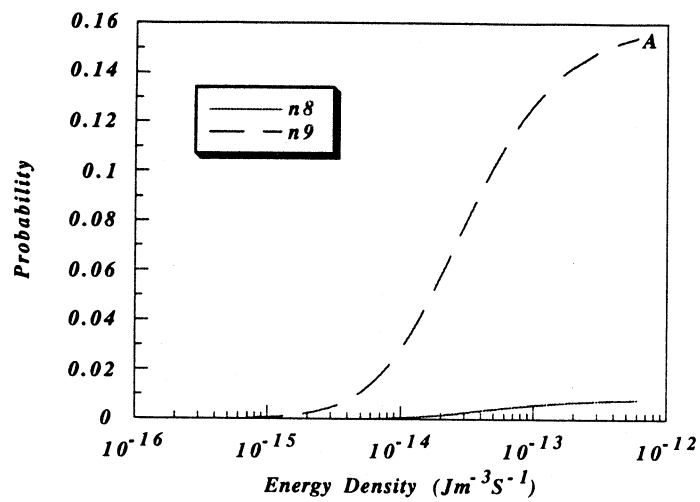
$$\sum_i n_i = 1 \quad (4.64)$$

It is possible to obtain a steady state solution by setting the left hand side of equations (4.53)-(4.62) to zero which yields the following solutions

$$n_1(\infty) = n_2(\infty) = \frac{\frac{1}{2} \left(126A_1B_2^2A_2 + 225A_1A_2^2B_2 + 750A_1^2B_2A_2 + 72B_2^2A_2B_1 + 120B_1B_2^2A_1 + 120B_2A_2^2B_1 + 500B_1A_2^2A_1 + 180A_1^2B_2^2 \right) + 500B_1B_2A_1A_2 + 750A_1^2A_2^2}{180A_1^2B_2^2 + 750A_1^2A_2^2 + 126A_1B_2^2A_2 + 225A_1A_2^2B_2 + 750A_1^2B_2A_2 + 240B_2^2A_2B_1 + 360B_1B_2^2A_1 + 1300B_1B_2A_1A_2 + 270B_2A_2^2B_1 + 1000B_1A_2^2A_1} \quad (4.65)$$

$$n_3(\infty) = n_6(\infty) = \frac{3(B_2\{2B_2 + 5A_2\}A_2B_1)}{180A_1^2B_2^2 + 750A_1^2A_2^2 + 126A_1B_2^2A_2 + 225A_1A_2^2B_2 + 750A_1^2B_2A_2 + 240B_2^2A_2B_1 + 360B_1B_2^2A_1 + 1300B_1B_2A_1A_2 + 270B_2A_2^2B_1 + 1000B_1A_2^2A_1} \quad (4.66)$$

$$n_4(\infty) = n_5(\infty) = \frac{2((3B_2 + 5A_2)\{6B_2A_2 + 10A_1B_2 + 25A_1A_2\}B_1)}{180A_1^2B_2^2 + 750A_1^2A_2^2 + 126A_1B_2^2A_2 + 225A_1A_2^2B_2 + 750A_1^2B_2A_2 + 240B_2^2A_2B_1 + 360B_1B_2^2A_1 + 1300B_1B_2A_1A_2 + 270B_2A_2^2B_1 + 1000B_1A_2^2A_1} \quad (4.67)$$



Graph 4.1: Populations Vs Energy Density

$$n_8(\infty) = n_{11}(\infty) = \frac{6(B_2^2 A_2 B_1)}{180A_1^2 B_2^2 + 750A_1^2 A_2^2 + 126A_1 B_2^2 A_2 + 225A_1 A_2^2 B_2 + 750A_1^2 B_2 A_2 + 240B_2^2 A_2 B_1 + 360B_1 B_2^2 A_1 + 1300B_1 B_2 A_1 A_2 + 270B_2 A_2^2 B_1 + 1000B_1 A_2^2 A_1} \quad (4.68)$$

$$n_9(\infty) = n_{10}(\infty) = \frac{6(B_2 \{6B_2 A_2 + 10A_1 B_2 + 25A_1 A_2\} B_1)}{180A_1^2 B_2^2 + 750A_1^2 A_2^2 + 126A_1 B_2^2 A_2 + 225A_1 A_2^2 B_2 + 750A_1^2 B_2 A_2 + 240B_2^2 A_2 B_1 + 360B_1 B_2^2 A_1 + 1300B_1 B_2 A_1 A_2 + 270B_2 A_2^2 B_1 + 1000B_1 A_2^2 A_1} \quad (4.69)$$

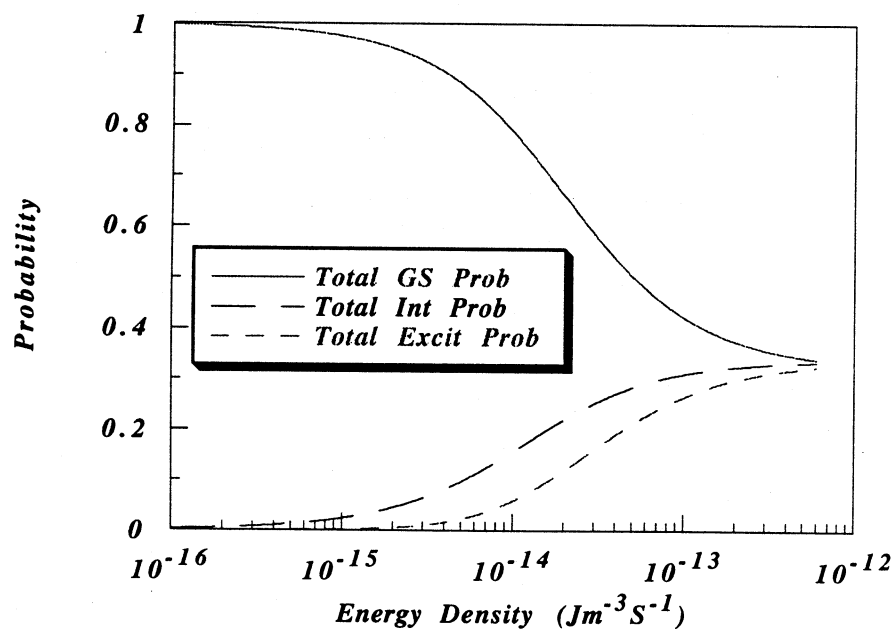
where

$$A_i = \Gamma_i \quad (4.70a)$$

$$B_i = \frac{3\lambda_i^3}{8\pi h} \Gamma_i W_i \quad (4.70b)$$

Γ_i is the total relaxation rate from the i th sublevel = $\frac{1}{\text{lifetime}}$. The scheme considered here has a wavelength of 589.160 nm for the $3^2S_{1/2} \rightarrow 3^2P_{3/2}$ and the lifetime of the $3^2P_{3/2}$ state is 16ns. The wavelength corresponding to the $3^2P_{3/2} \rightarrow 3^2D_{5/2}$ transition is 819.711 nm and the lifetime of the $3^2D_{5/2}$ state is 19ns.

Graphs 4.1a,b,c show the probability for substate population versus the energy density, W , at steady state which were obtained using equations (4.65)-(4.69). Both lasers have the same energy density. Graph 4.1C shows the n_1 probability as a function of the energy density. By symmetry n_2 has the identical probability and is not shown. At very low laser powers these probabilities remain almost constant until $10^{-15} \text{ Jm}^{-3}\text{s}^{-1}$, where the probability drops dramatically as the power is increased. This fast drop in probability slows at approximately



Graph 4.2: Total Sublevel Populations Vs Energy Density

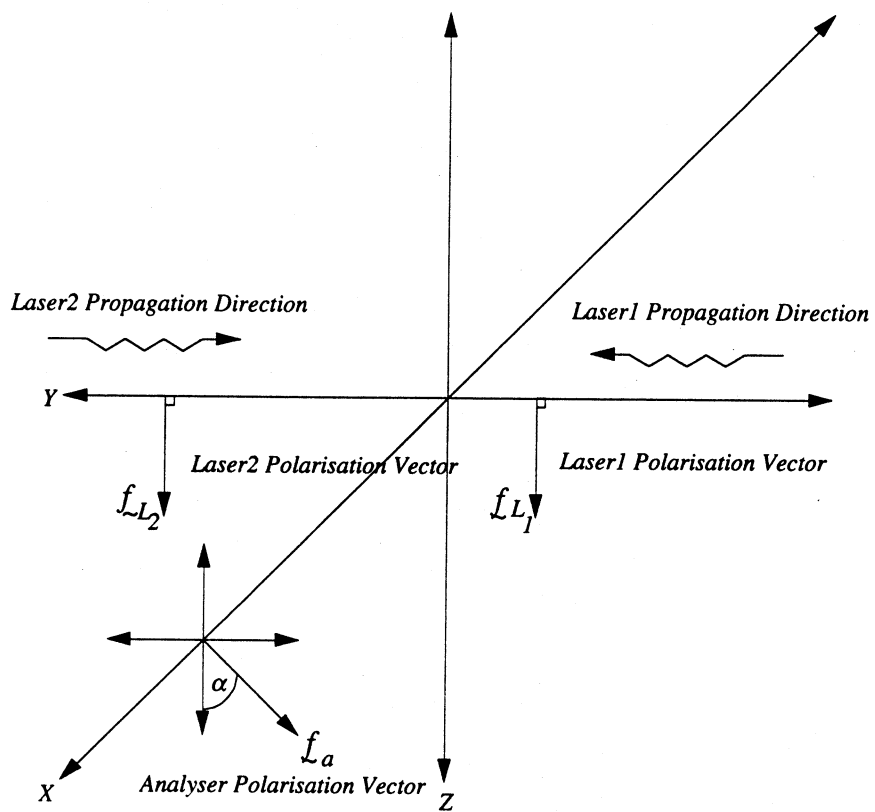


Figure 4.10: Stepwise Line Polarisation Geometry

Table 4.3

F_{ee}	Reduced Matrix Element
F_{88}	$\frac{3}{5}(4\cos^2\alpha + 3\sin^2\alpha) \langle 2 D 1\rangle ^2$
F_{99}	$\frac{3}{5}\left(\frac{1}{2}\sin^2\alpha + 6\cos^2\alpha + \frac{3}{2}\sin^2\alpha\right) \langle 2 D 1\rangle ^2$
F_{1010}	$\frac{3}{5}\left(\frac{1}{2}\sin^2\alpha + 6\cos^2\alpha + \frac{3}{2}\sin^2\alpha\right) \langle 2 D 1\rangle ^2$
F_{1111}	$\frac{3}{5}(4\cos^2\alpha + 3\sin^2\alpha) \langle 2 D 1\rangle ^2$

The Emission Matrix Elements In Terms of the Reduced Matrix element $|\langle 2||D||1\rangle|$

$10^{-13} \text{Jm}^{-3} \text{s}^{-1}$. Graphs 4.1B and 4.1A show the reverse situation whereby the probabilities for the intermediate and upper excited states steadily increases until $10^{-13} \text{Jm}^{-3} \text{s}^{-1}$ and then level off. At high intensities, the populations n_1, n_2, n_4, n_5, n_9 and n_{10} limit to an equal population of near $\frac{1}{6}$. It is also shown in these figures that the probabilities of exciting the n_8 and n_{11} substates is small which is due to the fact that the n_3 and the n_6 states can only be populated by relaxation. Graph 4.2 show the total sublevel probability versus energy density. This graph shows that probabilities converge to a similar value as the power is increased and that the intermediate state population remains higher than the upper excited state population.

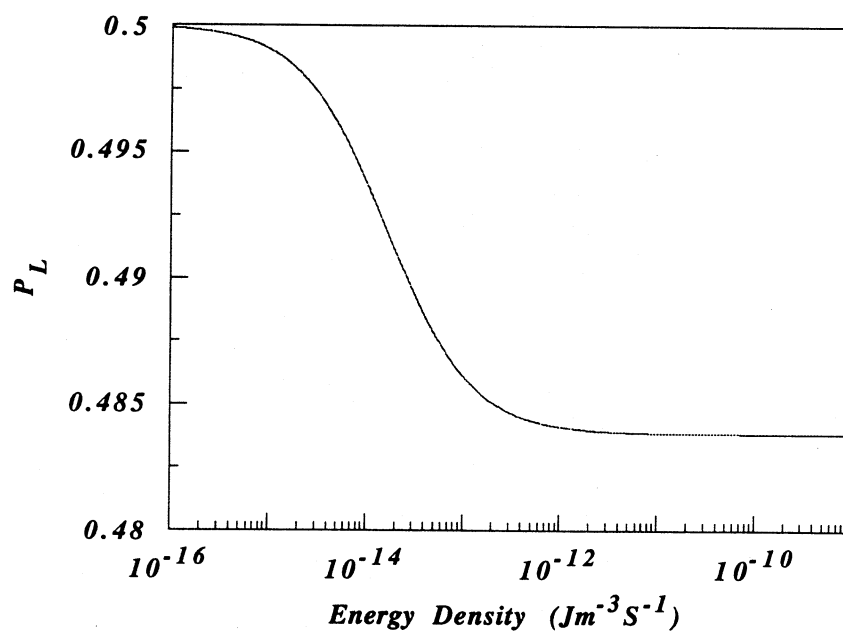
Knowledge of the excited state populations enables the line polarisation to be determined. Consider a line polarisation experiment of the fluorescence from the D state to the P state. The geometry of the experiment is depicted in figure 4.10. The expression for the intensity of the fluorescence scattered at right angles to the plane formed by the second lasers polarisation and propagation direction is given by equation (3.118). Application of this equation to the excited D states depicted in figure 4.9 gives

$$I = \rho_{88}^{L_2} F_{88}^D + \rho_{99}^{L_2} F_{99}^D + \rho_{1010}^{L_2} F_{1010}^D + \rho_{1111}^{L_2} F_{1111}^D \quad (4.71)$$

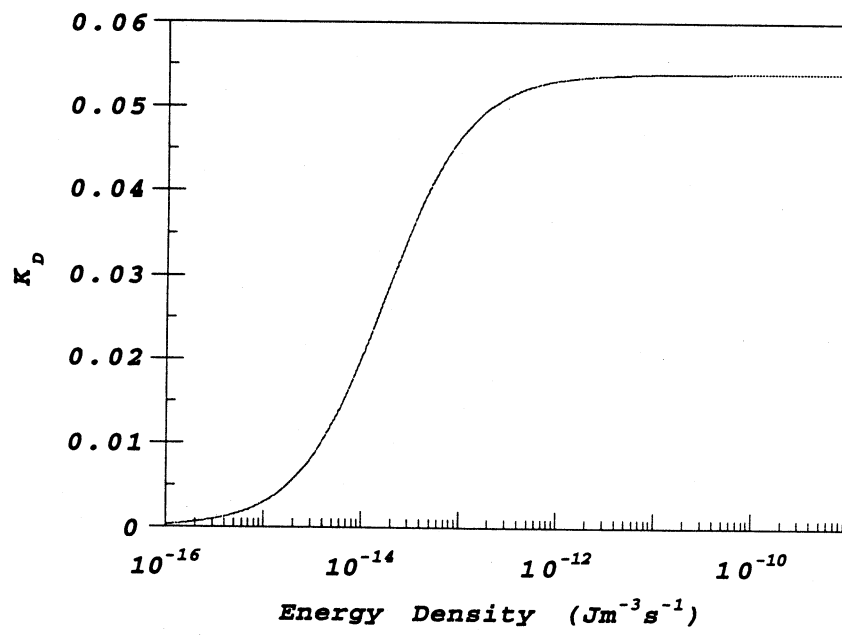
where $\rho_{ee}^{L_2}$ is the population formed by the second laser and F_{ee}^D is a fluorescence emission matrix element defined by equation (3.119). The elements may have their m dependence removed by applying the Wigner-Eckart theorem and reduced to L representation as in section 3.7. The results of the reduction are given in Table 4.3. Applying the results of Table 4.3 to equation (4.71) yields

$$I(\alpha) = \frac{3}{5} | \langle 2 || D || 1 \rangle |^2 \left\{ \rho_{88}^{L_2} (4 \cos^2 \alpha + 3 \sin^2 \alpha) + \rho_{99}^{L_2} \left(\frac{1}{2} \sin^2 \alpha + 6 \cos^2 \alpha + \frac{3}{2} \sin^2 \alpha \right) \right. \\ \left. + \rho_{1010}^{L_2} \left(\frac{1}{2} \sin^2 \alpha + 6 \cos^2 \alpha + \frac{3}{2} \sin^2 \alpha \right) + \rho_{1111}^{L_2} (4 \cos^2 \alpha + 3 \sin^2 \alpha) \right\} \quad (4.72)$$

where $| \langle 2 || D || 1 \rangle |$ is the reduced matrix element in L representation. Substitution of $\alpha=0, 90$ into equation (4.72) yields the fluorescence intensities,



Graph 4.3: Line Polarisation Vs Energy Density



Graph 4.4: K_D Vs Energy Density

$$I(0) = \frac{3}{5} | \langle 2 || D || I \rangle |^2 \left(4\rho_{88}^{L_2} + 6\rho_{99}^{L_2} + 6\rho_{1010}^{L_2} + 4\rho_{1111}^{L_2} \right) \quad (4.73a)$$

$$I(90) = \frac{3}{5} | \langle 2 || D || I \rangle |^2 \left(3\rho_{88}^{L_2} + 2\rho_{99}^{L_2} + 2\rho_{1010}^{L_2} + 3\rho_{1111}^{L_2} \right) \quad (4.73b)$$

Substitution of these intensities into the expression for the line polarisation given by equation (3.121) reveals

$$P_L = \frac{\rho_{88}^{L_2} + 4\rho_{99}^{L_2} + 4\rho_{1010}^{L_2} + \rho_{1111}^{L_2}}{7\rho_{88}^{L_2} + 8\rho_{99}^{L_2} + 8\rho_{1010}^{L_2} + 7\rho_{1111}^{L_2}} \quad (4.74)$$

Thus by using the populations evaluated by equations (4.65)-(4.69) a theoretical value for the line polarisation may be determined. Graph (4.3) shows the line polarisation as a function of the energy density of both lasers. Overall the line polarisation does not vary significantly and has a range of 0.5-0.485. The greatest variation occurs at low energy between 10^{-15} and $10^{-13} \text{ Jm}^{-3}\text{s}^{-1}$, as was the case with the variation in the populations shown in graphs 4.1 and 4.2. After $10^{-12} \text{ Jm}^{-3}\text{s}^{-1}$, the line polarisation takes the constant value of 0.484. The line polarisation was determined experimentally as 0.47 ± 0.09 with both lasers having a laser power of 40 mW/mm^2 which corresponds to an energy density of $4 \times 10^{-11} \text{ Jm}^{-3}\text{s}^{-1}$, the details of this experimental determination are given in Chapter Five.

Graph 4.4 depicts the optical parameter K_D (equation 4.27b) as a function of the energy density. This graph shows the reverse features to the line polarisation. At low powers this parameter approaches zero which is due to a small population in the $m_j = \pm \frac{3}{2}$ sub levels. K_D increases until the power reaches $10^{-12} \text{ Jm}^{-3}\text{s}^{-1}$, where it takes a constant value of 0.054. The small values of indicate K_D as in graph 4.1a that the population of the $m_j = \pm \frac{3}{2}$ is much smaller than that of the $m_j = \pm \frac{1}{2}$ populations. Experimentally the lasers were kept at 40 mW/mm^2 which corresponded to a theoretical value for K_D of 0.054. This can be compared to an experimentally determined value of K_D by the manipulation of the expression of the line polarisation give by equation (4.74). This expression can be written as

$$P_L \left(14\rho_{1111}^{L_2} + 16\rho_{1010}^{L_2} \right) - 2\rho_{1111}^{L_2} - 8\rho_{1010}^{L_2} = 0 \quad (4.75)$$

where the symmetry relations given by equation (4.17) have been used. Dividing equation (4.75) through by $\rho_{1010}^{L_2}$ yields

$$P_L \left\{ 14 \frac{\rho_{1111}^{L_2}}{\rho_{1010}^{L_2}} + 16 \right\} - 2 \frac{\rho_{1111}^{L_2}}{\rho_{1010}^{L_2}} - 8 = 0 \quad (4.76)$$

Comparing the fractions in this expression to equation (4.27b) and using some manipulation enables an expression for K_D to be written as

$$K_D = \frac{4-8P_L}{7P_L-1} \quad (4.77)$$

Using the experimental value of the line polarisation in this expression yields an experimental value for K_D of 0.11 ± 0.18 which is within experimental error of the rate equation result.

4.7 Conclusion

This chapter presented an initial investigation of the D-P collision process. The D state collision matrix was parameterised and it was found for the case of a D-S collision process that six independent parameters were required to specify the collision process. The case of a D-P collision process is much more complicated and requires more parameters to fully specify this collision matrix.

Three stepwise pseudo Stokes parameters were derived for the case when the two exciting lasers had parallel polarisations. The parameters that were derived for the linearly polarised laser showed that these parameters were functions of atomic collision parameters and an optical parameter. For circularly polarised light the stepwise pseudo Stokes parameter, P_3^S was a function of the atomic collision parameters only.

An example derivation of a stepwise pseudo Stokes parameter with non-parallel polarisations was also given and it was shown that these parameters are complicated functions of atomic collision parameters and optical parameters. It was emphasised that if determination of the optical parameters could be made, that the use of other polarisations may enable a full determination of the collision matrix.

A theoretical determination of the optical parameter K_D discussed in the parallel polarisation pseudo Stokes parameters was the final section in the chapter. This theoretical determination was performed using rate equations evaluated at steady state. A comparison between experiment and theory was performed via line polarisation measurements and the optical pumping parameter K_D which gave good agreement to within experimental error.

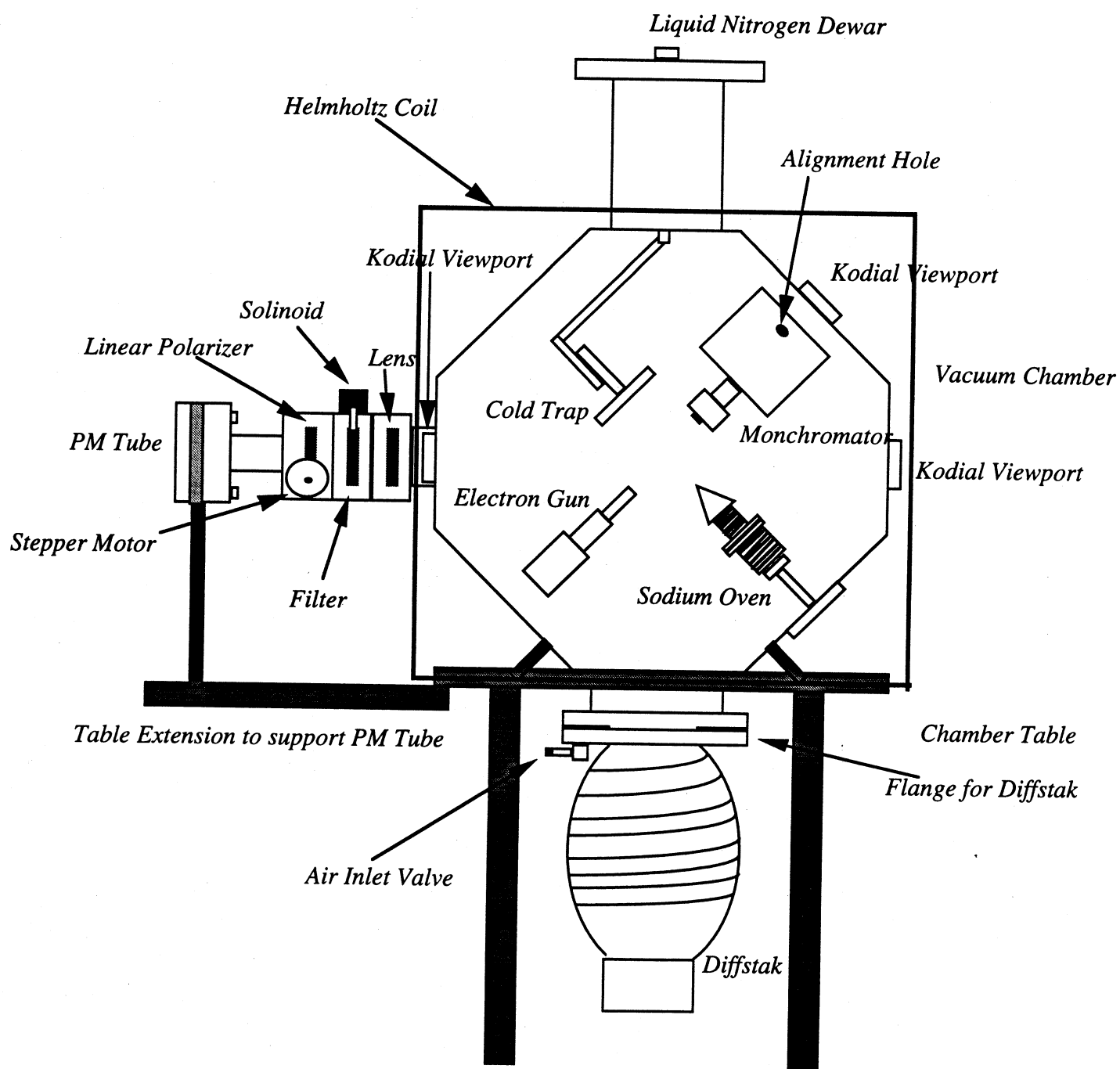


Figure 5.1: The Superelastic Scattering Experiment Apparatus

Chapter 5

The Superelastic Scattering Experiment

5.1 Introduction.

In this chapter a description of the experimental apparatus used is given. The chamber was commissioned prior to the start of this project (Farrell 1992). Figure 5.1 shows a general experimental arrangement of the elements used in the various superelastic scattering experiments.

In the case of a single step superelastic scattering experiment, a polarised laser beam travelling either in the $-Y_{\text{col}}$ direction (perpendicular to the scattering plane) or in the coplanar configuration in the Z_{col} direction, was tuned from the $3^2S_{1/2}$ ($F'=2$) ground states to $3^2P_{1/2}$ (F) excited states (See Chapter Two). This laser beam excited a beam of ground state atoms produced by a heat effused atomic beam. The atomic beam was placed in the scattering plane facing the negative X_{col} direction. An electron gun produced a beam of electrons of a particular energy at an angle θ_c to the quantisation axis, which were directed to the region where the atomic beam and the laser beam intersected. This region defined the interaction region. Electrons that passed this region would either pass without interaction or undergo a collision and be scattered at some scattering angle θ_c . The scattered electrons of a particular energy could then be detected at a desired scattering angle via an electron analyser in the negative Z_{col} direction. The electron energy analyser was energy selective so that superelastic collisions from the $3^2P_{1/2}$ (F) states could be isolated from other energy dependant collision interactions.

Folded step and stepwise superelastic scattering experiments were also performed in the same apparatus. The folded step experiments involved the use of one extra laser but was tuned to excite atoms from the $F'=1$ hyperfine ground state. This laser co-propagated in $-Y_{\text{col}}$

direction with the laser tuned from the $F'=2$ hyperfine ground state. The stepwise experiments also involved the use of two lasers which were directed so that the laser beams travelled in a counter-propagating configuration. This was due to the two laser beams being significantly different in frequency and required a set of optics for each wavelength.

The atomic oven, electron gun and electron analyser were all housed within a vacuum chamber. Laser and viewing entries were located on the front and rear of the chamber as well as the sides of the chamber. Controlling voltages, currents and signals from the channeltron were passed from the interior of the chamber to the exterior through electrical feedthroughs. Signals from the detection electronics could be then sent to various counters and a computer over a user defined time period and be processed.

5.2 The Vacuum Chamber

Experiments were performed in an evacuated stainless steel chamber (See figure 5.1). Non-magnetic, corrosion resistant stainless steel was used to construct the chamber by welding eight 10mm by 230mm by 300mm pieces into an octagonal shape. On the rear of this arrangement an octagonal back plate was welded and a flange to the front so a front plate could be attached. The front plate was sealed by an o-ring and was removable which enabled access to the interior of the chamber for maintenance. On the rear of the chamber were mounted two nineteen pin electrical feedthroughs (Vacuum Generators EFT 19) as well as one four pin high voltage electrical feedthrough (Vacuum Generators EFT 34A). The two nineteen pin voltage feedthroughs provided a passage for the voltages and currents required by the electron gun, electron analyser and sodium oven. The four pin high voltage connections carried the bias voltage to the channeltron as well as signal pulses from the channeltron. The chamber was lined with mu-metal to reduce the earth's and any other residual magnetic fields. This field was further reduced by the use of three pairs of orthogonal Helmholtz coils. In this configuration the magnetic field was reduced to less than 10^{-6} T in the interaction region.

Evacuation of the vacuum chamber was accomplished by using an Edwards 6" Diffstak attached to a flange welded to the bottom of the chamber. The chamber-vacuum pump connection was sealed by an o-ring and the chamber could be isolated from the diffusion pump by a pneumatically operated swing valve. The diffusion pump was charged by 250 ml of Santovac 5 low vapour pressure silicon oil and was backed by an Edwards EM12 rotary pump. The rotary pump served two purposes, the first of which was to back the diffusion pump, and the second to initially evacuate the chamber to a pressure such that the diffusion pump could operate (approximately 10^{-2} mbar). So that the rotary pump could serve these two purposes, an Edwards model BRV 25 backing/roughing valve was used that could switch the rotary pump to evacuate the chamber and isolated the diffusion pump or alternatively to back the diffusion pump. A foreline trap was mounted between the rotary pump and the backing/roughing valve so that backstreaming of oil from this pump would be minimised. Pressures that the rotary pump were achieving could be monitored by a Pirani gauge. The vacuum pressure of the chamber was measured using an Edwards ion-8 ionisation gauge and typical base pressures were of the order of 1×10^{-7} mbar. Typical operating pressures were in the range of 3×10^{-7} - 5×10^{-7} mbar. The vacuum system was interlocked to a protection system which if tripped would shut the swing valve thus isolating the vacuum chamber and the diffstak. The heating element of the diffusion pump would also be disabled. The protection system was set to trip for electrical failure, vacuum failure and also for over heating of the diffusion pump. The temperature of the diffusion pump was measured by a thermocouple located close to the heater element.

The chamber housed the electron gun and electron analyser, each of which were mounted on separate rotatable turntables. The position of the electron gun or the electron analyser could be altered by rotating one of the Vacuum Generator rotary motion feedthroughs (Vacuum Generator RD91) that were attached to the rear plate of the chamber. The rotary feedthroughs were geared down by a factor of ten and were initially adjusted manually. The interfacing of the experiment with a IBM compatible PC enabled the adjustment of turntables using a stepper motor. The PC controlled a stepper motor which was connected to the rotary

feedthrough via a drive belt. During an experiment, the electron analyser remained fixed and adjustments of the scattering angles were accomplished by rotating the electron gun.

The sodium oven was also located within the vacuum chamber. It was fixed to a mounting plate on one surface of the chamber which was sealed by a o-ring. Attached to the top of the chamber was a liquid nitrogen dewar which was in thermal contact with a cold finger via a bellows connection. The cold finger was constructed of copper which has a good thermal conduction. Connected to the end of the cold finger was a plate which acted as a trap for the sodium which had passed the interaction region. This reduced any radiation trapping effects outside the interaction region in line polarisation experiments and lowered the vacuum pressure of the tank by trapping impurities.

Five Kodial viewports (Vacuum Generators FC70) were located around the chamber. These acted as input ports for the laser radiation or output ports for fluorescence detection by photomultiplier tubes as well as providing visual inspection access. One of these viewports was located on the rear plate and one on the front plate of the chamber, the other three being positioned on the side of the chamber. Measurements that required the perpendicular geometry made use of a laser beam inserted through the viewport on the rear of the chamber and the beam would exit via the viewport mounted on the front plate of the chamber. For the case of counter propagating laser beams the second laser would enter the chamber via the viewport on the front plate. When the co-planar geometry was required, the laser beam gained entry by a viewport mounted behind the electron analyser on the side of the chamber. The laser beam would then enter an alignment hole in the electron analyser and exit via the electrostatic lens assembly to the interaction region.

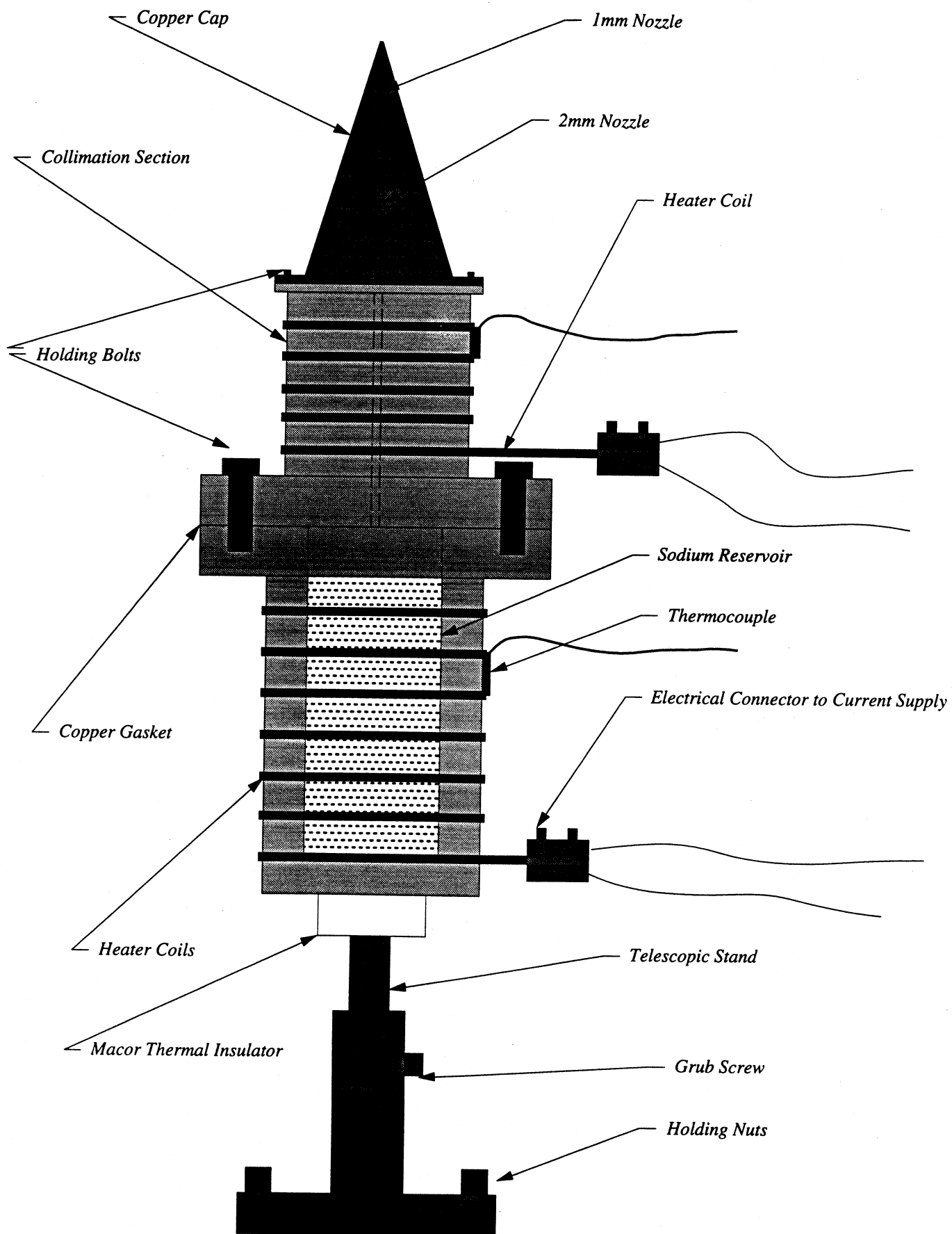


Figure 5.2: The Sodium Oven

direction with the laser tuned from the $F'=2$ hyperfine ground state. The stepwise experiments also involved the use of two lasers which were directed so that the laser beams travelled in a counter-propagating configuration. This was due to the two laser beams being significantly different in frequency and required a set of optics for each wavelength.

The atomic oven, electron gun and electron analyser were all housed within a vacuum chamber. Laser and viewing entries were located on the front and rear of the chamber as well as the sides of the chamber. Controlling voltages, currents and signals from the channeltron were passed from the interior of the chamber to the exterior through electrical feedthroughs. Signals from the detection electronics could be then sent to various counters and a computer over a user defined time period and be processed.

5.2 The Vacuum Chamber

Experiments were performed in an evacuated stainless steel chamber (See figure 5.1). Non-magnetic, corrosion resistant stainless steel was used to construct the chamber by welding eight 10mm by 230mm by 300mm pieces into an octagonal shape. On the rear of this arrangement an octagonal back plate was welded and a flange to the front so a front plate could be attached. The front plate was sealed by an o-ring and was removable which enabled access to the interior of the chamber for maintenance. On the rear of the chamber were mounted two nineteen pin electrical feedthroughs (Vacuum Generators EFT 19) as well as one four pin high voltage electrical feedthrough (Vacuum Generators EFT 34A). The two nineteen pin voltage feedthroughs provided a passage for the voltages and currents required by the electron gun, electron analyser and sodium oven. The four pin high voltage connections carried the bias voltage to the channeltron as well as signal pulses from the channeltron. The chamber was lined with mu-metal to reduce the earth's and any other residual magnetic fields. This field was further reduced by the use of three pairs of orthogonal Helmholtz coils. In this configuration the magnetic field was reduced to less than 10^{-6} T in the interaction region.

Evacuation of the vacuum chamber was accomplished by using an Edwards 6" Diffstak attached to a flange welded to the bottom of the chamber. The chamber-vacuum pump connection was sealed by an o-ring and the chamber could be isolated from the diffusion pump by a pneumatically operated swing valve. The diffusion pump was charged by 250 ml of Santovac 5 low vapour pressure silicon oil and was backed by an Edwards EM12 rotary pump. The rotary pump served two purposes, the first of which was to back the diffusion pump, and the second to initially evacuate the chamber to a pressure such that the diffusion pump could operate (approximately 10^{-2} mbar). So that the rotary pump could serve these two purposes, an Edwards model BRV 25 backing/roughing valve was used that could switch the rotary pump to evacuate the chamber and isolated the diffusion pump or alternatively to back the diffusion pump. A foreline trap was mounted between the rotary pump and the backing/roughing valve so that backstreaming of oil from this pump would be minimised. Pressures that the rotary pump were achieving could be monitored by a Pirani gauge. The vacuum pressure of the chamber was measured using an Edwards ion-8 ionisation gauge and typical base pressures were of the order of 1×10^{-7} mbar. Typical operating pressures were in the range of 3×10^{-7} - 5×10^{-7} mbar. The vacuum system was interlocked to a protection system which if tripped would shut the swing valve thus isolating the vacuum chamber and the diffstak. The heating element of the diffusion pump would also be disabled. The protection system was set to trip for electrical failure, vacuum failure and also for over heating of the diffusion pump. The temperature of the diffusion pump was measured by a thermocouple located close to the heater element.

The chamber housed the electron gun and electron analyser, each of which were mounted on separate rotatable turntables. The position of the electron gun or the electron analyser could be altered by rotating one of the Vacuum Generator rotary motion feedthroughs (Vacuum Generator RD91) that were attached to the rear plate of the chamber. The rotary feedthroughs were geared down by a factor of ten and were initially adjusted manually. The interfacing of the experiment with a IBM compatible PC enabled the adjustment of turntables using a stepper motor. The PC controlled a stepper motor which was connected to the rotary

feedthrough via a drive belt. During an experiment, the electron analyser remained fixed and adjustments of the scattering angles were accomplished by rotating the electron gun.

The sodium oven was also located within the vacuum chamber. It was fixed to a mounting plate on one surface of the chamber which was sealed by a o-ring. Attached to the top of the chamber was a liquid nitrogen dewar which was in thermal contact with a cold finger via a bellows connection. The cold finger was constructed of copper which has a good thermal conduction. Connected to the end of the cold finger was a plate which acted as a trap for the sodium which had passed the interaction region. This reduced any radiation trapping effects outside the interaction region in line polarisation experiments and lowered the vacuum pressure of the tank by trapping impurities.

Five kodial viewports (Vacuum Generators FC70) were located around the chamber. These acted as input ports for the laser radiation or output ports for fluorescence detection by photomultiplier tubes as well as providing visual inspection access. One of these viewports was located on the rear plate and one on the front plate of the chamber, the other three being positioned on the side of the chamber. Measurements that required the perpendicular geometry made use of a laser beam inserted through the viewport on the rear of the chamber and the beam would exit via the viewport mounted on the front plate of the chamber. For the case of counter propagating laser beams the second laser would enter the chamber via the viewport on the front plate. When the co-planar geometry was required, the laser beam gained entry by a viewport mounted behind the electron analyser on the side of the chamber. The laser beam would then enter an alignment hole in the electron analyser and exit via the electrostatic lens assembly to the interaction region.

5.3 The Sodium Oven

The sodium beam used in the experiment was produced by a stainless steel oven. This is depicted in figure 5.2. The oven consisted of two sections, a collimation section and a reservoir. The reservoir and collimation section were connected via bolts and sealed using knife edges on both sections onto a copper gasket. Both sections of the oven were in thermal contact with heating coils. The heating coils consisted of two wires which were encased in a magnesium oxide insulator and each were contained in stainless steel tubing. The two wires passed DC current in opposite directions so as to cancel any residual magnetic fields created by the circulating electron current. The resistances of the heater coils surrounding the reservoir and collimating section were measured to be 30.2Ω and 16.5Ω respectively. The currents to the two sections of the oven were provided by two separate D.C. current supplies, via the electrical feedthroughs located on the rear plate of the chamber. For typical experimental conditions, the coils heating the reservoir and the collimation section were maintained at 1.2A and 2.1A respectively.

The collimation section of the oven was maintained at higher temperatures than the reservoir so that blockages would not occur. The purpose of the section was to collimate the heat effused atoms. The atoms passed this section to a copper cap which provided further collimation and exited via a laval nozzle, which had an exiting orifice of 1mm in diameter, to the interaction region. On occasions the oven could become blocked with sodium residue. The orifice of the oven could be cleared by increasing the current in the coils surrounding the collimation section. To prevent any reoccurrence of the problem, the current in this section was left continuously running.

The oven was mounted on the chamber by an adjustable stand which allowed the nozzle to be moved toward or away from the interaction region. A macor block between the oven and the stand provided thermal insulation. The stand was mounted on the chamber on a removable plate. Two screws holding the oven to the plate enabled translational positioning of the oven. A grounding wire connected the collimation section of the oven to a common ground

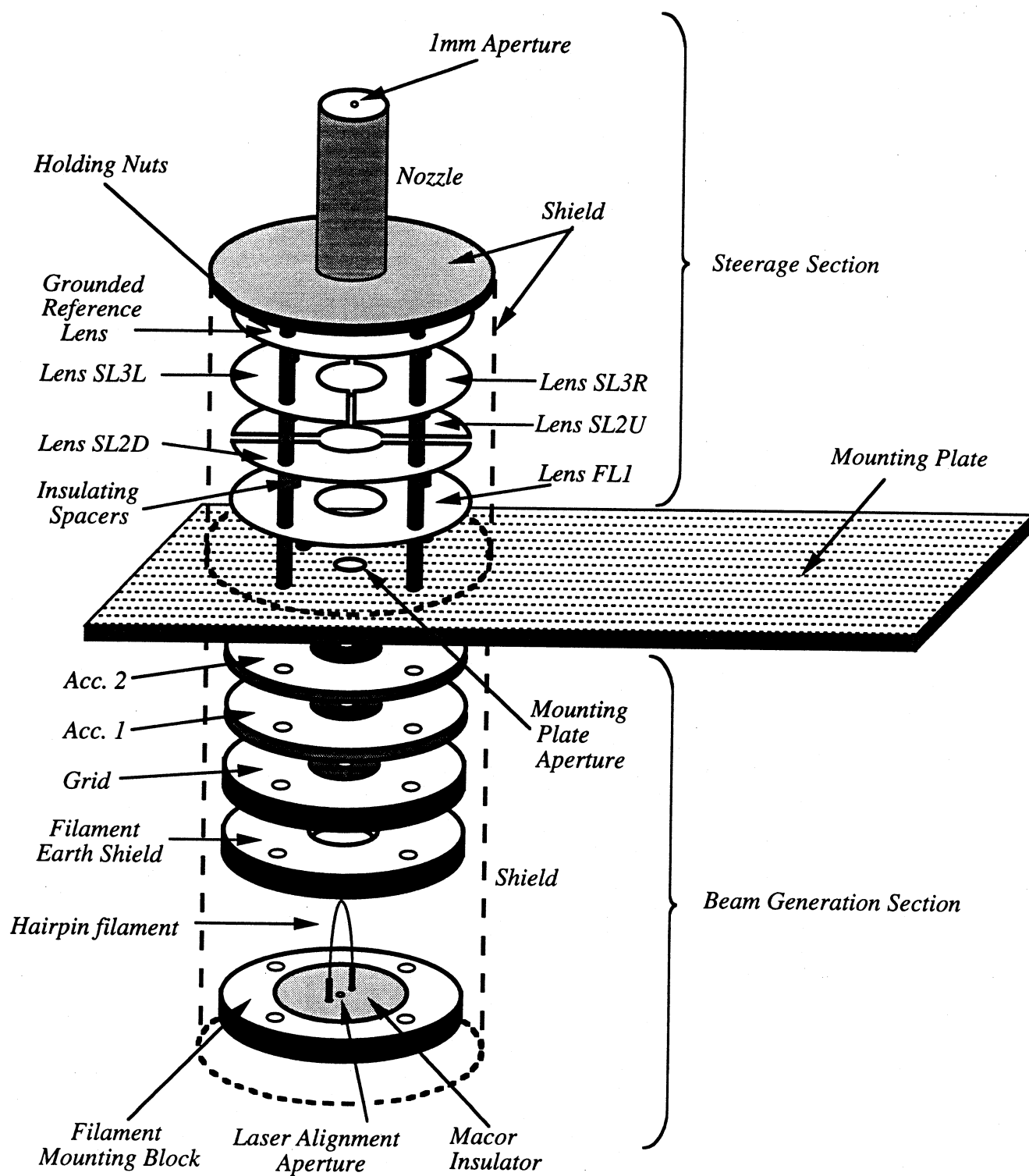


Figure 5.3: The Electron Gun

connection of the chamber which minimised any distorting electric fields that could be produced due charging effects.

5.4 The Electron Gun

The electron gun used in the experiments was originally designed by McLucas (1982) from the data of Harting and Read (1976). The gun is a two stage device as shown in figure 5.3. One stage, denoted as the beam generation section, contained a tungsten hair pin filament used as the source of electrons. Included in this section was the filament mounting block which consisted of a macor block surrounded by a grounded stainless steel shield. Following this element was a grid and two accelerating lenses (acc1 and acc2). The function of this section is to accelerate and focus a beam of thermally emitted electrons from the hair pin filament through an aperture in the mounting plate. The emerging electrons would then enter the second stage of the gun denoted as the steerage section. This section consisted of two full lenses and two split lenses. One of the full lenses FL1 provided further focussing, the other full lens was a grounded reference lens. The two split lenses provided two dimensional steerage of the beam as well as focussing. By setting the appropriate voltages to the lens elements allowed the electron beam to emerge the nozzle of the electron gun via two 1mm apertures located 10mm apart. The lenses of both sections were held in place by four stainless steel struts and each lens was electrically isolated by macor insulators. The lens assembly was fixed via four stainless steel nuts located at both the end of the mounting plate and at the end of the reference lens. The lens elements were also encased in two removable stainless steel shields which were both grounded to provided a reference for the electron energy.

The voltages to the lens elements were supplied by a voltage divider that was driven by a Kepco APH500M stabilised high voltage supply which was referenced to the filament potential. The current and the bias voltage of the filament were supplied by two separate Kepco power supplies. A Kepco ATE 6-5 6V supply running in constant current mode

Table 5.1

Typical Operating Voltages of the Electron Gun

<i>Lens</i>	<i>Voltage (V)</i>
<i>SL2U</i>	<i>10.7</i>
<i>SL2D</i>	<i>13.2</i>
<i>SL3L</i>	<i>73.6</i>
<i>SL3R</i>	<i>69.9</i>
<i>FL</i>	<i>667</i>
<i>ACC1</i>	<i>-28.7</i>
<i>ACC2</i>	<i>-29.0</i>
<i>GRID</i>	<i>-25.4</i>

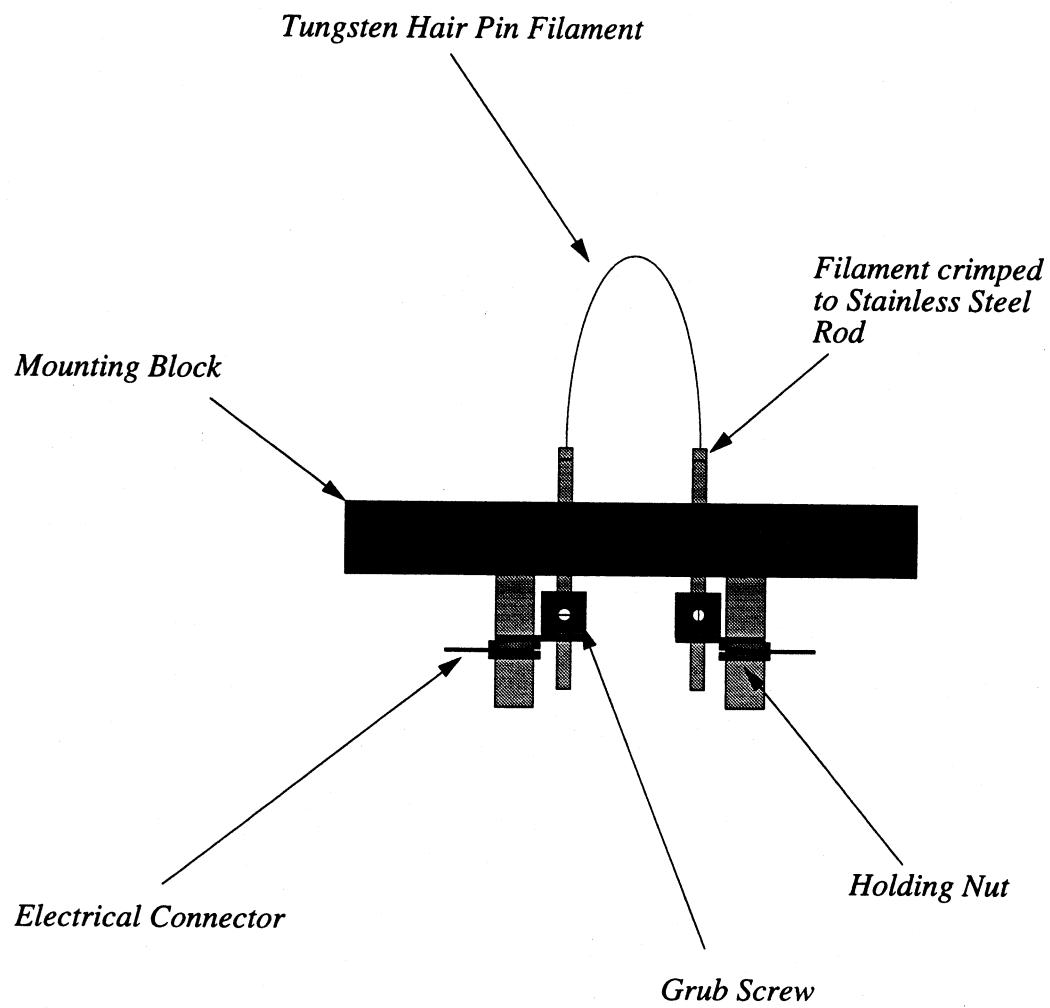


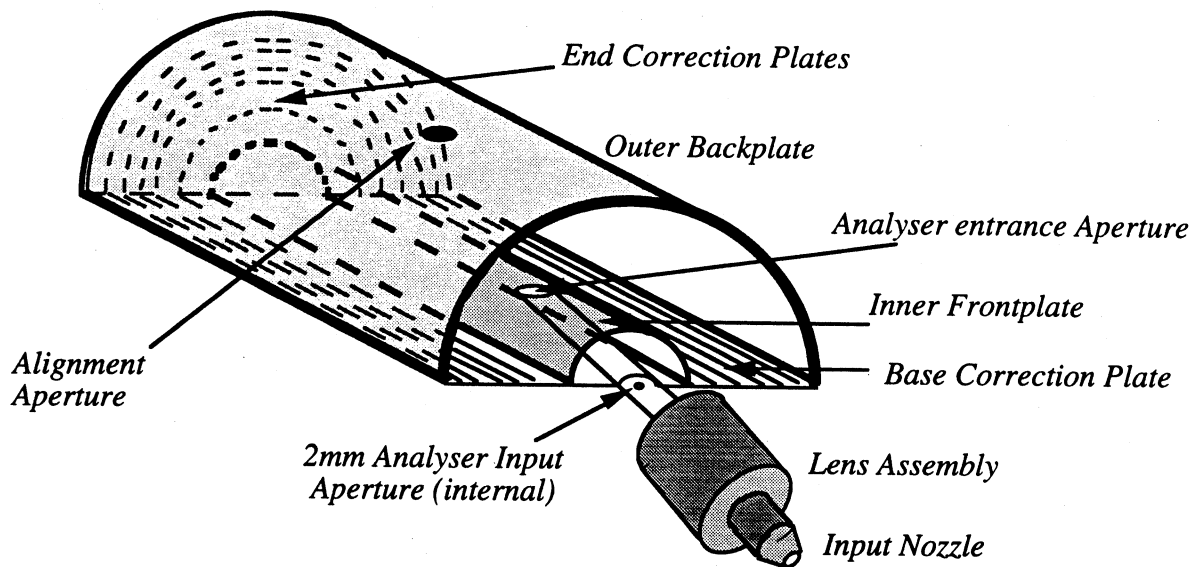
Figure 5.4: The Filament Mount

provided the filament current which typically ranged from 0.6A-0.85A. Lower filament currents produced the most stable electron beam and reduced background in the superelastic energy channel. The potential of the filament was supplied by a Kepco ATE 100-0.5M supply which operated in constant voltage mode and could range from 0V-100V. This was connected to one side of the filament. Table 5.1 shows the typical voltages for the lens elements with a filament potential of 20V.

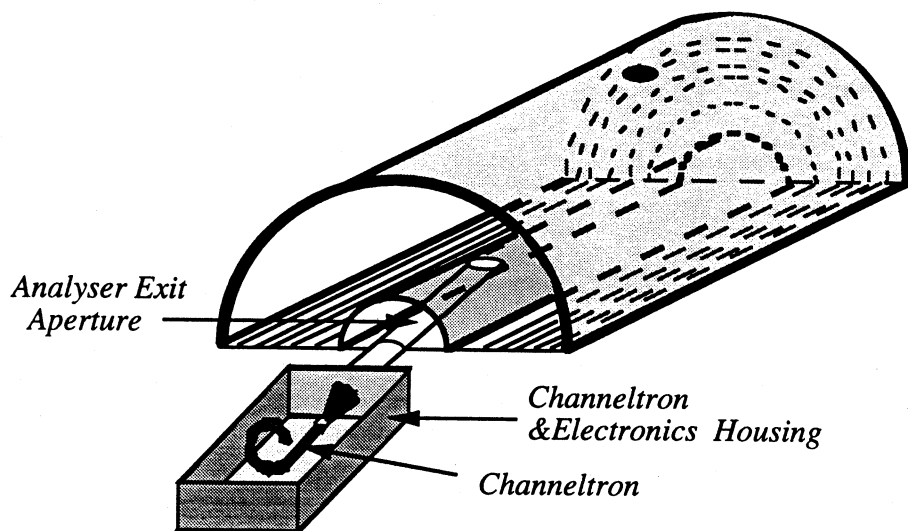
After a long operating period the electron gun would require maintenance. This would either be in the form of a filament change or cleaning of impurities from the surface of the lens elements. Any residues on the lens elements could charge over a period of time and produce patch fields which would cause instabilities with the operation of the gun. Any cleaned element of the gun would then only be handled using surgical gloves thus preventing contamination of the elements by oil from human skin.

The hair pin filament was constructed by crimping tungsten wire (0.046mm in diameter) to two 1mm stainless steel rods. The filament would be then bent into a V shape using a razor. This was a delicate procedure and the filament required visual inspection using a microscope for structural damage. If no structural damage was evident the filament could then be positioned in the macor mounting block by the use of two grub screws (see figure 5.4). These two screws allowed vertical movement of the filament so that it could be correctly positioned half way between the earth shield and the grid in the electron gun assembly. The resistance of a correctly mounted filament was in the range of 0.5Ω - 0.8Ω .

The cleaning of the electron gun required two processes. The gun would initially be dismantled and be sand blasted at low pressure. Typically these pressures were < 80 psi. After the sand blasting process the elements would be ultrasounded in an acetone bath for 10 minutes and left to dry. After the gun dried it was reassembled and returned to the vacuum chamber.



The Electron Analyser (front view)



The Electron Analyser (rear view)

Figure 5.5: The Electron Analyser

Table 5.2

Typical Operating Voltages of the Lens Stack of the Analyser

<i>Lens Element</i>	<i>Voltage (V)</i>
<i>Split Lens (Outer)</i>	<i>28.3 26.6</i>
<i>Split Lens (Inner)</i>	<i>79.0 82.6</i>
<i>Full Lens</i>	<i>32.3</i>
<i>Lens Case</i>	<i>Earth</i>

The realignment of the electron gun within the vacuum chamber was accomplished by removing the grounding shield that protected the beam generation section. The turntable would be rotated to zero degrees so that the electron gun and the electron analyser were parallel. A light source would be then placed behind the alignment hole in the filament mount. By visual inspection through an alignment hole in the electron analyser the gun could be seen. The gun would be positioned until both the aperture in the gun was seen as well as the light source. With this condition established, the gun was then aligned and the mounting screws on the turntable would be tightened and the earth shield would be replaced. The electrical connections of the gun could be then reconnected and the chamber could be closed ready to evacuate.

5.5 The Electron Analyser

The electron energy analyser used in the experiments was a cylindrical mirror type. Figure 5.5 depicts the front and rear view of the analyser which consisted of three main sections, the input lens stack, cylindrical mirror analyser and the channeltron which is also shown in figure 5.5.

Electrons scattered from the interaction region would pass through a 1mm aperture in the input nozzle to a lens stack. The input lens stack consisted of three lenses used to focus the interaction region. The lens stack was positioned so that the end of the input nozzle was 20mm from the interaction region and as such gave a solid angle of detection of approximately 0.002 steradians. Two of the lenses were split lenses the third was a full lens and optimisation of the signal was carried out by adjustments to the voltages of these elements. Voltages to the lenses were supplied by a voltage divider that also supplied the electron gun voltages. Typical lens voltages are shown in Table 5.2

The cylindrical mirror analyser (CMA) was constructed using the data from Risley 1972 which gives the design parameters to obtain second order focussing and optimum resolution. The CMA consisted of a semi-cylindrical inner plate constructed of solid stainless steel. Surrounding this was an outer plate also constructed of stainless steel. The outer semi-cylinder included an alignment aperture so that the analyser could be aligned with the vacuum system. The surfaces of both the semi-cylinders were coated with Aquadag colloidal graphite to minimise surface variations of the electric field. The semi-cylinders were mounted to a copper plated circuit board and the inner plate was electrically grounded. The outer semi-cylinder could be maintained at a constant voltage. This plate could also be scanned by applying a ramp voltage provided by a Ortec 197 multichannel analyser. The multichannel analyser could provide a ramp voltage of 0.0V to 4.6V. To get a useful energy range this ramp voltage was amplified so that a range of 0.0V to 9.0V was obtainable. Correction end plates were also fitted to the front and the rear of the analyser. These corrected the effect on the electron beam due to the finite length of the front and back plate by producing uniform end and base voltage drops across the gap. The end plates also consisted of a copper plated circuit board to which logarithmically spaced grooved lines were etched. The grooved lines separated regions which were connected by eight 820k Ω resistors. The entire CMA was encased in an earthed stainless steel case also with an alignment aperture so that the alignment hole in the back plate could be viewed.

The final section of the analyser was the electron detector. The detector and electronics were housed in a stainless steel box fixed to the end of the CMA. Once electrons of a selected energy passed the semicylinders through an exit aperture, they were detected by a Mullard X818-BL channel electron multiplier denoted in figure 5.5 as the channeltron. The channeltron amplified the incoming electrons using an avalanche effect. A single electron could produce a pulse of approximately 10mV. Rg-58 coaxial cable was used to transport the signal to external electronics. The cone of the channeltron was earthed to reduce unwanted background. The channeltron was operated typically at 2500V which was provided by an Ortec 459 power supply which was capable of delivering voltages up to 5000V.

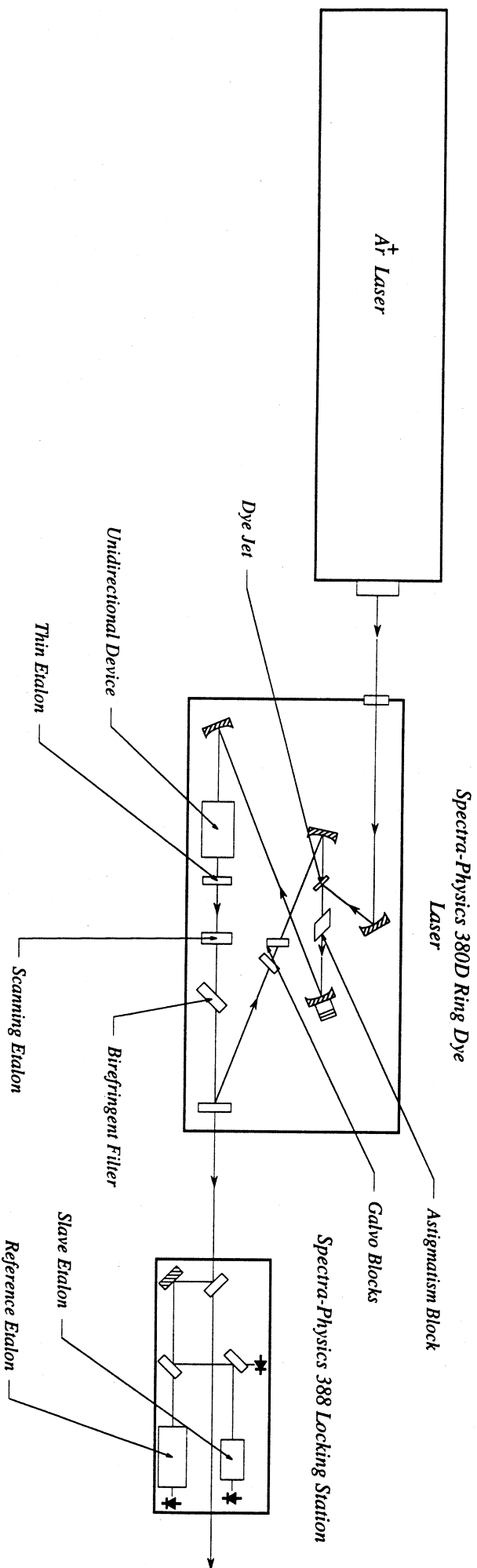


Figure 5.6: The Dye Laser System

5.6 The Laser Systems

The various superelastic scattering experiments were performed employing single mode continuous wave laser sources. In the case of single step experiments and folded step superelastic scattering experiments, laser light was provided by Spectra Physics 380D ring cavity resonator dye lasers which were used for exciting the D_2 line which had a vacuum wavelength of 598.160nm. In the case of the stepwise experiment a Coherent 899-21 Titanium Sapphire solid state ring laser was used for exciting the $3^2P_{3/2} \rightarrow 3^2D_{5/2}$ transition which required a laser beam with a vacuum wavelength of 819.711nm.

The Spectra Physics 380 D ring dye lasers were optically pumped by argon-ion lasers. The model 380D ring dye laser is a travelling wave, ring resonator continuous wave dye laser and provides tunable, high power, single frequency radiation. Unlike a standing wave resonator, the wave propagates around the cavity continuously so as not to create regions of unused gain in the dye and as such prevents spatial hole burning and therefore increasing the efficiency of the laser. The conversion efficiency from the argon-ion laser to the ring laser output were specified to be in the order 23 percent though usual operating efficiencies were in the order of 10 percent.

The ring laser is a four mirror cavity and the radiation travels in a figure eight pattern as illustrated in figure 5.6. Inside the free cavity the travelling wave could propagate in both directions. A Faraday rotator is introduced to produce directional anisotropy thus selecting a particular propagation direction. The 380D uses a flowing dye jet as the lasing medium. During an experiment, the driving pressure of the dye was maintained at 100psi and for exciting the D_2 line of sodium, Rhodamine 6G dye was used which has an emission peak at 590nm. The emission gain curve of this lasing dye extends over several tens of nanometers and as such simultaneous lasing can occur at a large number of cavity mode frequencies. In order to obtain single mode operation a number of frequency selecting elements were inserted into the cavity. In this particular dye laser, single mode operation is obtained using a

birefringent filter, fine etalon and an electronically tunable single frequency Fabry-Perot etalon. The birefringent filter allowed coarse tuning of the laser over the region of the dye profile. The fine etalon and the Fabry-Perot etalon introduce loss to all but one cavity mode. Two rotatable optical blocks are installed within the cavity to allow the path length of the cavity to be changed. Fine adjustments of the cavity were made using a Piezo-electrically driven mirror.

The output of the laser was monitored for instabilities by a Spectra Physics 389 reference station. The output beam was beam split so that a small amount of light could be sent to two interferometers. One of the interferometers was designated the reference interferometer which servo locked the laser onto one of its fringes by the use of external electronics. The other interferometer was the slave interferometer which was used for corrections when mode hops occurred. The use of this station enabled the laser to be locked to a single frequency for up to 10 hours.

The tuning of the laser to the D_2 line was accomplished via the Spectra physics 481B scanning electronics used in conjunction with a Burleigh WA20 wavemeter. Fine tuning of the laser was performed by observing the fluorescence emitted by the excited sodium atoms through a Kodial viewport on one side of the vacuum chamber. An IBM PC clone using an Arcom PCDAC12-4 card was also able to control tuning conditions by providing an interface to the Spectra Physics 481B station. The PCDAC12-4 card provided four 12 bit digital to analog converters two of which could be used for two lasers in two laser experiments such as the folded step or the stepwise experiments. A PM tube monitoring the scattered fluorescence could also be used over long run times to provide feedback to the PC in case of large mode hops which the 389 reference station failed to correct. In this case, when the laser was detuned, the PC would use a routine written in turbo pascal to scan the laser to a frequency so that the PM tube gave a maximum fluorescence signal which indicated that the laser was retuned.

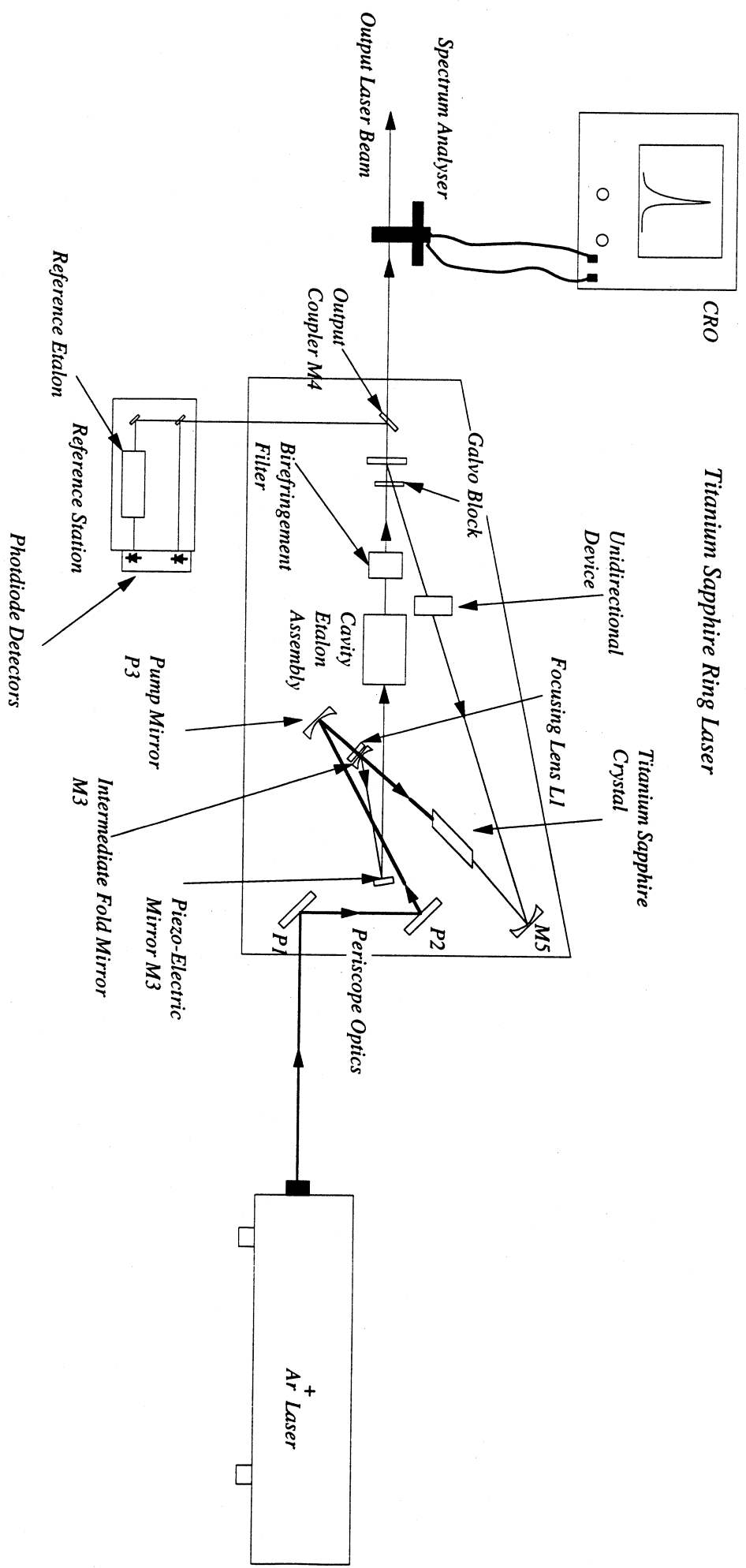


Figure 5.7: The Titanium Sapphire Laser System

The Coherent 899-21 titanium sapphire ring laser was pumped with a Coherent Innova 90-D argon-ion Laser. The Innova 90-D was rated at 5W but could easily deliver an unapertured output of 6.5W. The titanium sapphire laser provides a continuous wave, single frequency, tunable infrared laser light. The internal cavity optics are interchangeable with three different sets of optics (short wavelength, medium wavelength and long wavelength) allowing a tuning range of 680nm to 1250nm in the infrared spectrum. In the stepwise experiment short wavelength optics were used which enabled a tuning range of 680nm to 850nm. The free running cavity with all frequency selecting optics delivered a laser beam with a jitter band of approximately 10 MHz which could be reduced to 1 MHz by the use of an external reference station.

The laser cavity consisted of four mirrors and formed a figure eight pattern and traversed the path indicated in figure 5.7. Also shown in this figure are the optics used to direct the pump laser to the crystal. The pump beam initially gained access to the cavity by the use of periscope which guided the beam to the pump mirror. The pump mirror then directed this beam to the cooled titanium sapphire crystal via a lens and the intermediate fold mirror M1. The M1 mirror was coated for reflection of infrared light and the transmission of the pump beam. The crystal was cooled via circulating chilled water which passed through a tube in thermal contact with crystal mounting bracket. This bracket was also rotatable so that the pump beam would strike the crystal at the Brewsters angle.

Lasing in a single direction was maintained by the use of a Faraday rotator located within the cavity. Frequency selection was obtained by the use of a birefringent filter, and a thick and thin etalon. The birefringent filter allowed a frequency band of 2 GHz and the thick and the thin etalons further reduce this frequency bandwidth to approximately 1 MHz when actively stabilised. Single frequency operation was accomplished by the use of an external reference station. After the laser beam exited the cavity it was beam split so that a small portion of this beam could be directed into the reference station which was mounted to the external casing of the cavity. This beam was again further beam split so that one beam was directed to a

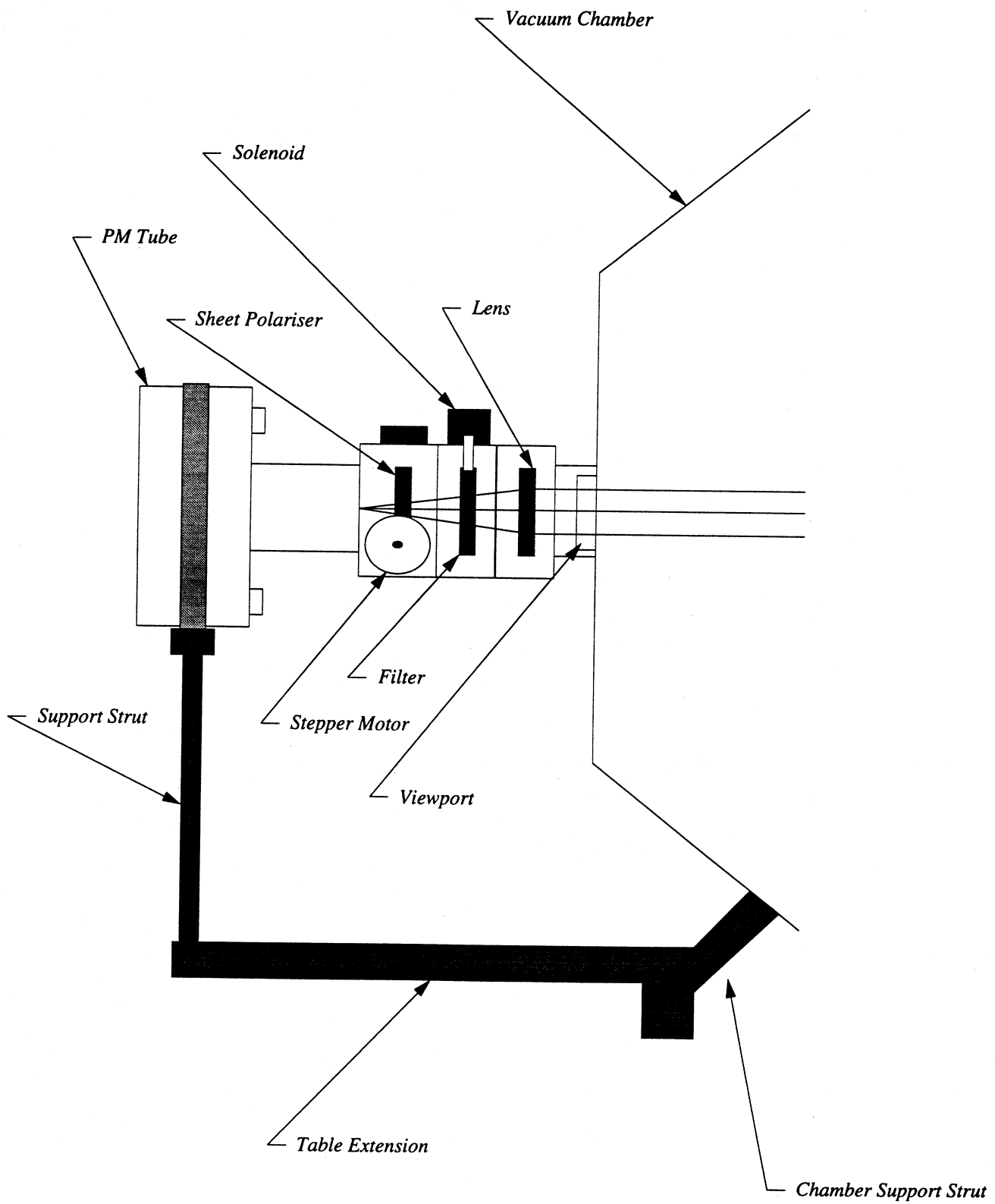


Figure 5.8: The Photon Detection System

photodiode which was used for an intensity reference. The other beam was directed into a Fabry-Perot etalon. The fringes of the Fabry-Perot was monitored by a further photodiode. This photodiode provided an error signal to the servo loop when a frequency shift occurred. For the case of slow frequency changes caused by changes of the cavity length from environmental conditions, a galvo plate was used to correct the frequency change. In the case of a larger frequency change a Piezo-electrically driven mirror M3 could be used for frequency correction.

The tuning of the laser to the $3^2D_{5/2}$ state was performed by scanning electronics in conjunction with a Burleigh WA20 wavemeter. Further fine tuning was accomplished by the viewing the scattered stepwise fluorescence via an infrared viewer. A filter was required due to the large background fluorescence from the first laser step. This laser was also interfaced to the IMB PC clone which enabled via an interface, to scan the frequency of the laser. Both the ring and the pump laser were mounted to a Newport Research 8 optics table.

5.7 The Photon Detection System

The determination of the line polarisation of the scattered fluorescence required a photon detection system which was mounted on one of the vacuum chambers viewports. The photon detection system may be seen in figure 5.8. The system consisted of a lens which focussed the fluorescence from the interaction region via a filter and a sheet polariser to a photomultiplier tube. The optical elements were all encased within a brass cylinder which reduced the amount of background light.

Light from the interaction region was collimated by the use of a 100 mm biconvex lens. A selection of filters were positioned in cradle which was connected to a solenoid. The solenoid could either be operated manually or by computer and enabled the positioning of one of two narrow band frequency filters to be inserted into the photon path when stepwise laser excited

experiments were performed. In the case of single step experiments only one filter was required and the solenoid remained in one position.

A sheet polariser following the filter arrangement was rotated by the use of a small stepper motor which was mounted to the brass tube. The stepper motor was interfaced with a laboratory computer which would rotate the polarisation axis of the sheet polariser to the desired positions for the line polarisation measurements, that is, either parallel or perpendicular to the quantisation axis.

Following the sheet polariser was a photomultiplier tube. Initially, for single step experiments, the PM tube was a Phillips 150AVP 26mm diameter fast photon counting photomultiplier tube operated at 1800V which was supplied by an Ortec 556 high voltage power supply. This PM tube was optimised to give high gain and good efficiency in the photon counting mode. Typical output pulses were of the order of 100-200 mV with a rise time of approximately 2ns. The entire PM tube was mounted in a brass casing which was held in place by a support strut from the chamber and by grub screws on the tube containing the lens, filters and sheet polariser.

Stepwise experiments required detection of fluorescence in the infrared and required a PM tube with a sensitivity in this region of the spectrum. A Hamamatsu R2949 photomultiplier tube was used for this case and was chosen for its high gain in the infrared region. This PM tube had a side window and featured low dark counts and high quantum efficiency. To reduce noise, the photocathode was negatively biased at -700V and the PM tube operated also in photon counting mode.

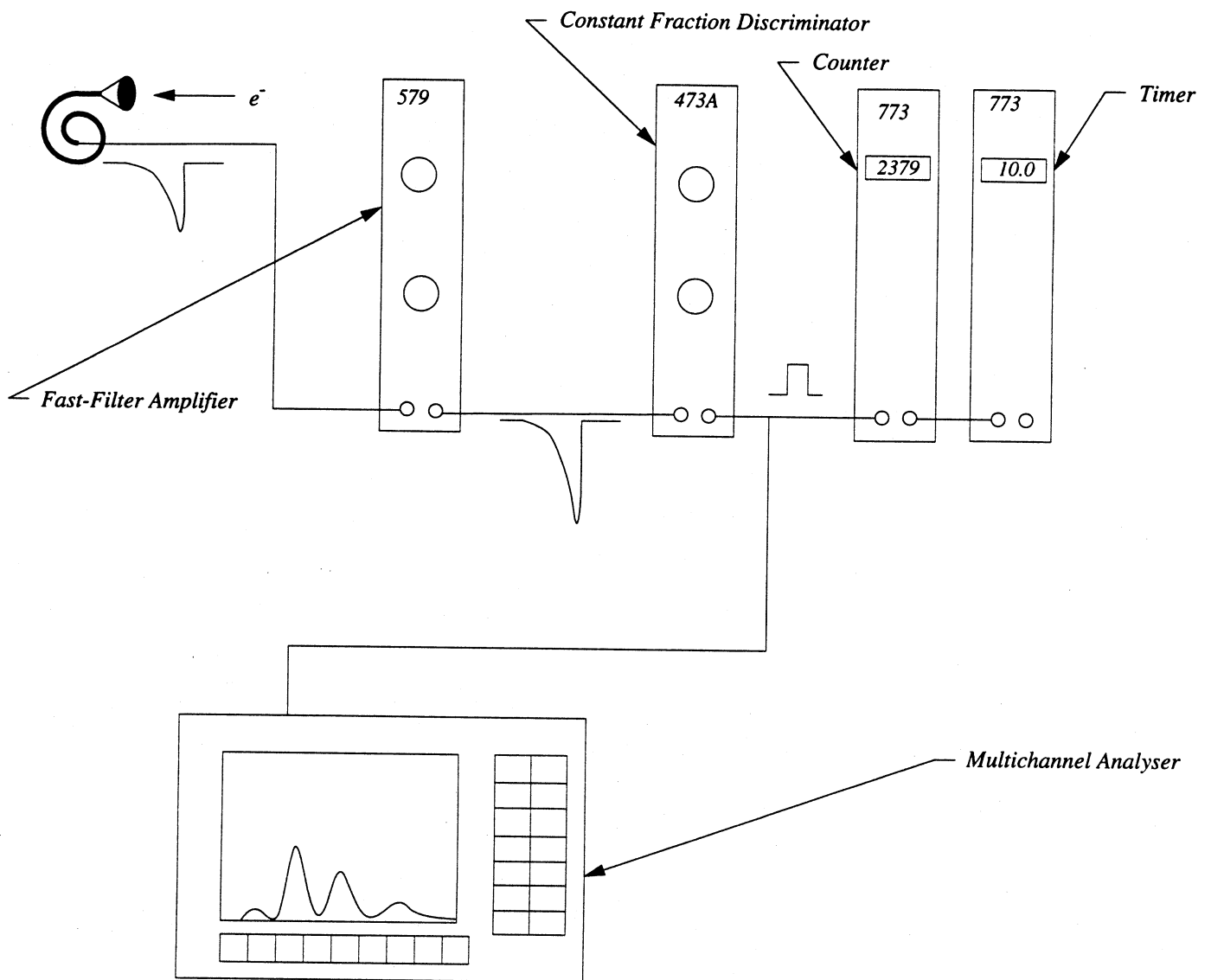


Figure 5.9: The Detection Electronics

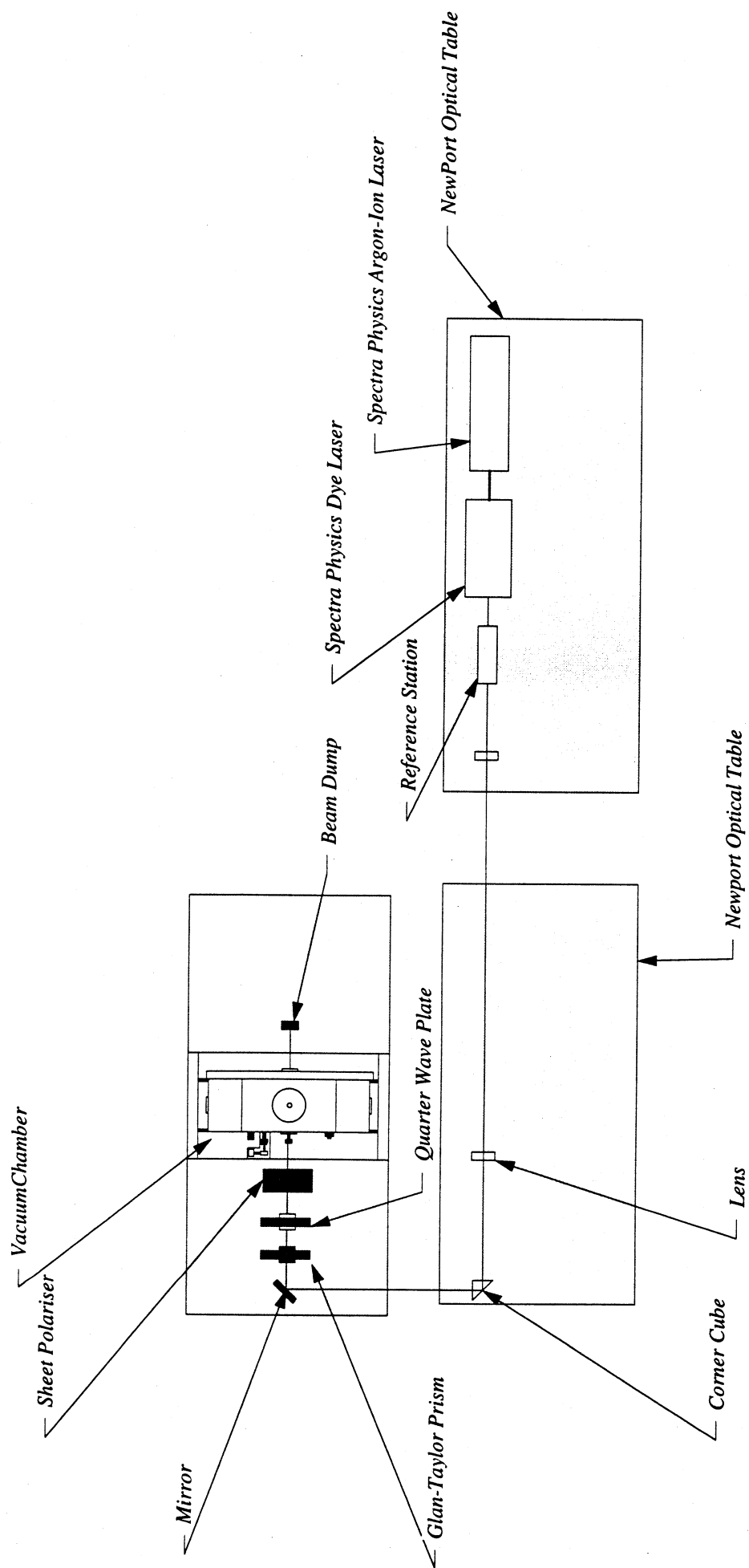


Figure 5.10: The Optics Configuration for the Superelastic Scattering Experiment

5.8 Detection Electronics

The signals from both the electron and photon detection system required amplification and processing using standard NIM electronics. For the case of electron detection, the detection arrangement is shown in figure 5.9. Signals from the channeltron of the order of negative 20mV were amplified by an Ortec 579 Timing Filter Amplifier to approximately 250mV so that the signal could be processed for noise suppression. Background noise was discriminated against by the use of an Ortec 473A Constant Fraction Discriminator. The Constant Fraction Discriminator produced a standard NIM output signal which was sent to either a set of Ortec 773 Timer/Counters or to an Ortec 197 MultiChannel Analyser. The multichannel analyser had 1024 channels and, for the present experimental arrangement, corresponded to an energy resolution per channel of 0.01eV. All of the NIM units were powered and operated within an Ortec 401A Bin power supply.

The electronics for the photon detection system were exactly the same as the electron detection system except that instead of the signal being sent to the multichannel analyser, it was monitored on a laboratory computer. The computer was able to store fluorescence scans in a similar manner to the multichannel analyser. The PC used a 12 bit DA converter which made a possible 4096 channels available.

5.9 The Polarising Optics

The production of correctly polarised light in a superelastic scattering experiment is of vital importance in the determination of the pseudo Stokes parameters. The polarising optics for the single step experiments may be seen in figure 5.10. The single step experiment required the use of either linearly or circularly polarised radiation. The laser beam, after passing the reference station, was collimated by the use of two fused silica symmetric convex lenses with a transmittance of 99.5% and was directed to the vacuum chamber via a corner cube and

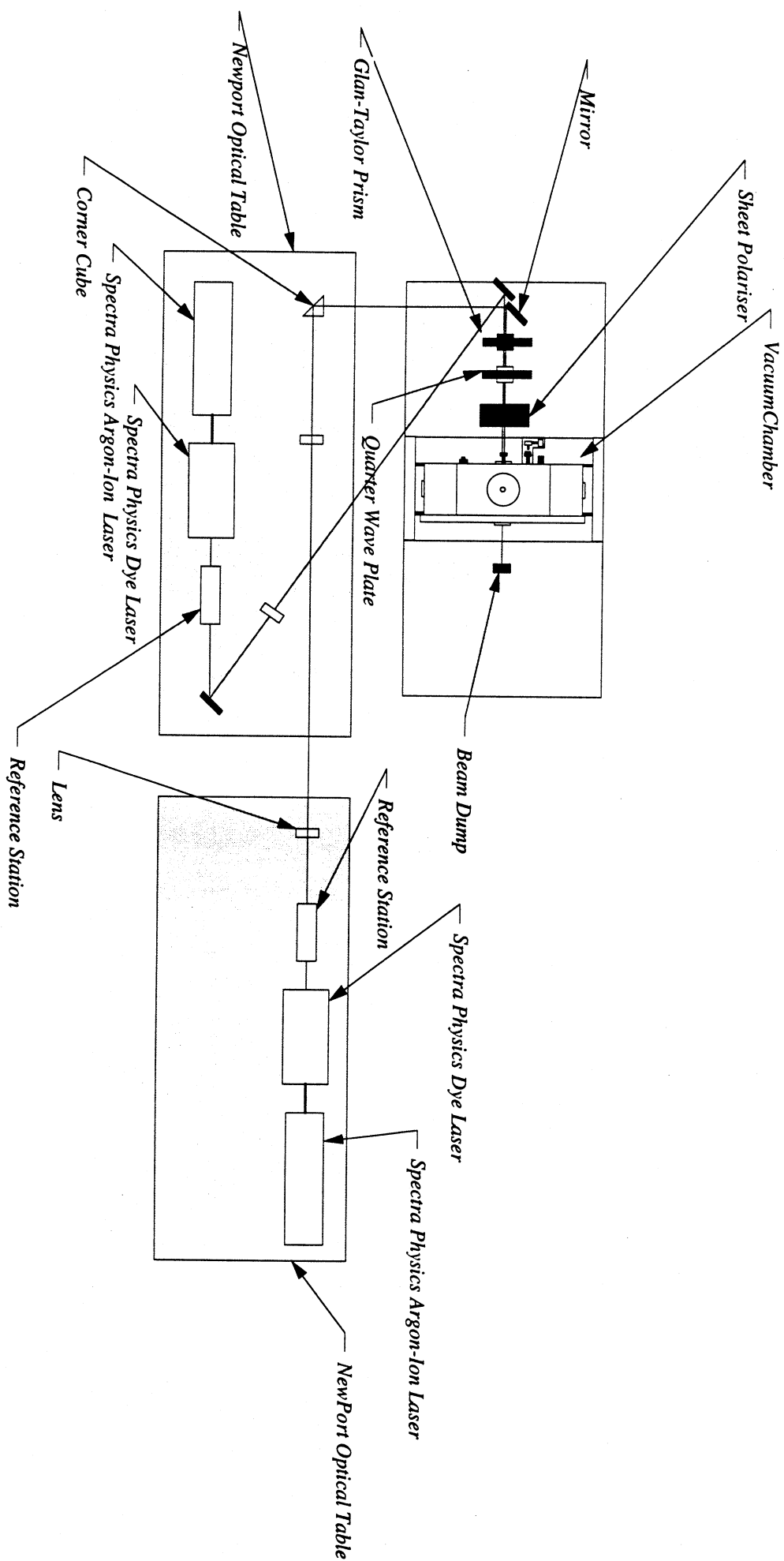


Figure 5.11: The Optics Configuration for the Folded Step Superelastic Scattering Experiment

a high reflective mirror. Prior to the beam entering the vacuum chamber it was passed through polarising optics. First was a Glan-Taylor prism polariser which corrected for depolarisation after reflection from the final mirror. The beam then passed through a B. Halle 589nm zero order mica quarter wave plate which had a bandwidth of 10nm and finally through a Melles Griot model 03FPG0-003 dichroic sheet polariser. The sheet polariser had a operating wavelength range of 350nm-700nm and was chosen over a prism polariser as this type of polariser does not displace the beam with rotation of the polarisation. They do however have the disadvantage of only a 33% transmission for a non polarised beam.

To test the quality of the quarter wave plate, a mirror replaced the sheet polariser and the laser beam was reflected back through the quarter wave plate. The optical axis of the quarter wave plate was then rotated to a position such that the reflected beam was extinguished thus indicating complete circular polarisation. One further check was to replace the sheet polariser and observe the power of the transmitted beam as its polarisation axis was rotated. Variations in the power with rotation indicated the beam contained some degree of linear polarisation and hence the optical axis of the quarter wave plate required minor adjustment.

When linearly polarised light was required for the single laser experiment, the sheet polariser was mounted in a stepper motor which could rotate the polariser to the desired angles for the pseudo Stokes parameter measurements and was controlled by the laboratory computer. For the case when circularly polarised light was required, the linear polariser was removed and the quarter wave plate was placed within a mount connected to a stepper motor.

Folded step experiments required the use of two dye lasers which the output laser beams were separated in frequency by 1.77 GHz. Because of this small separation both lasers could use the identical optics outlined above and the experiment could be configured so that both laser beams could co-propagate to the interaction region. This situation is depicted in figure 5.11.

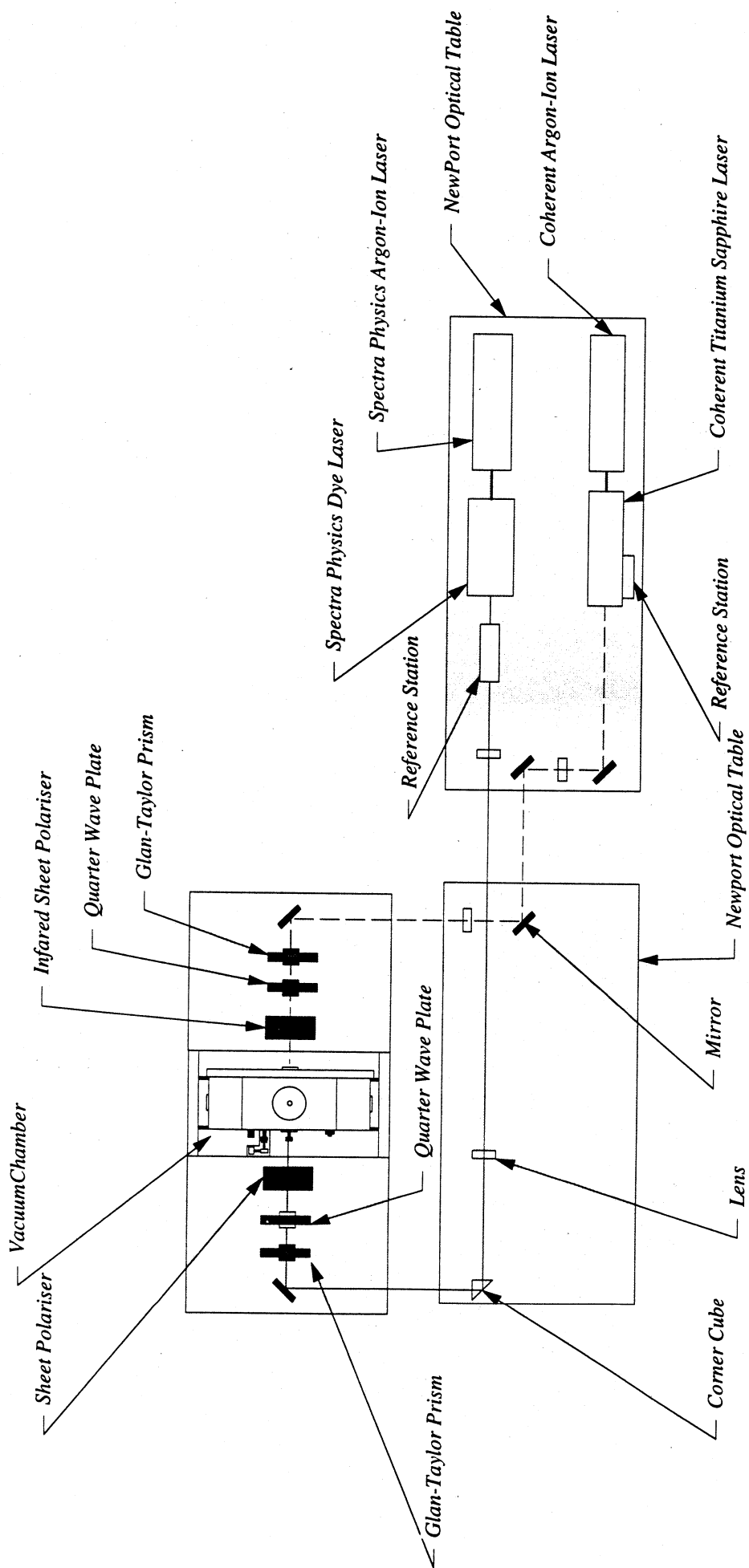


Figure 5.12: The Optics Configuration for the Stepwise Experiment

The stepwise superelastic scattering experiment required the use of both a dye laser and a titanium sapphire laser. The first laser transition required the use of the optics outline previously. The titanium sapphire laser produced a beam in the infrared at 820nm and required a further set of optics for this wavelength. A Glan-Taylor prism was used to re-polarise the beam after it had been directed via mirrors and lenses from the laser. To create circularly polarised light this beam was then sent through a zero order quartz quarter wave plate designed for a 800nm central wavelength. If linearly polarised light was required then the emerging beam would finally pass through a Polarcor sheet polariser. The Polarcor sheet polariser is an infrared sheet polariser designed for 90% transmission over a wavelength range of 740nm - 860nm. These infrared optics were arranged in the identical manner to that of the visible optical configuration, except that this laser beam was directed so that it travelled in a counter-propagating direction to the visible laser beam as is shown in figure 5.12.

5.10 Superelastic Scattering Experiment Protocol and Procedures

The experiment involved arranging the intersection of an atom beam, electron beam and laser beam. The alignment of the electron gun was outline previously in section 5.4. This served as a reference and the atomic beam was aligned by placing a target in the orifice of the oven's nozzle. The oven was then positioned such that the centre of the target crossed the path of the light beam produced by a spot light behind the alignment hole of the electron gun. Once this was accomplished the oven was aligned. The alignment of the laser beam was performed with the system evacuated and once an energy loss spectrum was obtained. The system typically required 24 hrs to reach the pressures required for experiments and once this pressure was obtained the heater coils in the oven were then switched on and the temperature then raised to the usual operating conditions. The current in the filament of the electron gun was then raised to the operating current. Care had to be taken at this point because a rapid rise in the current of the filament could take the current higher than threshold for burn out of the filament. It was necessary once the filament was at operating conditions to allow enough time for stabilisation of the emission current.

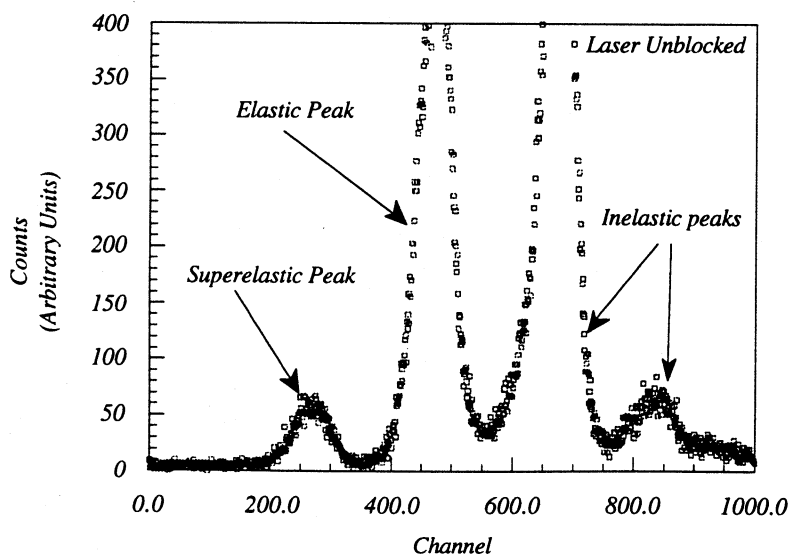
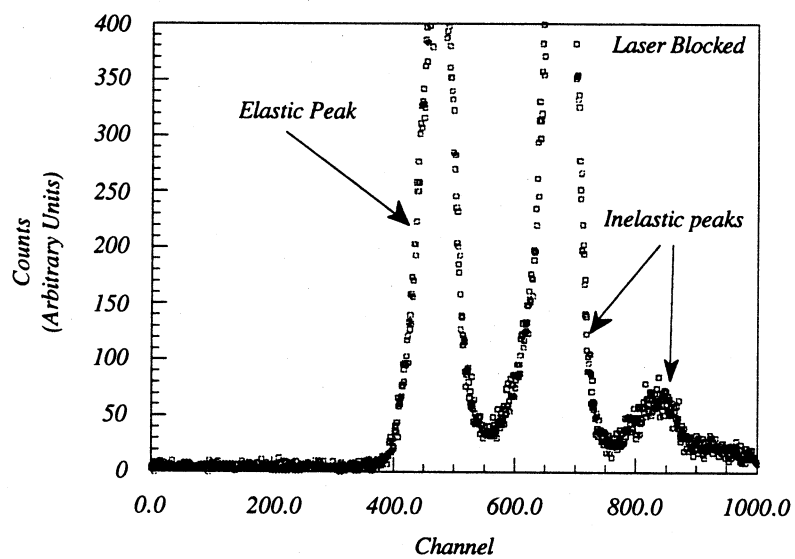


Figure 5.13: Energy Spectrum with Laser Blocked and Laser Unblocked

The electron gun was initially tuned by optimising the emission current on each of the lens elements using a Keithley 485 picoammeter with the gun at zero degree scattering angle. Once the current was optimised on the last lens element, the current on the cone of the electron energy analyser was monitored. This element, under normal conditions, was grounded via an electrical connection to a common ground which was external to the vacuum chamber. The electron gun once tuned, was then rotated to the desired scattering angle and the voltage to the channeltron applied. The electron analyser was then tuned by scanning the voltage on the backplate of the monochromator so that the intensity of the inelastically scattered electrons could be measured. The lens elements of the analyser were then tuned to maximise this signal and once this was accomplished the laser beam could be injected into the vacuum chamber.

The laser was initially tuned using a Burleigh WA20 wavemeter to the $3^2S_{1/2} \rightarrow 3^2P_{3/2}$ transition. The laser beam was directed into the vacuum chamber via a set of mirrors, corner cubes and some polarising optics as discussed in section 5.9 and was fine tuned by viewing the fluorescence emitted through spontaneous emission. The back plate of the electron analyser would then be then set such that the superelastically scattered electrons could be counted. Fine tuning of the electron analyser was then performed which was followed by sight adjustments of the position of the laser to maximise the superelastic electron count rate. Figure 5.13 shows two typical energy spectrums with 20eV incident electron energy at 15° scattering angle. The first spectrum is a typical energy loss spectrum which shows an elastic peak and inelastic peaks due the electron excitation of higher lying states. After inserting laser radiation tuned to the transition of interest, a further peak appears which is shown in the second diagram. This peak is to the left of the elastic peak which is opposite to the inelastic peaks which is in the energy gain region of the spectrum and hence is due scattered electrons which have gained energy.

All data collection was made under computer control using an IBM compatible XT clone and the data collection used the following protocol. The backplate of the analyser was set to the voltage which corresponded to the maximum superelastic count rate. The data collection

program was then run for a predetermined time and the user was required to input the following parameters: number of measurements, data file name, polariser offset and the polariser angles for the pseudo Stokes parameter being measured. In most experimental runs, the counting time used was 10 seconds.

After the user defined input, a background count was taken. The laser beam was blocked via a beam stop connected to a solenoid. When superelastic count rates were taken the beam stop would be retracted so that the laser could pass and for the case of linearly polarised light a sheet polariser was rotated to the first of the desired polarisation angles. Three sets of counts would be then taken after which the polariser was rotated to the second polarisation angle and a further three sets of counts were taken. Finally the solenoid reinserted the beam block so that one further background measurement could be made. The data from this measurement was then saved to a floppy disk. Measurements requiring circularly polarised light required the rotation of a quarter wave plate as mentioned in the previous section and the same procedure would be implemented.

Any asymmetries in the polariser were checked by turning the sheet polariser by 180° and repeating the measurements. To within statistical error, the measurements were symmetric. Correct angular alignment of the electron gun was tested by measurements of the pseudo Stokes parameters at negative scattering angles which also yielded symmetrical results indicating that the electron gun had been correctly tuned and aligned.

Folded step experiments followed the identical procedure except that two lasers were used. The two exciting transitions were easily distinguished by the intensity of the scattered fluorescence with fluorescence from the transition connected to the $F'=1$ ground state the less intense. Data collection was performed using the laboratory computer which used the single step program and the identical experimental procedures were used. The results of both the single step experiments and folded step experiments are given in the following chapter and are compared to current theories as well as some previous experimental results.

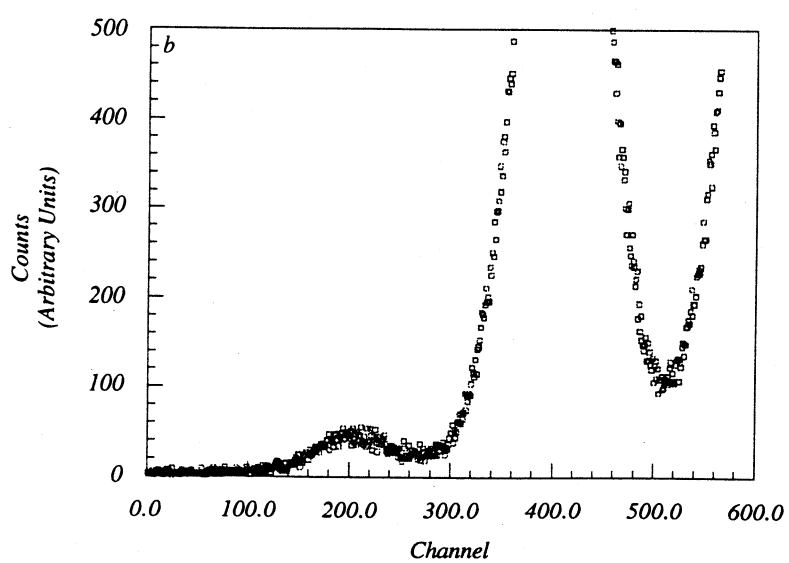
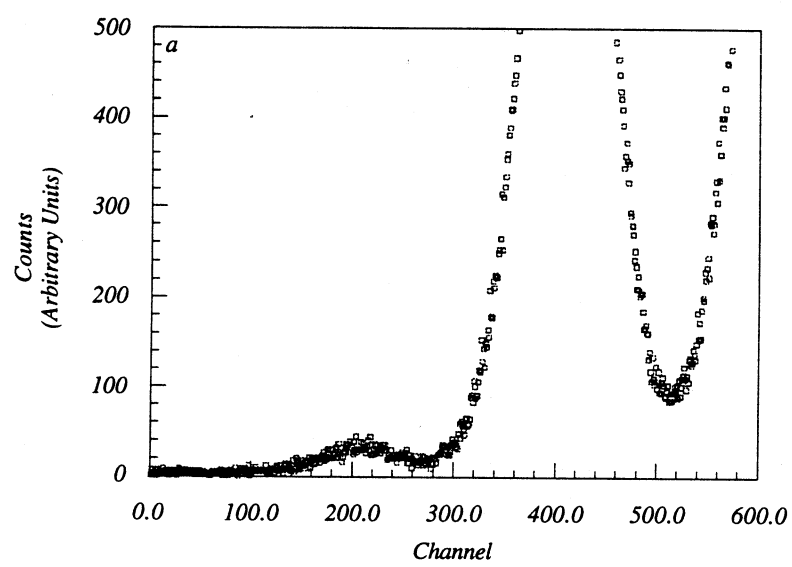


Figure 5.14: Stepwise Superelastic Energy Loss Spectrum

To obtain the reduced pseudo Stokes parameters, a measure of the optical pumping parameter K was required. In Chapter Three it was shown that the optical pumping parameter K was equivalent to the line polarisation of the fluorescence scattered perpendicular to the plane formed by the laser propagation direction and the polarisation vector of the laser. The laser beam was directed into the vacuum chamber via a set of mirrors and polarisers identical to that of the single step superelastic scattering experiment as discussed in section 5.9 so that it was vertically polarised. Scattered fluorescence was monitored via the photon detection system which was discussed in section 5.7. Data collection was accomplished using the laboratory computer which controlled the counter/timers, the photon detection system and a beam block. The program carried out measurements identical to that of a P_1 measurement except that instead of the laser polarisation being rotated, the fluorescence polariser was rotated.

Stepwise experiments involved the use of two lasers which were significantly different in wavelength. The tuning of the lasers was again accomplished using a wavemeter and fine tuning was performed by visual inspection of fluorescence. The first transition was same as the single step laser transition which was in the visible region of the electromagnetic spectrum. The second transition was monitored by an infrared viewer. Figure 5.14a shows an energy loss/gain spectra (each channel correspond to 0.01eV) with the infrared laser blocked and the usual symmetric superelastic peak may be seen. Figure 5.14b depicts an energy loss/gain spectra with both lasers injected. It shows that the superelastic peak has increased. The region between the superelastic peak and the elastic peak also displays an increase in counts. This increase is due to a convolution of the $3^2P_{3/2} \rightarrow 3^2S_{1/2}$ superelastic collision with the $3^2D_{5/2} \rightarrow 3^2P_{3/2\&1/2}$ electron de-excitation. $3^2D_{5/2} \rightarrow 3^2P_{3/2\&1/2}$ electron de-excitation corresponds to an electron energy gain of approximately 1.6eV so that both peaks do not exactly overlap.

Data again was taken using the aid of a laboratory computer which used a modified code of the single step program so that two polarisers were rotated. Background measurements were

taken with the infrared laser blocked. More detail about background subtraction is given in the next chapter. The computer program followed the same protocol as the single step experiment program. The results of these experiments are given in the next chapter.

Chapter 6

Experimental Results and Discussion

6.1 Introduction

The results of the experiments discussed in the previous chapters are presented here. The first section of the chapter gives the results obtained from single step and folded step superelastic scattering experiments most of which has been recently published in Sang *et al.* 1994, as well as a description of three current electron-atom collision theories with which the data is compared. The results presented include pseudo Stokes parameters measured at five incident energies with scattering angles ranging between (7° - 25°). This data is also compared to existing experimental data for electron-sodium collisions at 12eV and 20eV and it will be shown that there is a good agreement between two experimental groups while a third group has data that agrees in general except at 10° at an incident electron energy of 20eV. This is a well known discrepancy in the literature (Farrell *et al.* 1989) and part of the motivation behind these single step experiments was to remove this controversy and test for systematic errors. One of the test for errors included a check for finite volume effects (Zetner *et al.* 1989) and it will be shown that by using the combined results of co-planar and perpendicular geometry single step superelastic measurements, that no volumetric effects at the scattering angles investigated for this effect were evident.

The final section of the chapter deals with the stepwise superelastic scattering experiment discussed in Chapter Four. Stepwise pseudo Stokes parameters are measured for the D-P collision process with an electron incident energy of 20eV at three scattering angles. No comparison with theory can be made at present as there are currently no published theoretical results for this particular experiment in sodium.

6.2 Electron-Atom Collision Theories

There are many electron-atom scattering theories which may be applied to the electron-sodium collision processes. To select a theory which can be compared with validity to experimental data, requires a knowledge of the approximations used for that theory. At the low energy scale, that is, incident electron energies below the ionisation energy, it is seen that perturbative techniques such as Close Coupling calculations display excellent agreement with experiment. In this type of calculation the effect of the continuum is ignored and only a selected number of bound state potentials are taken into consideration. This calculation is accurate provided that all of the target states lying close to the initial and final states are included in the calculation. At high energies, other perturbation techniques such as the Born Approximation are more appropriate. These techniques rely on an approximation which basically assumes that there is little interaction between the target and projectile. Collisions involving intermediate energies are the most complicated collision process to model, as both the effects of the continuum and bound states play a large role in the scattering process. It is for this reason that experimentally measured Stokes parameters for sodium in the energy range of 10eV - 20eV have been previously taken and used to compared with theoretical calculations. There are many different of theories which model this energy regime. Some of the more recent calculations used for electron-sodium collisions include: the R-Matrix method, Distorted Wave Born Approximation, Second Order Distorted Wave Born Approximation (Madison *et al.* 1991, Madison *et al.* 1992), Coupled-Channel Optical method (McCarthy and Bray 1983, Bray *et al.* 1992) and Convergent Close Coupling method (Bray *et al.* 1994).

The new experimental results presented in this thesis cover the energy range of 10eV-30eV and these results are compared to a 15 state Close Coupling calculation (Bray *et al.* 1992), Coupled-Channel Optical method (McCarthy and Bray 1983, Bray *et al.* 1992) and finally the Second Order Distorted Wave Born Approximation (Madison *et al.* 1991, Madison *et al.* 1992). A brief summary of each theory is given below:

Close Coupling Calculation:

The total wavefunction for the system of projectile and the target is expanded in terms of a complete set of eigenfunctions ψ_o of the target Hamiltonian. An accurate knowledge of these eigenfunctions is required. The collision of an electron with an N-electron atom, wave function of the system may be written as (McDaniel 1989)

$$\psi(r_1, r_2) = A \sum_{\gamma} F_{\gamma}(r_1) \psi_o(\gamma, r_2) \quad (6.1)$$

where r_1 represents the spatial and the spin coordinates of the electron and r_2 the coordinates of the atomic electrons. All possible combinations of good quantum numbers of the total system is given by γ . A is an antisymmetrizing operator which allows the total wavefunction to be antisymmetrized. The coefficients $F_{\gamma}(r_1)$ describe the radial motion of the electron relative to the target atom in its various quantum states. The number of terms chosen in equation (6.1) designates the number of channels considered and in the Close Coupling approximation only a limited number of terms are used.

The radial partial wave scattering functions $F_i(r)$ in equation (6.1) satisfy a set of coupled integrodifferential equations of the form (McDaniel 1989)

$$\left[\frac{d^2}{dr^2} + k_i^2 - \frac{l_i(l_i+1)\hbar^2}{2m_e r^2} \right] F_i(r) = \sum_{j=1}^m V_{ij}(r) F_j(r) + \int_0^{\infty} W_{ij}(r, r') F_j(r') dr' \quad (6.2)$$

where V_{ij} is a direct electron-electron plus electron-nucleus potential, and W_{ij} is known as an exchange kernel and accounts for the possibility of exchange between the incident and target electrons. r' refers to the exchanged electron. This form of calculation is accurate provide that all of the target states that are lying close to the initial and final states in energy are included. Difficulties arise as the impact energy is increased as more states become

accessible. This can greatly increase the number of terms in the expansion to a point where the problem becomes intractable.

Second Order Distorted Wave Born Approximation

The description given here follows that of Madison *et al.* 1992. In this calculation for electron-sodium collisions, the sodium atom is essentially treated as a one electron atom, with the other ten electrons representing a frozen inert core which enables the sodium atom to be treated in a similar sense to that of hydrogen. The T-matrix, the elements of which are proportional to scattering amplitudes, may be written to second order as

$$T_{fi} = T_{fi}^1 + T_{fi}^2 \quad (6.3)$$

where T_{fi}^1 is the first order amplitude which may be expressed as

$$T_{fi}^1 = D + (-)^S E \quad (6.4)$$

D and E are direct and exchange amplitudes and S correspond to a particular channel. $S = 0, 1$ refers to singlet and triplet channel respectively. T_{fi}^2 is the second order amplitude and is given by (Madison *et al.* 1992)

$$T_{fi}^2 = 2 \langle \chi_f(0) \psi_f(1) | [V - U_f(0)] A [E^+ - K]^{-1} A [V - U_i(0)] | \psi_i(1) \chi_i^+(0) \rangle \quad (6.5)$$

$\psi_i(1)$ and $\psi_f(1)$ are the initial and final atomic state wavefunctions respectively for the single active electron, U_i and U_f are the initial and final distorting potentials which are used to determine the initial (χ_i) and final (χ_f) state distorted waves. V is the interaction potentials between the incident electron and the target atom, $[E^+ - K]^{-1}$ is the free particle Green's function and A is an antisymmetrizing operator for particles 0 and 1. The two antisymmetrizing operators in equation (6.5) produce four terms which enables equation (6.5) to be rewritten as

$$T_{fi}^2 = DD + (-)^S DE + (-)^S ED + EE \quad (6.6)$$

where DD is the second order direct scattering amplitude, DE correspond to a direction collision process followed by an exchange collision process, ED is the reverse situation to this i.e. exchange first followed by a direct process and EE is two exchange collisions.

The primary difficulty with this calculation is the evaluation of the Green's function which may be expanded as

$$[E^+ - K]^{-1} = [E^+ - h_a - T_p]^{-1} \quad (6.7)$$

where h_a and T_p are the Hamiltonians of the target atom and incident electron respectively.

The usual mechanism is to use a complete set of eigenfunctions of both particles to evaluate the Green's function. The inclusion of all eigenfunctions creates many terms in the integration and the number of terms is reduced by the separation of the active electron from core electrons by applying the frozen core approximation.

The distorted waves contain static spherically symmetric distorting potentials for the sodium atom, either in the ground state or the final excited state. Because sodium is a multi-electron atom, it may be polarised and as such the effect of this atomic polarisation on the incident electron must be included. The distorted waves must also be able to differentiate between incident particles such that they can distinguish between an electron and an otherwise equivalent particle that is not an electron. For many electron atoms, the wavefunctions of these two particles may be very different (Madison *et al.* 1992). This is corrected for by the addition of an extra distorting potential labelled the exchange distortion which takes into account the identical nature of several electrons.

It is expected that the Second Order Distorted Wave Born approximation will show good agreement with experiment at high energies. At lower energies Madison *et al.* 1991 have concluded that the calculation was accurate for hydrogen at 30eV which is of the order of 2-3 times the ionisation energy potential of that atom. Applying the same approach to sodium would imply that this calculation be accurate from 10eV-15eV.

Coupled-Channel Optical Method:

The Coupled-Channel Optical method is basically a generalisation of the Close Coupling formalism. In the Coupled-Channel Optical method, a finite set of low lying target discrete states are coupled together in a space called P space. Unlike the Close Coupling approximation, this calculation includes higher lying bound states and the continuum which are represented in a second space labelled Q space. The Q-space states are taken into account by using a complex non-local polarisation potential which is calculated *ab initio* in the weak coupling approximation (Bray *et al.* 1991). This approximation implies that there is no coupling between Q-space states but allows couplings between P-space and Q-space states.

The computation of this solution is accomplished via the Lippmann-Schwinger equation which is recasted into momentum space. This equation constitutes a reformulation of the scattering problem and only good solutions can be obtained with good initial wavefunctions and by using the appropriate potential. It is usual in this calculation to treat the electron-sodium problem as a three body problem of a frozen inert core, one outer shell electron and one projectile electron and to include the effects of distorted waves due to the target atom potential.

McCarthy and coworkers claim that this theory should be accurate over all energy ranges and that the computation time of the method is significantly reduced as only relatively few P states are required (Bray *et al.* 1992). The limiting factor to this calculation is to determine the number of states to include in P-space. Bray and Stelbovics 1992 have developed a method whereby they use the Close Coupling formalism to determine the minimum number

of discrete states so that numerical convergence occurs, after which they add the effects of the continuum. The theory compared here is labelled 15CCO6 which refers to 15 P space states and the 6 refers to the number of states which have continuum contributions.

6.3 Determination of Errors for the Measured Pseudo Stokes Parameters and Coherence Parameters

This section presents the method by which the uncertainties in the pseudo Stokes parameters and the coherence parameters $|\mu|$ and P_{TOT} were determined. The pseudo Stokes parameters were determined using equations (2.49) from the measurements of several superelastic differential cross sections. The total error of a function F that involves several measurements x_i is given by

$$\Delta F = \sqrt{\sum_i \left\{ \frac{\partial F}{\partial x_i} \Delta x_i \right\}^2} \quad (6.8)$$

The pseudo Stokes parameter P_I^S is defined in terms of superelastic differential cross section by equation (2.49). To obtain the superelastic differential cross section experimentally, a background subtraction was required and as such the definition of the pseudo Stokes parameter was modified to account for background subtraction. The experimentally measured pseudo Stokes parameter P_I^S may be redefined as

$$P_I^S = \frac{\sigma_{(0)} - \sigma_{(90)}}{\sigma_{(0)} + \sigma_{(90)} - 2\sigma_{(B)}} \quad (6.9)$$

where $\sigma_{(\alpha)}$ represents the measured electron count rate with the sheet polariser at the angles indicated. $\sigma_{(B)}$ represents the background electron count rate. The count rates are electron count rates and it is assumed that this counting process is Poisson such that the variance in the individual count σ is given by

$$\Delta\sigma = \sqrt{\sigma} \quad (6.10)$$

Applying equation (6.8) yields the following error in P_I^S :

$$\Delta P_I^S = \frac{2\sqrt{\sigma_{(0)}(\sigma_{(90)}^2 - 6\sigma_{(90)}\sigma_{(B)} + \sigma_{(B)}^2) + \sigma_{(90)}(\sigma_{(0)}^2 + \sigma_{(B)}^2) + \sigma_{(B)}(\sigma_{(0)}^2 + \sigma_{(90)}^2)}}{\{\sigma_{(0)} + \sigma_{(90)} - 2\sigma_{(B)}\}^2} \quad (6.11)$$

It follows that the measured P_2^S , P_3^S and their associated errors are given by

$$P_2^S = \frac{\sigma_{(45)} - \sigma_{(135)}}{\sigma_{(45)} + \sigma_{(135)} - 2\sigma_{(B)}} \quad (6.12)$$

$$\Delta P_2^S = \frac{2\sqrt{\sigma_{(45)}(\sigma_{(135)}^2 - 6\sigma_{(135)}\sigma_{(B)} + \sigma_{(B)}^2) + \sigma_{(135)}(\sigma_{(45)}^2 + \sigma_{(B)}^2) + \sigma_{(B)}(\sigma_{(45)}^2 + \sigma_{(135)}^2)}}{\{\sigma_{(45)} + \sigma_{(135)} - 2\sigma_{(B)}\}^2} \quad (6.13)$$

$$P_3^S = \frac{\sigma_{(RHC)} - \sigma_{(LHC)}}{\sigma_{(RHC)} + \sigma_{(LHC)} - 2\sigma_{(B)}} \quad (6.14)$$

$$\Delta P_3^S = \frac{2\sqrt{\sigma_{(RHC)}(\sigma_{(LHC)}^2 - 6\sigma_{(LHC)}\sigma_{(B)} + \sigma_{(B)}^2) + \sigma_{(LHC)}(\sigma_{(RHC)}^2 + \sigma_{(B)}^2) + \sigma_{(B)}(\sigma_{(RHC)}^2 + \sigma_{(LHC)}^2)}}{\{\sigma_{(RHC)} + \sigma_{(LHC)} - 2\sigma_{(B)}\}^2} \quad (6.15)$$

The coplanar parameter r was defined by equation (2.65) and experimentally was determined using the following formula

$$r = \frac{\sigma_{(para)} - \sigma_{(B)}}{\sigma_{(perp)} - \sigma_{(B)}} \quad (6.16)$$

where $\sigma_{(para)}$ and $\sigma_{(perp)}$ is the electron count rate measured with the laser polarisation parallel and perpendicular to the scattering plane respectively. Applying equation (6.8) and assuming Poisson statistics the following error formula is obtained:

$$\Delta r = \frac{\sqrt{\sigma_{(para)}(\sigma_{(perp)}^2 - 6\sigma_{(perp)}\sigma_{(B)} + \sigma_{(B)}^2) + \sigma_{(perp)}(\sigma_{(para)}^2 + \sigma_{(B)}^2) + \sigma_{(B)}(\sigma_{(perp)}^2 + \sigma_{(para)}^2)}}{\{\sigma_{(perp)} - \sigma_{(B)}\}^2} \quad (6.17)$$

The experimental data was accumulated over different run times which, depending on the stability of the system and the count rates at different scattering angles, could give different errors. To calculate a mean value of each pseudo Stokes parameter from a set of data, a weighted average was applied viz:

$$\langle P_i^S \rangle = \frac{\sum_{j=1}^n W_j P_{i(j)}^S}{\sum_{j=1}^n W_j} \quad (i = 1, 2, 3) \quad (6.18)$$

where

$$W_j = \frac{1}{\sigma^2(P_{i(j)}^S)} \quad (6.19)$$

W_j is a weighting factor for each individual measurement and $\sigma(P_{i(j)}^S)$ is the variance of the individual measurements. The variance of the mean weighted pseudo Stokes parameter is given by

$$\sigma(\langle P_i^S \rangle) = \sqrt{\frac{1}{\sum_{j=1}^n W_j}} \quad (6.20)$$

The averaging procedure used in this analysis was such that any data that was two standard deviations from the mean was rejected and a new mean and variance would be recalculated. The data present here is compared to theories which determine the reduced Stokes parameters and therefore to compare to theory requires the averaged pseudo Stokes parameters to be expressed as reduced Stokes parameters. The pseudo Stokes parameters share the following relationships with the reduced Stokes parameter (from this point onward the reduced Stokes parameters will be denoted as the Stokes parameters):

$$P_1 = \frac{P_1^S}{K} \quad (6.21)$$

$$P_2 = \frac{P_2^S}{K} \quad (6.22)$$

$$P_3 = \frac{P_3^S}{K'} \quad (6.23)$$

It was detailed in previous chapters that the parameter K' is taken as unity and the parameter K could be obtained through a series of line polarisation measurements or by using a combination of coplanar and perpendicular geometries (see section 2.6). The error in obtaining K through a series of line polarisation measurements is given by the P_1^S measurement as both experimental determinations are essentially the same except that the line polarisation experiments involve the measurement of photons rather than electrons as in the case of a P_1^S measurement. Using equation (6.8) enables the following error formulas for the Stokes parameters to be derived:

$$\Delta P_1 = \sqrt{\frac{\Delta P_1^S}{K^2} + \frac{P_1^2 \Delta K^2}{K^4}} \quad (6.24)$$

$$\Delta P_2 = \sqrt{\frac{\Delta P_2^S}{K^2} + \frac{P_2^2 \Delta K^2}{K^4}} \quad (6.25)$$

$$\Delta P_3 = \sqrt{\frac{\Delta P_3^S}{K'^2} + \frac{P_3^2 \Delta K'^2}{K'^4}} \quad (6.26)$$

The coherence parameters $|\mu|$ and P_{TOT} were defined in Chapter Two as functions of the pseudo Stokes parameters these may be redefined in terms of the Stokes parameters as

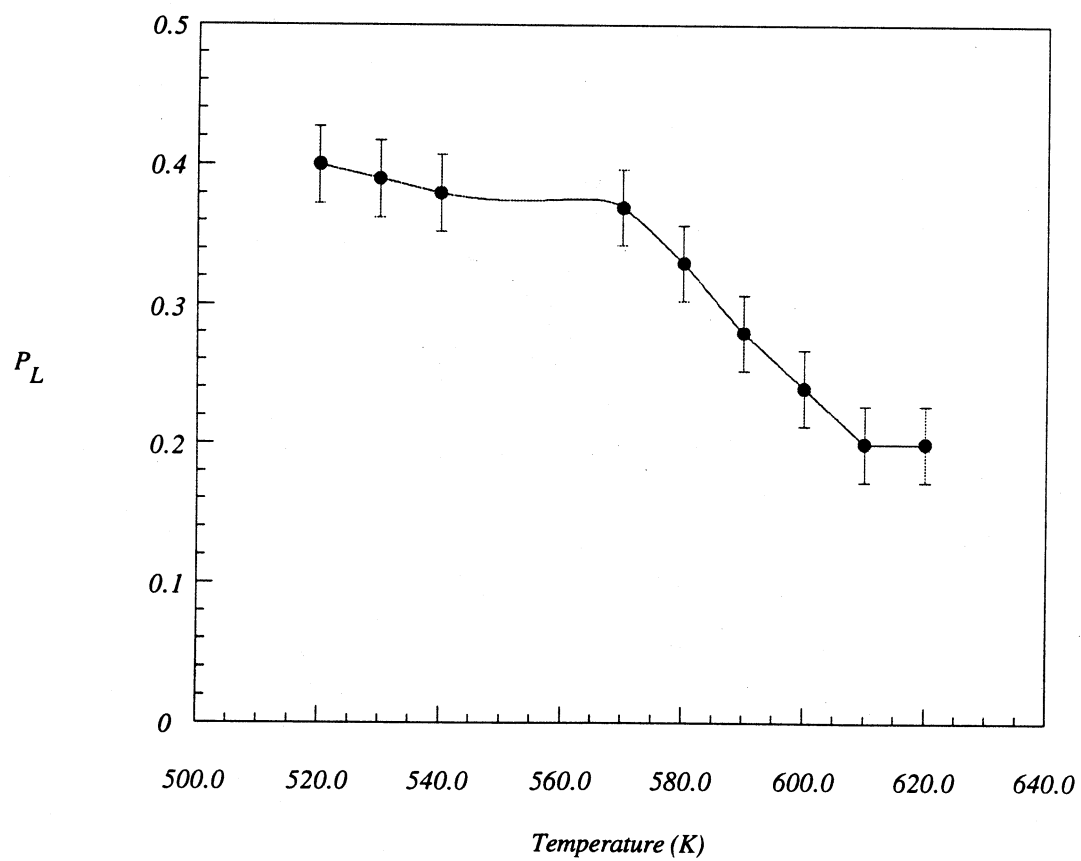
$$P_{TOT} = \sqrt{P_1^2 + P_2^2 + P_3^2} \quad (6.27)$$

$$|\mu| = \sqrt{\frac{P_2^2 + P_3^2}{1 - P_1^2}} \quad (6.28)$$

Applying equation (6.8) yields their associated errors as

$$\Delta P_{TOT} = \sqrt{\frac{P_1^2 \Delta P_1^2 + P_2^2 \Delta P_2^2 + P_3^2 \Delta P_3^2}{P_1^2 + P_2^2 + P_3^2}} \quad (6.29)$$

$$\Delta |\mu| = \sqrt{\frac{(P_2^2 + P_3^2) P_1^2 \Delta P_1^2}{(1 - P_1^2)^3} + \frac{P_2^2 \Delta P_2^2 + P_3^2 \Delta P_3^2}{(P_2^2 + P_3^2)(1 - P_1^2)}} \quad (6.30)$$



Graph 6.1: Line Polarisation Vs Temperature

Table 6.1

Comparison of the Optical Pumping Parameter K Determined Using Various Methods

<i>Scattering Angle</i>	<i>r</i>	<i>K_r</i>	<i>K_{OED}</i>	<i>K_{line pol}</i>
<i>10°</i>	<i>2.2±0.1</i>	<i>0.42±0.05</i>	<i>0.42</i>	<i>0.39±0.01</i>
<i>15°</i>	<i>2.2±0.03</i>	<i>0.39±0.04</i>	<i>0.42</i>	<i>0.39±0.01</i>

6.2(d) 25eV Data

θ_c	P_1^S	P_2^S	P_3^S	P_1	P_2	P_3	P_{TOT}	$ u $
7°	-0.30 ± 0.006	-0.21 ± 0.01	-0.11 ± 0.002	-0.769 ± 0.016	-0.539 ± 0.026	-0.11 ± 0.002	0.945 ± 0.098	0.86 ± 0.17
10°	-0.3 ± 0.002	-0.12 ± 0.002	-0.15 ± 0.02	-0.769 ± 0.005	-0.31 ± 0.05	-0.15 ± 0.02	0.842 ± 0.084	0.536 ± 0.098
15°	-0.28 ± 0.01	-0.08 ± 0.007	-0.24 ± 0.004	-0.718 ± 0.026	-0.205 ± 0.017	-0.24 ± 0.004	0.784 ± 0.077	0.454 ± 0.062
18°			-0.33 ± 0.003			-0.33 ± 0.003		
20°			-0.40 ± 0.007			-0.40 ± 0.007		
22°			-0.47 ± 0.01			-0.47 ± 0.01		
24°			-0.56 ± 0.04			-0.56 ± 0.04		

6.2(e) 30eV Data

θ_c	P_1^S	P_2^S	P_3^S	P_1	P_2	P_3	P_{TOT}	$ u $
5°			-0.07 ± 0.004			-0.07 ± 0.004		
7°	-0.27 ± 0.003	-0.22 ± 0.002	-0.09 ± 0.002	-0.692 ± 0.009	-0.564 ± 0.007	-0.09 ± 0.002	0.898 ± 0.09	0.791 ± 0.12
10°	-0.35 ± 0.002	-0.16 ± 0.019	-0.12 ± 0.004	-0.897 ± 0.005	-0.41 ± 0.05	-0.12 ± 0.004	0.99 ± 0.11	0.969 ± 0.43
15°	-0.35 ± 0.013	-0.07 ± 0.012	-0.26 ± 0.006	-0.897 ± 0.033	-0.18 ± 0.031	-0.26 ± 0.006	0.95 ± 0.1	0.716 ± 0.33

6.2(c) 20eV Data

θ_c	P_1^S	P_2^S	P_3^S	P_1	P_2	P_3	P_{TOT}	$ \mu $
7°	-0.261	-0.183	-0.084	-0.67	-0.47	-0.084	0.823	0.643
	± 0.008	± 0.004	± 0.01	± 0.02	± 0.01	± 0.01	± 0.09	± 0.09
10°	-0.269	-0.129	-0.11	-0.69	-0.33	-0.11	0.773	0.481
	± 0.008	± 0.004	± 0.01	± 0.02	± 0.01	± 0.01	± 0.08	± 0.07
15°	-0.3354	-0.109	-0.24	-0.86	-0.28	-0.24	0.936	0.723
	± 0.008	± 0.004	± 0.01	± 0.02	± 0.01	± 0.01	± 0.09	± 0.2
18°	-0.3354	-0.074	-0.38	-0.86	-0.19	-0.38	0.959	0.833
	± 0.008	± 0.004	± 0.01	± 0.02	± 0.01	± 0.01	± 0.09	± 0.25
20°	-0.261	-0.152	-0.47	-0.67	-0.39	-0.47	0.907	0.823
	± 0.008	± 0.004	± 0.01	± 0.02	± 0.01	± 0.01	± 0.07	± 0.09
22°	-0.25	-0.140	-0.58	-0.64	-0.36	-0.58	0.936	0.888
	± 0.008	± 0.004	± 0.01	± 0.02	± 0.01	± 0.01	± 0.06	± 0.08

Table 6.2(a) 10eV Data

θ_c	P_1^S	P_2^S	P_3^S	P_1	P_2	P_3	P_{TOT}	μ
7°	-0.297 ± 0.01	-0.276 ± 0.01	-0.12 ± 0.003	-0.761 ± 0.03	-0.708 ± 0.03	-0.12 ± 0.003	1.046 ± 0.11	1.106 ± 0.21
10°	-0.33 ± 0.01	-0.20 ± 0.02	-0.154 ± 0.006	-0.846 ± 0.03	-0.513 ± 0.05	-0.154 ± 0.006	1.001 ± 0.11	1.005 ± 0.30
15°	-0.31 ± 0.02	-0.12 ± 0.03	-0.25 ± 0.02	-0.795 ± 0.05	-0.308 ± 0.076	-0.25 ± 0.02	0.888 ± 0.10	0.653 ± 0.15
18°			-0.35 ± 0.016			-0.35 ± 0.016		

Table 6.2(b) 15eV Data

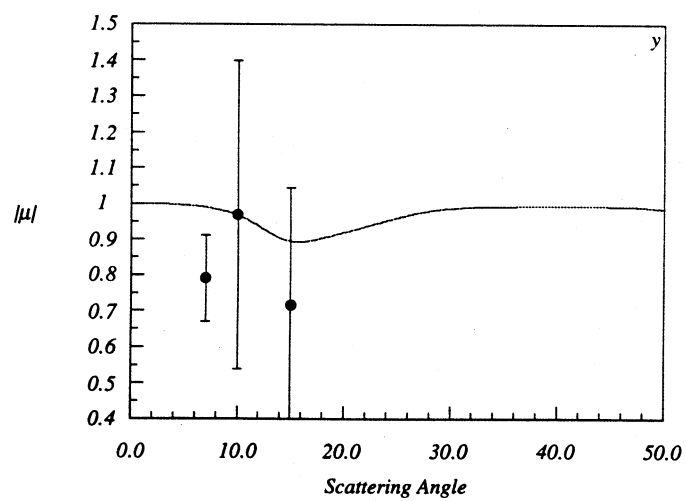
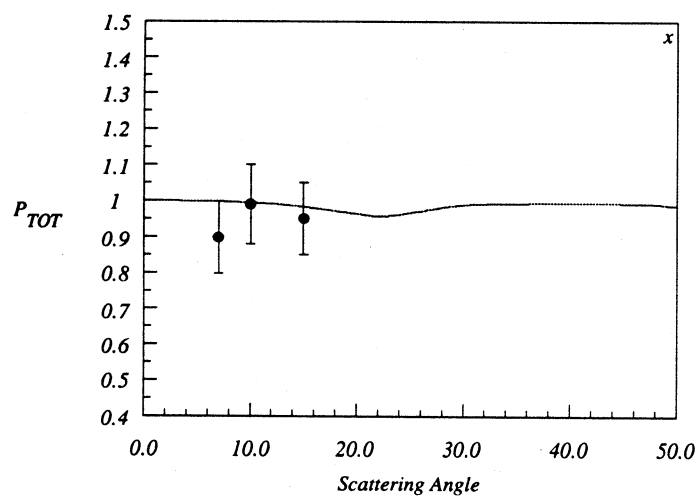
θ_c	P_1^S	P_2^S	P_3^S	P_1	P_2	P_3	P_{TOT}	μ
10°	-0.35 ± 0.003	-0.21 ± 0.002	-0.11 ± 0.002	-0.897 ± 0.008	-0.538 ± 0.005	-0.11 ± 0.002	1.0523 ± 0.1	1.25 ± 0.5
15°	-0.34 ± 0.01	-0.14 ± 0.007	-0.22 ± 0.006	-0.872 ± 0.03	-0.359 ± 0.02	-0.22 ± 0.006	0.968 ± 0.1	0.86 ± 0.3
18°			-0.30 ± 0.01			-0.30 ± 0.01		

6.4 Single Step and Folded Step Superelastic Scattering Experimental Results

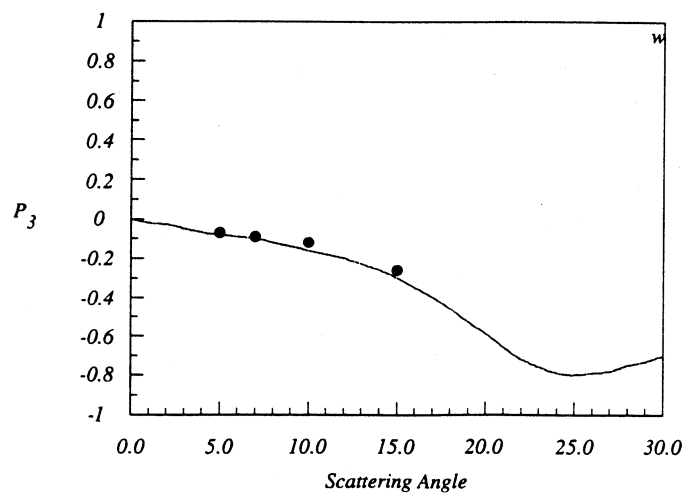
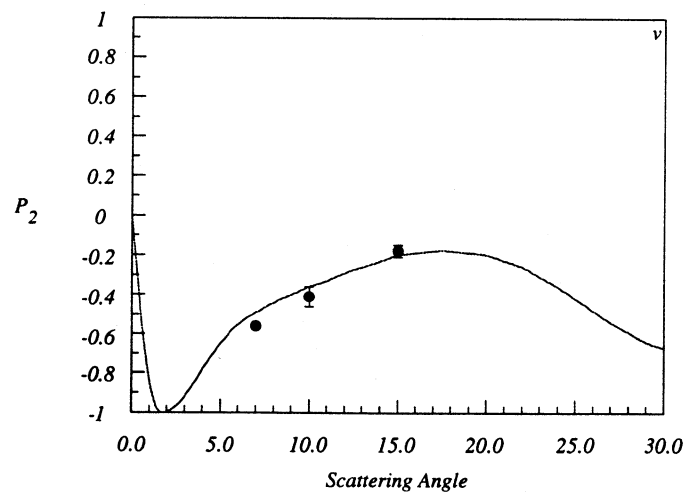
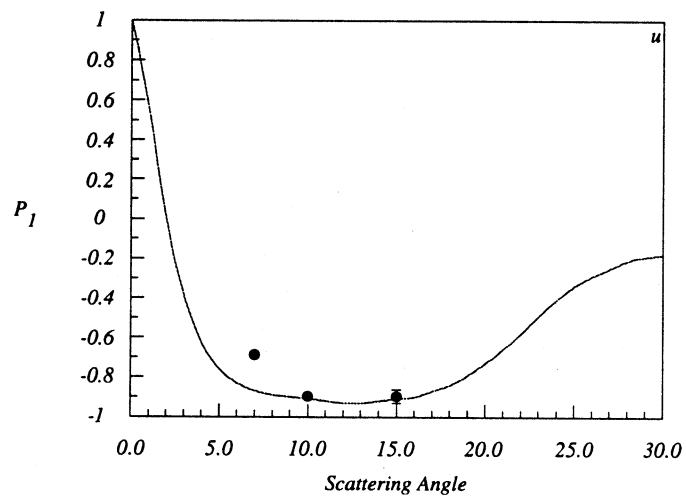
Graph 6.1 show the line polarisation as a function of temperature of the oven for a single laser. The laser was maintained with a constant intensity of 80 mW/mm^2 in the interaction region. The graph clearly displays that a low temperature the line polarisation takes a constant value of approximately 0.39. As the temperature is raised the line polarisation decreases in value as radiation trapping effects cause depolarisation. During experimental runs the temperature of the oven was maintained at 520K which clearly, from graph 6.1 is in a temperature region where the effects of radiation trapping are negligible. The line polarisation at this temperature was measured many times and gave an average value of $P_L = 0.39 \pm 0.01$ where the average value and error was obtained using the error analysis detailed in the previous section.

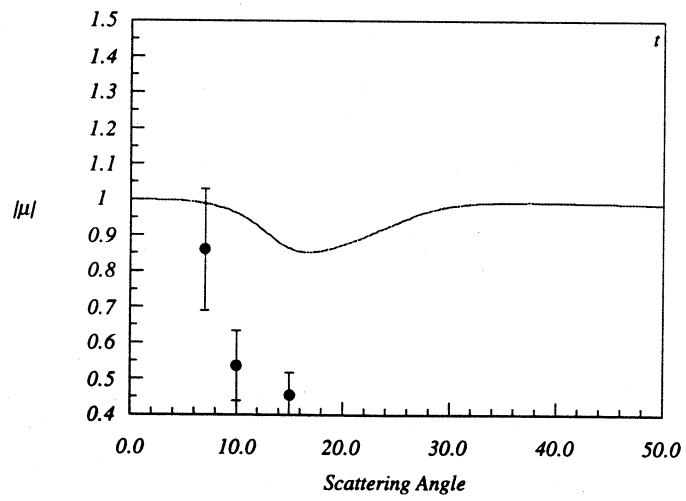
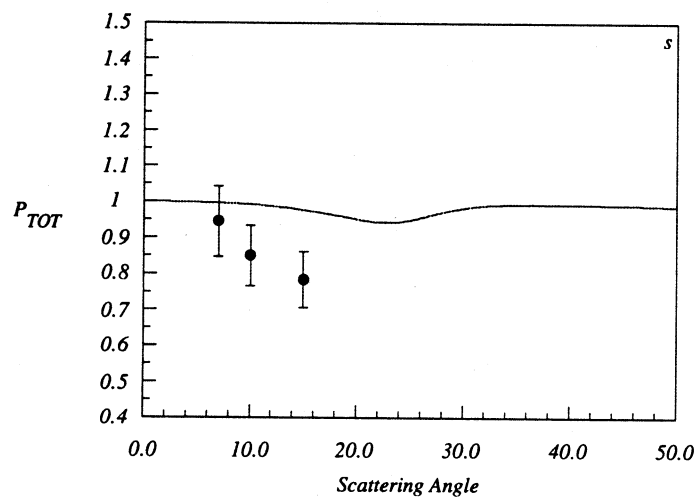
K was also determined using a combination of coplanar measurements of r and perpendicular measurements of P_I^S with an incident energy of 20eV at 10° and 15° scattering angle. These results as well as the calculated K , which were determined using equation (2.72), are given in Table 6.1. K_r is the K parameter determined using the experimentally determined r value. K_{QED} is the theoretically determined K value from Chapter Three and $K_{line\ pol}$ is the K parameter determined using the line polarisation experiment. Good agreement is seen with the experimentally determined K parameters and the K parameter determined using the QED theory.

Single step and folded step experimentally determined Stokes parameters are given in Table 6.2. All of the data except at 20eV at angles greater than 18° are single step superelastic measurements. The K value used for the single step measurements was the value determined using the coplanar measurements at 15° scattering angle. K' was taken as unity. For those angles greater than 18° , the folded step excitation mechanism was used and therefore required the determination of the optical pumping parameter \bar{K} . The Stokes

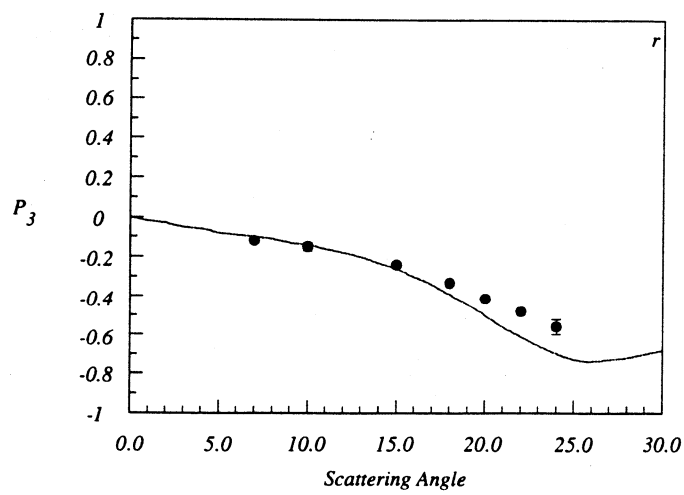
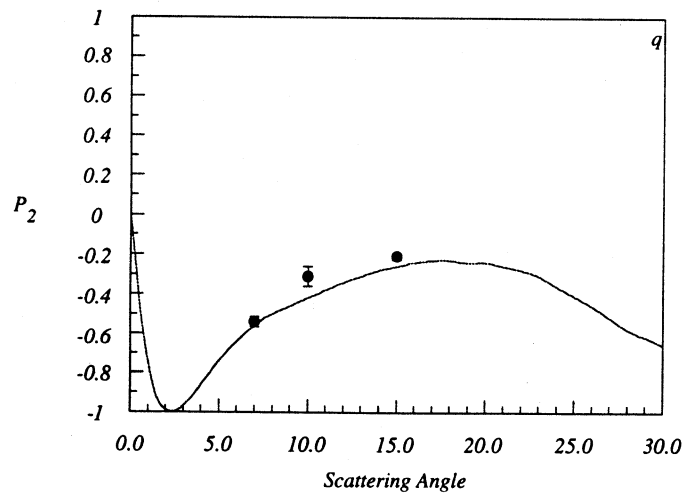
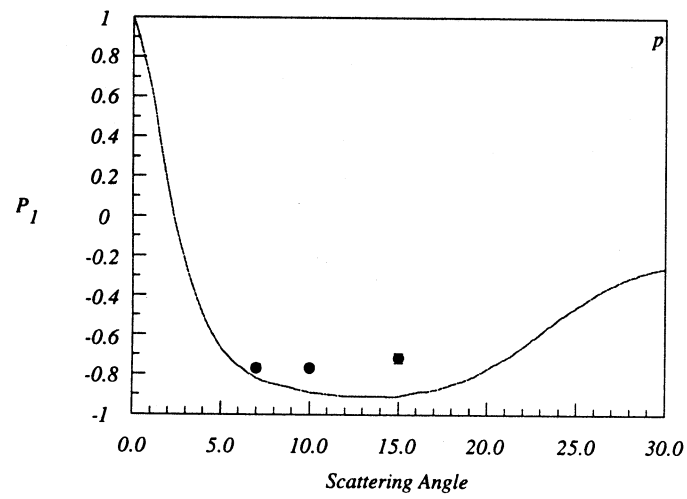


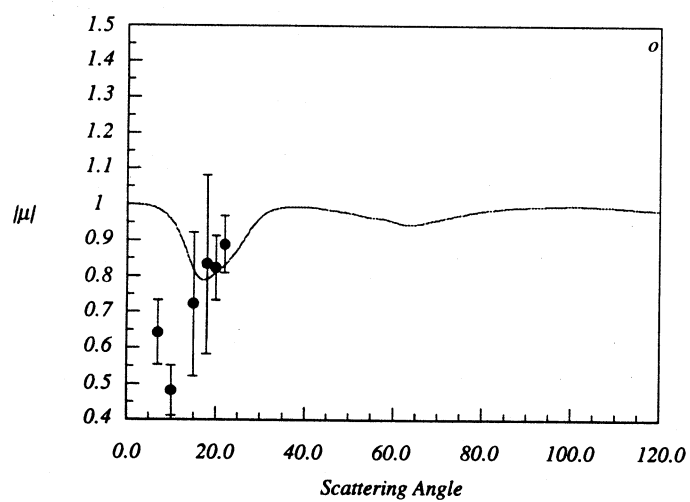
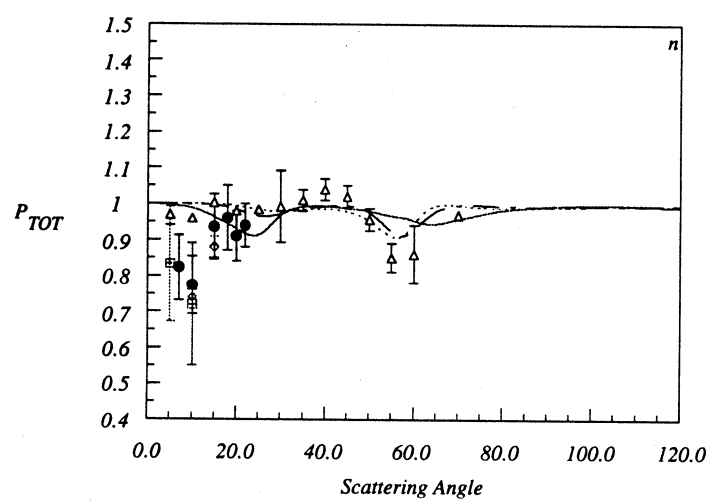
30eV



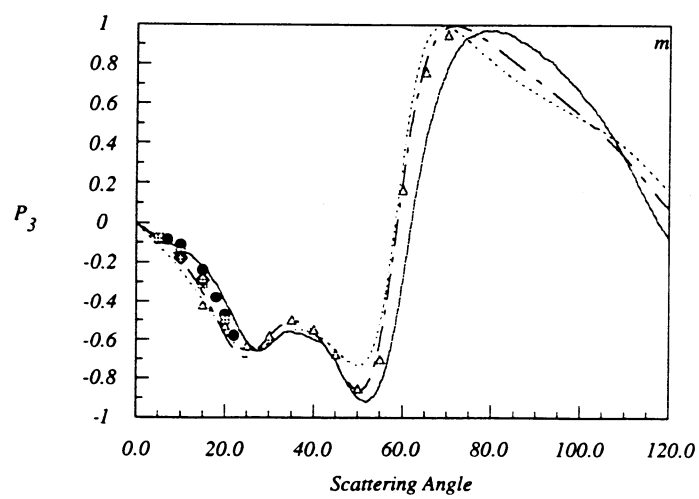
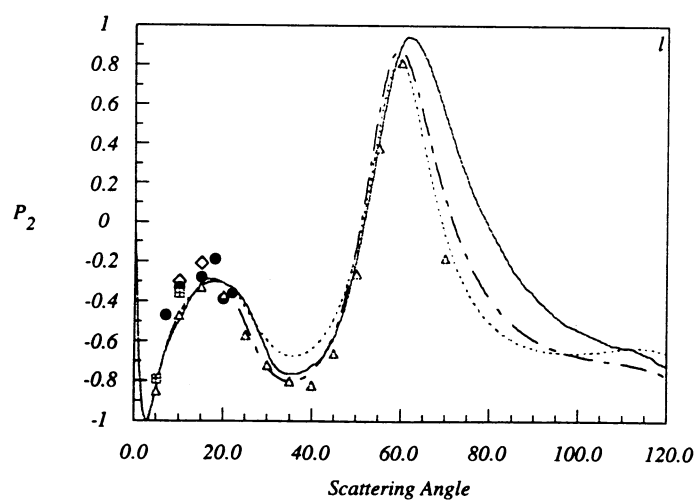
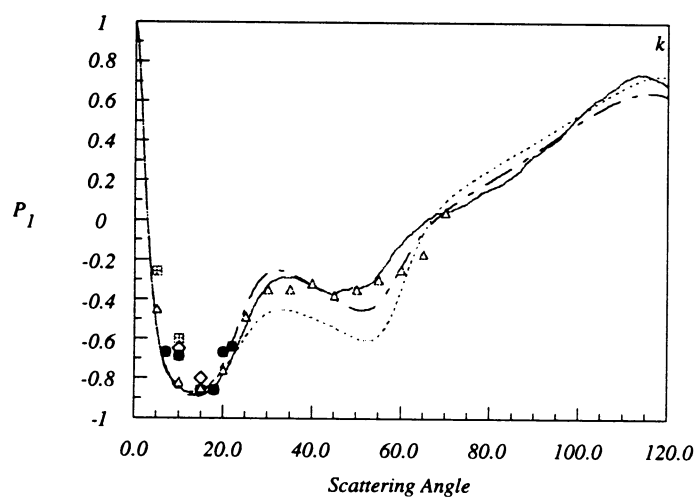


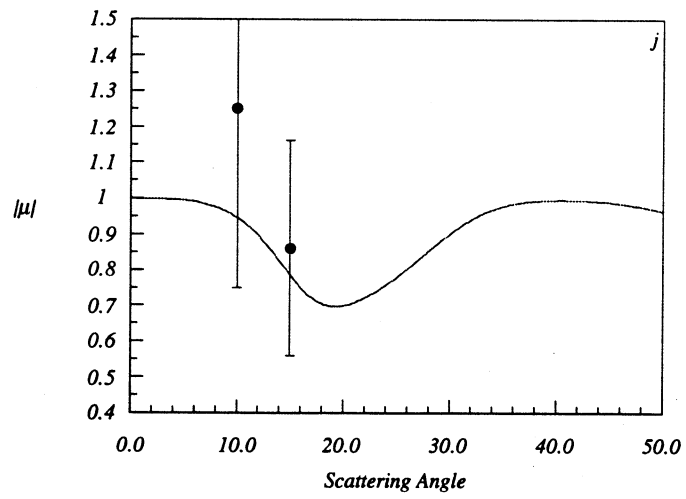
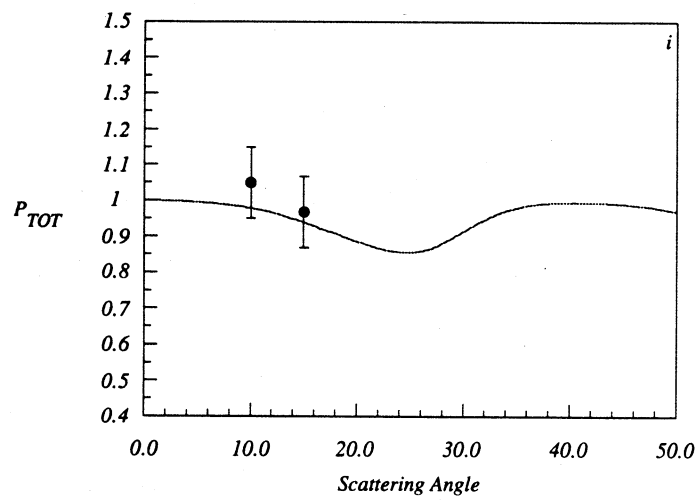
25eV



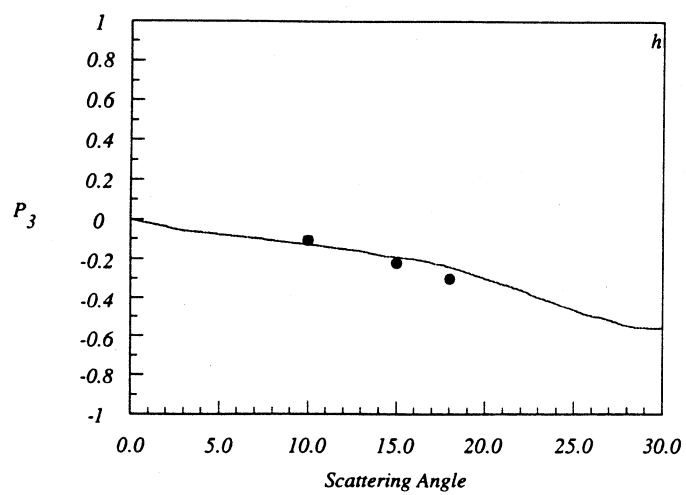
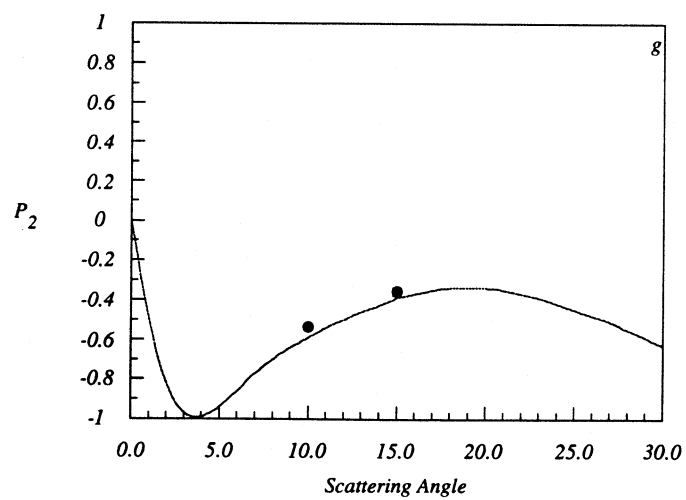
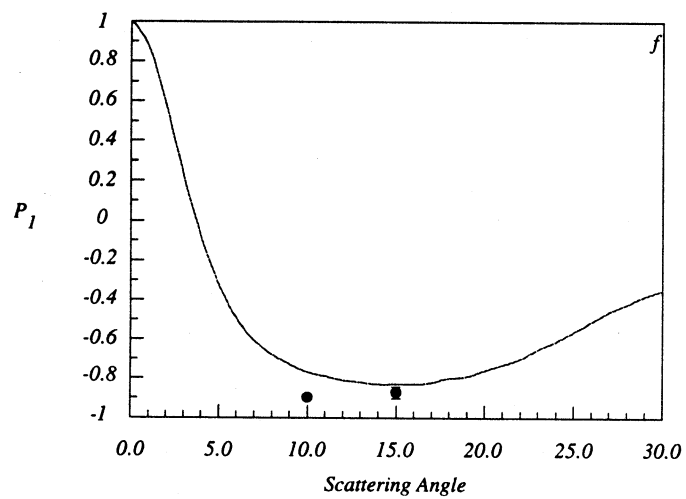


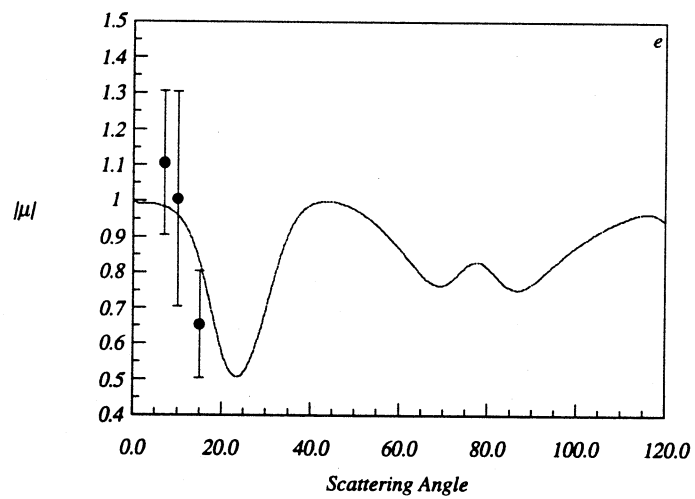
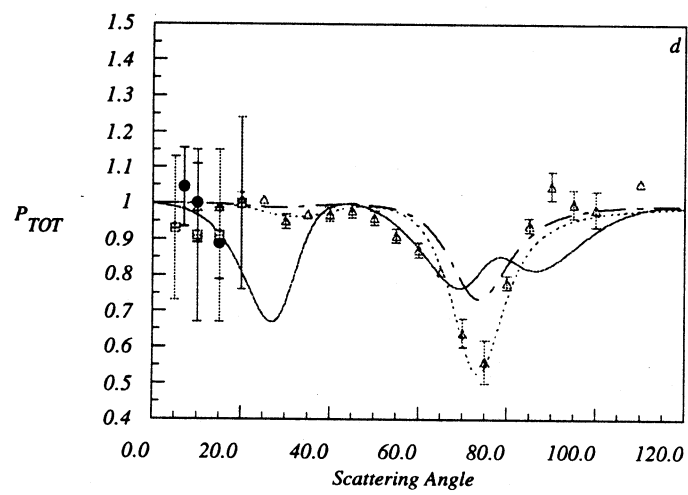
20eV



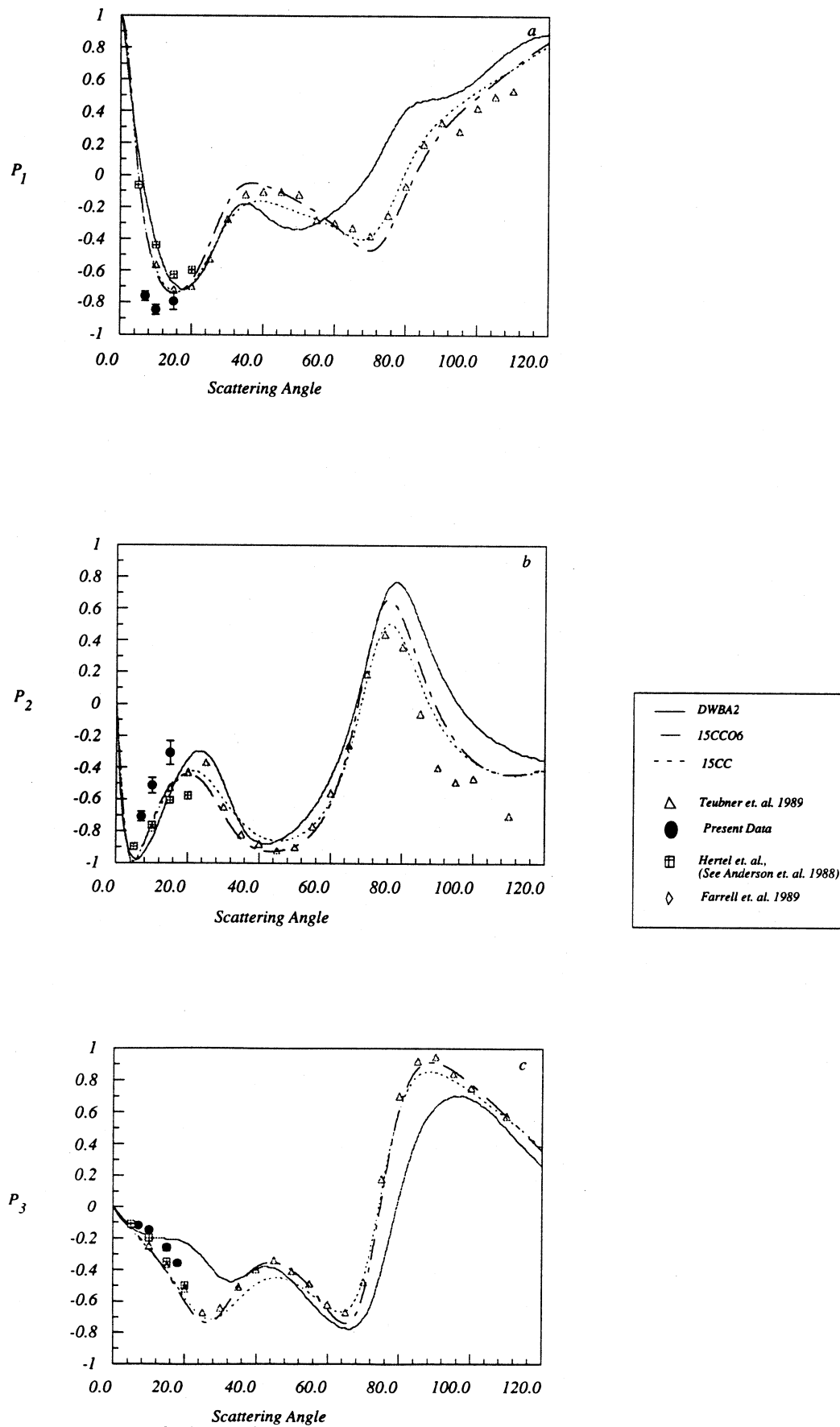


15eV





10eV



Graph 6.2 Stokes and Coherence Parameters Vs Scattering Angle

parameters and the pseudo Stokes parameters for the folded step experiment share the following relationships

$$P_1 = \frac{P_1^{S_f}}{\bar{K}} \quad (6.31)$$

$$P_2 = \frac{P_2^{S_f}}{\bar{K}} \quad (6.32)$$

where $P_i^{S_f}$ is a pseudo Stokes parameter for the folded step laser excitation scheme. It was shown previously that \bar{K} could be determined through line polarisation measurements. It is also possible to determine the \bar{K} by the use of a combination of single step and folded step measurements at one scattering angle. Using the equations (6.21), (6.22), (6.31) and (6.32) it is possible to solve for \bar{K} :

$$\bar{K} = K \frac{P_i^{S_f}}{P_i^S} \quad (i=1,2) \quad (6.33)$$

This measurement was performed at 10° scattering angle for the P_1 Stokes parameter which showed a negligible difference between $P_1^{S_f}$ and P_1^S . This gives a ratio of unity and implies that for the current experimental conditions that $\bar{K} = K = 0.39 \pm 0.03$ which is in good agreement with the QED calculation results given in Chapter Three.

The Stokes parameters are plotted as a function of scattering angle in graphs 6.2 for five different energies. The Stokes and coherence parameters are compared to the Second Order Distorted Wave Born Approximation (DWBA2) theory of Madison *et al.* 1992 for all five energies. At 20eV and 10eV this data is also compared to the 15 state Close Coupling (15CC) calculation of Bray *et al.* 1992 and the Coupled Channel Optical calculation (15CCO6) of Bray and McCathy 1992 as well as the data from Farrell *et al.* 1989, Teubner *et al.* 1990 and Hertel *et al.* (1974a&b, 1976, 1977). The data of Teubner *et al.* 1990 have the greatest angular range which extends to 80° for the 20eV work and 110° for the 10eV

work while the data presented here has the greatest incident energy range 10eV to 30eV but have a smaller angular range 5° - 25° .

Considering the first set of superelastic data for the 10eV energy range as shown in graphs 6.2 (a-c). These plots show that there is some disagreement with the experimental data at small scattering angles for the Stokes parameters P_1 . The 15CCO6 theory and 15 state Close Coupling theory are in good agreement in most of the angular range. The DWBA2 theory also agrees with these two theories for P_1 and P_2 at small scattering angles in the range of 0° - 30° but disagrees significantly for the P_3 parameter over the same angular range. The experimental data for this parameter tend to support the 15CC and 15CCO6 theories.

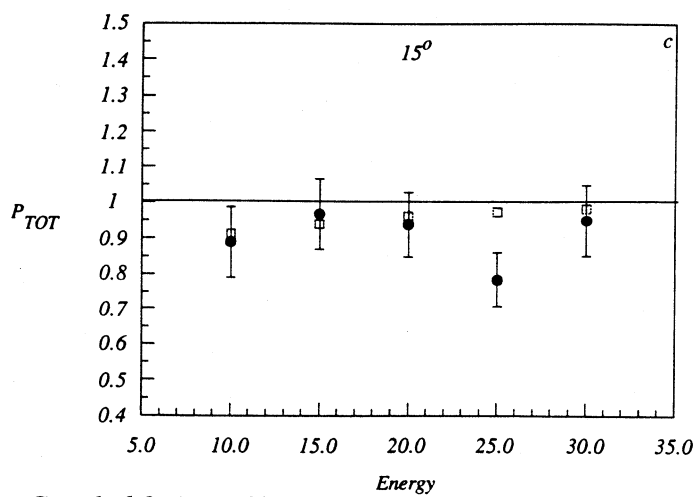
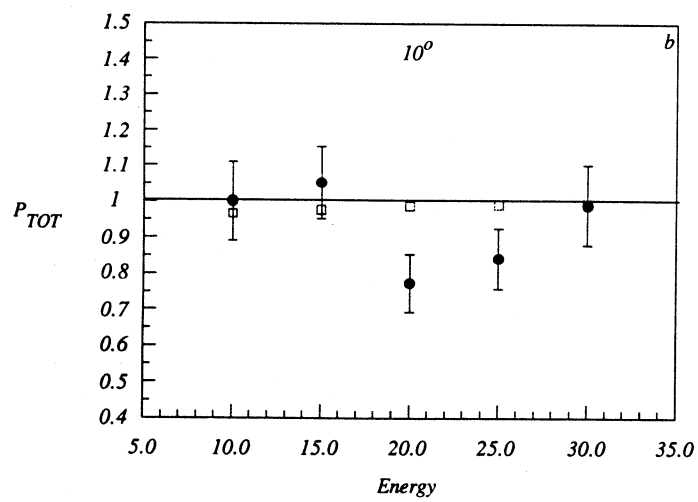
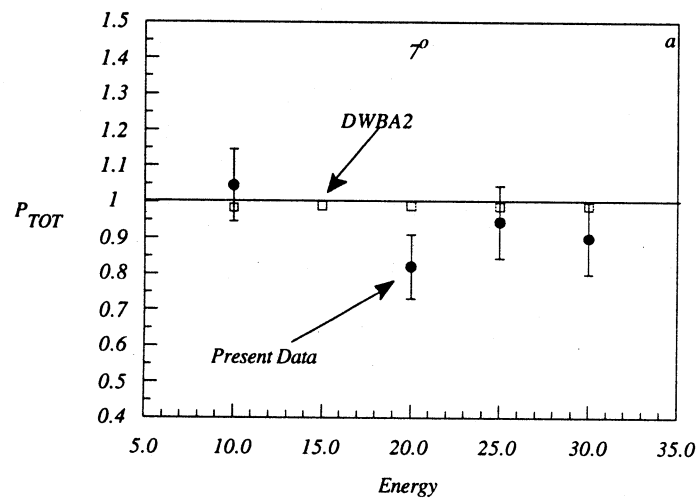
Figure 5d shows the experimental results for P_{TOT} which shows that all the experimental data is in good agreement. The only large angle data of Teubner *et al.* 1990 shows a substantial loss of coherence in the 60° - 80° angular range. The three theories are in some disagreement over the entire energy range. At small scattering angles the DWBA2 shows a very large loss of coherence as well as smaller losses of coherence in the angular range of 60° - 100° . The 15CC and 15CCO6 calculations basically show the same structures but differ in magnitude and only the 15CC calculation obtains the correct magnitude in the loss of coherence. Graph 6.2(e) shows the coherence parameter $|\mu|$ for the current experimental data. The relatively large error bars associated with this parameter compared to the P_{TOT} parameter come from the large percentage errors that are associated with the $(1-P_1^2)$ factor that appears in denominator of equation (6.28) as P_1 approaches unity. This parameter also supports the P_{TOT} parameter that there is no loss of coherence at small scattering angles.

Graphs 6.2(f-j) displays the present results from a 15eV incident electron energy experiment which is compared to the DWBA2 calculation. This is the only available data at this energy. The experimental data and the theory are in excellent agreement for the angles shown. The

theory shows a loss of coherence at small scattering angles which is better seen with the more sensitive parameter $|\mu|$.

The graphs 6.2(k-o) show the data for 20eV incident energy and has had the greatest attention to date. The present P_1 and P_2 Stokes parameters from this work at angles greater than 18° were obtained using the folded step superelastic experiment. The data for the P_1 Stokes parameter, graph (6.2k) is overall in good agreement except at 10° scattering angle where there is a significant difference between the Teubner *et al.* 1989 data compared to all other experimental data for this angle. The DWBA2 and 15CCO6 theories are basically in good accord for this parameter which is not the case for the 15CC theory in the angular range of 25° - 70° . The P_2 Stokes parameter shows good agreement for all the experimental data. The DWBA2 and 15CCO6 theories are in good accord from 0° - 70° after which differences appear. The 15CCO6 and 15CC calculations agree in general except for the angular region of 30° - 50° . The 15CCO6 shows the best general agreement with the data. The P_3 parameter shows good agreement from all experimental groups. The theories show a small amount of discrepancies at small scattering angles with the DWBA2 giving the best comparison the data in this range. At larger angles there is not much difference except in the angular range of 40° - 60° where the 15CC calculation diverges from the general structure of the experimental data and the 15CCO6 and DWBA2 theories.

P_{TOT} as a function of scattering angle is depicted in graph 6.2(n). All of the experimental data except that of Teubner *et al.* 1989 shows a sharp drop in coherence at 10° scattering angle. The Teubner *et al.* 1989 data shows a decrease in the coherence around 50° - 70° . No theory correctly predicts the magnitude of these features, except that the DWBA2 calculation shows two minimums, one minimum at small scattering angles and a further minimum at larger scattering angles. The 10° measurement has been a subject of intense investigation because of the controversy that was created because of the different experimental results obtained by different groups. This resulted in an extensive investigation into systematic errors such as checks on the laser polarisation, depolarisation effects due to the kodial



Graph 6.3: P_{TOT} Vs Energy (Various Scattering Angles)

viewports, electron gun alignment and finally the finite volume effect (Zetner *et al.* 1989). The finite volume effect will be discussed in the next section and it will be shown that no volumetric effects were evident at this scattering angle. As discussed in the previous chapter, these checks were part of the daily experimental protocol.

Graphs 6.2(p-t) show the only available experimental data with an incident electron energy of 25eV which is compared to the DWBA2 calculation. There is a small amount of disagreement for the P_1 Stokes parameter at 15° . P_2 and P_3 show good agreement overall with the theory. The experimental data shown in figure 6.2(s) and 6.2(t) displays a loss of coherence at small scattering angles. The theory also predicts this loss of coherence but does not have the same magnitude as the experimental data. The 30eV data, graphs 6.2(u-y) shows a good agreement overall with the DWBA2 theory and to within experimental error shows no loss of coherence.

Graphs 6.3(a-c) show P_{TOT} as a function of incident electron energy for three different scattering angles 7° , 10° and 15° . Also plotted here are the DWBA2 theoretical points at these energies. These plots suggest that the maximum loss of coherence occurs at 10° at 20eV incident electron energy with very little or no loss of coherence at other energies. The 7° scattering angle displays a very similar behaviour. At the 15° scattering angle shows the major loss of coherence to occur at 25eV.

6.5 The Finite Volume Effect

The finite volume effect (Zetner *et al.* 1989, McConkey *et al.* 1991, Murray *et al.* 1992) comes from the fact that in any real experimental situation, the interaction region has a finite size because of the finite size of the electron beam, acceptance angle of electron detector and finite size of the laser beam. At small scattering angles, it is possible that the finite volume

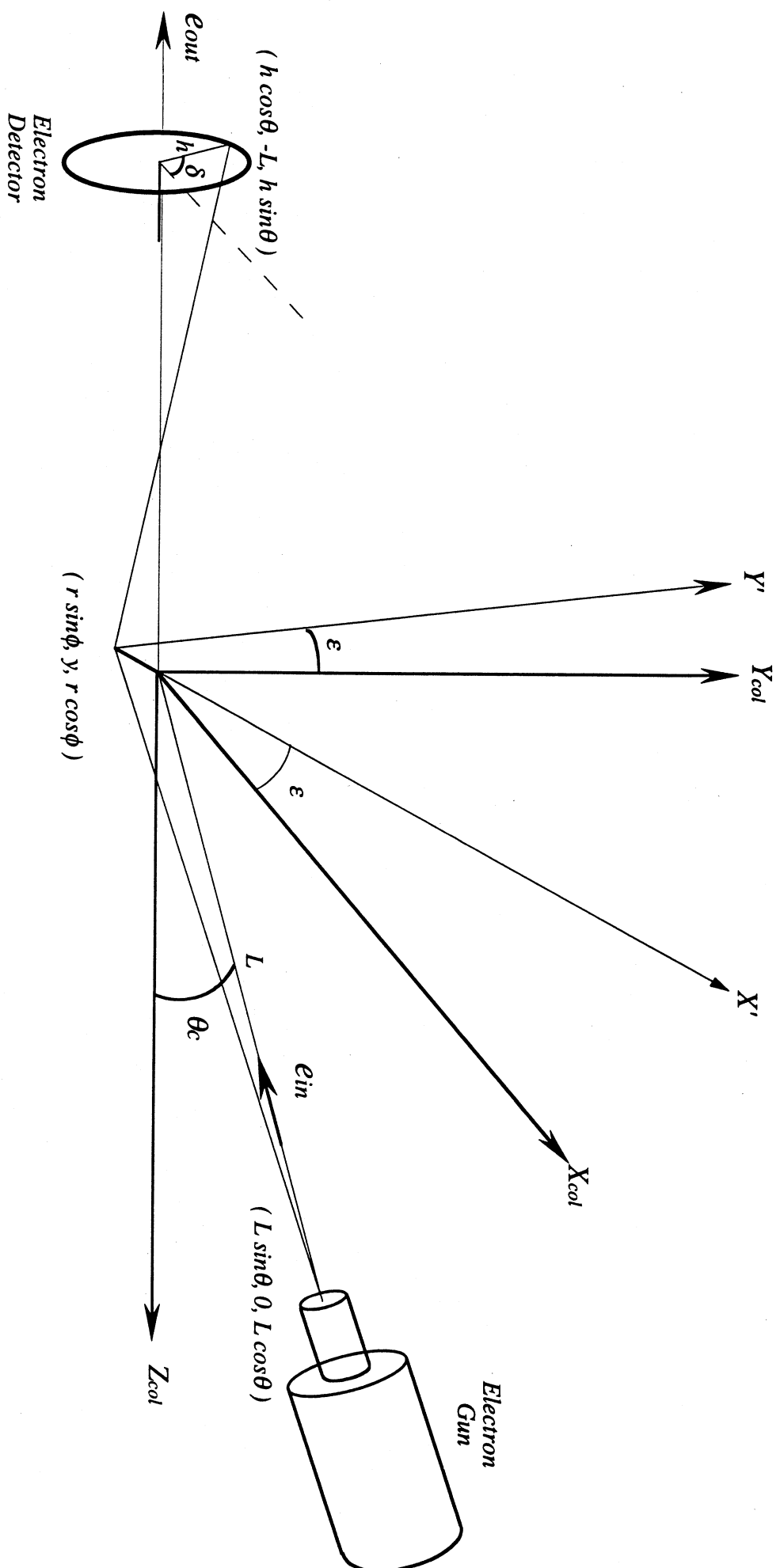


Figure 6.1: Roation of the Scattering Plane by Angle ϵ due to the Finite Volume Effect

of the interaction region leads to an effective rotation of the scattering plane. To a very good approximation it can be shown this shift from the nominal scattering plane is basically a rotation about the Z_{col} axis by an angle ϵ as shown in figure 6.1. This effective rotation of the scattering plane can cause series departures of the measured parameters from the actual parameters and is much more susceptible to coplanar parameters such as the P_4 Stokes and r parameters (McConkey *et al.* 1991, Murray *et al.* 1992, Meng 1992).

The pseudo Stokes parameters may be modified to incorporate this roll over angle ϵ of the scattering plane. Recall from Chapter Two that the superelastic differential cross section for the linearly polarised case was given by equation (2.41). To determine the superelastic differential cross section as a function of the laser polarisation, a rotation to the scattering plane was applied using the rotation transformation given by equation (2.42) with Euler angles $(0, -\beta, 0)$. To include finite volume effect, the rotation of the scattering plane about the Z_{col} axis by the angle ϵ is required to be included in the Euler angle rotation. The Euler angles for the rotation including this effect are given by $\omega = (0, -\beta, \epsilon)$ which yields the following rotation matrix:

$$D_{m'm}^J(\omega) = \begin{pmatrix} e^{i\epsilon} \frac{1}{2}(1 + \cos\beta) & -e^{i\epsilon} \frac{1}{\sqrt{2}} \sin\beta & e^{i\epsilon} \frac{1}{2}(1 - \cos\beta) \\ \frac{1}{\sqrt{2}} \sin\beta & \cos\beta & -\frac{1}{\sqrt{2}} \sin\beta \\ e^{-i\epsilon} \frac{1}{2}(1 - \cos\beta) & e^{-i\epsilon} \frac{1}{\sqrt{2}} \sin\beta & e^{-i\epsilon} \frac{1}{2}(1 + \cos\beta) \end{pmatrix} \quad (6.34a)$$

and

$$D_{m'm}^{J*}(\omega) = \begin{pmatrix} e^{-i\epsilon} \frac{1}{2}(1 + \cos\beta) & -e^{-i\epsilon} \frac{1}{\sqrt{2}} \sin\beta & e^{-i\epsilon} \frac{1}{2}(1 - \cos\beta) \\ \frac{1}{\sqrt{2}} \sin\beta & \cos\beta & -\frac{1}{\sqrt{2}} \sin\beta \\ e^{i\epsilon} \frac{1}{2}(1 - \cos\beta) & e^{i\epsilon} \frac{1}{\sqrt{2}} \sin\beta & e^{i\epsilon} \frac{1}{2}(1 + \cos\beta) \end{pmatrix} \quad (6.34b)$$

Applying the rotation transformation equation (2.42) yields the following rotated density matrix elements

$$\rho_{11}^{e(L)} = \frac{1}{2}(1 + \cos^2\beta - \sin^2\beta \cos 2\varepsilon)\rho_{11}^e + \frac{1}{2}\sin^2\beta\rho_{00}^e - i\sqrt{2}\sin\beta\sin\varepsilon\text{Re}\rho_{10}^e + \sqrt{2}\sin\beta\cos\beta\cos\varepsilon\text{Re}\rho_{10}^e \quad (6.35a)$$

$$\rho_{00}^{e(L)} = (\sin^2\beta + \sin^2\beta \cos 2\varepsilon)\rho_{11}^e + \cos^2\beta\rho_{00}^e - 2\sqrt{2}\sin\beta\cos\beta\cos\varepsilon\text{Re}\rho_{10}^e \quad (6.35b)$$

$$\rho_{-1-1}^{e(L)} = \frac{1}{2}(1 + \cos^2\beta - \sin^2\beta \cos 2\varepsilon)\rho_{11}^e + \frac{1}{2}\sin^2\beta\rho_{00}^e + i\sqrt{2}\sin\beta\sin\varepsilon\text{Re}\rho_{10}^e + \sqrt{2}\sin\beta\cos\beta\cos\varepsilon\text{Re}\rho_{10}^e \quad (6.35c)$$

Substituting these rotated density matrix elements into the expression for the superelastic differential cross section given by equation (2.41) yields

$$S(\beta) = \alpha \left\{ (1 + \cos^2\beta - \sin^2\beta \cos 2\varepsilon)\rho_{11}^e + \sin^2\beta\rho_{00}^e + 2\sqrt{2}\sin\beta\cos\beta\cos\varepsilon\text{Re}\rho_{10}^e \right\} + \gamma \left\{ (\sin^2\beta + \sin^2\beta \cos 2\varepsilon)\rho_{11}^e + \cos^2\beta\rho_{00}^e - 2\sqrt{2}\sin\beta\cos\beta\cos\varepsilon\text{Re}\rho_{10}^e \right\} \quad (6.36)$$

Setting $\beta=0^\circ$ and 90° into the above equation gives the following differential cross sections:

$$S(0) = \alpha 2\rho_{11}^e + \gamma\rho_{00}^e \quad (6.37a)$$

$$S(90) = \alpha((1 - \cos 2\varepsilon)\rho_{11}^e + \rho_{00}^e) + \gamma((1 + \cos 2\varepsilon)\rho_{11}^e) \quad (6.37b)$$

Substitution of these expression into the definition for the pseudo Stokes parameter P_I^S given by equation (2.49a) reveals

$$P_I^S = \frac{\alpha(\rho_{11}^e + \cos 2\varepsilon\rho_{11}^e - \rho_{00}^e) + \gamma(\rho_{00}^e - \rho_{11}^e - \cos 2\varepsilon\rho_{11}^e)}{\alpha(3\rho_{11}^e - \cos 2\varepsilon\rho_{11}^e + \rho_{00}^e) + \gamma(\rho_{00}^e + \rho_{11}^e + \cos 2\varepsilon\rho_{11}^e)} \quad (6.38)$$

Using the definition of K (equation(2.51)) and the relationships given by equations (2.25) enable P_I^S to be written in terms of optical pumping and atomic collision parameters as

$$P_I^S = \frac{K \{ (3\lambda - 1) - (1 - \lambda) \cos 2\varepsilon \}}{(2 - K) + K \{ (\lambda + (1 - \lambda) \cos 2\varepsilon) \}} \quad (6.39)$$

Using equation (6.36) it may be shown that the correction for P_2^S defined by equation (2.49b) is given by

$$P_2^S = \frac{K \{ [\lambda(1 - \lambda)]^{1/2} \cos \chi \cos \varepsilon \}}{(2 - K) + K \{ (\lambda + (1 - \lambda) \cos 2\varepsilon) \}} \quad (6.40)$$

The correction expression for P_2^S in Sang *et al.* 1994 is incorrect as it gives the trigonometric factor in the denominator as $\cos \varepsilon$ rather than the correct factor of $\cos 2\varepsilon$. It may be similarly shown that the finite volume affected P_3^S and r are given by

$$P_3^S = \frac{4K'[\lambda(1 - \lambda)]^{1/2} \sin \phi \cos \varepsilon}{(2 - K') + K'[\lambda + (1 - \lambda) \cos 2\varepsilon]} \quad (6.41)$$

$$r = \frac{1 - K[\lambda - (1 - \lambda) \cos 2\varepsilon]}{1 - K[\lambda + (1 - \lambda) \cos 2\varepsilon]} \quad (6.42)$$

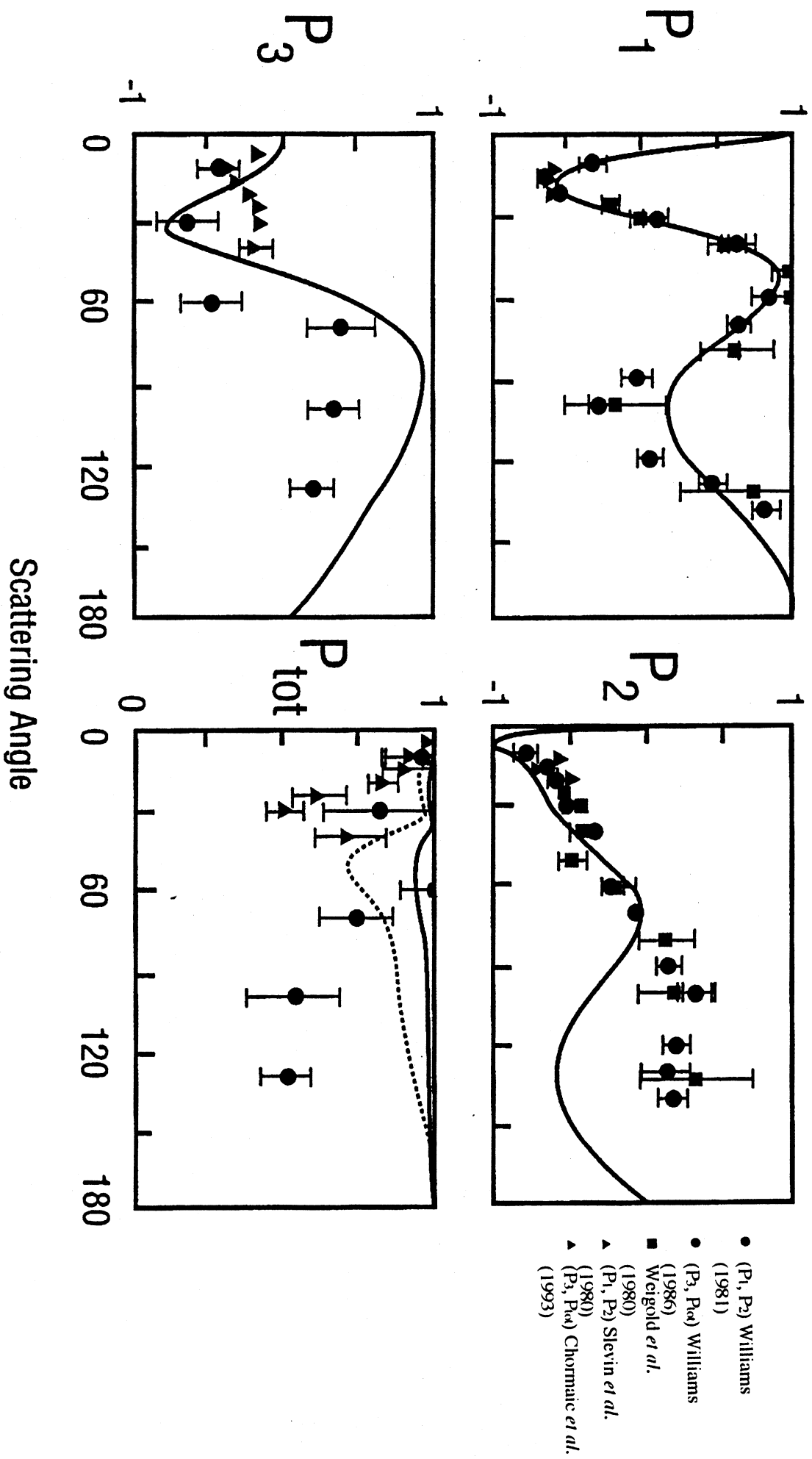
It was mentioned previously that the finite volume effect has a more severe effect on coplanar parameters than the perpendicular Stokes parameters. This may be demonstrated using the following example: Using the 20eV data at 10° and assuming $\varepsilon = 0^\circ$, $r = 2.08$ and P_I^S was measured to be -0.27 ± 0.01 . Applying equation (2.52a) with $K = 0.39 \pm 0.01$ reveals that $\lambda = 0.16$. Applying a roll over angle of 20° to equations (6.39) and (6.42) shows that $r = 1.73$ and $P_I^S = -0.24$. The perpendicular parameter shows a change of only 11% while the coplanar parameter shows a change of 17% which clearly demonstrates that coplanar measurements are more susceptible to volumetric effects than the perpendicular geometry measurements.

The finite volume effect is more dominate at small scattering angles and it is therefore desirable to make measurements to test for these effects at the smallest possible scattering angle. In the present apparatus the smallest angle that a coplanar measurement could be made was at 10° scattering angle with an incident electron energy of 20eV. As shown above the P_I^S measurement is much less susceptible to this effect and given this measurement and a measurement of K , it is possible to predict a value for $r_{(0)}$ using equation (2.71). The presence of a finite volume effect would manifest itself if the measured value of $r_{(0)}$ is smaller than the predicted value. Using the value of the K found by line polarisation measurements ($K=0.39\pm0.01$) and the measured value of P_I^S at 10° scattering angle with 20eV incident energy = -0.27 ± 0.01 . Substitution of these values into equation (2.71) yields a predicted value of $r_{(0)} = 2.08\pm0.04$ which is in a reasonable agreement compared to the measured value of 2.2 ± 0.10 , indicating there is no significant volume effect at 10° . This also indicates that the significant loss of coherence observed at this scattering angle and incident energy can not be caused by this effect.

6.6 Single and Folded Step Experiment Discussion

The previous section has shown that there exists a large amount of experimental data and theoretical calculations for the Stokes and coherence parameters for intermediate energy, electron-sodium atom collisions. The overall agreement between theory and experiment for the Stokes parameters is reasonable with most of the theories reproducing the detailed structure over a wide angular range. The present results are in best agreement with the theoretical calculation of Madison *et al.* 1992. As mentioned in section 6.2 this is a perturbative calculation which is expanded to second order in the Born series and is accurate to 2-3 times the ionisation potential. The 15CCO6 calculation also displayed a reasonable agreement over the entire energy range. It was expected that the 15CC calculation display good agreement with experiment as the incident electron energy is lowered. The past and

Graph 6.4: Stokes Parameters for electron-Hydrogen Scattering



present experimental data seems to support this view with a better agreement with the 15CC calculation at 10eV.

The most striking feature of the present data is the loss of coherence at small scattering angles in the incident energy range of 20-25eV. This is not well accounted for by the present theories. Of the three research groups involved with the experimental investigation, only two have recorded such losses at 20eV. This has raised the question that the two experiments have suffered from some systematic error. The comprehensive investigation of such effects as the optical pumping process and target state preparation, finite volume effect and radiation trapping in this thesis, indicate that none of these systematic errors could have caused this loss of coherence for the present data.

Recent experiments in electron-hydrogen atom scattering (Chormaic *et al.* 1993) have reported similar behaviour in that substantial losses of coherence have been observed at small scattering angles with an incident electron energy of 54.4eV. Graphs 6.4 display Stokes parameter and the P_{TOT} coherence parameter as a function of scattering angle for the experimental data of Chormaic *et al.* 1993, Weigold *et al.* 1980 and Williams 1986 compared to the DWBA2 calculation of Madison *et al.* 1992. P_{TOT} is not given for the Weigold *et al.* 1980 data as no P_3 measurement was made. The data of Chormaic *et al.* 1993 shows a large loss of coherence at 30° scattering angle. The data of Williams *et al.* 1986 indicates a loss of coherence at larger scattering angles. In the case of the Chormaic *et al.* 1993 data, the results for the P_3 parameter are significantly smaller in magnitude than the DWBA2 calculation between 20° and 40° which accounts for the loss of coherence in that angular range. In the case of sodium the loss of coherence at 10° at 20eV incident energy arises mainly from P_1 and P_2 Stokes parameters.

The loss of coherence in an electron-atom collision process changes for different atoms. Anderson *et al.* 1988 expect full coherence for the case of an electron-atom collision for an atomic species which has two valence electrons with LS coupling holding and where

relativistic effects can be ignored. Once such atomic species is helium and experimental conformation of total coherence was made by Standage and Kleinpoppen 1976. In the case of sodium this atomic species has only one valence electron and as such the value of P_{TOT} which differ from unity, may be found with experiments using unpolarised electron beams. This loss of coherence is due to two spin channels being open for the collision. At the time of electron atom impact, the sodium atom may form either a singlet or triplet spin state. Because the spin of the system is unknown in a non-spin resolved experiment not all of the information about the system is known which results in a loss of coherence in the collision process (Anderson *et al.* 1988). If the spin channels were resolved then a P_{TOT} of unity for each channel would be expected. The Stokes parameters for a spin unresolved experiment may be expressed in terms of spin resolved parameters as follows: (Sang *et al.* 1994)

$$P_i = \frac{1}{4} \frac{\sigma^{sing}}{\sigma} P_i^{sing} + \frac{3}{4} \frac{\sigma^{trip}}{\sigma} P_i^{trip} \quad (6.43)$$

where σ^{sing} is the singlet differential cross section, σ^{trip} is the triplet differential cross section, σ is the spin unresolved differential cross section and P_i^{sing} (P_i^{trip}) are the Stokes parameters for singlet and (triplet) scattering. For the spin resolved case the following relationship applies

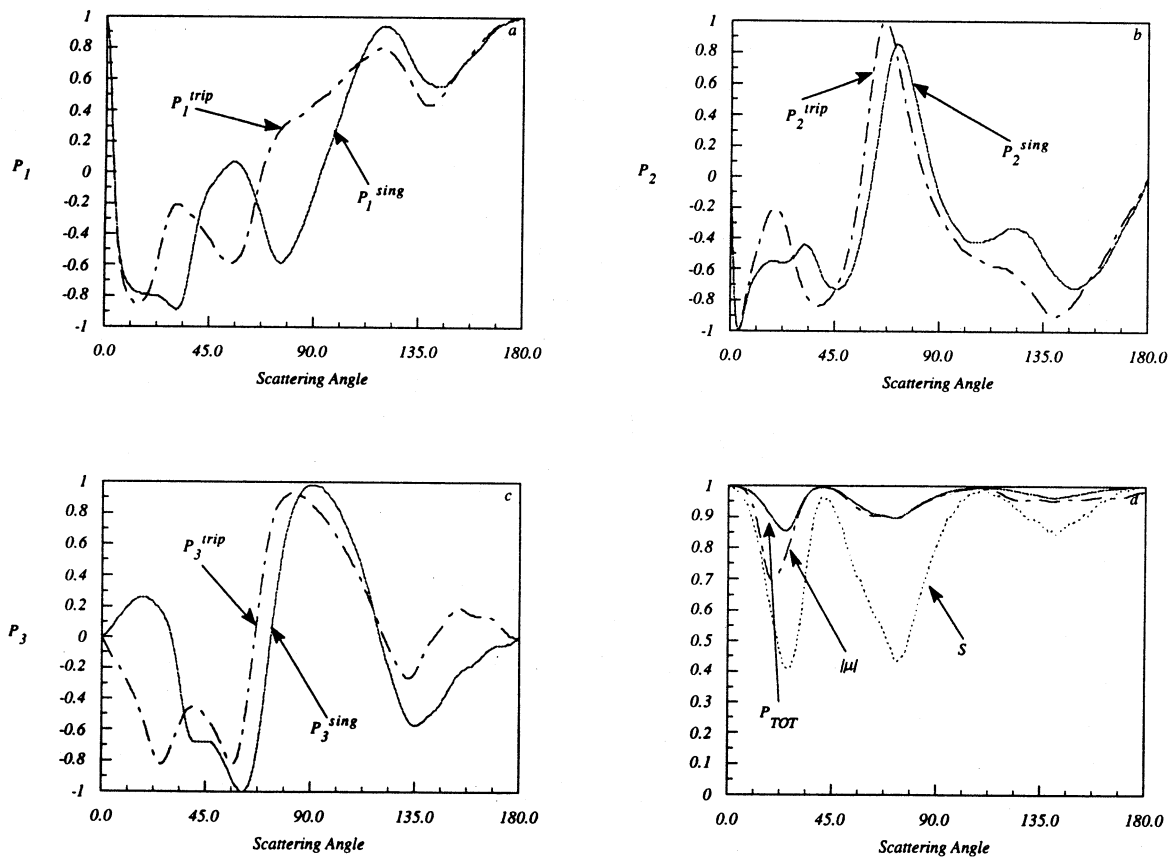
$$(P_{TOT}^k)^2 = (P_1^k)^2 + (P_2^k)^2 + (P_3^k)^2 = 1 \quad k = sing, trip \quad (6.44)$$

Using equations (6.43) and (6.44) it may be shown that P_{TOT} may be expressed in terms of the spin resolved case as

$$P_{TOT} = \sqrt{1 + \frac{3}{8} \frac{\sigma^{sing} \sigma^{trip}}{\sigma^2} (S-1)} \quad (6.45)$$

where the parameter S is given by

$$S = P_1^{sing} P_1^{trip} + P_2^{sing} P_2^{trip} + P_3^{sing} P_3^{trip} \quad (6.46)$$



Graph 6.5: The Spin Resolved Stokes Parameters and Coherence Parameters Calculated by the DWBA2 Method

The parameter S directly reflects the importance of exchange since it will be unity when exchange is unimportant (the S parameter should not be confused with the symbol for the differential cross section given in previous chapters). Equation (6.45) shows that P_{TOT} is not in general unity. For the case of high incident energies, the singlet and triplet Stokes parameters become equal and S and P_{TOT} will be unity. For low incident energies these parameters become unequal indicating exchange is important and S and P_{TOT} would be expected to deviate from unity. Graphs 6.5 show the DWBA2 calculation at with a 15eV incident electron energy for the spin resolved Stokes parameters and the coherence parameters P_{TOT} , $|\mu|$ and the parameter S . It is interesting to see that even though the singlet and triplet Stokes parameters are quite different at some scattering angles, P_{TOT} does not deviate very much from unity. The degree of coherence $|\mu|$ is more sensitive while the S parameter is the most sensitive of all to exchange effects. The large deviations from unity seen in experimental determinations of P_{TOT} and $|\mu|$ clearly show that the exchange effects must be large and a measurement using a spin resolved apparatus of S would offer an extremely sensitive test to exchange.

The experimental evidence for sodium and hydrogen suggest that some type of exchange mechanism has not been accounted for in current electron- atom scattering theories and this exchange effect is more important than the exchange effects already included in current calculations. It would seem that for the present results in sodium that more work is required on the theoretical aspects of the collision process and perhaps more understanding of exchange effects can come from spin resolved experiments.

6.7 Stepwise Superelastic Experimental Results

In this section the experimental results for stepwise pseudo Stokes parameters which were discussed in Chapter Four are given. In this experimental investigation, the pseudo Stokes parameters for parallel laser polarisations were measured at three scattering angles for the P_3^S parameter and two scattering angles for the P_1^S and P_2^S parameters with an incident electron energy of 20eV. The stepwise pseudo Stokes parameters were defined in Chapter Four and to determine these experimentally, background subtractions were required as in the case of the experimental determination of the single and folded step pseudo Stokes parameters. In the stepwise case the situation is more complicated as the superelastic peaks from the $3^2P_{3/2} \rightarrow 3^2S_{1/2}$ and $3^2D_{5/2} \rightarrow 3^2P_{3/2,1/2}$ electron de-excitations are convoluted. To determine the background count rate for the $3^2D_{5/2} \rightarrow 3^2P_{3/2,1/2}$ superelastic events, the laser exciting the $3^2P_{3/2} \rightarrow 3^2D_{5/2}$ transition was blocked and counts of background electrons were then taken. Because both lasers are identically polarised, the background count rate was different for different polarisations. The experimentally determined stepwise Stokes parameters and their associated errors determined using equation (6.8) are given by

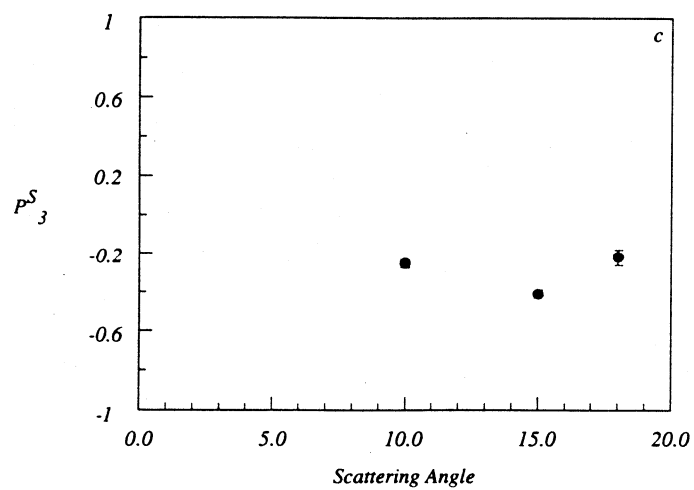
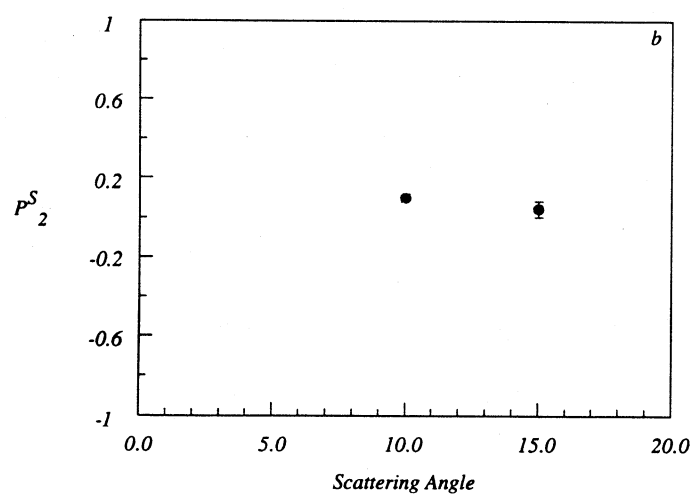
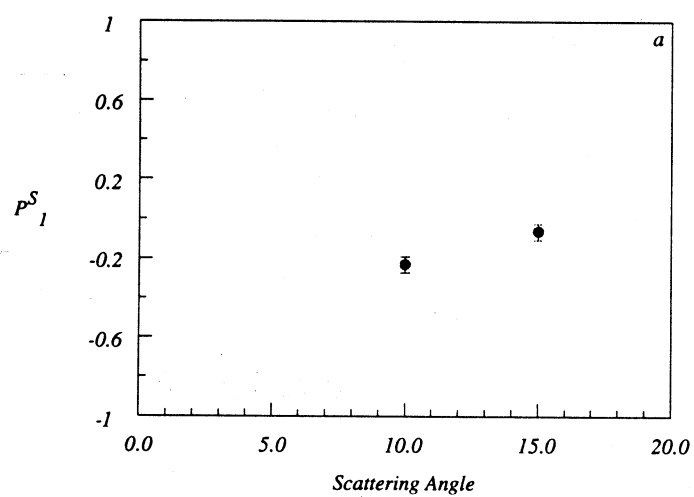
$$P_1^S = \frac{\sigma_{(0)} - \sigma_{(90)} - \sigma_{(B_0)} + \sigma_{(B_{90})}}{\sigma_{(0)} + \sigma_{(90)} - \sigma_{(B_0)} - \sigma_{(B_{90})}} \quad (6.47a)$$

$$\Delta P_1^S = \frac{2 \sqrt{\begin{aligned} &\sigma_{(0)}^2 \sigma_{(90)}^2 - 2\sigma_{(0)}\sigma_{(90)}\sigma_{(b_{90})} + \sigma_{(0)}^2 \sigma_{(b_{90})}^2 + \sigma_{(90)}^2 \sigma_{(0)}^2 - 2\sigma_{(90)}\sigma_{(0)}\sigma_{(b_0)} + \sigma_{(90)}^2 \sigma_{(b_0)}^2 + \sigma_{(b_0)}^2 \sigma_{(90)}^2 \\ &- 2\sigma_{(b_0)}\sigma_{(90)}\sigma_{(b_{90})} + \sigma_{(b_0)}^2 \sigma_{(b_{90})}^2 + \sigma_{(b_{90})}^2 \sigma_{(0)}^2 - 2\sigma_{(b_{90})}\sigma_{(0)}\sigma_{(b_0)} + \sigma_{(b_{90})}^2 \sigma_{(b_0)}^2 \end{aligned}}}{\left\{ -\sigma_{(0)} - \sigma_{(90)} + \sigma_{(b_0)} + \sigma_{(b_{90})} \right\}^2}} \quad (6.47b)$$

$$P_2^S = \frac{\sigma_{(45)} - \sigma_{(135)} - \sigma_{(B_{45})} + \sigma_{(B_{135})}}{\sigma_{(45)} + \sigma_{(135)} - \sigma_{(B_{45})} - \sigma_{(B_{135})}} \quad (6.48a)$$

Table 6.3: Stepwise pseudo Stokes Parameters

<i>Scattering Angle</i>	P_1^S	P_2^S	P_3^S
10°	-0.23 ± 0.04	0.10 ± 0.02	-0.25 ± 0.02
15°	-0.065 ± 0.04	0.043 ± 0.04	-0.41 ± 0.02
18°			-0.22 ± 0.04



Graph 6.6: Stepwise Stokes Parameters 20eV incident energy

$$\Delta P_2^S = \frac{2 \sqrt{\sigma_{(45)}^2 \sigma_{(135)}^2 - 2 \sigma_{(45)} \sigma_{(135)} \sigma_{(b_{135})} + \sigma_{(45)}^2 \sigma_{(b_{135})}^2 + \sigma_{(135)}^2 \sigma_{(45)}^2 - 2 \sigma_{(135)} \sigma_{(45)} \sigma_{(b_{45})} + \sigma_{(135)}^2 \sigma_{(b_{45})}^2 + \sigma_{(b_{45})}^2 \sigma_{(135)}^2 - 2 \sigma_{(b_{45})} \sigma_{(135)} \sigma_{(b_{135})} + \sigma_{(b_{45})}^2 \sigma_{(b_{135})}^2 + \sigma_{(b_{135})}^2 \sigma_{(45)}^2 - 2 \sigma_{(b_{135})} \sigma_{(45)} \sigma_{(b_{45})} + \sigma_{(b_{135})}^2 \sigma_{(b_{45})}^2}}{\left\{ -\sigma_{(45)} - \sigma_{(135)} + \sigma_{(b_{45})} + \sigma_{(b_{135})} \right\}^2} \quad (6.48b)$$

$$P_3^S = \frac{\sigma_{(RHC)} - \sigma_{(LHC)} - \sigma_{(B_{RHC})} + \sigma_{(B_{LHC})}}{\sigma_{(RHC)} + \sigma_{(LHC)} - \sigma_{(B_{RHC})} - \sigma_{(B_{LHC})}} \quad (6.49a)$$

$$\Delta P_3^S = \frac{2 \sqrt{\sigma_{(RHC)}^2 \sigma_{(LHC)}^2 - 2 \sigma_{(RHC)} \sigma_{(LHC)} \sigma_{(b_{LHC})} + \sigma_{(RHC)}^2 \sigma_{(b_{LHC})}^2 + \sigma_{(LHC)}^2 \sigma_{(RHC)}^2 - 2 \sigma_{(LHC)} \sigma_{(RHC)} \sigma_{(b_{RHC})} + \sigma_{(LHC)}^2 \sigma_{(b_{RHC})}^2 + \sigma_{(b_{RHC})}^2 \sigma_{(LHC)}^2 - 2 \sigma_{(b_{RHC})} \sigma_{(LHC)} \sigma_{(b_{LHC})} + \sigma_{(b_{RHC})}^2 \sigma_{(b_{LHC})}^2 + \sigma_{(b_{LHC})}^2 \sigma_{(RHC)}^2 - 2 \sigma_{(b_{LHC})} \sigma_{(RHC)} \sigma_{(b_{RHC})} + \sigma_{(b_{LHC})}^2 \sigma_{(b_{RHC})}^2}}{\left\{ -\sigma_{(RHC)} - \sigma_{(LHC)} + \sigma_{(b_{RHC})} + \sigma_{(b_{LHC})} \right\}^2} \quad (6.49b)$$

where σ_α represents the electron count rate with both lasers polarised at angle α to the quantisation axis and σ_{b_α} is the background count rate with the second exciting laser blocked and the first exciting laser polarised at angle α . For the P_3^S case the lasers are either right or left handed circularly polarised. The results of the measurements are given in Table 6.3 and may be seen graphically in graphs 6.6.

Graph 6.6 shows the stepwise pseudo Stokes parameters as a function of scattering angle for an incident electron energy of 20eV. All three Stokes parameters were measured at only two scattering angles due to large amount of data required to obtain reasonable statistics. Graph 6.6a shows the P_1^S parameter as a function of scattering angle. This parameter is negative at both scattering angles and is quite small in magnitude. The P_2^S parameter

displayed in graph 6.6b also is small in magnitude but is positive. The P_3^S parameter is shown in figure 6.6c. This parameter is negative and over this angular range is quite differential in scattering angle and relatively large in magnitude compared to the other stepwise pseudo Stokes parameters.

The parameters measured here show that the stepwise superelastic experiment is feasible experiment and the results from this type of experiment will be useful to use as a test in current theories for the scattering from higher excited states.

Chapter Seven

Conclusion

7.1 Summary

This thesis has presented various aspects of electron-sodium superelastic collision experiments. Following an introduction and a review section provided by Chapter One, Chapter Two provided theoretical aspects of electron-atom collisions. This chapter comprised of a section which formulated the electron-atom collision problem using density matrices. It was demonstrated that the collision density matrix, which fully describes the collision process, involving the excitation of a ground state atom to a $L=1$ excited state, by using certain arguments, that out of a possible nine elements, only three elements were required to fully specify the collision density matrix. It was also shown that these three independent density matrix elements could be related to three parameters denoted the atomic collision parameters.

Chapter Two also demonstrated for this system that it was possible to obtain all of the atomic collision parameters using a superelastic scattering experiment. Sodium was chosen as the target atom because there are transitions which are easily accessible using tunable dye lasers from the ground state and there are many theoretical calculations with which experimental data can be compared. The superelastic experiment involved initially preparing an atom in a excited state using laser radiation of a particular polarisation. The excited atoms were the induced to relax non-radiatively via a superelastic collision with an electron. Measurement of the superelastic differential cross section as a function of the laser polarisation enables pseudo Stokes parameter to be deduced. It was shown in Chapter Two that these pseudo Stokes parameters are functions of both atomic collision parameters and optical pumping parameters. The

atomic collision parameters are functions of collision density matrix elements and the optical pumping parameters are purely functions of laser-atom density matrix elements. In the single step superelastic scattering experiment, the lasers were tuned from the $3^2S_{1/2}$ ($F'=2$) hyperfine ground state transition to the $3^2P_{3/2}$ ($F=3$) excited hyperfine state. This restricted the number of ground substates that can be excited from to a possible five out of eight. The excited state population was further reduced as the laser power in experiments were great enough to induce power broadening so that other excited hyperfine transitions could be excited. When this occurs relaxation to the $F'=1$ ground hyperfine sublevel is allowed. This $F'=1$ ground hyperfine sublevel effectively acts as a sink as the power broadening is not great enough to broaden the ground sublevels and hence a reduced excited state population is produced. This can be a problem in a superelastic scattering experiment at larger scattering angles where the electron scattering cross section drops dramatically. To obtain a better superelastic scattering signal at larger scattering angles a new laser excitation mechanism was introduced in which two lasers were used to increase the population of the $3^2P_{3/2}$ state by laser exciting from the two hyperfine ground states. In this folded step mechanism, one laser was tuned from the $F'=2$ hyperfine ground state to the $3^2P_{3/2}$ state hyperfine manifold while a second laser was resonant with the $F'=1$ hyperfine ground state to the $3^2P_{3/2}$ excited state transition. Both lasers shared the identical polarisation and co-propagated to the interaction region.

Chapter Three introduced a full non-relativistic quantum electrodynamic theory of the laser-atom interaction where no approximations except the usual rotating wave, dipole and harmonic approximations were made. The Heisenberg equation of motion was used to obtain a set of coupled differential equations which were solved under various conditions. It was shown that the line polarisation of the fluorescence scattered perpendicular to the plane formed by the laser's polarisation vector and the laser's propagation direction was identical to the optical pumping parameter K . The calculation converged with the J representation calculation in Chapter Two and the Pegg-

MacGillivray high intensity transformation (Pegg and MacGillivray 1986) at high laser powers. The folded step laser excitation mechanism was also modelled in this chapter. It was further demonstrated that for this scheme that the line polarisation was identical to the line polarisation of the fluorescence perpendicular to the plane formed by the two co-propagating lasers and their polarisation vectors.

Chapter Four was devoted to a preliminary investigation of a stepwise superelastic scattering experiment. Ground state sodium atoms were initially excited to the $3^2P_{3/2}$ excited state. These atoms were then further excited to the $3^2D_{5/2}$ state using a second laser beam. The stepwise excited atom would then undergo a superelastic collision with an electron leaving the atom in either the $3^2P_{3/2}$ or $3^2P_{1/2}$ state. Three stepwise pseudo Stokes parameters were defined for the lasers with parallel polarisation and it was demonstrated that in J representation, as in the case of the single step superelastic experiment, that these stepwise Stokes parameters were related to both optical parameters and atomic collision parameters. The optical parameters could be related to the same type of line polarisation measurement as in the single step case except instead of monitoring the $3^2P_{3/2}$ to the $3^2S_{1/2}$ transition fluorescence, the fluorescence from the $3^2D_{5/2}$ to the $3^2P_{3/2}$ transition was monitored. An initial model using rate equations was used to model the stepwise laser-atom interaction and agreement to within experimental uncertainties between theory and experiment was observed.

Chapter Four also demonstrated that other collision density matrix elements could be experimentally determined by measuring stepwise pseudo Stokes parameters with the two exciting lasers at different polarisations. This was a quite complicated procedure as the two exciting lasers would have two different excitation reference frames and to account for this, various rotations were required. An example of the derivation, one of these type of stepwise pseudo Stokes parameters was derived and it was found to be a complicated function of both optical parameters and atomic collision parameters.

Chapter five presented a section which described the various experimental apparatus used for the different types of superelastic experiments and the line polarisation measurements. This chapter also described the experimental protocol and also gave a description of the computer control.

Chapter Six presents the results of the various experiments described in the preceding chapters. Line polarisation measurements for the single step experiment were reported for various experimental conditions. This was followed by a section describing the various electron-sodium collision models with which the data was compared with. Single step data was presented for five different incident electron energies over a scattering angle range of 5° - 25° . This data was also compared to some other experimental results at 10eV and 20eV. There was a good agreement with all of the experimental data except at some angles at 20eV. The theoretical comparison also demonstrated a fair to good agreement over most of the energy range. The loss of coherence at small scattering angles observed by the current data was poorly modelled by all of the theories.

Systematic tests were performed to determine whether certain losses of coherence could be attributed to certain artefacts. One of these test was the test for the presence of finite volume effects. Correction expressions for the pseudo Stokes parameters were obtained. A series of experiments using coplanar and perpendicular geometries demonstrated that the losses of coherences could not be produced by this particular effect.

Chapter Six also present the results of the first stepwise superelastic measurements discussed in Chapter Four. Stepwise pseudo Stokes parameters were obtained for three different scattering angles with an electron incident energy of 20eV. No comparison with theory is given as there is currently no theoretical calculations with which the data can be compared with.

7.2 Extensions and Improvements

The most obvious extension to the single step experiments is to perform spin resolved experiments. Previous spin polarised superelastic experiments have concentrated their efforts to the measurement of the P_3 parameter. The measurement of other pseudo Stokes parameters would enable the S parameter introduced in Chapter Six to be determined. This coherence parameter is the most sensitive test to the role of exchange effects and would be most useful to test the small scattering angle loss of coherence.

The stepwise experiments have opened up a new set of experiments so that the properties of excited state to excited state collisions can be qualitatively measured. A natural extension of this experiment would be to measure the stepwise Stokes parameters for a non-parallel polarisation case. It would also be advantageous to perform a full QED calculation to model the laser atom interaction at higher laser intensities.

The apparatus could be improved by replacing the oil diffusion pump with a turbo molecular pump. The oil diffusion pump induces problems due to back streaming of oil which causes the lens elements in the gun and analyser to get covered with these oil coatings. These oil coating charge over a period of time and hence reduce the stability of the electron gun. When this occurred, the vacuum chamber required opening and the electron gun or the electron analyser would be cleaned. Replacement of this pump would greatly reduce down time of the apparatus.

Improvements for the single to noise ratio in the stepwise experiment could be improved by using a higher electron energy resolution system. The current resolution of the combined analyser and gun was in the order of 500meV. If this was reduced to 250meV, the stepwise and the single step superelastic peaks in the stepwise experiments would be clearly resolved which would greatly enhance the signal to noise

ratio. The signal to noise ratio could also be increased via the use of an electro-optic modulator which could be used to modulated the first laser step so that both of the hyperfine ground states could be pumped out off. This would act like the folded step excitation mechanism which greatly increase the population in the $3^2P_{3/2}$ state.

Appendix 1

Component Equations of Motion: Single Laser Case

The following equations are the component equations of motion for a single laser which were derived using the general equations of motion in section 3.3 of Chapter Three.

$$\begin{aligned}\dot{\langle \chi_{4,4} \rangle} = & -i \Omega_{13,4} (\langle \chi_{4,13} \rangle - \langle \chi_{13,4} \rangle) \\ & -i \Omega_{19,4} (\langle \chi_{4,19} \rangle - \langle \chi_{19,4} \rangle) \\ & + \Gamma_{10,4} \langle \chi_{10,10} \rangle \\ & + \Gamma_{13,4} \langle \chi_{13,13} \rangle \\ & + \Gamma_{14,4} \langle \chi_{14,14} \rangle \\ & + \Gamma_{19,4} \langle \chi_{19,19} \rangle \\ & + \Gamma_{20,4} \langle \chi_{20,20} \rangle \\ & + \Gamma_{19,13,4} (\langle \chi_{19,13} \rangle + \langle \chi_{13,19} \rangle) \\ & + \Gamma_{14,10,4} (\langle \chi_{14,10} \rangle + \langle \chi_{10,14} \rangle) \\ & + \Gamma_{20,10,4} (\langle \chi_{20,10} \rangle + \langle \chi_{10,20} \rangle) \\ & + \Gamma_{20,14,4} (\langle \chi_{20,14} \rangle + \langle \chi_{14,20} \rangle)\end{aligned}\tag{1}$$

$$\begin{aligned}\dot{\langle \chi_{5,5} \rangle} = & -i \Omega_{10,5} (\langle \chi_{5,10} \rangle - \langle \chi_{10,5} \rangle) \\ & -i \Omega_{14,5} (\langle \chi_{5,14} \rangle - \langle \chi_{14,5} \rangle) \\ & -i \Omega_{20,5} (\langle \chi_{5,20} \rangle - \langle \chi_{20,5} \rangle) \\ & + \Gamma_{10,5} \langle \chi_{10,10} \rangle \\ & + \Gamma_{11,5} \langle \chi_{11,11} \rangle \\ & + \Gamma_{13,5} \langle \chi_{13,13} \rangle \\ & + \Gamma_{14,5} \langle \chi_{14,14} \rangle\end{aligned}$$

$$\begin{aligned}
& + \Gamma_{19,5} \langle \chi_{19,19} \rangle \\
& + \Gamma_{20,5} \langle \chi_{20,20} \rangle \\
& + \Gamma_{21,5} \langle \chi_{21,21} \rangle \\
& + \Gamma_{19,13,5} (\langle \chi_{19,13} \rangle + \langle \chi_{13,19} \rangle) \\
& + \Gamma_{14,10,5} (\langle \chi_{14,10} \rangle + \langle \chi_{10,14} \rangle) \\
& + \Gamma_{20,10,5} (\langle \chi_{20,10} \rangle + \langle \chi_{10,20} \rangle) \\
& + \Gamma_{20,14,5} (\langle \chi_{20,14} \rangle + \langle \chi_{14,20} \rangle) \\
& + \Gamma_{21,11,5} (\langle \chi_{21,11} \rangle + \langle \chi_{11,21} \rangle)
\end{aligned} \tag{2}$$

$$\begin{aligned}
\dot{\langle \chi_{6,6} \rangle} = & -i \Omega_{11,6} (\langle \chi_{6,11} \rangle - \langle \chi_{11,6} \rangle) \\
& -i \Omega_{21,6} (\langle \chi_{6,21} \rangle - \langle \chi_{21,6} \rangle) \\
& + \Gamma_{10,6} \langle \chi_{10,10} \rangle \\
& + \Gamma_{11,6} \langle \chi_{11,11} \rangle \\
& + \Gamma_{12,6} \langle \chi_{12,12} \rangle \\
& + \Gamma_{14,6} \langle \chi_{14,14} \rangle \\
& + \Gamma_{16,6} \langle \chi_{16,16} \rangle \\
& + \Gamma_{20,6} \langle \chi_{20,20} \rangle \\
& + \Gamma_{21,6} \langle \chi_{21,21} \rangle \\
& + \Gamma_{22,6} \langle \chi_{22,22} \rangle \\
& + \Gamma_{14,10,6} (\langle \chi_{14,10} \rangle + \langle \chi_{10,14} \rangle) \\
& + \Gamma_{20,10,6} (\langle \chi_{20,10} \rangle + \langle \chi_{10,20} \rangle) \\
& + \Gamma_{20,14,6} (\langle \chi_{20,14} \rangle + \langle \chi_{14,20} \rangle) \\
& + \Gamma_{21,11,6} (\langle \chi_{21,11} \rangle + \langle \chi_{11,21} \rangle) \\
& + \Gamma_{16,12,6} (\langle \chi_{16,12} \rangle + \langle \chi_{12,16} \rangle) \\
& + \Gamma_{22,12,6} (\langle \chi_{22,12} \rangle + \langle \chi_{12,22} \rangle) \\
& + \Gamma_{22,16,6} (\langle \chi_{22,16} \rangle + \langle \chi_{16,22} \rangle)
\end{aligned} \tag{3}$$

$$\begin{aligned}
\dot{\langle \chi_{7,7} \rangle} = & -i \Omega_{12,7} (\langle \chi_{7,12} \rangle - \langle \chi_{12,7} \rangle) \\
& -i \Omega_{16,7} (\langle \chi_{7,16} \rangle - \langle \chi_{16,7} \rangle)
\end{aligned}$$

$$\begin{aligned}
& -i \Omega_{22,7} (\langle \chi_{7,22} \rangle - \langle \chi_{22,7} \rangle) \\
& + \Gamma_{11,7} \langle \chi_{11,11} \rangle \\
& + \Gamma_{12,7} \langle \chi_{12,12} \rangle \\
& + \Gamma_{16,7} \langle \chi_{16,16} \rangle \\
& + \Gamma_{17,7} \langle \chi_{17,17} \rangle \\
& + \Gamma_{21,7} \langle \chi_{21,21} \rangle \\
& + \Gamma_{22,7} \langle \chi_{22,22} \rangle \\
& + \Gamma_{23,7} \langle \chi_{23,23} \rangle \\
& + \Gamma_{21,11,7} (\langle \chi_{21,11} \rangle + \langle \chi_{11,21} \rangle) \\
& + \Gamma_{16,12,7} (\langle \chi_{16,12} \rangle + \langle \chi_{12,16} \rangle) \\
& + \Gamma_{22,12,7} (\langle \chi_{22,12} \rangle + \langle \chi_{12,22} \rangle) \\
& + \Gamma_{22,16,7} (\langle \chi_{22,16} \rangle + \langle \chi_{16,22} \rangle) \\
& + \Gamma_{23,17,7} (\langle \chi_{23,17} \rangle + \langle \chi_{17,23} \rangle)
\end{aligned} \tag{4}$$

$$\begin{aligned}
\dot{\langle \chi_{8,8} \rangle} = & -i \Omega_{17,8} (\langle \chi_{8,17} \rangle - \langle \chi_{17,8} \rangle) \\
& -i \Omega_{23,8} (\langle \chi_{8,23} \rangle - \langle \chi_{23,8} \rangle) \\
& + \Gamma_{12,8} \langle \chi_{12,12} \rangle \\
& + \Gamma_{16,8} \langle \chi_{16,16} \rangle \\
& + \Gamma_{17,8} \langle \chi_{17,17} \rangle \\
& + \Gamma_{22,8} \langle \chi_{22,22} \rangle \\
& + \Gamma_{23,8} \langle \chi_{23,23} \rangle \\
& + \Gamma_{16,12,8} (\langle \chi_{16,12} \rangle + \langle \chi_{12,16} \rangle) \\
& + \Gamma_{22,12,8} (\langle \chi_{22,12} \rangle + \langle \chi_{12,22} \rangle) \\
& + \Gamma_{22,16,8} (\langle \chi_{22,16} \rangle + \langle \chi_{16,22} \rangle) \\
& + \Gamma_{23,17,8} (\langle \chi_{23,17} \rangle + \langle \chi_{17,23} \rangle)
\end{aligned} \tag{5}$$

$$\begin{aligned}
\dot{\langle \chi_{10,10} \rangle} = & -i \Omega_{10,5} (\langle \chi_{10,5} \rangle - \langle \chi_{5,10} \rangle) \\
& - \Gamma_{10} \langle \chi_{10,10} \rangle
\end{aligned} \tag{6}$$

$$\begin{aligned} \langle \dot{\chi}_{11,11} \rangle = & -i \Omega_{11,6} (\langle \chi_{11,6} \rangle - \langle \chi_{6,11} \rangle) \\ & - \Gamma_{11} \langle \chi_{11,11} \rangle \end{aligned} \quad (7)$$

$$\begin{aligned} \langle \dot{\chi}_{12,12} \rangle = & -i \Omega_{12,7} (\langle \chi_{12,7} \rangle - \langle \chi_{7,12} \rangle) \\ & - \Gamma_{12} \langle \chi_{12,12} \rangle \end{aligned} \quad (8)$$

$$\begin{aligned} \langle \dot{\chi}_{13,13} \rangle = & -i \Omega_{13,4} (\langle \chi_{13,4} \rangle - \langle \chi_{4,13} \rangle) \\ & - \Gamma_{13} \langle \chi_{13,13} \rangle \end{aligned} \quad (9)$$

$$\begin{aligned} \langle \dot{\chi}_{14,14} \rangle = & -i \Omega_{14,5} (\langle \chi_{14,5} \rangle - \langle \chi_{5,14} \rangle) \\ & - \Gamma_{14} \langle \chi_{14,14} \rangle \end{aligned} \quad (10)$$

$$\begin{aligned} \langle \dot{\chi}_{16,16} \rangle = & -i \Omega_{16,7} (\langle \chi_{16,7} \rangle - \langle \chi_{7,16} \rangle) \\ & - \Gamma_{16} \langle \chi_{16,16} \rangle \end{aligned} \quad (11)$$

$$\begin{aligned} \langle \dot{\chi}_{17,17} \rangle = & -i \Omega_{17,8} (\langle \chi_{17,8} \rangle - \langle \chi_{8,17} \rangle) \\ & - \Gamma_{17} \langle \chi_{17,17} \rangle \end{aligned} \quad (12)$$

$$\begin{aligned} \langle \dot{\chi}_{19,19} \rangle = & -i \Omega_{19,4} (\langle \chi_{19,4} \rangle - \langle \chi_{4,19} \rangle) \\ & - \Gamma_{19} \langle \chi_{19,19} \rangle \end{aligned} \quad (13)$$

$$\begin{aligned} \langle \dot{\chi}_{20,20} \rangle = & -i \Omega_{20,5} (\langle \chi_{20,5} \rangle - \langle \chi_{5,20} \rangle) \\ & - \Gamma_{20} \langle \chi_{20,20} \rangle \end{aligned} \quad (14)$$

$$\begin{aligned} \langle \dot{\chi}_{21,21} \rangle = & -i \Omega_{21,6} (\langle \chi_{21,6} \rangle - \langle \chi_{6,21} \rangle) \\ & - \Gamma_{21} \langle \chi_{21,21} \rangle \end{aligned} \quad (15)$$

$$\langle \dot{\chi}_{22,22} \rangle = -i \Omega_{22,7} (\langle \chi_{22,7} \rangle - \langle \chi_{7,22} \rangle)$$

$$- \Gamma_{22} \langle \chi_{22,22} \rangle \quad (16)$$

$$\begin{aligned} \dot{\langle \chi_{23,23} \rangle} = & -i \Omega_{23,8} (\langle \chi_{23,8} \rangle - \langle \chi_{8,23} \rangle) \\ & - \Gamma_{23} \langle \chi_{23,23} \rangle \end{aligned} \quad (17)$$

$$\begin{aligned} \dot{\langle \chi_{19,13} \rangle} = & i \Delta_1 \langle \chi_{19,13} \rangle \\ & - i \Omega_{13,4} \langle \chi_{19,4} \rangle + i \Omega_{19,4} \langle \chi_{4,13} \rangle \\ & - \frac{\Gamma_{19} + \Gamma_{13}}{2} \langle \chi_{19,13} \rangle \end{aligned} \quad (18)$$

$$\begin{aligned} \dot{\langle \chi_{13,19} \rangle} = & -i \Delta_1 \langle \chi_{13,19} \rangle \\ & + i \Omega_{13,4} \langle \chi_{4,19} \rangle - i \Omega_{19,4} \langle \chi_{13,4} \rangle \\ & - \frac{\Gamma_{19} + \Gamma_{13}}{2} \langle \chi_{19,13} \rangle \end{aligned} \quad (19)$$

$$\begin{aligned} \dot{\langle \chi_{14,10} \rangle} = & i \Delta_2 \langle \chi_{14,10} \rangle \\ & - i \Omega_{10,5} \langle \chi_{14,5} \rangle + i \Omega_{14,5} \langle \chi_{5,10} \rangle \\ & - \frac{\Gamma_{14} + \Gamma_{10}}{2} \langle \chi_{14,10} \rangle \end{aligned} \quad (20)$$

$$\begin{aligned} \dot{\langle \chi_{10,14} \rangle} = & -i \Delta_2 \langle \chi_{10,14} \rangle \\ & + i \Omega_{10,5} \langle \chi_{5,14} \rangle - i \Omega_{14,5} \langle \chi_{10,5} \rangle \\ & - \frac{\Gamma_{14} + \Gamma_{10}}{2} \langle \chi_{10,14} \rangle \end{aligned} \quad (21)$$

$$\begin{aligned} \dot{\langle \chi_{20,10} \rangle} = & i (\Delta_1 + \Delta_2) \langle \chi_{20,10} \rangle \\ & - i \Omega_{10,5} \langle \chi_{20,5} \rangle + i \Omega_{20,5} \langle \chi_{5,10} \rangle \\ & - \frac{\Gamma_{20} + \Gamma_{10}}{2} \langle \chi_{20,10} \rangle \end{aligned} \quad (22)$$

$$\begin{aligned} \dot{\langle \chi_{10,20} \rangle} = & -i (\Delta_1 + \Delta_2) \langle \chi_{10,20} \rangle \\ & + i \Omega_{10,5} \langle \chi_{5,20} \rangle - i \Omega_{20,5} \langle \chi_{10,5} \rangle \end{aligned}$$

$$-\frac{\Gamma_{20}+\Gamma_{10}}{2} \langle \chi_{10,20} \rangle \quad (23)$$

$$\begin{aligned} \dot{\langle \chi_{20,14} \rangle} = & i \Delta_1 \langle \chi_{20,14} \rangle \\ & - i \Omega_{14,5} \langle \chi_{20,5} \rangle + i \Omega_{20,5} \langle \chi_{5,14} \rangle \\ & - \frac{\Gamma_{20}+\Gamma_{14}}{2} \langle \chi_{20,14} \rangle \end{aligned} \quad (24)$$

$$\begin{aligned} \dot{\langle \chi_{14,20} \rangle} = & - i \Delta_1 \langle \chi_{14,20} \rangle \\ & + i \Omega_{14,5} \langle \chi_{5,20} \rangle - i \Omega_{20,5} \langle \chi_{14,5} \rangle \\ & - \frac{\Gamma_{20}+\Gamma_{14}}{2} \langle \chi_{14,20} \rangle \end{aligned} \quad (25)$$

$$\begin{aligned} \dot{\langle \chi_{21,11} \rangle} = & i (\Delta_1 + \Delta_2) \langle \chi_{21,11} \rangle \\ & - i \Omega_{11,6} \langle \chi_{21,6} \rangle + i \Omega_{21,6} \langle \chi_{6,11} \rangle \\ & - \frac{\Gamma_{21}+\Gamma_{11}}{2} \langle \chi_{21,11} \rangle \end{aligned} \quad (26)$$

$$\begin{aligned} \dot{\langle \chi_{11,21} \rangle} = & - i (\Delta_1 + \Delta_2) \langle \chi_{11,21} \rangle \\ & + i \Omega_{11,6} \langle \chi_{6,21} \rangle - i \Omega_{21,6} \langle \chi_{11,6} \rangle \\ & - \frac{\Gamma_{21}+\Gamma_{11}}{2} \langle \chi_{11,21} \rangle \end{aligned} \quad (27)$$

$$\begin{aligned} \dot{\langle \chi_{16,12} \rangle} = & i \Delta_2 \langle \chi_{16,12} \rangle \\ & - i \Omega_{12,7} \langle \chi_{16,7} \rangle + i \Omega_{16,7} \langle \chi_{7,12} \rangle \\ & - \frac{\Gamma_{16}+\Gamma_{12}}{2} \langle \chi_{16,12} \rangle \end{aligned} \quad (28)$$

$$\begin{aligned} \dot{\langle \chi_{12,16} \rangle} = & - i \Delta_2 \langle \chi_{12,16} \rangle \\ & + i \Omega_{12,7} \langle \chi_{7,16} \rangle - i \Omega_{16,7} \langle \chi_{12,7} \rangle \\ & - \frac{\Gamma_{16}+\Gamma_{12}}{2} \langle \chi_{12,16} \rangle \end{aligned} \quad (29)$$

$$\dot{\langle \chi_{22,12} \rangle} = i (\Delta_1 + \Delta_2) \langle \chi_{22,12} \rangle$$

$$\begin{aligned}
& -i \Omega_{12,7} \langle \chi_{22,7} \rangle + i \Omega_{22,7} \langle \chi_{7,12} \rangle \\
& - \frac{\Gamma_{22} + \Gamma_{12}}{2} \langle \chi_{22,12} \rangle
\end{aligned} \tag{30}$$

$$\begin{aligned}
\dot{\langle \chi_{12,22} \rangle} = & -i (\Delta_1 + \Delta_2) \langle \chi_{12,22} \rangle \\
& + i \Omega_{12,7} \langle \chi_{7,22} \rangle - i \Omega_{22,7} \langle \chi_{12,7} \rangle \\
& - \frac{\Gamma_{22} + \Gamma_{12}}{2} \langle \chi_{12,22} \rangle
\end{aligned} \tag{31}$$

$$\begin{aligned}
\dot{\langle \chi_{22,16} \rangle} = & i \Delta_1 \langle \chi_{22,16} \rangle \\
& - i \Omega_{16,7} \langle \chi_{22,7} \rangle + i \Omega_{22,7} \langle \chi_{7,16} \rangle \\
& - \frac{\Gamma_{22} + \Gamma_{16}}{2} \langle \chi_{22,16} \rangle
\end{aligned} \tag{32}$$

$$\begin{aligned}
\dot{\langle \chi_{16,22} \rangle} = & -i \Delta_1 \langle \chi_{16,22} \rangle \\
& + i \Omega_{16,7} \langle \chi_{7,22} \rangle - i \Omega_{22,7} \langle \chi_{16,7} \rangle \\
& - \frac{\Gamma_{22} + \Gamma_{16}}{2} \langle \chi_{16,22} \rangle
\end{aligned} \tag{33}$$

$$\begin{aligned}
\dot{\langle \chi_{23,17} \rangle} = & i \Delta_1 \langle \chi_{23,17} \rangle \\
& - i \Omega_{17,8} \langle \chi_{23,8} \rangle + i \Omega_{23,8} \langle \chi_{8,17} \rangle \\
& - \frac{\Gamma_{23} + \Gamma_{17}}{2} \langle \chi_{23,17} \rangle
\end{aligned} \tag{34}$$

$$\begin{aligned}
\dot{\langle \chi_{17,23} \rangle} = & -i \Delta_1 \langle \chi_{17,23} \rangle \\
& + i \Omega_{17,8} \langle \chi_{8,23} \rangle - i \Omega_{23,8} \langle \chi_{17,8} \rangle \\
& - \frac{\Gamma_{23} + \Gamma_{17}}{2} \langle \chi_{17,23} \rangle
\end{aligned} \tag{35}$$

$$\begin{aligned}
\dot{\langle \chi_{13,4} \rangle} = & -i (\Delta_L + \Delta_1) \langle \chi_{13,4} \rangle \\
& - i \Omega_{13,4} \langle \chi_{13,13} \rangle - i \Omega_{19,4} \langle \chi_{13,19} \rangle \\
& + i \Omega_{13,4} \langle \chi_{4,4} \rangle
\end{aligned}$$

$$-\frac{\Gamma_{13}}{2} \langle \chi_{13,4} \rangle \quad (36)$$

$$\begin{aligned} \dot{\langle \chi_{4,13} \rangle} = & i(\Delta_L + \Delta_I) \langle \chi_{4,13} \rangle \\ & + i\Omega_{13,4} \langle \chi_{13,13} \rangle + i\Omega_{19,4} \langle \chi_{19,13} \rangle \\ & - i\Omega_{13,4} \langle \chi_{4,4} \rangle \\ & - \frac{\Gamma_{13}}{2} \langle \chi_{4,13} \rangle \end{aligned} \quad (37)$$

$$\begin{aligned} \dot{\langle \chi_{19,4} \rangle} = & -i\Delta_L \langle \chi_{19,4} \rangle \\ & - i\Omega_{19,4} \langle \chi_{19,19} \rangle - i\Omega_{13,4} \langle \chi_{19,13} \rangle \\ & + i\Omega_{19,4} \langle \chi_{4,4} \rangle \\ & - \frac{\Gamma_{19}}{2} \langle \chi_{19,4} \rangle \end{aligned} \quad (38)$$

$$\begin{aligned} \dot{\langle \chi_{4,19} \rangle} = & i\Delta_L \langle \chi_{4,19} \rangle \\ & + i\Omega_{19,4} \langle \chi_{19,19} \rangle + i\Omega_{13,4} \langle \chi_{13,19} \rangle \\ & - i\Omega_{19,4} \langle \chi_{4,4} \rangle \\ & - \frac{\Gamma_{19}}{2} \langle \chi_{4,19} \rangle \end{aligned} \quad (39)$$

$$\begin{aligned} \dot{\langle \chi_{10,5} \rangle} = & -i(\Delta_L + \Delta_I + \Delta_2) \langle \chi_{10,5} \rangle \\ & - i\Omega_{10,5} \langle \chi_{10,10} \rangle - i\Omega_{14,5} \langle \chi_{10,14} \rangle - i\Omega_{20,5} \langle \chi_{10,20} \rangle \\ & + i\Omega_{10,5} \langle \chi_{5,5} \rangle \\ & - \frac{\Gamma_{10}}{2} \langle \chi_{10,5} \rangle \end{aligned} \quad (40)$$

$$\begin{aligned} \dot{\langle \chi_{5,10} \rangle} = & i(\Delta_L + \Delta_I + \Delta_2) \langle \chi_{5,10} \rangle \\ & + i\Omega_{10,5} \langle \chi_{10,10} \rangle + i\Omega_{14,5} \langle \chi_{14,10} \rangle + i\Omega_{20,5} \langle \chi_{20,10} \rangle \\ & - i\Omega_{10,5} \langle \chi_{5,5} \rangle \\ & - \frac{\Gamma_{10}}{2} \langle \chi_{5,10} \rangle \end{aligned} \quad (41)$$

$$\begin{aligned}
\dot{\langle \chi_{14,5} \rangle} = & -i(\Delta_L + \Delta_I) \langle \chi_{14,5} \rangle \\
& -i\Omega_{14,5} \langle \chi_{14,14} \rangle - i\Omega_{10,5} \langle \chi_{14,10} \rangle - i\Omega_{20,5} \langle \chi_{14,20} \rangle \\
& + i\Omega_{14,5} \langle \chi_{5,5} \rangle \\
& - \frac{\Gamma_{14}}{2} \langle \chi_{14,5} \rangle
\end{aligned} \tag{42}$$

$$\begin{aligned}
\dot{\langle \chi_{5,14} \rangle} = & i(\Delta_L + \Delta_I) \langle \chi_{5,14} \rangle \\
& + i\Omega_{14,5} \langle \chi_{14,14} \rangle + i\Omega_{10,5} \langle \chi_{10,14} \rangle + i\Omega_{20,5} \langle \chi_{20,14} \rangle \\
& - i\Omega_{14,5} \langle \chi_{5,5} \rangle \\
& - \frac{\Gamma_{14}}{2} \langle \chi_{5,14} \rangle
\end{aligned} \tag{43}$$

$$\begin{aligned}
\dot{\langle \chi_{20,5} \rangle} = & -i\Delta_L \langle \chi_{20,5} \rangle \\
& -i\Omega_{20,5} \langle \chi_{20,20} \rangle - i\Omega_{10,5} \langle \chi_{20,10} \rangle - i\Omega_{14,5} \langle \chi_{20,14} \rangle \\
& + i\Omega_{20,5} \langle \chi_{5,5} \rangle \\
& - \frac{\Gamma_{20}}{2} \langle \chi_{20,5} \rangle
\end{aligned} \tag{44}$$

$$\begin{aligned}
\dot{\langle \chi_{5,20} \rangle} = & i\Delta_L \langle \chi_{5,20} \rangle \\
& + i\Omega_{20,5} \langle \chi_{20,20} \rangle + i\Omega_{10,5} \langle \chi_{10,20} \rangle + i\Omega_{14,5} \langle \chi_{14,20} \rangle \\
& - i\Omega_{20,5} \langle \chi_{5,5} \rangle \\
& - \frac{\Gamma_{20}}{2} \langle \chi_{5,20} \rangle
\end{aligned} \tag{45}$$

$$\begin{aligned}
\dot{\langle \chi_{11,6} \rangle} = & -i(\Delta_L + \Delta_I + \Delta_2) \langle \chi_{11,6} \rangle \\
& - \frac{1}{2} i\Omega_{11,6} \langle \chi_{11,11} \rangle - \frac{1}{2} i\Omega_{21,6} \langle \chi_{11,21} \rangle \\
& + \frac{1}{2} i\Omega_{11,6} \langle \chi_{6,6} \rangle \\
& - \frac{\Gamma_{11}}{2} \langle \chi_{11,6} \rangle
\end{aligned} \tag{46}$$

$$\begin{aligned}
\dot{\langle \chi_{6,11} \rangle} = & i(\Delta_L + \Delta_I + \Delta_2) \langle \chi_{6,11} \rangle \\
& + i\Omega_{11,6} \langle \chi_{11,11} \rangle + i\Omega_{21,6} \langle \chi_{21,11} \rangle
\end{aligned}$$

$$\begin{aligned}
& -i \Omega_{11,6} \langle \chi_{6,6} \rangle \\
& -\frac{\Gamma_{11}}{2} \langle \chi_{6,11} \rangle
\end{aligned} \tag{47}$$

$$\begin{aligned}
\dot{\langle \chi_{21,6} \rangle} = & -i \Delta_L \langle \chi_{21,6} \rangle \\
& -i \Omega_{21,6} \langle \chi_{21,21} \rangle - i \Omega_{11,6} \langle \chi_{21,11} \rangle \\
& + i \Omega_{21,6} \langle \chi_{6,6} \rangle \\
& -\frac{\Gamma_{21}}{2} \langle \chi_{21,6} \rangle
\end{aligned} \tag{48}$$

$$\begin{aligned}
\dot{\langle \chi_{6,21} \rangle} = & i \Delta_L \langle \chi_{6,21} \rangle \\
& + i \Omega_{21,6} \langle \chi_{21,21} \rangle + i \Omega_{11,6} \langle \chi_{11,21} \rangle \\
& - i \Omega_{21,6} \langle \chi_{6,6} \rangle \\
& -\frac{\Gamma_{21}}{2} \langle \chi_{6,21} \rangle
\end{aligned} \tag{49}$$

$$\begin{aligned}
\dot{\langle \chi_{12,7} \rangle} = & -i (\Delta_L + \Delta_1 + \Delta_2) \langle \chi_{12,7} \rangle \\
& -i \Omega_{12,7} \langle \chi_{12,12} \rangle - i \Omega_{16,7} \langle \chi_{12,16} \rangle - i \Omega_{22,7} \langle \chi_{12,22} \rangle \\
& + i \Omega_{12,7} \langle \chi_{7,7} \rangle \\
& -\frac{\Gamma_{12}}{2} \langle \chi_{12,7} \rangle
\end{aligned} \tag{50}$$

$$\begin{aligned}
\dot{\langle \chi_{7,12} \rangle} = & i (\Delta_L + \Delta_1 + \Delta_2) \langle \chi_{7,12} \rangle \\
& + i \Omega_{12,7} \langle \chi_{12,12} \rangle + i \Omega_{16,7} \langle \chi_{16,12} \rangle + i \Omega_{22,7} \langle \chi_{22,12} \rangle \\
& - i \Omega_{12,7} \langle \chi_{7,7} \rangle \\
& -\frac{\Gamma_{12}}{2} \langle \chi_{7,12} \rangle
\end{aligned} \tag{51}$$

$$\begin{aligned}
\dot{\langle \chi_{16,7} \rangle} = & -i (\Delta_L + \Delta_1) \langle \chi_{16,7} \rangle \\
& -i \Omega_{16,7} \langle \chi_{16,16} \rangle - i \Omega_{12,7} \langle \chi_{16,12} \rangle - i \Omega_{22,7} \langle \chi_{16,22} \rangle \\
& + i \Omega_{16,7} \langle \chi_{7,7} \rangle \\
& -\frac{\Gamma_{16}}{2} \langle \chi_{16,7} \rangle
\end{aligned} \tag{52}$$

$$\begin{aligned}
\dot{\langle \chi_{7,16} \rangle} = & i(\Delta_L + \Delta_I) \langle \chi_{7,16} \rangle \\
& + i\Omega_{16,7} \langle \chi_{16,16} \rangle + i\Omega_{12,7} \langle \chi_{12,16} \rangle + i\Omega_{22,7} \langle \chi_{22,16} \rangle \\
& - i\Omega_{16,7} \langle \chi_{7,7} \rangle \\
& - \frac{\Gamma_{16}}{2} \langle \chi_{7,16} \rangle
\end{aligned} \tag{53}$$

$$\begin{aligned}
\dot{\langle \chi_{22,7} \rangle} = & -i\Delta_L \langle \chi_{22,7} \rangle \\
& - i\Omega_{22,7} \langle \chi_{22,22} \rangle - i\Omega_{12,7} \langle \chi_{22,12} \rangle - i\Omega_{16,7} \langle \chi_{22,16} \rangle \\
& + i\Omega_{22,7} \langle \chi_{7,7} \rangle \\
& - \frac{\Gamma_{22}}{2} \langle \chi_{22,7} \rangle
\end{aligned} \tag{54}$$

$$\begin{aligned}
\dot{\langle \chi_{7,22} \rangle} = & i\Delta_L \langle \chi_{7,22} \rangle \\
& + i\Omega_{22,7} \langle \chi_{22,22} \rangle + i\Omega_{12,7} \langle \chi_{12,22} \rangle + i\Omega_{16,7} \langle \chi_{16,22} \rangle \\
& - i\Omega_{22,7} \langle \chi_{7,7} \rangle \\
& - \frac{\Gamma_{22}}{2} \langle \chi_{7,22} \rangle
\end{aligned} \tag{55}$$

$$\begin{aligned}
\dot{\langle \chi_{17,8} \rangle} = & -i(\Delta_L + \Delta_I) \langle \chi_{17,8} \rangle \\
& - i\Omega_{17,8} \langle \chi_{17,17} \rangle - i\Omega_{23,8} \langle \chi_{17,23} \rangle \\
& + i\Omega_{17,8} \langle \chi_{8,8} \rangle \\
& - \frac{\Gamma_{17}}{2} \langle \chi_{17,8} \rangle
\end{aligned} \tag{56}$$

$$\begin{aligned}
\dot{\langle \chi_{8,17} \rangle} = & i(\Delta_L + \Delta_I) \langle \chi_{8,17} \rangle \\
& + i\Omega_{17,8} \langle \chi_{17,17} \rangle + i\Omega_{23,8} \langle \chi_{23,17} \rangle \\
& - i\Omega_{17,8} \langle \chi_{8,8} \rangle \\
& - \frac{\Gamma_{17}}{2} \langle \chi_{8,17} \rangle
\end{aligned} \tag{57}$$

$$\begin{aligned}
\dot{\langle \chi_{23,8} \rangle} = & -i\Delta_L \langle \chi_{23,8} \rangle \\
& - i\Omega_{23,8} \langle \chi_{23,23} \rangle - i\Omega_{17,8} \langle \chi_{23,17} \rangle
\end{aligned}$$

$$\begin{aligned}
& + i \Omega_{23,8} \langle \chi_{8,8} \rangle \\
& - \frac{\Gamma_{23}}{2} \langle \chi_{23,8} \rangle
\end{aligned} \tag{58}$$

$$\begin{aligned}
\dot{\langle \chi_{8,23} \rangle} = & i \Delta_L \langle \chi_{8,23} \rangle \\
& + i \Omega_{23,8} \langle \chi_{23,23} \rangle + i \Omega_{17,8} \langle \chi_{17,23} \rangle \\
& - i \Omega_{23,8} \langle \chi_{8,8} \rangle \\
& - \frac{\Gamma_{23}}{2} \langle \chi_{8,23} \rangle
\end{aligned} \tag{59}$$

Appendix 2

Component Equations of Motion: Folded Step Laser Excitation Case

The following equations are the component equations of motion for two lasers exciting from the two hyperfine ground states in sodium to the $3^2P_{3/2}$ excited state which were derived using the general equations of motion in section 3.6 of Chapter Three.

$$\begin{aligned}\dot{\langle \chi_{1,1} \rangle} = & -i \Omega_{10,1} (\langle \chi_{1,10} \rangle - \langle \chi_{10,1} \rangle) \\ & -i \Omega_{14,1} (\langle \chi_{1,14} \rangle - \langle \chi_{14,1} \rangle) \\ & + \Gamma_{9,1} \langle \chi_{9,9} \rangle \\ & + \Gamma_{10,1} \langle \chi_{10,10} \rangle \\ & + \Gamma_{11,1} \langle \chi_{11,11} \rangle \\ & + \Gamma_{13,1} \langle \chi_{13,13} \rangle \\ & + \Gamma_{14,1} \langle \chi_{14,14} \rangle \\ & + \Gamma_{15,1} \langle \chi_{15,15} \rangle \\ & + \Gamma_{14,10,1} (\langle \chi_{14,10} \rangle + \langle \chi_{10,14} \rangle) \\ & + \Gamma_{15,9,1} (\langle \chi_{15,9} \rangle + \langle \chi_{9,15} \rangle)\end{aligned}\tag{1}$$

$$\begin{aligned}\dot{\langle \chi_{2,2} \rangle} = & -i \Omega_{9,2} (\langle \chi_{2,9} \rangle - \langle \chi_{9,2} \rangle) \\ & -i \Omega_{15,2} (\langle \chi_{2,15} \rangle - \langle \chi_{15,2} \rangle) \\ & + \Gamma_{9,2} \langle \chi_{9,9} \rangle \\ & + \Gamma_{10,2} \langle \chi_{10,10} \rangle \\ & + \Gamma_{12,2} \langle \chi_{12,12} \rangle \\ & + \Gamma_{14,2} \langle \chi_{14,14} \rangle \\ & + \Gamma_{15,2} \langle \chi_{15,15} \rangle\end{aligned}$$

$$\begin{aligned}
& + \Gamma_{16,2} \langle \chi_{16,16} \rangle \\
& + \Gamma_{14,10,2} (\langle \chi_{14,10} \rangle + \langle \chi_{10,14} \rangle) \\
& + \Gamma_{15,9,2} (\langle \chi_{15,9} \rangle + \langle \chi_{9,15} \rangle) \\
& + \Gamma_{16,12,2} (\langle \chi_{16,12} \rangle + \langle \chi_{12,16} \rangle)
\end{aligned} \tag{2}$$

$$\begin{aligned}
\dot{\langle \chi_{3,3} \rangle} = & -i \Omega_{12,3} (\langle \chi_{3,12} \rangle - \langle \chi_{12,3} \rangle) \\
& -i \Omega_{16,3} (\langle \chi_{3,16} \rangle - \langle \chi_{16,3} \rangle) \\
& + \Gamma_{9,3} \langle \chi_{9,9} \rangle \\
& + \Gamma_{11,3} \langle \chi_{11,11} \rangle \\
& + \Gamma_{12,3} \langle \chi_{12,12} \rangle \\
& + \Gamma_{15,3} \langle \chi_{15,15} \rangle \\
& + \Gamma_{16,3} \langle \chi_{16,16} \rangle \\
& + \Gamma_{17,3} \langle \chi_{17,17} \rangle \\
& + \Gamma_{15,9,3} (\langle \chi_{15,9} \rangle + \langle \chi_{9,15} \rangle) \\
& + \Gamma_{16,12,3} (\langle \chi_{16,12} \rangle + \langle \chi_{12,16} \rangle)
\end{aligned} \tag{3}$$

$$\begin{aligned}
\dot{\langle \chi_{4,4} \rangle} = & -i \Omega_{13,4} (\langle \chi_{4,13} \rangle - \langle \chi_{13,4} \rangle) \\
& -i \Omega_{19,4} (\langle \chi_{4,19} \rangle - \langle \chi_{19,4} \rangle) \\
& + \Gamma_{10,4} \langle \chi_{10,10} \rangle \\
& + \Gamma_{13,4} \langle \chi_{13,13} \rangle \\
& + \Gamma_{14,4} \langle \chi_{14,14} \rangle \\
& + \Gamma_{19,4} \langle \chi_{19,19} \rangle \\
& + \Gamma_{20,4} \langle \chi_{20,20} \rangle \\
& + \Gamma_{19,13,4} (\langle \chi_{19,13} \rangle + \langle \chi_{13,19} \rangle) \\
& + \Gamma_{14,10,4} (\langle \chi_{14,10} \rangle + \langle \chi_{10,14} \rangle) \\
& + \Gamma_{20,10,4} (\langle \chi_{20,10} \rangle + \langle \chi_{10,20} \rangle) \\
& + \Gamma_{20,14,4} (\langle \chi_{20,14} \rangle + \langle \chi_{14,20} \rangle)
\end{aligned} \tag{4}$$

$$\dot{\langle \chi_{5,5} \rangle} = -i \Omega_{10,5} (\langle \chi_{5,10} \rangle - \langle \chi_{10,5} \rangle)$$

$$\begin{aligned}
& -i\Omega_{14,5}(\langle\chi_{5,14}\rangle - \langle\chi_{14,5}\rangle) \\
& -i\Omega_{20,5}(\langle\chi_{5,20}\rangle - \langle\chi_{20,5}\rangle) \\
& +\Gamma_{10,5}\langle\chi_{10,10}\rangle \\
& +\Gamma_{11,5}\langle\chi_{11,11}\rangle \\
& +\Gamma_{13,5}\langle\chi_{13,13}\rangle \\
& +\Gamma_{14,5}\langle\chi_{14,14}\rangle \\
& +\Gamma_{15,5}\langle\chi_{15,15}\rangle \\
& +\Gamma_{19,5}\langle\chi_{19,19}\rangle \\
& +\Gamma_{20,5}\langle\chi_{20,20}\rangle \\
& +\Gamma_{21,5}\langle\chi_{21,21}\rangle \\
& +\Gamma_{19,13,5}(\langle\chi_{19,13}\rangle + \langle\chi_{13,19}\rangle) \\
& +\Gamma_{14,10,5}(\langle\chi_{14,10}\rangle + \langle\chi_{10,14}\rangle) \\
& +\Gamma_{20,10,5}(\langle\chi_{20,10}\rangle + \langle\chi_{10,20}\rangle) \\
& +\Gamma_{20,14,5}(\langle\chi_{20,14}\rangle + \langle\chi_{14,20}\rangle) \\
& +\Gamma_{21,11,5}(\langle\chi_{21,11}\rangle + \langle\chi_{11,21}\rangle)
\end{aligned} \tag{5}$$

$$\begin{aligned}
\dot{\langle\chi_{6,6}\rangle} = & -i\Omega_{11,6}(\langle\chi_{6,11}\rangle - \langle\chi_{11,6}\rangle) \\
& -i\Omega_{21,6}(\langle\chi_{6,21}\rangle - \langle\chi_{21,6}\rangle) \\
& +\Gamma_{10,6}\langle\chi_{10,10}\rangle \\
& +\Gamma_{11,6}\langle\chi_{11,11}\rangle \\
& +\Gamma_{12,6}\langle\chi_{12,12}\rangle \\
& +\Gamma_{14,6}\langle\chi_{14,14}\rangle \\
& +\Gamma_{16,6}\langle\chi_{16,16}\rangle \\
& +\Gamma_{20,6}\langle\chi_{20,20}\rangle \\
& +\Gamma_{21,6}\langle\chi_{21,21}\rangle \\
& +\Gamma_{22,6}\langle\chi_{22,22}\rangle \\
& +\Gamma_{14,10,6}(\langle\chi_{14,10}\rangle + \langle\chi_{10,14}\rangle) \\
& +\Gamma_{20,10,6}(\langle\chi_{20,10}\rangle + \langle\chi_{10,20}\rangle) \\
& +\Gamma_{20,14,6}(\langle\chi_{20,14}\rangle + \langle\chi_{14,20}\rangle)
\end{aligned}$$

$$\begin{aligned}
& + \Gamma_{21,11,6} (\langle \chi_{21,11} \rangle + \langle \chi_{11,21} \rangle) \\
& + \Gamma_{16,12,6} (\langle \chi_{16,12} \rangle + \langle \chi_{12,16} \rangle) \\
& + \Gamma_{22,12,6} (\langle \chi_{22,12} \rangle + \langle \chi_{12,22} \rangle) \\
& + \Gamma_{22,16,6} (\langle \chi_{22,16} \rangle + \langle \chi_{16,22} \rangle)
\end{aligned} \tag{6}$$

$$\begin{aligned}
\dot{\langle \chi_{7,7} \rangle} = & -i \Omega_{12,7} (\langle \chi_{7,12} \rangle - \langle \chi_{12,7} \rangle) \\
& -i \Omega_{16,7} (\langle \chi_{7,16} \rangle - \langle \chi_{16,7} \rangle) \\
& -i \Omega_{22,7} (\langle \chi_{7,22} \rangle - \langle \chi_{22,7} \rangle) \\
& + \Gamma_{11,7} \langle \chi_{11,11} \rangle \\
& + \Gamma_{12,7} \langle \chi_{12,12} \rangle \\
& + \Gamma_{15,7} \langle \chi_{15,15} \rangle \\
& + \Gamma_{16,7} \langle \chi_{16,16} \rangle \\
& + \Gamma_{17,7} \langle \chi_{17,17} \rangle \\
& + \Gamma_{21,7} \langle \chi_{21,21} \rangle \\
& + \Gamma_{22,7} \langle \chi_{22,22} \rangle \\
& + \Gamma_{23,7} \langle \chi_{23,23} \rangle \\
& + \Gamma_{21,11,7} (\langle \chi_{21,11} \rangle + \langle \chi_{11,21} \rangle) \\
& + \Gamma_{16,12,7} (\langle \chi_{16,12} \rangle + \langle \chi_{12,16} \rangle) \\
& + \Gamma_{22,12,7} (\langle \chi_{22,12} \rangle + \langle \chi_{12,22} \rangle) \\
& + \Gamma_{22,16,7} (\langle \chi_{22,16} \rangle + \langle \chi_{16,22} \rangle) \\
& + \Gamma_{23,17,7} (\langle \chi_{23,17} \rangle + \langle \chi_{17,23} \rangle)
\end{aligned} \tag{7}$$

$$\begin{aligned}
\dot{\langle \chi_{8,8} \rangle} = & -i \Omega_{17,8} (\langle \chi_{8,17} \rangle - \langle \chi_{17,8} \rangle) \\
& -i \Omega_{23,8} (\langle \chi_{8,23} \rangle - \langle \chi_{23,8} \rangle) \\
& + \Gamma_{12,8} \langle \chi_{12,12} \rangle \\
& + \Gamma_{16,8} \langle \chi_{16,16} \rangle \\
& + \Gamma_{17,8} \langle \chi_{17,17} \rangle \\
& + \Gamma_{22,8} \langle \chi_{22,22} \rangle \\
& + \Gamma_{23,8} \langle \chi_{23,23} \rangle
\end{aligned}$$

$$\begin{aligned}
& + \Gamma_{16,12,8} (\langle \chi_{16,12} \rangle + \langle \chi_{12,16} \rangle) \\
& + \Gamma_{22,12,8} (\langle \chi_{22,12} \rangle + \langle \chi_{12,22} \rangle) \\
& + \Gamma_{22,16,8} (\langle \chi_{22,16} \rangle + \langle \chi_{16,22} \rangle) \\
& + \Gamma_{23,17,8} (\langle \chi_{23,17} \rangle + \langle \chi_{17,23} \rangle)
\end{aligned} \tag{8}$$

$$\begin{aligned}
\dot{\langle \chi_{9,9} \rangle} = & -i \Omega_{9,2} (\langle \chi_{9,2} \rangle - \langle \chi_{2,9} \rangle) \\
& - \Gamma_9 \langle \chi_{9,9} \rangle
\end{aligned} \tag{9}$$

$$\begin{aligned}
\dot{\langle \chi_{10,10} \rangle} = & -i \Omega_{10,1} (\langle \chi_{10,1} \rangle - \langle \chi_{1,10} \rangle) \\
& -i \Omega_{10,5} (\langle \chi_{10,5} \rangle - \langle \chi_{5,10} \rangle) \\
& - \Gamma_{10} \langle \chi_{10,10} \rangle
\end{aligned} \tag{10}$$

$$\begin{aligned}
\dot{\langle \chi_{11,11} \rangle} = & -i \Omega_{11,6} (\langle \chi_{11,6} \rangle - \langle \chi_{6,11} \rangle) \\
& - \Gamma_{11} \langle \chi_{11,11} \rangle
\end{aligned} \tag{11}$$

$$\begin{aligned}
\dot{\langle \chi_{12,12} \rangle} = & -i \Omega_{12,3} (\langle \chi_{12,3} \rangle - \langle \chi_{3,12} \rangle) \\
& -i \Omega_{12,7} (\langle \chi_{12,7} \rangle - \langle \chi_{7,12} \rangle) \\
& - \Gamma_{12} \langle \chi_{12,12} \rangle
\end{aligned} \tag{12}$$

$$\begin{aligned}
\dot{\langle \chi_{13,13} \rangle} = & -i \Omega_{13,4} (\langle \chi_{13,4} \rangle - \langle \chi_{4,13} \rangle) \\
& - \Gamma_{13} \langle \chi_{13,13} \rangle
\end{aligned} \tag{13}$$

$$\begin{aligned}
\dot{\langle \chi_{14,14} \rangle} = & -i \Omega_{14,1} (\langle \chi_{14,1} \rangle - \langle \chi_{1,14} \rangle) \\
& -i \Omega_{14,5} (\langle \chi_{14,5} \rangle - \langle \chi_{5,14} \rangle) \\
& - \Gamma_{14} \langle \chi_{14,14} \rangle
\end{aligned} \tag{14}$$

$$\begin{aligned}
\dot{\langle \chi_{15,15} \rangle} = & -i \Omega_{15,2} (\langle \chi_{15,2} \rangle - \langle \chi_{2,15} \rangle) \\
& - \Gamma_{15} \langle \chi_{15,15} \rangle
\end{aligned} \tag{15}$$

$$\begin{aligned}
\dot{\langle \chi_{16,16} \rangle} = & -i \Omega_{16,3} (\langle \chi_{16,3} \rangle - \langle \chi_{3,16} \rangle) \\
& -i \Omega_{16,7} (\langle \chi_{16,7} \rangle - \langle \chi_{7,16} \rangle) \\
& -\Gamma_{16} \langle \chi_{16,16} \rangle
\end{aligned} \tag{16}$$

$$\begin{aligned}
\dot{\langle \chi_{17,17} \rangle} = & -i \Omega_{17,8} (\langle \chi_{17,8} \rangle - \langle \chi_{8,17} \rangle) \\
& -\Gamma_{17} \langle \chi_{17,17} \rangle
\end{aligned} \tag{17}$$

$$\begin{aligned}
\dot{\langle \chi_{19,19} \rangle} = & -i \Omega_{19,4} (\langle \chi_{19,4} \rangle - \langle \chi_{4,19} \rangle) \\
& -\Gamma_{19} \langle \chi_{19,19} \rangle
\end{aligned} \tag{18}$$

$$\begin{aligned}
\dot{\langle \chi_{20,20} \rangle} = & -i \Omega_{20,5} (\langle \chi_{20,5} \rangle - \langle \chi_{5,20} \rangle) \\
& -\Gamma_{20} \langle \chi_{20,20} \rangle
\end{aligned} \tag{19}$$

$$\begin{aligned}
\dot{\langle \chi_{21,21} \rangle} = & -i \Omega_{21,6} (\langle \chi_{21,6} \rangle - \langle \chi_{6,21} \rangle) \\
& -\Gamma_{21} \langle \chi_{21,21} \rangle
\end{aligned} \tag{20}$$

$$\begin{aligned}
\dot{\langle \chi_{22,22} \rangle} = & -i \Omega_{22,7} (\langle \chi_{22,7} \rangle - \langle \chi_{7,22} \rangle) \\
& -\Gamma_{22} \langle \chi_{22,22} \rangle
\end{aligned} \tag{21}$$

$$\begin{aligned}
\dot{\langle \chi_{23,23} \rangle} = & -i \Omega_{23,8} (\langle \chi_{23,8} \rangle - \langle \chi_{8,23} \rangle) \\
& -\Gamma_{23} \langle \chi_{23,23} \rangle
\end{aligned} \tag{22}$$

$$\begin{aligned}
\dot{\langle \chi_{19,13} \rangle} = & i \Delta_1 \langle \chi_{19,13} \rangle \\
& -i \Omega_{13,4} \langle \chi_{19,4} \rangle \\
& + i \Omega_{19,4} \langle \chi_{4,13} \rangle \\
& - \frac{\Gamma_{19} + \Gamma_{13}}{2} \langle \chi_{19,13} \rangle
\end{aligned} \tag{23}$$

$$\dot{\langle \chi_{13,19} \rangle} = -i \Delta_1 \langle \chi_{13,19} \rangle$$

$$\begin{aligned}
& + i \Omega_{13,4} \langle \chi_{4,19} \rangle \\
& - i \Omega_{19,4} \langle \chi_{13,4} \rangle \\
& - \frac{\Gamma_{19} + \Gamma_{13}}{2} \langle \chi_{19,13} \rangle
\end{aligned} \tag{24}$$

$$\begin{aligned}
\dot{\langle \chi_{14,10} \rangle} = & i \Delta_2 \langle \chi_{14,10} \rangle \\
& - i \Omega_{10,1} \langle \chi_{14,1} \rangle - i \Omega_{10,5} \langle \chi_{14,5} \rangle \\
& + i \Omega_{14,1} \langle \chi_{1,10} \rangle + i \Omega_{14,5} \langle \chi_{5,10} \rangle \\
& - \frac{\Gamma_{14} + \Gamma_{10}}{2} \langle \chi_{14,10} \rangle
\end{aligned} \tag{25}$$

$$\begin{aligned}
\dot{\langle \chi_{10,14} \rangle} = & - i \Delta_2 \langle \chi_{10,14} \rangle \\
& + i \Omega_{10,1} \langle \chi_{1,14} \rangle + i \Omega_{10,5} \langle \chi_{5,14} \rangle \\
& - i \Omega_{14,1} \langle \chi_{10,1} \rangle - i \Omega_{14,5} \langle \chi_{10,5} \rangle \\
& - \frac{\Gamma_{14} + \Gamma_{10}}{2} \langle \chi_{10,14} \rangle
\end{aligned} \tag{26}$$

$$\begin{aligned}
\dot{\langle \chi_{20,10} \rangle} = & i (\Delta_1 + \Delta_2) \langle \chi_{20,10} \rangle \\
& - i \Omega_{10,5} \langle \chi_{20,5} \rangle + i \Omega_{20,5} \langle \chi_{5,10} \rangle \\
& - \frac{\Gamma_{20} + \Gamma_{10}}{2} \langle \chi_{20,10} \rangle
\end{aligned} \tag{27}$$

$$\begin{aligned}
\dot{\langle \chi_{10,20} \rangle} = & - i (\Delta_1 + \Delta_2) \langle \chi_{10,20} \rangle \\
& + i \Omega_{10,5} \langle \chi_{5,20} \rangle - i \Omega_{20,5} \langle \chi_{10,5} \rangle \\
& - \frac{\Gamma_{20} + \Gamma_{10}}{2} \langle \chi_{10,20} \rangle
\end{aligned} \tag{28}$$

$$\begin{aligned}
\dot{\langle \chi_{20,14} \rangle} = & i \Delta_1 \langle \chi_{20,14} \rangle \\
& - i \Omega_{14,5} \langle \chi_{20,5} \rangle + i \Omega_{20,5} \langle \chi_{5,14} \rangle \\
& - \frac{\Gamma_{20} + \Gamma_{14}}{2} \langle \chi_{20,14} \rangle
\end{aligned} \tag{29}$$

$$\dot{\langle \chi_{14,20} \rangle} = - i \Delta_1 \langle \chi_{14,20} \rangle$$

$$\begin{aligned}
& + i \Omega_{14,5} \langle \chi_{5,20} \rangle - i \Omega_{20,5} \langle \chi_{14,5} \rangle \\
& - \frac{\Gamma_{20} + \Gamma_{14}}{2} \langle \chi_{14,20} \rangle
\end{aligned} \tag{30}$$

$$\begin{aligned}
\dot{\langle \chi_{15,9} \rangle} = & i (\Delta_2 + \Delta_3) \langle \chi_{15,9} \rangle \\
& - i \Omega_{9,2} \langle \chi_{15,2} \rangle \\
& + i \Omega_{15,2} \langle \chi_{2,9} \rangle \\
& - \frac{\Gamma_{15} + \Gamma_9}{2} \langle \chi_{15,9} \rangle
\end{aligned} \tag{31}$$

$$\begin{aligned}
\dot{\langle \chi_{9,15} \rangle} = & - i (\Delta_2 + \Delta_3) \langle \chi_{9,15} \rangle \\
& + i \Omega_{9,2} \langle \chi_{2,15} \rangle \\
& - i \Omega_{15,2} \langle \chi_{9,2} \rangle \\
& - \frac{\Gamma_{15} + \Gamma_9}{2} \langle \chi_{9,15} \rangle
\end{aligned} \tag{32}$$

$$\begin{aligned}
\dot{\langle \chi_{21,11} \rangle} = & i (\Delta_1 + \Delta_2) \langle \chi_{21,11} \rangle \\
& - i \Omega_{11,6} \langle \chi_{21,6} \rangle \\
& + i \Omega_{21,6} \langle \chi_{6,11} \rangle \\
& - \frac{\Gamma_{21} + \Gamma_{11}}{2} \langle \chi_{21,11} \rangle
\end{aligned} \tag{33}$$

$$\begin{aligned}
\dot{\langle \chi_{11,21} \rangle} = & - i (\Delta_1 + \Delta_2) \langle \chi_{11,21} \rangle \\
& + i \Omega_{11,6} \langle \chi_{6,21} \rangle \\
& - i \Omega_{21,6} \langle \chi_{11,6} \rangle \\
& - \frac{\Gamma_{21} + \Gamma_{11}}{2} \langle \chi_{11,21} \rangle
\end{aligned} \tag{34}$$

$$\begin{aligned}
\dot{\langle \chi_{16,12} \rangle} = & i \Delta_2 \langle \chi_{16,12} \rangle \\
& - i \Omega_{12,3} \langle \chi_{16,3} \rangle - i \Omega_{12,7} \langle \chi_{16,7} \rangle \\
& + i \Omega_{16,3} \langle \chi_{3,12} \rangle + i \Omega_{16,7} \langle \chi_{7,12} \rangle \\
& - \frac{\Gamma_{16} + \Gamma_{12}}{2} \langle \chi_{16,12} \rangle
\end{aligned} \tag{35}$$

$$\begin{aligned}
\dot{\langle \chi_{12,16} \rangle} = & -i \Delta_2 \langle \chi_{12,16} \rangle \\
& + i \Omega_{12,3} \langle \chi_{3,16} \rangle + i \Omega_{12,7} \langle \chi_{7,16} \rangle \\
& - i \Omega_{16,3} \langle \chi_{12,3} \rangle - i \Omega_{16,7} \langle \chi_{12,7} \rangle \\
& - \frac{\Gamma_{16} + \Gamma_{12}}{2} \langle \chi_{12,16} \rangle
\end{aligned} \tag{36}$$

$$\begin{aligned}
\dot{\langle \chi_{22,12} \rangle} = & i (\Delta_1 + \Delta_2) \langle \chi_{22,12} \rangle \\
& - i \Omega_{12,7} \langle \chi_{22,7} \rangle + i \Omega_{22,7} \langle \chi_{7,12} \rangle \\
& - \frac{\Gamma_{22} + \Gamma_{12}}{2} \langle \chi_{22,12} \rangle
\end{aligned} \tag{37}$$

$$\begin{aligned}
\dot{\langle \chi_{12,22} \rangle} = & -i (\Delta_1 + \Delta_2) \langle \chi_{12,22} \rangle \\
& + i \Omega_{12,7} \langle \chi_{7,22} \rangle - i \Omega_{22,7} \langle \chi_{12,7} \rangle \\
& - \frac{\Gamma_{22} + \Gamma_{12}}{2} \langle \chi_{12,22} \rangle
\end{aligned} \tag{38}$$

$$\begin{aligned}
\dot{\langle \chi_{22,16} \rangle} = & i \Delta_1 \langle \chi_{22,16} \rangle \\
& - i \Omega_{16,7} \langle \chi_{22,7} \rangle + i \Omega_{22,7} \langle \chi_{7,16} \rangle \\
& - \frac{\Gamma_{22} + \Gamma_{16}}{2} \langle \chi_{22,16} \rangle
\end{aligned} \tag{39}$$

$$\begin{aligned}
\dot{\langle \chi_{16,22} \rangle} = & -i \Delta_1 \langle \chi_{16,22} \rangle \\
& + i \Omega_{16,7} \langle \chi_{7,22} \rangle - i \Omega_{22,7} \langle \chi_{16,7} \rangle \\
& - \frac{\Gamma_{22} + \Gamma_{16}}{2} \langle \chi_{16,22} \rangle
\end{aligned} \tag{40}$$

$$\begin{aligned}
\dot{\langle \chi_{23,17} \rangle} = & i \Delta_1 \langle \chi_{23,17} \rangle \\
& - i \Omega_{17,8} \langle \chi_{23,8} \rangle \\
& + i \Omega_{23,8} \langle \chi_{8,17} \rangle \\
& - \frac{\Gamma_{23} + \Gamma_{17}}{2} \langle \chi_{23,17} \rangle
\end{aligned} \tag{41}$$

$$\begin{aligned}
\dot{\langle \chi_{17,23} \rangle} = & -i \Delta_1 \langle \chi_{17,23} \rangle \\
& + i \Omega_{17,8} \langle \chi_{8,23} \rangle \\
& - i \Omega_{23,8} \langle \chi_{17,8} \rangle \\
& - \frac{\Gamma_{23} + \Gamma_{17}}{2} \langle \chi_{17,23} \rangle
\end{aligned} \tag{42}$$

$$\begin{aligned}
\dot{\langle \chi_{10,1} \rangle} = & -i (\Delta_{L1} + \Delta_2) \langle \chi_{10,1} \rangle \\
& - i \Omega_{10,1} \langle \chi_{10,10} \rangle - i \Omega_{14,1} \langle \chi_{10,14} \rangle \\
& + i \Omega_{10,1} \langle \chi_{1,1} \rangle \\
& - \frac{\Gamma_{10}}{2} \langle \chi_{10,1} \rangle
\end{aligned} \tag{43}$$

$$\begin{aligned}
\dot{\langle \chi_{1,10} \rangle} = & i (\Delta_{L1} + \Delta_2) \langle \chi_{1,10} \rangle \\
& + i \Omega_{10,1} \langle \chi_{10,10} \rangle + i \Omega_{14,1} \langle \chi_{14,10} \rangle \\
& - i \Omega_{10,1} \langle \chi_{1,1} \rangle \\
& - \frac{\Gamma_{10}}{2} \langle \chi_{1,10} \rangle
\end{aligned} \tag{44}$$

$$\begin{aligned}
\dot{\langle \chi_{14,1} \rangle} = & -i \Delta_{L1} \langle \chi_{14,1} \rangle \\
& - i \Omega_{14,1} \langle \chi_{14,14} \rangle - i \Omega_{10,1} \langle \chi_{14,10} \rangle \\
& + i \Omega_{14,1} \langle \chi_{1,1} \rangle \\
& - \frac{\Gamma_{14}}{2} \langle \chi_{14,1} \rangle
\end{aligned} \tag{45}$$

$$\begin{aligned}
\dot{\langle \chi_{1,14} \rangle} = & i \Delta_{L1} \langle \chi_{1,14} \rangle \\
& + i \Omega_{14,1} \langle \chi_{14,14} \rangle + i \Omega_{10,1} \langle \chi_{10,14} \rangle \\
& - i \Omega_{14,1} \langle \chi_{1,1} \rangle \\
& - \frac{\Gamma_{14}}{2} \langle \chi_{1,14} \rangle
\end{aligned} \tag{46}$$

$$\begin{aligned}
\dot{\langle \chi_{9,2} \rangle} = & -i (\Delta_{L1} + \Delta_2 + \Delta_3) \langle \chi_{9,2} \rangle \\
& - i \Omega_{9,2} \langle \chi_{9,9} \rangle - i \Omega_{15,2} \langle \chi_{9,15} \rangle
\end{aligned}$$

$$\begin{aligned}
& + i \Omega_{9,2} \langle \chi_{2,2} \rangle \\
& - \frac{\Gamma_9}{2} \langle \chi_{9,2} \rangle
\end{aligned} \tag{47}$$

$$\begin{aligned}
\dot{\langle \chi_{2,9} \rangle} = & i (\Delta_{L1} + \Delta_2 + \Delta_3) \langle \chi_{2,9} \rangle \\
& + i \Omega_{9,2} \langle \chi_{9,9} \rangle + i \Omega_{15,2} \langle \chi_{15,9} \rangle \\
& - i \Omega_{9,2} \langle \chi_{2,2} \rangle \\
& - \frac{\Gamma_9}{2} \langle \chi_{2,9} \rangle
\end{aligned} \tag{48}$$

$$\begin{aligned}
\dot{\langle \chi_{15,2} \rangle} = & - i \Delta_{L1} \langle \chi_{15,2} \rangle \\
& - i \Omega_{15,2} \langle \chi_{15,15} \rangle - i \Omega_{9,2} \langle \chi_{15,9} \rangle \\
& + i \Omega_{15,2} \langle \chi_{2,2} \rangle \\
& - \frac{\Gamma_{15}}{2} \langle \chi_{15,2} \rangle
\end{aligned} \tag{49}$$

$$\begin{aligned}
\dot{\langle \chi_{2,15} \rangle} = & i \Delta_{L1} \langle \chi_{2,15} \rangle \\
& + i \Omega_{15,2} \langle \chi_{15,15} \rangle + i \Omega_{9,2} \langle \chi_{9,15} \rangle \\
& - i \Omega_{15,2} \langle \chi_{2,2} \rangle \\
& - \frac{\Gamma_{15}}{2} \langle \chi_{2,15} \rangle
\end{aligned} \tag{50}$$

$$\begin{aligned}
\dot{\langle \chi_{12,3} \rangle} = & - i (\Delta_{L1} + \Delta_2) \langle \chi_{12,3} \rangle \\
& - i \Omega_{12,3} \langle \chi_{12,12} \rangle - i \Omega_{16,3} \langle \chi_{12,16} \rangle \\
& + i \Omega_{12,3} \langle \chi_{3,3} \rangle \\
& - \frac{\Gamma_{12}}{2} \langle \chi_{12,3} \rangle
\end{aligned} \tag{51}$$

$$\begin{aligned}
\dot{\langle \chi_{3,12} \rangle} = & i (\Delta_{L1} + \Delta_2) \langle \chi_{3,12} \rangle \\
& + i \Omega_{12,3} \langle \chi_{12,12} \rangle + i \Omega_{16,3} \langle \chi_{16,12} \rangle \\
& - i \Omega_{12,3} \langle \chi_{3,3} \rangle \\
& - \frac{\Gamma_{12}}{2} \langle \chi_{3,12} \rangle
\end{aligned} \tag{52}$$

$$\begin{aligned}
\dot{\langle \chi_{16,3} \rangle} = & -i \Delta_{L1} \langle \chi_{16,3} \rangle \\
& -i \Omega_{16,3} \langle \chi_{16,16} \rangle - i \Omega_{12,3} \langle \chi_{16,12} \rangle \\
& + i \Omega_{16,3} \langle \chi_{3,3} \rangle \\
& - \frac{\Gamma_{16}}{2} \langle \chi_{16,3} \rangle
\end{aligned} \tag{53}$$

$$\begin{aligned}
\dot{\langle \chi_{3,16} \rangle} = & i \Delta_{L1} \langle \chi_{3,16} \rangle \\
& + i \Omega_{16,3} \langle \chi_{16,16} \rangle + i \Omega_{12,3} \langle \chi_{12,16} \rangle \\
& - i \Omega_{16,3} \langle \chi_{3,3} \rangle \\
& - \frac{\Gamma_{16}}{2} \langle \chi_{3,16} \rangle
\end{aligned} \tag{54}$$

$$\begin{aligned}
\dot{\langle \chi_{13,4} \rangle} = & -i \Delta_{L2} \langle \chi_{13,4} \rangle \\
& -i \Omega_{13,4} \langle \chi_{13,13} \rangle - i \Omega_{19,4} \langle \chi_{13,19} \rangle \\
& + i \Omega_{13,4} \langle \chi_{4,4} \rangle \\
& - \frac{\Gamma_{13}}{2} \langle \chi_{13,4} \rangle
\end{aligned} \tag{55}$$

$$\begin{aligned}
\dot{\langle \chi_{4,13} \rangle} = & i \Delta_{L2} \langle \chi_{4,13} \rangle \\
& + i \Omega_{13,4} \langle \chi_{13,13} \rangle + i \Omega_{19,4} \langle \chi_{19,13} \rangle \\
& - i \Omega_{13,4} \langle \chi_{4,4} \rangle \\
& - \frac{\Gamma_{13}}{2} \langle \chi_{4,13} \rangle
\end{aligned} \tag{56}$$

$$\begin{aligned}
\dot{\langle \chi_{19,4} \rangle} = & -i (\Delta_{L2} - \Delta_1) \langle \chi_{19,4} \rangle \\
& -i \Omega_{19,4} \langle \chi_{19,19} \rangle - i \Omega_{13,4} \langle \chi_{19,13} \rangle \\
& + i \Omega_{19,4} \langle \chi_{4,4} \rangle \\
& - \frac{\Gamma_{19}}{2} \langle \chi_{19,4} \rangle
\end{aligned} \tag{57}$$

$$\dot{\langle \chi_{4,19} \rangle} = i (\Delta_{L2} - \Delta_1) \langle \chi_{4,19} \rangle$$

$$\begin{aligned}
& + i \Omega_{19,4} \langle \chi_{19,19} \rangle + i \Omega_{13,4} \langle \chi_{13,19} \rangle \\
& - i \Omega_{19,4} \langle \chi_{4,4} \rangle \\
& - \frac{\Gamma_{19}}{2} \langle \chi_{4,19} \rangle
\end{aligned} \tag{58}$$

$$\begin{aligned}
\dot{\langle \chi_{10,5} \rangle} = & - i (\Delta_{L2} + \Delta_2) \langle \chi_{10,5} \rangle \\
& - i \Omega_{10,5} \langle \chi_{10,10} \rangle - i \Omega_{14,5} \langle \chi_{10,14} \rangle - i \Omega_{20,5} \langle \chi_{10,20} \rangle \\
& + i \Omega_{10,5} \langle \chi_{5,5} \rangle \\
& - \frac{\Gamma_{10}}{2} \langle \chi_{10,5} \rangle
\end{aligned} \tag{59}$$

$$\begin{aligned}
\dot{\langle \chi_{5,10} \rangle} = & i (\Delta_{L2} + \Delta_2) \langle \chi_{5,10} \rangle \\
& + i \Omega_{10,5} \langle \chi_{10,10} \rangle + i \Omega_{14,5} \langle \chi_{14,10} \rangle + i \Omega_{20,5} \langle \chi_{20,10} \rangle \\
& - i \Omega_{10,5} \langle \chi_{5,5} \rangle \\
& - \frac{\Gamma_{10}}{2} \langle \chi_{5,10} \rangle
\end{aligned} \tag{60}$$

$$\begin{aligned}
\dot{\langle \chi_{14,5} \rangle} = & - i \Delta_{L2} \langle \chi_{14,5} \rangle \\
& - i \Omega_{14,5} \langle \chi_{14,14} \rangle - i \Omega_{10,5} \langle \chi_{14,10} \rangle - i \Omega_{20,5} \langle \chi_{14,20} \rangle \\
& + i \Omega_{14,5} \langle \chi_{5,5} \rangle \\
& - \frac{\Gamma_{14}}{2} \langle \chi_{14,5} \rangle
\end{aligned} \tag{61}$$

$$\begin{aligned}
\dot{\langle \chi_{5,14} \rangle} = & i \Delta_{L2} \langle \chi_{5,14} \rangle \\
& + i \Omega_{14,5} \langle \chi_{14,14} \rangle + i \Omega_{10,5} \langle \chi_{10,14} \rangle + i \Omega_{20,5} \langle \chi_{20,14} \rangle \\
& - i \Omega_{14,5} \langle \chi_{5,5} \rangle \\
& - \frac{\Gamma_{14}}{2} \langle \chi_{5,14} \rangle
\end{aligned} \tag{62}$$

$$\begin{aligned}
\dot{\langle \chi_{20,5} \rangle} = & - i (\Delta_{L2} - \Delta_1) \langle \chi_{20,5} \rangle \\
& - i \Omega_{20,5} \langle \chi_{20,20} \rangle - i \Omega_{10,5} \langle \chi_{20,10} \rangle - i \Omega_{14,5} \langle \chi_{20,14} \rangle \\
& + i \Omega_{20,5} \langle \chi_{5,5} \rangle
\end{aligned}$$

$$-\frac{\Gamma_{20}}{2} \langle \chi_{20,5} \rangle \quad (63)$$

$$\begin{aligned} \dot{\langle \chi_{5,20} \rangle} = & i(\Delta_{L2} - \Delta_1) \langle \chi_{5,20} \rangle \\ & + i\Omega_{20,5} \langle \chi_{20,20} \rangle + i\Omega_{10,5} \langle \chi_{10,20} \rangle + i\Omega_{14,5} \langle \chi_{14,20} \rangle \\ & - i\Omega_{20,5} \langle \chi_{5,5} \rangle \\ & - \frac{\Gamma_{20}}{2} \langle \chi_{5,20} \rangle \end{aligned} \quad (64)$$

$$\begin{aligned} \dot{\langle \chi_{11,6} \rangle} = & -i(\Delta_{L2} + \Delta_2) \langle \chi_{11,6} \rangle \\ & - \frac{1}{2} i\Omega_{11,6} \langle \chi_{11,11} \rangle - \frac{1}{2} i\Omega_{21,6} \langle \chi_{11,21} \rangle \\ & + \frac{1}{2} i\Omega_{11,6} \langle \chi_{6,6} \rangle \\ & - \frac{\Gamma_{11}}{2} \langle \chi_{11,6} \rangle \end{aligned} \quad (65)$$

$$\begin{aligned} \dot{\langle \chi_{6,11} \rangle} = & i(\Delta_{L2} + \Delta_2) \langle \chi_{6,11} \rangle \\ & + i\Omega_{11,6} \langle \chi_{11,11} \rangle + i\Omega_{21,6} \langle \chi_{21,11} \rangle \\ & - i\Omega_{11,6} \langle \chi_{6,6} \rangle \\ & - \frac{\Gamma_{11}}{2} \langle \chi_{6,11} \rangle \end{aligned} \quad (66)$$

$$\begin{aligned} \dot{\langle \chi_{21,6} \rangle} = & -i(\Delta_{L2} - \Delta_1) \langle \chi_{21,6} \rangle \\ & - i\Omega_{21,6} \langle \chi_{21,21} \rangle - i\Omega_{11,6} \langle \chi_{21,11} \rangle \\ & + i\Omega_{21,6} \langle \chi_{6,6} \rangle \\ & - \frac{\Gamma_{21}}{2} \langle \chi_{21,6} \rangle \end{aligned} \quad (67)$$

$$\begin{aligned} \dot{\langle \chi_{6,21} \rangle} = & i(\Delta_{L2} - \Delta_1) \langle \chi_{6,21} \rangle \\ & + i\Omega_{21,6} \langle \chi_{21,21} \rangle + i\Omega_{11,6} \langle \chi_{11,21} \rangle \\ & - i\Omega_{21,6} \langle \chi_{6,6} \rangle \\ & - \frac{\Gamma_{21}}{2} \langle \chi_{6,21} \rangle \end{aligned} \quad (68)$$

$$\begin{aligned}
\dot{\langle \chi_{12,7} \rangle} = & -i(\Delta_{L2} + \Delta_2) \langle \chi_{12,7} \rangle \\
& -i\Omega_{12,7} \langle \chi_{12,12} \rangle - i\Omega_{16,7} \langle \chi_{12,16} \rangle - i\Omega_{22,7} \langle \chi_{12,22} \rangle \\
& + i\Omega_{12,7} \langle \chi_{7,7} \rangle \\
& - \frac{\Gamma_{12}}{2} \langle \chi_{12,7} \rangle
\end{aligned} \tag{69}$$

$$\begin{aligned}
\dot{\langle \chi_{7,12} \rangle} = & i(\Delta_{L2} + \Delta_2) \langle \chi_{7,12} \rangle \\
& + i\Omega_{12,7} \langle \chi_{12,12} \rangle + i\Omega_{16,7} \langle \chi_{16,12} \rangle + i\Omega_{22,7} \langle \chi_{22,12} \rangle \\
& - i\Omega_{12,7} \langle \chi_{7,7} \rangle \\
& - \frac{\Gamma_{12}}{2} \langle \chi_{7,12} \rangle
\end{aligned} \tag{70}$$

$$\begin{aligned}
\dot{\langle \chi_{16,7} \rangle} = & -i\Delta_{L2} \langle \chi_{16,7} \rangle \\
& -i\Omega_{16,7} \langle \chi_{16,16} \rangle - i\Omega_{12,7} \langle \chi_{16,12} \rangle - i\Omega_{22,7} \langle \chi_{16,22} \rangle \\
& + i\Omega_{16,7} \langle \chi_{7,7} \rangle \\
& - \frac{\Gamma_{16}}{2} \langle \chi_{16,7} \rangle
\end{aligned} \tag{71}$$

$$\begin{aligned}
\dot{\langle \chi_{7,16} \rangle} = & i\Delta_{L2} \langle \chi_{7,16} \rangle \\
& + i\Omega_{16,7} \langle \chi_{16,16} \rangle + i\Omega_{12,7} \langle \chi_{12,16} \rangle + i\Omega_{22,7} \langle \chi_{22,16} \rangle \\
& - i\Omega_{16,7} \langle \chi_{7,7} \rangle \\
& - \frac{\Gamma_{16}}{2} \langle \chi_{7,16} \rangle
\end{aligned} \tag{72}$$

$$\begin{aligned}
\dot{\langle \chi_{22,7} \rangle} = & -i(\Delta_{L2} - \Delta_1) \langle \chi_{22,7} \rangle \\
& -i\Omega_{22,7} \langle \chi_{22,22} \rangle - i\Omega_{12,7} \langle \chi_{22,12} \rangle - i\Omega_{16,7} \langle \chi_{22,16} \rangle \\
& + i\Omega_{22,7} \langle \chi_{7,7} \rangle \\
& - \frac{\Gamma_{22}}{2} \langle \chi_{22,7} \rangle
\end{aligned} \tag{73}$$

$$\begin{aligned}
\dot{\langle \chi_{7,22} \rangle} = & i(\Delta_{L2} - \Delta_1) \langle \chi_{7,22} \rangle \\
& + i\Omega_{22,7} \langle \chi_{22,22} \rangle + i\Omega_{12,7} \langle \chi_{12,22} \rangle + i\Omega_{16,7} \langle \chi_{16,22} \rangle
\end{aligned}$$

$$\begin{aligned}
& -i \Omega_{22,7} \langle \chi_{7,7} \rangle \\
& -\frac{\Gamma_{22}}{2} \langle \chi_{7,22} \rangle
\end{aligned} \tag{74}$$

$$\begin{aligned}
\dot{\langle \chi_{17,8} \rangle} = & -i \Delta_{L2} \langle \chi_{17,8} \rangle \\
& -i \Omega_{17,8} \langle \chi_{17,17} \rangle - i \Omega_{23,8} \langle \chi_{17,23} \rangle \\
& + i \Omega_{17,8} \langle \chi_{8,8} \rangle \\
& -\frac{\Gamma_{17}}{2} \langle \chi_{17,8} \rangle
\end{aligned} \tag{75}$$

$$\begin{aligned}
\dot{\langle \chi_{8,17} \rangle} = & i \Delta_{L2} \langle \chi_{8,17} \rangle \\
& + i \Omega_{17,8} \langle \chi_{17,17} \rangle + i \Omega_{23,8} \langle \chi_{23,17} \rangle \\
& - i \Omega_{17,8} \langle \chi_{8,8} \rangle \\
& -\frac{\Gamma_{17}}{2} \langle \chi_{8,17} \rangle
\end{aligned} \tag{76}$$

$$\begin{aligned}
\dot{\langle \chi_{23,8} \rangle} = & -i (\Delta_{L2} - \Delta_1) \langle \chi_{23,8} \rangle \\
& -i \Omega_{23,8} \langle \chi_{23,23} \rangle - i \Omega_{17,8} \langle \chi_{23,17} \rangle \\
& + i \Omega_{23,8} \langle \chi_{8,8} \rangle \\
& -\frac{\Gamma_{23}}{2} \langle \chi_{23,8} \rangle
\end{aligned} \tag{77}$$

$$\begin{aligned}
\dot{\langle \chi_{8,23} \rangle} = & i (\Delta_{L2} - \Delta_1) \langle \chi_{8,23} \rangle \\
& + i \Omega_{23,8} \langle \chi_{23,23} \rangle + i \Omega_{17,8} \langle \chi_{17,23} \rangle \\
& - i \Omega_{23,8} \langle \chi_{8,8} \rangle \\
& -\frac{\Gamma_{23}}{2} \langle \chi_{8,23} \rangle
\end{aligned} \tag{78}$$

References

- Ackerhalt J.R. and Eberly J.H., 1974, *Phys. Rev. D* **10**, 3350.
- Ackerhalt J.R., Knight P.L. and Eberly J.H., 1973 *Phys. Rev. Lett.* **30**, 456.
- Allen L. and Eberly J.H. 1975, *Optical Resonance and Two Level Atoms*, (Wiley, New York).
- Anderson N., Gallagher G.W. and Hertel I.V., 1988, *Phys. Rep.* **65**, 1.
- Bartschat K. and Blum K., 1982, *Z. Phys. A* **304**, 85.
- Baum G., 1994, Private Communication.
- Bhaskar N.D., Jaduszliwer B. and Bederson B., 1977, *Phys. Rev. Lett.* **38**, 14.
- Becker K., Dassen H.W. and McConkey J.W., 1984, *J. Phys. B* **17**, 2535.
- Bederson B., 1969a, *Comment. At. Mol. Phys.* **1**, 41.
- Bederson B., 1969b, *Comment. At. Mol. Phys.* **1**, 65.
- Blum K., 1981, *Density Matrix Theory and Applications*, (Plenum, New York).
- Burden R.L. and Faires J.D., 1989, *Numerical Analysis*, (PWS-KENT, Boston)
- Bray I., Konovalov D.A., McCarthy I.E., 1991, *Phys. Rev. A* **43**, 5878.

- Cardimona D.A., Raymer M.G. and Stroud C.R., 1982, *J. Phys. B* **15**, 55.
- Cardimona D.A. and Stroud C.R., 1983, *Phys. Rev. A* **27**, 2456.
- Chormaic S.N., Chwirot S. and Slevin J., 1993, *J. Phys. B* **26**, 139.
- Condon E.U. and Shortley G.H., 1967, *The Theory of Atomic Spectra*, (Cambridge University Press)
- Corney A., 1977, *Atomic and Laser Spectroscopy*, (Clarendon Press, Oxford).
- Ducloy M., 1973, *Phys. Rev. A* **8**, 1844.
- Edmonds A.R., 1974, *Angular Momentum in Quantum Mechanics*, (Princeton University Press, Princeton, NJ).
- Eminyan M., MacAdam K.B., Slevin J. and Kleinpopp H., 1973, *Phys. Rev. Lett.* **31**, 576.
- Eminyan M., MacAdam K.B., Slevin J., Standage M.C. and Kleinpopp H., 1974, *J. Phys. B* **7**, 1519.
- Eminyan M., MacAdam K.B., Slevin J., Standage M.C. and Kleinpopp H., 1975, *J. Phys. B* **8**, 2058.
- Fano U., 1957, *Rev. Mod. Phys.* **45**, 553.
- Fano U. and Macek J.H., 1973, *Rev. Mod. Phys.* **45**, 553.

- Farrell P.M., MacGillivray W.R. and Standage M.C., 1988, *Phys. Rev A* **37**, 4240.
- Farrell P.M., MacGillivray W.R. and Standage M.C., 1989, *J. Phys. B* **22**, L527.
- Farrell P.M., MacGillivray W.R. and Standage M.C., 1991, *Phys. Rev A* **44**, 1828.
- Farrell P.M., 1992, PhD Thesis, (Griffith University, Unpublished).
- Farrell P.M. and MacGillivray W.R., 1994, *J. Phys A*, In Press
- Fischer A. and Hertel I.V., 1982, *Z. Phys. A* **304**, 103.
- Hanne G.F., 1983, *Phys. Rep.* **95**, 95.
- Harting E. and Read F.H., 1976, *Electrostatic Lenses*, (Elsevier Scientific Publishing Company).
- Heddle D.W.O., 1983, *J. Phys. B* **16**, 275.
- Heddle D.W.O., 1989, *Rev. Mod. Phys.* **61**, 221.
- Hermann H.W., Hertel I.V., Reiland W., Stamatovic A. and Stoll W., 1977, *J. Phys. B* **10**, 251.
- Hermann I.V., Hertel I.V. and Kelly M.H., 1980. *J. Phys. B* **13**, 3465.
- Hermann I.V. and Hertel I.V., 1982, *Comments At. Mol. Phys.* **12**, 61.

- Hertel I.V. and Stoll W., 1974a, *J. Phys. B* **7**, 570.
- Hertel I.V. and Stoll W., 1974b, *J. Phys. B* **7**, 583.
- Hertel I.V. and Stoll W., 1976, *J. Phys. B* **47**, 214.
- Hertel I.V. and Stoll W., 1977, *Adv. At. Mol. Phys.* **13**, 113.
- Jaduszliwer B., Weiss P., Tino A. and Bederson B., 1984, *Phys. Rev. A* **30**, 1255.
- Kessler J., 1976, *Polarised Electrons*, (Springer-Verlag, Berlin).
- King G.C.M., Adams A. and Read F.H., 1972, *J. Phys. B* **5**, L254.
- Knight P.L., 1980, *Opt. Commun.* **32**, 261.
- Knight P.L., 1992, *Proceedings of the 5th Physics Summer School: Atomic and Molecular Physics and Quantum Optics*, edited by Bachor H-A., Kumar K., and Robson B.A., (World Scientific, Singapore).
- Law M.R. and Teubner P.J.O., 1993, *Australian Conference on Optics, Lasers and Spectroscopy*, Book of Abstracts (Melbourne).
- van Linden van den Heuvell H.B., Nienhuis G., van Eck J. and Heideman H.G.M., 1981, *J. Phys. B* **14**, 2667.
- van Linden van den Heuvell H.B., van Gasteren E.M., van Eck J. and Heideman H.G.M., 1983, *J. Phys. B* **16**, 1619.

- Loudon R., 1983, *The Quantum Theory of Light* Second Edition, (Clarendon Press, Oxford).
- McCarthy I.E., 1992, *Proceedings of the 5th Physics Summer School: Atomic and Molecular Physics and Quantum Optics*, Ed. Bachor H-A., Kumar K., and Robson B.A., (World Scientific, Singapore).
- McCarthy I.E. and Stelbovics A.T., 1983, *Phys. Rev. A* **28**, 2693.
- Macek J. and Jaecks D.H., 1971, *Phys. Rev. A* **4**, 2288.
- Macek J.H. and Hertel I.V., 1974, *J. Phys. B* **7**, 2173.
- MacGillivray W.R. and Standage M.C., 1988, *Phys. Rep.* **168**, 1.
- MacGillivray W.R. and Standage M.C., 1991, *Comment. At. Mol. Phys.* **26**, 179.
- MacGillivray W.R., 1993, Lecture Notes, (Griffith University, Unpublished).
- Madison D.H., Bray I., and McCarthy I.E., 1991, *J.Phys. B* **25**, 5199.
- Madison D.H., Bartschat K. and McEachran R. P., 1992, *J.Phys. B* **24**, 3861.
- McClelland J.J. and Kelly M.H., 1985, *Phys. Rev. A* **31**, 3704.
- McClelland J.J., Kelly M.H. and Celotta R.J., 1985, *Phys. Rev. Lett.* **55**, 688.
- McClelland J.J., Kelly M.H. and Celotta R.J., 1986, *Phys. Rev. Lett.* **56**, 1362.

- McClelland J.J., Kelly M.H. and Celotta R.J., 1987, *J. Phys. B* **20**, L385.
- McClelland J.J., Kelly M.H. and Celotta R.J., 1989, *Phys. Rev. A* **40**, 2321.
- McClelland J.J., Hanne G.F., Scholten R.E. and Celotta R.J., 1993, *7th International Symposium on Polarisation and Correlation in Electronic and Atomic Collisions*, Book Abstracts (Bielefeld, Germany).
- McConkey J.W., Trajmar S., Nickel J.C. and Csanak G., 1986, *J. Phys. B* **19**, 2377.
- McConkey J.W., van der Burgt P.J.M., Corr J.J. and Plessis P., 1989, *Proc. Int. Symp. Correlation and Polarisation in Electronic and Atomic Collisions* (Hoboken, NJ) (NIST Special Publication no 789), ed P.A. Neil, K.H. Becker and M.H. Kelly, 45.
- McConkey J.W., van der Burgt P.J.M. and Corr J.J., 1991, *Proc. Int. Symp. Correlation and Polarisation in Electronic and Atomic Collisions* (Adelaide, Australia) (Institute of Physics Conference Series Number 122), Ed. P.J.O. Teubner and E. Weigold, 77.
- McDaniel E.W., 1989, *Atomic Collisions*, (Wiley, New York).
- McLucas C.W., 1982, PhD Thesis, (Griffith University, Unpublished).
- Messiah A., 1965, *Quantum Mechanics 2*, (Wiley, New York).
- Meng X-K., 1992, Private Communication.
- Meng X-K., MacGillivray W.R. and Standage M.C., 1992, *Phys. Rev. A* **45**, 1767.

- Milonni P.W., 1976, *Phys. Rep.* **25**, 1.
- Mitroy J., McCarthy I.E. and Stelbovics A.T., 1987, *J. Phys. B* **20**, 4827.
- Moore D.L. and Norcross, 1972, *J. Phys. B* **5**, 1482.
- Murray A.J., Webb C.J., MacGillivray W.R. and Standage M.C., 1989, *Phys. Rev. Lett.* **62**, 411.
- Murray A.J., Pascual R., MacGillivray W.R. and Standage M.C., 1992, *J. Phys. B* **25**, 1915.
- Nienhuis G., 1980, *Coherence and Correlation in Atomic Collisions*, edited by Kleinpoppen H. and Williams J.F., (Plenum, New York), 121.
- Pegg D.T., 1980, *Laser Physics*, edited by Walls D.F. and Harvey J.D., (Academic, Sydney).
- Pegg D.T. and MacGillivray W.R., 1986, *Opt. Commun.* **59**, 113.
- Percival I.C. and Seaton M.J., 1958, *Phil. Trans. R. Soc.* **A251**, 113.
- Register D.F., Trajmar S., Jensen S.W. and Poe R.T., 1978, *Phys. Rev. Lett.* **41**, 749.
- Riley J.L., Teubner P.J.O. and Brunger M.J., 1985, *Phys. Rev. A* **31**, 1959.
- Riley J.L., Teubner P.J.O. and Brunger M.J., 1986, *J. Phys. B* **19**, 129.
- Risley J.S., 1972, *Rev. Sci. Instrum.* **43**, 95.

- Slevin J., Eminiyan M.J., Woolsey J.M., Vassilev G. and Porter H.Q., 1980, *J. Phys. B* **13**, L341.
- Sobelman I.I., 1979, *Atomic Spectra and Radiative Transitions*, (Springer-Verlag, Berlin).
- Sang R.T., MacGillivray W.R. and Standage M.C., 1991, *Eighteenth International Conference on the Physics of Electronic and Atomic Collisions* (Brisbane), Book of Abstracts, 107.
- Sang R.T., Farrell P.M., Madison D.H., MacGillivray W.R. and Standage M.C., 1994, *J. Phys. B* **27**, 1187.
- Scholten R.E., Anderson T. and Teubner P.J.O., 1988, *J. Phys. B* **21**, L473.
- Scholten R.E., Shen G.F. and Teubner P.J.O., 1993, *J. Phys. B* **26**, 987.
- Standage M.C. and Kleinpoppen, 1976, *Phys. Rev. Lett.* **36**, 577.
- Summy G.S., Lohmann B., MacGillivray W.R. and Standage M.C., 1994, *Z. Phys. D* **30**, 155.
- Teubner P.J.O., Riley J.O., Brunger M.J. and Buckman S.J., 1986, *J. Phys. B* **19**, 3313.
- Teubner P.J.O., Scholten R.E. and Shen G.F., 1989, *Proc. Int. Symp. Correlation and Polarisation in Electronic and Atomic Collisions* (Hoboken, NJ) (NIST Special Publication no 789), Ed. P.A. Neil, K.H. Becker and M.H. Kelly, 45.

- Teubner P.J.O., Scholten R.E. and Shen G.F., 1990, *J. Mod. Opt.* **37**, 1761.
- Trajmar S. and Cartwright D.C., 1984, Excitation of Molecules by Electron Impact, *Electron-Molecule Interactions and Their Applications*, Vol 1 , Ed. L.G. Christophorou (Academic, New York).
- Varshalovich D.A., Moskalev A.N. and Khersonskii, 1988, Quantum Theory of Angular Momentum, (World Scientific, Singapore).
- Weigold E., Frost L. and Nygaard K.J., 1980, *Phys. Rev. A* **21**, 1950.
- Whitley R.M. and Stroud C.R., 1976, *Phys. Rev. A* **14**, 1498.
- Williams J.F., 1981, *J. Phys. B* **39**, 621.
- Williams J.F., 1986, *Aust. J. Phys.* **39**, 621.
- Wolcke A., Goeke J., Hanne G.F., Kessler J., Vollmer W., Bartschat K., and Blum K., 1984, *Phys. Rev. Lett.* **52**, 1108.
- Zetner P.W., Trajmar S., Csanak G. and Clark R.E.H., 1989, *Phys. Rev. A* **39**, 6022.
- Zipf E.C., 1984, Dissociation of Molecules by Electron Impact, *Electron-Molecule Interactions and Their Applications*, Vol 1 , Ed. L.G. Christophorou (Academic, New York).
- Zuo M., Jiang T.Y., Vuskovic L. and Bederson B., 1990, *Phys. Rev. A* **41**, 2489.